Investigations of optimum design of heat exchangers of thermoacoustic engines

Haruko Ishikawa, B.Sc.

Department of Mechanical Engineering
The University of Queensland

A thesis submitted for the degree of Doctor of Philosophy
December 1999

Abstract

The study of thermoacoustic effects is a relatively new area, particularly in application to thermoacoustic engines. For thermoacoustic engines to be commercially viable, there are still many aspects to be investigated, not only practical aspects but also at the fundamental level of physics. Particularly lacking is research on heat exchangers in thermoacoustic engines, despite the fact that this is one of the most important components, for which a design methodology does not yet exist.

The primary aim of this work was to investigate the design methodology for heat exchangers in thermoacoustic devices to improve their efficiency. In this work, second law analysis was chosen as the design methodology and was applied to a simplified model of heat exchangers in thermoacoustic engines and its validity was examined. However, for the analysis to be useful to design practical devices, further knowledge of the heat transfer mechanism in oscillatory, compressible flow, and on the development of boundary layers under such conditions are required. This is not currently available for thermoacoustic devices.

The commercial software PHOENICS was used to investigate this oscillatory heat transfer problem numerically. To test the capability of the software for simulating thermoacoustic phoenomena, two dimensional standing waves and thermoacoustic couples were simulated at various operating conditions and geometries, including conditions very close to those at heat exchangers in thermoacoustic engines. The results were compared with existing analytical solutions and the results of numerical simulations from others and showed that PHOENICS is capable of simulating thermoacoustic effects. However, the accuracy of second order effects, such as heat flux induced by thermoacoustic effects, was limited by the capability of PHOENICS and the results should be interpreted with this in mind.

Energy and flow fields from thermoacoustic couple simulations were investigated from plots of energy vectors, energy lines, instantaneous velocity fields, particle traces and energy dissipation. The dependence of such quantities on plate spacing, plate length and Mach numbers are presented. One important result from these test which is relevant to the design of regenerators or heat exchangers in thermoacoustic engines was that a net heat pumping effect appears only near the edges of thermoacoustic couple plates, within about a particle displacement distance from the edges. Also it was observed that the energy dissipation near the plate is proportional to the plate surface area but increases quadratically as the plate spacing is reduced. The results also indicated the presence of larger scale vortical motion outside the plates which disappeared as the plate spacing was reduced. The presence of such vortical motion did not seem to influence the heat transfer to the plates.

In order to simulate heat exchangers in thermoacoustic engines without simulating the whole device, boundary conditions representative of those near the ends of the regenerator plate were considered and tested. Although in some test cases, the simulation converged to a solution with minimal energy imbalances, there was a major discontinuity in the energy flux vectors near the boundary. Further investigations (both numerical and experimental) are required to provide further insight into the boundary conditions which need to be specified for future simulations of heat exchangers in thermoacoustic engines.

Originality

The work presented in this thesis is, to the best of the author's knowledge and belief, original and the author's own, except as acknowledged in the text. The material contained in this thesis has not been submitted, either in whole or in part, for another degree at The University of Queensland or any other university.

Haruko Ishikawa

Related Publications

Ishikawa, H. and Hobson, P. A. “Optimisation of heat exchanger design in a thermoacoustic engine using a second law analysis”, *Int. Comm. Heat Mass Transfer.*, Vol. 23, No. 3, 1996.

Ishikawa, H. and Mee, D. J, “Numerical investigations of thermoacoustic effects on isothermal plates”, *61st Meeting on Cryogenics and Superconductivity.*, Tokyo, November 1999.

Ishikawa, H. and Mee, D. J. “Numerical investigations of flow and energy fields near a thermoacoustic couple”, *being prepared for publication.*

Acknowledgment

My deepest gratitude goes to my supervisor Dr. D. J. Mee for his patience and generous support and for taking the place of Dr. P. A. Hobson after his departure from the department, despite the fact that thermoacoustic engines were totally new to him.

I am also grateful to Dr. P. A. Hobson (Sugar Research Institute, Queensland) to whom I owe the idea and the outline of the current work. I am grateful to the valuable discussions and guidance by over 500 e-mails and phone calls particularly between 1995 and 1996 after resource constraints forced me to change my thesis outline from experimental to 'something else'.

Many thanks to the head of department, Prof. K. Bremhorst, my associate supervisor Dr. T. Steinberg and all the staff at the Mechanical Engineering Department particularly to Mr. S. Kimball and Mr. B. Daniel for always solving problems with the use of computers and to Mr. C. Beech and Mr. T. Olds for help in constructing the demonstrative thermoacoustic device although in the end it was not implemented in the current work, is now enjoyed by undergraduate students. I am also grateful to the University of Queensland for the writhing thesis scholarship awards.

My special thanks goes to my friends and great mentors Dr. K. Weinmann (Deutsche Luft und Raumfahrt Gesellschaft), Mr. M. Nichols (High Performance Computing Information Technology Services, The University of Queensland), Dr. P. Jacob, Associate Prof. L. Kwok (City University of Hongkong), Prof. A. Ohuchi (Hokkaido University) for their kind support and advise on the computational fluid dynamics, the use of the high performance computing facilities and on research in general.

I appreciate the valuable discussions with Prof. M. Ozawa (Kansai University), Mr. T. Inoue (Aishin Seiki Co. Ltd.), Prof. Yazaki (Aichi University of Education), Dr. Tominaga (Tsukuba University) that enabled me to regain confidence in the current work. I would also like to thank Dr. G. Swift (Los Alamos National Laboratory) for always sending me the latest papers and software on thermoacoustic engines.

My sincere thanks goes to Miss. Morrison, the head of Grace College, to the late Mr. N. Asakuno of Tokyo Gas Co. Ltd. and to my close friends in Australia who constantly encouraged me to continue to complete this work.

Finally and most importantly, many thanks to my dear friends and family in Japan for their understanding and long term support, and particularly to my parents, two of the hardest working business people, for being my only sponsors.

Contents

List of Figures

List of Tables

Nomenclature

Symbols

A	Area, m^2
a	Sound speed, m/s
c_p	Specific heat at constant pressure, J/KgK
d	Diameter of the tube, m
$\dot{e}$	Energy flux density, W/m^2
$\mathbf{e}$	Energy flux vector, W/m^2
e_i	Internal energy per unit mass, J/Kg
$\dot{H}$	Energy flux, W
h	Enthalpy per unit mass, J/Kg
Im	Imaginary part of
K	Thermal conductivity, W/m K
l_0	Plate half spacing, m
M	Mach number
Nu	Nusselt number
P, p	Pressure, Pa
Pe_ω	Oscillating Peclet number
Pr	Prandtl number
$\dot{Q}$	Heat flux, W
$\dot{q}$	Heat flux per unit area, W/m^2
$\mathbf{q}$	Heat flux vector, W/m^2
R	Resonator radius, m; Gas constant, J/Kg K
r	volume fraction of phase
Re	Reynolds number; Real part of
S	Entropy, J/K
s	Entropy per unit mass, J/K Kg
$\dot{S}_{gen}$	Entropy generation rate, W/K
$\dot{s}_{gen}$	Entropy generation rate per unit volume, W/K m^3
$\mathbf{s}$	Entropy flux vector per unit volume, W/K m^3

T	Temperature, K
t	Time, s
$\mathbf{v}$	Velocity vector, m/s
v	Velocity, m/s
u	x-component velocity, m/s
v	y-component velocity, m/s
v_x	x-component velocity, m/s (used in sections 2.2 and 3.2.2)
v_y	y-component velocity, m/s (used in sections 2.2 and 3.2.2)
$\dot{W}$	Work flux, W
x	Position along sound wave propagation, m
y	Position perpendicular to sound wave propagation in the gas, m
y'	Position perpendicular to sound wave propagation in the plate, m
y_0	Plate half spacing, m
α	Thermal diffusivity, m^2/s
α_{reg-T}	Temporal phase shift between the temperature and the pressure at regenerator, rad
α_{reg-u}	Temporal phase shift between the temperature and the velocity at regenerator, rad
β	Thermal expansion coefficient, 1/K
Δ	Grid size; Increment
δ	Penetration depth, m
Γ	Normalized temperature gradient
γ	Specific heat ratio
κ	Wave number
ω	Angular frequency, rad/s
λ	Wave length, m
μ	Dynamic viscosity, Kg/m s
ν	Kinematic viscosity, m^2/s
Σ	Viscous stress tensor, Pa
Π	Perimeter, m
ρ	Density, Kg/m^3
Φ	Dissipation function, W/m^3
Φ_H	Heat function, W/m

Subscripts

1	First order
2	Second order
A	Amplitude
a	Offset from the mean
b	Bulk
C	Cold
cen	Center
cl	Closed end
$crit$	Critical
$diss$	Dissipation
err	Error
H	Hot
he	Heat exchanger
in	Inner
L	Plate length
m	Mean
pl	Plate
x	x-component
y	y-component
s	Solid
κ	Thermal
ν	Viscous

Superscripts

s	Standing wave
$\sim$	Complex conjugation

Acronyms

CFD	Computational Fluid Dynamics
COP	Coefficients of performance
EFF	Efficiency
PHOENICS	Parabolic Hyperbolic Or Elliptic Numerical Integration Code Series

Chapter 1

Introduction

The destruction of the ozone layer by chlorofluorocarbons (CFCs) is increasing at an alarming rate. CFCs are used in various applications, such as plastic insulation for buildings and appliances, solvents for cleaning and as refrigerants in domestic and industrial refrigeration and air conditioning (Fischer 1993). In the last two decades, international regulations have been set to ultimately diminish the use of CFCs by developing alternative methods that are environmentally benign.

Thermoacoustic engines that were invented in the United States in the 1980s, were originally considered appropriate for cryogenic applications. However, the fact that they can provide cooling (or heating) using environmentally benign gases is ideal for the current environmental situation.

Despite these merits, there are still many fundamental aspects that need further investigation to fully control the performance of thermoacoustic devices. Particularly lacking is research into heat exchangers in thermoacoustic engines despite the fact that without heat exchangers, thermoacoustic engines can not operate.

This chapter gives a brief introduction to thermoacoustic engines, and provides the aims, an outline and the contributions of the current work.

1.1 Thermoacoustic engines

A thermoacoustic engine is a device which makes use of the thermoacoustic phenomenon and functions as a heat pump or a prime mover. The thermoacoustic phenomenon can be generally described as a heat transportation or a work generation in the direction of sound wave propagation, due to the interaction between the sound wave and a second medium (such as a plate or a tube wall). Details of the way the direction of heat or work flux are determined are described in section 2.1 of chapter 2. Simple examples of the thermoacoustic phenomenon can be observed either when a large temperature gradient or a sound wave is applied to a tube. In the first case, it emits a sound (i.e. operating as a prime mover) and in the latter case, one part of the tube wall is cooled and the other part becomes hotter (i.e. operating as a heat pump).

The earliest observed example of the thermoacoustic phenomenon was in 1777 by Higgins in which acoustic oscillation in a large pipe was excited by suitable placement of a hydrogen flame inside the pipe (Swift 1988). Another example was observed by glass blowers over 100 years ago. When the glass bulb was attached to a cool glass tubular stem, the stem tip sometimes emitted sound. The phenomenon was qualitatively discussed by Lord Rayleigh (1878).

A more recent example is the Taconis oscillation that has been considered a nuisance phenomenon by cryogenic physicists. In particular, this phenomenon is observed in the pumping line from a liquid helium reservoir to a room temperature system, along which a steep temperature gradient is maintained. Within the tube, acoustic oscillation with high pressure amplitude, accompanied by a considerable amount of heat flux along it into the helium liquid reservoir, is observed (Yazaki *et al.* 1979, 1980, Kuzmina 1992).

Recognition of the usefulness of the thermoacoustic phenomenon, particularly as a refrigerator for low temperature science, was first made by John C. Wheatley and his colleagues at the Los Alamos National Laboratory in 1982 (Wheatley 1982). They considered that, by using the phenomenon, they could build a reliable, low vibrational, environmentally friendly and compact device which would meet the demand identified in cryogenic physics. Their earlier version of the demonstrative thermoacoustic engine called the 'beer cooler' (Swift 1988, Wheatley *et al.* 1985, 1986, 1989) is shown in figure 1.1. This is a heat driven heat pump which consists of prime mover and heat pump stacks and four heat exchangers in a sealed resonator. It has a half meter long tube terminating with a 2 liter bulb and contains helium at a mean pressure of 3 bar. The 'stack' is a block consisting of thin plates aligned at a constant spacing. The heat exchangers in this demonstration device have a similar configuration to the stacks. When heat is applied to the hot heat exchanger, some of the heat is used to generate an acoustic wave at the prime mover stack and the rest of the heat is dumped at the room temperature heat exchanger. Then at the heat pump stack, the acoustic wave works to carry heat from the cold heat exchanger and dumps heat at the room temperature heat exchanger. With 350 W of heat applied at the hot heat exchanger at 390° C, it resonated at 585 Hz and the cold end of heat exchanger temperature reached 0°C. The beer cooler has no moving parts (neglecting how the heat is removed from heat exchanger) yet achieves cooling.

The heart of the thermoacoustic engine requires a maximum of only one moving part (that being the diaphragm of the speaker if the heat pump is not heat driven) and an environmentally benign working fluid to achieve cooling, heating or both. Similar devices to the thermoacoustic engine are the well known Stirling engine and pulse tube refrigerators that have favorable characteristics very similar to those of the thermoacoustic engine. These characteristics are:

- Minimal pollution (an environmentally friendly medium is used)

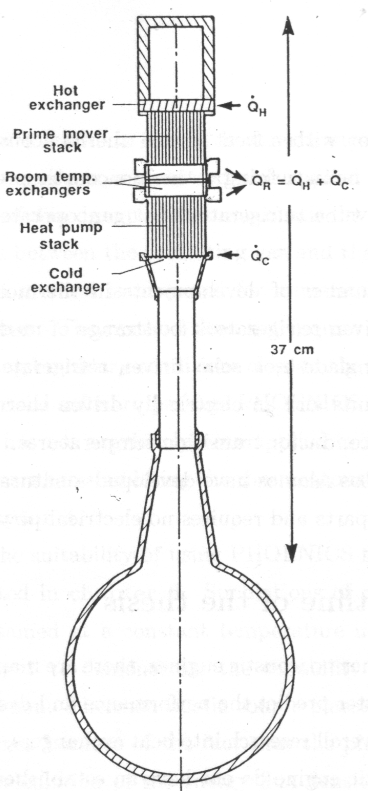

Figure 1.1: The beer cooler. (Source: Fig.3 of Swift 1988)

- Low levels of noise and vibration (No moving parts except for the speaker diaphragm when it is sound driven)

- Flexibility in terms of energy sources (gas, solar power, etc.) that can be used to drive the engine as long as a sufficiently high temperature can be provided.

Configurations of thermoacoustic engines are simpler than Stirling engines or pulse tube refrigerators, and, as a consequence, they are expected to have better reliability. These features were considered ideal for refrigeration in spaceships where long term reliability and low vibration levels are required.

In addition to these merits, both Minner *et al.* (1997) and Ozawa (1997) indicate that the coefficients of performance (COP) of thermoacoustic refrigerators are comparable to those of existing vapor compression type refrigerators.

A wide variety of applications have been developed to date. Garrett *et al.* (1992) built the loud speaker driven Space Thermoacoustic Refrigerator (STAR) which was flown on the space shuttle (STS42) in January 1992. Garrett (1993b) later constructed the Thermoacoustic Life Sciences Refrigerator (TALSR) which is more like a domestic refrigerator, also intended for use in space.

Since the early 1980s, prototypes of many applications have been investigated and developed. These are the under water sound generator (Gabrielson 1991), the frequency projectors (Ward and Merrigan 1992), and the Acoustic cryocooler (Swift *et al.* 1989) which is a pulse tube refrigerator with a heat driven thermoacoustic driver. Godshalk (1991) investigated a method of miniaturizing a thermoacoustic pressure wave generator for use as the driver of a pulse tube refrigerator that can operate at a wide variety of frequencies.

Garrett (1993a) reports a number of developments in thermoacoustic refrigeration. These are thermoacoustically driven refrigerators for storage of medical supplies and vaccine by burning kerosene in Bangladesh, a solar driven refrigerated cargo container for the transportation of tropical fruits and an electrically driven thermoacoustic cryocooler designed to reach high-T_C superconductor transition temperatures.

More recently, Cryenco and Los Alamos have developed a natural gas powered natural gas liquifier that has no moving parts and requires no electrical power (Swift 1997).

1.2 Aims and the outline of the thesis

Despite all the developments in thermoacoustic engines, there are many remaining problems to be investigated in order to better predict the performance and design of thermoacoustic engines. Particularly lacking is overall research into heat exchangers, and as a consequence, heat exchangers in thermoacoustic engine do not have an established method of design.

Heat exchangers in thermoacoustic engines are crucial for engines to be utilized in any application. It is important to make the heat exchange process in heat exchangers efficient to improve the overall efficiency of the thermoacoustic device.

Based on the literature survey it is clear that:

- there is a lack of knowledge on the energy transfer in heat exchangers of thermoacoustic engines,
- it is difficult to isolate and investigate the heat exchanger section of a thermoacoustic engine and there has been no experimental or analytical work of the kind to date, and
- there is no method available for optimizing the design of the heat exchangers in thermoacoustic engines.

The aim of the current work is to investigate the operation and the optimum design of the heat exchangers in thermoacoustic engines with a view to improving overall efficiency.

In order to achieve these aims, first, in **chapter 2**, the mechanisms of thermoacoustic engines are discussed and compared to other reciprocating devices. Then the governing equations and existing analytical models are described. A literature survey has been carried out to clarify issues that need further research in thermoacoustic engines. Surveys were also carried out on similar devices in order to compensate for the lack of information on the energy transfer mechanism near the plate surface subject to the oscillatory flow inside thermoacoustic devices.

In **chapter 3**, a method to design heat exchangers in the thermoacoustic engines based on second law analysis is discussed and applied to existing devices. However, for this method to be useful in design of thermoacoustic devices, further knowledge of the heat transfer mechanisms between the oscillating gas and the plate are required.

In **chapter 5**, a method is proposed for numerically simulating heat exchangers in thermoacoustic engines. The method does not require the whole engine to be simulated but involves specifying boundary conditions close to the heat exchangers of thermoacoustic devices. The commercial software package PHOENICS is used for performing the simulations. This package has not previously been applied to thermoacoustic simulations; therefore possible problems when simulating the thermoacoustic phenomenon using PHOENICS are discussed in **chapter 4**.

Following this, the suitability of using PHOENICS for simulation of acoustic standing waves is demonstrated in **chapter 6**. Simulations of a thermoacoustic couple (which is a single plate maintained at a constant temperature in the acoustic standing wave) are reported in **chapter 7** to demonstrate the capability of PHOENICS to simulate thermoacoustic phenomenon. Thermoacoustic couple plates are similar to heat exchangers in thermoacoustic engines because of the fact that the plates are maintained at a constant temperature. The calculation of the energy flux density and entropy generation at various test conditions revealed some interesting features of the thermoacoustic phenomenon at plate edges that have not been investigated previously. However various tests in **chapter 7** also indicate possible problems that may occur when simulating only the heat exchangers without simulating the whole thermoacoustic device.

In **chapter 8**, another step towards simulation of heat exchangers is made by simulations of thermoacoustic couples using geometries and operating conditions that are typical of heat exchangers in existing thermoacoustic devices. Findings from these tests give more understanding to the energy transfer mechanism in heat exchangers and regenerators in thermoacoustic devices. The current work is one of a few numerical investigations of this type. Then the boundary condition at the end of the regenerator, which are proposed in chapter 5 for simulation of heat exchangers, are tested. Although in terms of the overall energy balance of the simulation domain, the simulations at certain operating conditions met the criteria established in chapter 4 for the simulation to be considered valid, a major problem was observed in energy vectors near where the regenerator boundary conditions are imposed.

Based on the findings in both chapter 7 and chapter 8, proposals for further research are made in **chapter 9**, along with a summary and conclusions of the thesis.

The outcomes of the research will lead to further understanding of the energy transfer process in an oscillating flow near a plate. The information obtained from the simulations will be useful not only in thermoacoustic devices but for other devices such as those that have components subject to oscillatory flows.

Chapter 2

Background theory

In this chapter, first, the mechanism of thermoacoustic engines and other similar devices and their differences are described. Then the most widely used analytical models of thermoacoustic engines are described.

Following this, the literature is reviewed in order to clarify what has been done and what are the further investigations needed in the development of thermoacoustic engines. Literature surveys have not been limited only to thermoacoustic engines but also cover some other reciprocating devices. Based on the survey, further research that is required, particularly to meet the purpose of the current work, is discussed.

2.1 Mechanism

2.1.1 Thermoacoustic engines

As described by Swift (1988), the acoustic wave in a thermoacoustic engine is a resonant fundamental mode standing wave. The thermoacoustic effect occurs as a consequence of the interaction between the standing wave and a second medium such as a plate. In an ideal standing wave set up in an adiabatic enclosure, the temperature and pressure oscillations are in phase and the velocity oscillation is 90° out of phase. In an ideal standing wave in the absence of viscosity, the gas at each location oscillates but there is no mean flow velocity.

Distributions of the pressure and the velocity amplitudes in a quarter wave length resonator are shown in figure 2.1. The closed end of the resonator is at $x = 0$. The amplitudes of the fluctuating pressure and velocity for an unperturbed one dimensional standing wave are:

$$p_1^s = P_A cos(kx) \tag{2.1}$$

$$u_1^s = \frac{-P_A}{\rho_m a} sin(kx), \tag{2.2}$$

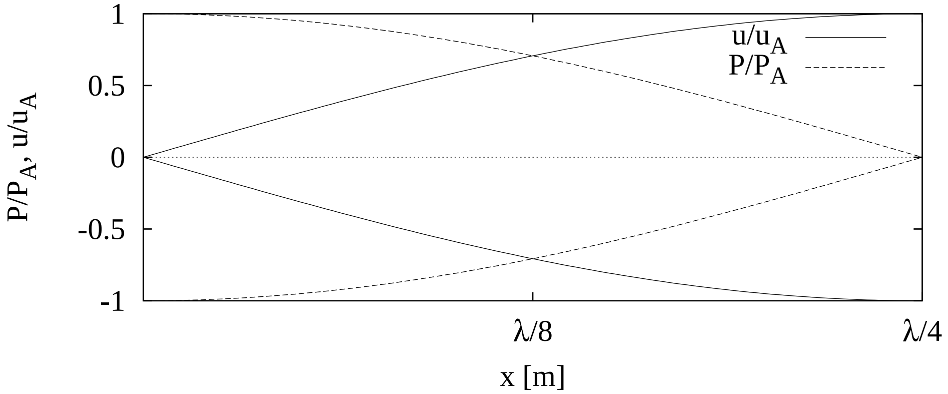

Figure 2.1: Pressure and velocity amplitudes of the standing wave.

where k is the wave number and, for an inviscid gas, $k = \omega/a$. Subscript m indicates the mean value, 1 indicates only the first order amplitudes are considered and subscript s indicates the ideal standing wave. The temperature fluctuations can be derived from the pressure fluctuations by assuming that the fluctuations are small and that the sound wave is adiabatic. Following Swift (1988), the pressure and temperature fluctuations can be related by

$$T_1^s = (\frac{\partial T}{\partial p})_s p_1^s.$$

using one of the Maxwell relations and properties of the partial derivative. Again from one of the Maxwell relations,

$$(\frac{\partial T}{\partial p})_s = -\frac{1}{\rho_m^2}(\frac{\partial \rho}{\partial s})_p.$$

Noting that

$$(\frac{\partial \rho}{\partial s})_p = (\frac{\partial \rho}{\partial T})_p(\frac{\partial T}{\partial s})_p,$$

we can write

$$T_1^s = -\frac{1}{\rho_m^2}(\frac{\partial \rho}{\partial T})_p(\frac{\partial T}{\partial s})_p p_1^s.$$

Introducing the thermal expansion coefficient

$$\beta = -\frac{1}{\rho_m}(\frac{\partial \rho}{\partial T})_\rho$$

and noting that

$$(\frac{\partial T}{\partial s})_p = \frac{T_m}{c_p}$$

and for an ideal gas, $T_m\beta = 1$, we obtain

$$T_1^s = \frac{p_1^s}{\rho_m c_p}. \tag{2.3}$$

In order to explain the mechanism, first, a thermoacoustic couple is considered. The thermoacoustic couple was originally designed by Wheatley *et al.* (1983) in order to clearly demonstrate the thermoacoustic phenomenon. The thermoacoustic couple is a stack of a few short plates in a resonator and is designed so that stack can be placed at any position within the standing wave.

Initially when the standing wave is set up in the resonator, heat is pumped along the plate towards the closed end (x=0 in figure 2.1) developing a mean temperature gradient in the plate and the gas near the plate. Temperature gradient does not continue to increase because of the heat conduction in the gas and the plate. At the steady state the amount of heat that is pumped towards the closed end and that conducted down the temperature gradient by conduction balances.

In order to simplify the explanation, we look at a single plate where the plate temperature is held constant and we consider the two dimensional case. The plate is short in comparison with the wave length and it is placed between x=0 and $\lambda/4$. The viscosity of the gas is ignored so that the temporal phase difference between the pressure and the velocity is 90° even near the plate.

Consider a block of gas near the plate, as a 'gas parcel' as in figure 2.2. In picture (1) of figure 2.2 (a), the gas parcel on the right, shown by the dotted line, is at the point in the cycle where the pressure amplitude is negative and maximum while the velocity amplitude is zero. The smaller gas parcel shown by the solid line on the left in pictures (1) and (2) is approximately a half of a cycle later. At this point in the cycle, the pressure amplitude is at its maximum while the velocity amplitude is zero. The gas parcel is compressed and the temperature of the parcel temporarily becomes higher than that of the plate and heat is transferred from the gas parcel to the nearby plate surface as in picture (2). The temperature of the gas parcel after it ejects the heat should be approximately equal to the temperature of the plate. As it returns to right as shown in picture (3), while the pressure amplitude decreases and the velocity amplitude reaches zero, the gas parcel expands and the temperature of the parcel becomes lower than that of the plate and therefore it receives heat from the plate as in picture (4). This process occurs all along the plate surface and, as a consequence, heat is carried through the gas towards the pressure antinode (i.e. towards the closed end).

When a modest temperature gradient is applied to the plate (with the higher temperature being at the plate edge closest to the closed end of the tube), if there is sufficient acoustic work to compress gases, heat will be pumped from the colder end of the plate to the hotter end, i.e. the regenerator pumps heat up the temperature gradient.

These heat pumping or work generation effects occur due the non-oscillatory boundary condition imposed by the plate and temporary heat storage provided by the plate. (This causes a temporal phase shift in temperature oscillations different from that in a standing wave.)

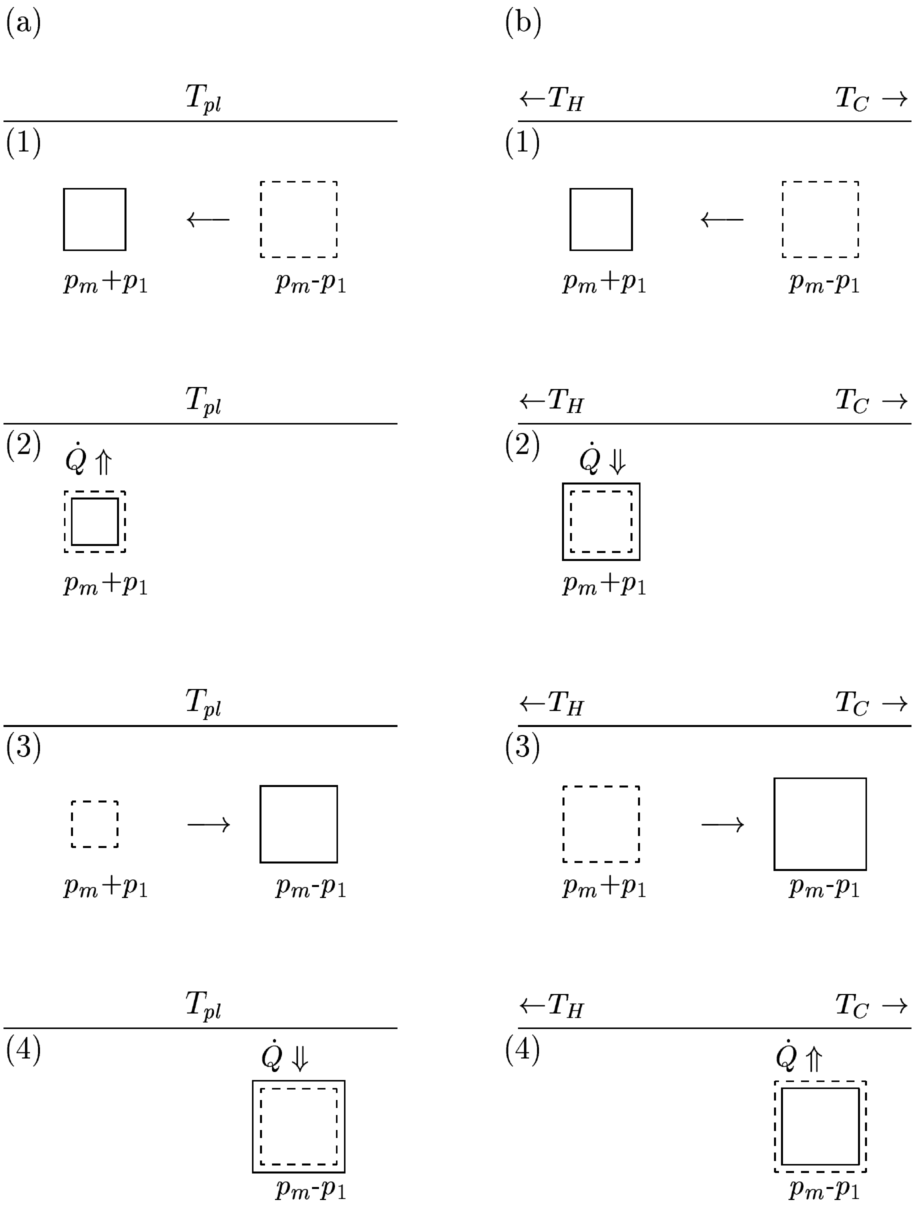

Figure 2.2: (a) Gas parcels near the thermoacoustic couple and (b) prime mover.

Whether a heat pumping effect or a work generation (in the form of a sound wave) occurs is determined by the temperature gradient imposed along the plate.

If the temperature gradient is increased further, as in the case of figure 2.2 (b), the gas near the plate generates sound, i.e. functioning as a prime mover.

The temporal amplitudes of the pressure and the velocity of the gas parcel in the pictures (1) to (4) in figure 2.2 (b) are the same as those of figure 2.2 (a) except for the temperature gradient imposed on the plate surface. As a consequence, the gas parcel in picture (2) of figure 2.2 (b) receives heat from the plate even though the gas is at a higher pressure at that location. In picture (4), although the gas is at a lower pressure, and it is expanding, the temperature of the plate surface is lower than that of the gas parcel because the temperature gradient at the plate is very steep. Therefore, the gas parcel experiences expansion at the higher pressure and the contraction at the lower pressure, therefore generating sound.

The temperature gradient on the plate surface which determines the operating mode, (i.e. either heat pump or prime mover mode) is called the 'critical temperature gradient'. Its definition will be shown in section 2.4.

In order to harness the thermoacoustic phenomenon, and to enhance its performance for practical devices, multiple plates should be used and, at both ends of the plates, something to constantly remove heat from or put heat into the tube is required. The part where heat pumping or sound generation occurs, is called a regenerator or a stack; components that exchange heat between outside and inside of the resonator are called heat exchangers.

2.1.2 Similar devices

In this section, in order to clearly identify the differences between thermoacoustic engines and other reciprocating devices, mechanisms of the well-known Stirling engine, traveling wave heat engine, pulse tube refrigerator and dream pipe are explained in a similar manner to the description of thermoacoustic devices given in section 2.1.1.

It is important to recognize the differences and similarities between the mechanisms, because research into these devices have a longer history than do thermoacoustic devices (except for the dream pipe) and each field has different strengths. As research into thermoacoustic engines is relatively young and there are many issues that need to be solved (see section 2.7), the research results from other devices may be useful.

In figure 2.3, simplified schematics of a Stirling heat pump (a), a traveling wave heat-driven refrigerator (b), a pulse tube refrigerator (c) and a dream pipe (d) are shown. The locations of the heat exchangers in devices (a) to (c) are indicated by small circles.

The sizes of all devices are of the order of 1m. The operating frequencies for Stirling engines and pulse tube refrigerators are generally up to 10 Hz, for the traveling wave engine up to 100 Hz and the dream pipe up to 1 Hz.

Brief descriptions of the basic configurations, their operation and their mechanisms of

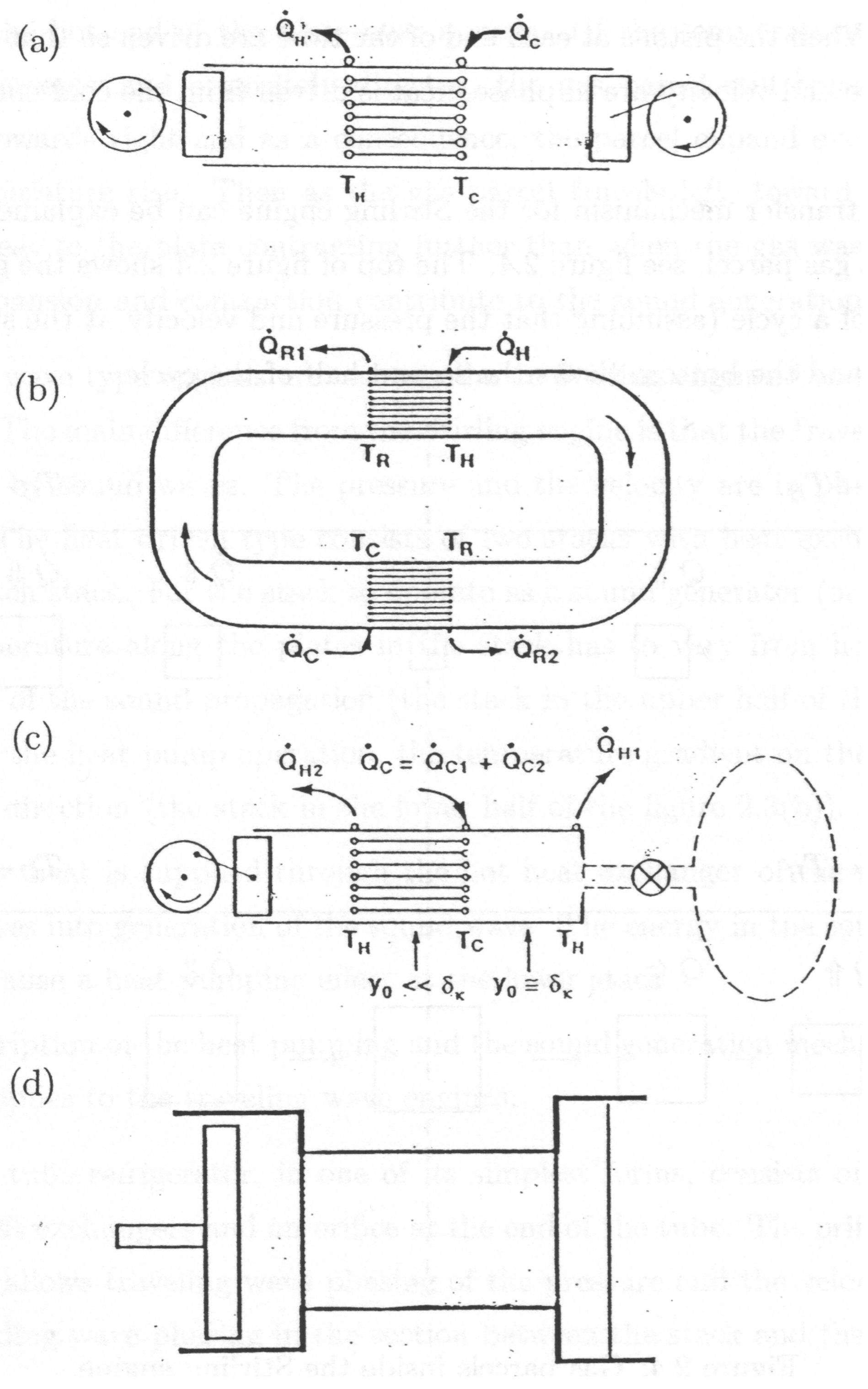

Figure 2.3: Various devices that are subject to oscillatory flow. (a) Stirling heat pump, (b) traveling wave heat-driven refrigerator, (c) pulse tube refrigerator (all from Swift 1988) and (d) Dream pipe (from Tominaga 1998).

each device are as follows.

(a) Stirling engines consist of two pistons, a stack (commonly called the regenerator in a Stirling engine) and two heat exchangers in a gas filled tube. The plate spacing in the stack must be small enough so that the plate temperature prevails throughout the gas. When the pistons at each end of the tube are driven so that the fluctuations of pressure and velocity are in phase, heat is driven from the cold end of stack to the hot end.

The heat transfer mechanism for the Stirling engine can be explained by again considering a gas parcel, see figure 2.4. The top of figure 2.4 shows the gas parcel in the first half of a cycle (assuming that the pressure and velocity at the start of the cycle are zero) and the bottom shows the second half of the cycle.

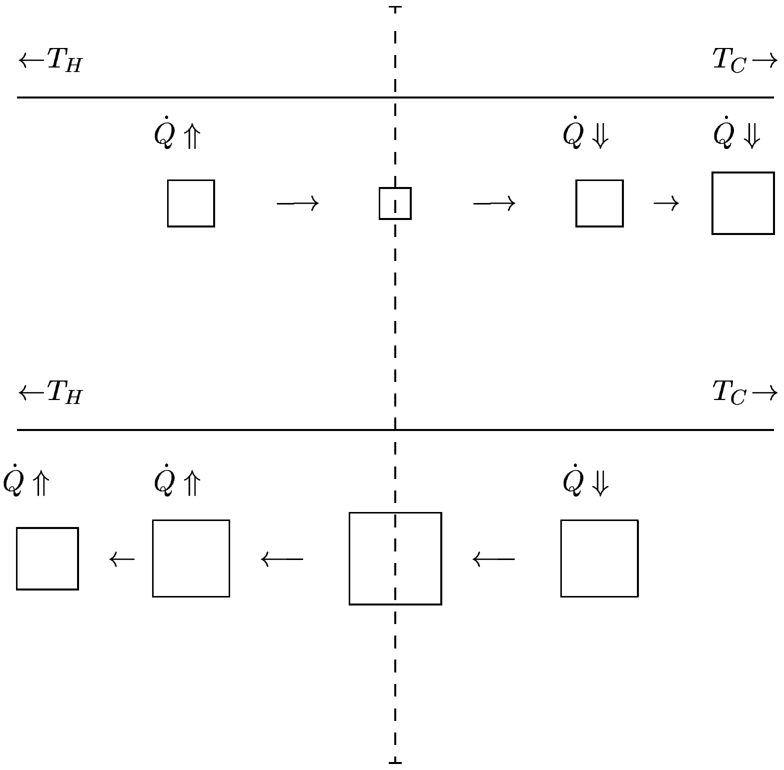

Figure 2.4: Gas parcels inside the Stirling engine.

The leftmost gas parcel of the top picture is at 1/8th of the cycle where the parcel starts to accelerate and be compressed. Because the parcel travels from the left, it has a higher temperature than the plate as it starts to travel. As it travels towards the right while it is being compressed, it rejects heat to the plate and the temperature of the parcel drops. The smallest parcel in the top picture is at a quarter of a cycle where the pressure and velocity amplitudes are greatest. Then the third and the fourth parcels in the top pictures which are at 3/8th and 4/8th of the cycle start to expand, slow down and receive heat from the plate. The second half of the cycle starts with the parcel returning towards its initial position. The gas parcel expands and receives heat from the plate, raising its temperature. The largest parcel in the bottom half of the picture is at the point in the cycle where the pressure and velocity amplitudes are at a minimum. As it continues moving to the left it is compressed and heat is rejected to the plate again. As a consequence, heat is carried from the cold to the hot end of the plate over a cycle. (If the temperature gradient on the plate is steeper and oppositely directed, the gas parcel still receives a heat as it travels towards right and as a consequence, the parcel expand even further due to the temperature rise. Then as the gas parcel travels left, toward the cold end, it rejects heat to the plate contracting further than when the gas was adiabatic. This extra expansion and contraction contribute to the sound generation.)

(b) Traveling wave type engines are very similar to Stirling engines but they do not have pistons. The main difference from the Stirling engine is that the traveling wave engine is driven by sound waves. The pressure and the velocity are in phase as in Stirling engine. The heat driven type consists of two stacks with heat exchangers on either side of each stack. For the stack to operate as a sound generator (or a prime mover), the temperature along the plates in the stack has to vary from hot to cold in the direction of the sound propagation (the stack in the upper half of the figure 2.3(b)), while for the heat pump operation, the temperature gradient on the plates is in the opposite direction (the stack in the lower half of the figure 2.3(b)).

When the heat is supplied through the hot heat exchanger of the upper stack, the energy goes into generation of the sound wave. The energy in the sound wave is then used to cause a heat pumping effect at the lower stack.

The description of the heat pumping and the sound generation mechanism of Stirling engine applies to the traveling wave engines.

(c) The pulse tube refrigerator, in one of its simplest forms, consists of an oscillator, a stack, heat exchangers and an orifice at the end of the tube. The orifice at the end of the tube allows traveling wave phasing of the pressure and the velocity at the stack and standing wave phasing in the section between the stack and the orifice.

Therefore when the gas oscillates, heat pumping at the stack occurs by the same principal as for the Stirling engine while at the tube wall the heat pumping effect as in the thermoacoustic engines.

(d) The dream pipe consists of a tube filled with a fluid that is attached to heat reservoirs at either end of the tube. One end of the tube is maintained at a higher temperature than the other end of the tube. At one end of the tube the gas is oscillated (such as with a piston as indicated in figure 2.3(d)) and the other end the tube is either closed by a diaphragm or is left open. This drives a heat flux from the hot end of the tube to the cold. The heat flux of ten to 100 times that due to conduction only are achievable.

The concept of the fluid block model by Ozawa and Kawamoto (1991), shown in figure 2.5, is used to explain the heat transfer mechanisms. Oscillation of the fluid in the pipe is modeled by the square wave.

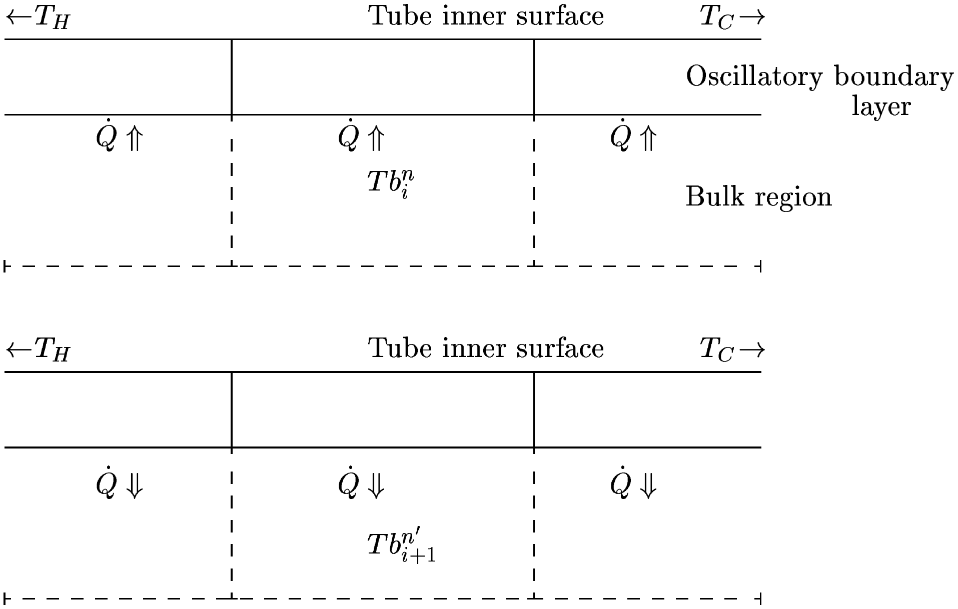

Figure 2.5: Gas blocks inside the dream pipe.

The top half of figure 2.5 is at an arbitrary time, n, when the fluid flows into the domain from the left. The bottom half is at a later time, n' when the fluid flows into the domain from the right.

Two regions with the fluid are considered. The region within the viscous penetration depth (defined in section 2.2) which is the approximate distance shear diffuses in time $1/\omega$, is called the 'oscillatory boundary layer' by Ozawa (1991, 1997). The region further away from the tube wall is called the 'bulk region'. The model assumes that the oscillatory boundary layer does not move. This is because the temporal phase of the velocity is significantly different from that in the bulk region.

At time n, fluid in the bulk region flows into the domain from the left, the fluid blocks have a temperature higher than that of the oscillatory boundary layer and there will be heat transfer to the oscillatory boundary layer. While the temperature of the fluid in the oscillatory boundary layer rises, at time n' the fluid in the bulk region flows into the domain from the right and the bulk receives heat from the oscillatory boundary layer.

If this process is repeated, heat is carried from the hot end to the cold end of the tube. The magnitude of heat transfer from the hot to the cold end is significantly greater than that of the heat conduction in the fluid.

Although the main heat transfer mechanisms at the regenerators differ from those of thermoacoustic engines, an appreciation of the characteristics of various types of oscillatory heat transfer is important. This is because both effects exist inside thermoacoustic engines. (The traveling wave component was known to exist inside standing wave type thermoacoustic engines). The dream pipe effect is a loss in thermoacoustic engines.

2.2 The first order analytical model

In this section, the most general analytical model described by Swift (1988) to predict the performance of the thermoacoustic engine is outlined. This model is commonly used in designing thermoacoustic engines and is used in the commercial code DELTAE (Ward and Swift 1993). This model is based on Rott's pioneering work in thermoacoustic theory described in section 2.5.1 (Rott 1969, 1973, 1974, 1975 and 1980). The analysis is also applicable to regenerators in Stirling engines and pulse tube refrigerators. Semi-analytical expressions are available for the amplitudes of pressure, p_1, temperature, T_1, velocity, $\mathbf{v}$, density, ρ_1, energy flux, $\dot{H}$, and work flux, $\dot{W}$, between the parallel plates with or without a temperature gradient.

First, the continuity, momentum and energy equations for a compressible gas in two-dimensional cartesian coordinates (that can be found in fundamental texts of fluid dynamics, eg. Goldstein, 1965;, Lamb, 1932) are listed.

The continuity equation is

$$\frac{\partial \rho}{\partial t} + \frac{\partial}{\partial x}(\rho v_x) + \frac{\partial}{\partial y}(\rho v_y) = 0. \tag{2.4}$$

The x-component of the momentum equation is

$$\rho(\frac{\partial v_x}{\partial t} + v_x\frac{\partial v_x}{\partial x} + v_y\frac{\partial v_x}{\partial y}) = -\frac{\partial p}{\partial x} + \frac{\partial}{\partial x}(\frac{2}{3}\mu(2\frac{\partial v_x}{\partial x} - \frac{\partial v_y}{\partial y})) + \frac{\partial}{\partial y}(\mu(\frac{\partial v_x}{\partial y} + \frac{\partial v_y}{\partial x})), \tag{2.5}$$

where μ is the dynamic viscosity. The y-component of the momentum equation is

$$\rho(\frac{\partial v_y}{\partial t} + v_x\frac{\partial v_y}{\partial x} + v_y\frac{\partial v_y}{\partial y}) = -\frac{\partial p}{\partial y} + \frac{\partial}{\partial y}(\frac{2}{3}\mu(2\frac{\partial v_y}{\partial y} - \frac{\partial v_x}{\partial x})) + \frac{\partial}{\partial x}(\mu(\frac{\partial v_x}{\partial y} + \frac{\partial v_y}{\partial x})). \tag{2.6}$$

The energy equation is

$$\rho c_p(\frac{\partial T}{\partial t} + v_x\frac{\partial T}{\partial x} + v_y\frac{\partial T}{\partial y}) - (\frac{\partial p}{\partial t} + v_x\frac{\partial p}{\partial x} + v_y\frac{\partial p}{\partial y}) = K(\frac{\partial^2 T}{\partial x^2} + \frac{\partial^2 T}{\partial y^2}) + \Phi, \tag{2.7}$$

where K is the thermal conductivity, c_p is the specific heat of the gas and Φ is the dissipation function which, for a 2-D compressible gas, is

$$\Phi = \mu\left\{-\frac{2}{3}(\frac{\partial v_x}{\partial x} + \frac{\partial v_y}{\partial y})^2 + 2(\frac{\partial v_x}{\partial x})^2 + 2(\frac{\partial v_y}{\partial y})^2 + (\frac{\partial v_y}{\partial x} + \frac{\partial v_x}{\partial y})^2\right\}. \tag{2.8}$$

The energy equation in the plate is

$$\rho c_{p_s}\frac{\partial T}{\partial t} = K_s(\frac{\partial^2 T}{\partial x^2} + \frac{\partial^2 T}{\partial y^2}) \tag{2.9}$$

where c_{p_s} and K_s are the specific heat and the thermal conductivity of the plate.

In order to linearize the equations and to model the oscillating gas between parallel plates, particularly in regenerators and heat exchangers, the following assumptions are made.

- The plate is perfectly rigid.
- A first order expansion in the amplitude is sufficient for all variables.
- All terms that are higher than first order are neglected, except for the energy flux, $\dot{H}$, and the work flux, $\dot{W}$.
- The time-averaged gas velocity $\mathbf{v}_m$ equals zero.
- Pressure is not a function of the y-coordinate.

Swift (1988) chose to set y=0 midway between consecutive plates and y=y_0 as the boundary where the gas and the plate surface are in contact. The y-coordinate of the plate is expressed as y'. y'=0 is the center of the plate and y'=l_0 is at the plate surface. As a consequence, the plate spacing is $2y_0$ and its thickness is $2l_0$. It must be noted that y and y' are oppositely directed.

All dependent variables, pressure, p, density, ρ, velocity, $\mathbf{v}$, temperature of the gas, T, temperature of the solid, T_s, and entropy, s, are expressed in terms of a mean component (subscript m) and the first order fluctuating component (subscript 1). Complex notation is used for the fluctuating component. The hat indicates a unit vector (i.e. $\hat{x}$ is the unit vector in the x-direction)'

$$p = p_m + p_1(x)e^{i\omega t} \tag{2.10}$$

$$\rho = \rho_m(x) + \rho_1(x,y)e^{i\omega t} \tag{2.11}$$

$$\mathbf{v} = \hat{x}u_1(x,y)e^{i\omega t} + \hat{y}v_1(x,y)e^{i\omega t} \tag{2.12}$$

$$T = T_m(x) + T_1(x,y)e^{i\omega t} \tag{2.13}$$

$$T_s = T_m(x) + T_{s1}(x,y')e^{i\omega t} \tag{2.14}$$

$$s = s_m(x) + s_1(x,y)e^{i\omega t} \tag{2.15}$$

where ω is the angular frequency and i is a complex number. When simplifying the momentum and energy equations, further assumptions that are appropriate for thermoacoustic phenomena are made.

- Dependence of viscosity on fluctuations of temperature about its mean is ignored.
- The acoustic wave length is much larger than the viscous penetration depth.
- The velocity in the y-direction is much smaller than that in the x-direction.

Based on these assumptions, the continuity equation reduces to

$$i\omega\rho_1 + \frac{\partial}{\partial x}(\rho_m u_1) + \rho_m \frac{\partial v_1}{\partial y} = 0, \tag{2.16}$$

and the momentum equation reduces to

$$i\omega\rho_m u_1 = -\frac{dp_1}{dx} + \mu\frac{\partial^2 u_1}{\partial y^2}, \tag{2.17}$$

and consequently the energy equation in the plate is

$$i\omega T_{s1} = \frac{K_s}{\rho_s c_{p_s}} \frac{\partial^2 T_{s1}}{\partial y'^2}, \tag{2.18}$$

and the energy equation in the gas is,

$$\rho_m c_p \left(i\omega T_1 + u_1 \frac{dT_m}{dx} \right) - i\omega T_m \beta p_1 = K\frac{\partial^2 T_1}{\partial y^2}. \tag{2.19}$$

The time-averaged energy flux, $\dot{H}_2$, (which is the sum of heat and work fluxes) along the regenerator plates is calculated by taking the time-average of the 'energy flux density' and integrating it in the y-direction. The 'energy flux density' has units of W/m^2 and is given as

$$\mathbf{e} = \rho\mathbf{v}(v^2/2 + h) - K\nabla T - \mathbf{v} \cdot \mathbf{\Sigma} \tag{2.20}$$

where h is the enthalpy and Σ is the viscous stress tensor.

The first order analytical model is expected to disagree with experiments at operating conditions where the assumptions made above become inappropriate. Neglecting higher order terms eliminate the effect of the generation of higher harmonics, acoustic streaming and the distortion of the sinusoidal time dependency. Turbulence and plate end effects are also not considered in the model.

In the next three sections, analytical expressions that are appropriate for each section of the thermoacoustic engines are listed; those sections are the regenerator (or stack), the heat exchangers and the empty section in the resonator.

2.2.1 Regenerator

The function of the regenerator is to pump heat or generate acoustic work in the thermoacoustic engines. Regenerators generally consist of a stack of thin plates with constant spacing, constructed of honeycomb or a porous material.

The following solutions (Swift 1988) are for the gas in between the parallel plates in the regenerator. The velocity amplitude derived from the linearized momentum equation is

$$u_1 = \frac{i}{\omega\rho_m}\frac{dp_1}{dx}\Big(1 - \frac{cosh[(1+i)y/\delta_\nu]}{cosh[(1+i)y_0/\delta_\nu]}\Big) \tag{2.21}$$

where the viscous penetration depth which is defined as $\delta_\nu=\sqrt{2\nu/\omega}$. The temperature amplitude of the gas is

$$\begin{aligned} T_1 &= \frac{T_m\beta p_1}{\rho_m c_p} - \frac{1}{\rho_m\omega^2}\Big(1 - \frac{Pr\ cosh[(1+i)y/\delta_\nu]}{(Pr-1)cosh[(1+i)y_0/\delta_\nu]}\Big)\frac{dp_1}{dx}\frac{dT_m}{dx} \\ &-\Big[\frac{T_m\beta p_1}{\rho_m c_p} + \frac{(dp_1/dx)(dT_m/dx)}{(Pr-1)\rho_m\omega^2}(1+\frac{\epsilon_s f_\nu}{f_\kappa})\Big]\frac{cosh[(1+i)y/\delta_\kappa]}{(1+\epsilon_s)cosh[(1+i)y_0/\delta_\kappa]} \end{aligned} \tag{2.22}$$

where Pr is the Prandtl number, $\delta_k = \sqrt{2K/\omega\rho_m C_p}$ is defined as the thermal penetration depth and β is the thermal expansion coefficient (for an ideal gas, $T_m\beta = 1$) and f_ν, f_κ and ϵ_s are defined as follows.

$$f_\nu = \frac{tanh[(1+i)y_0/\delta_\nu]}{(1+i)y_0/\delta_\nu} \tag{2.23}$$

$$f_\kappa = \frac{tanh[(1+i)y_0/\delta_\kappa]}{(1+i)y_0/\delta_\kappa} \tag{2.24}$$

$$\epsilon_s = \frac{\rho_m c_p \delta_\kappa tanh[(1+i)y_0/\delta_\kappa]}{\rho_s c_s \delta_s tanh[(1+i)l/\delta_s]} \tag{2.25}$$

The thermal penetration depth δ_k is approximately the distance that heat can diffuse through the fluid during a time $1/\omega$ and the viscous penetration depth δ_ν is approximately the distance that shear diffuses in a time $1/\omega$. For more details, see section 4 of Wheatley *et al.* 1985.

The pressure wave equation in the regenerator section was derived by manipulating and combining equations (2.17), (2.16) and the equation of state, substituting equations (2.22) and (2.21) for T_1 and u_1 and integrating the equation with respect to y from 0 to y_0. This yields

$$\Big(1 + \frac{(\gamma-1)f_\kappa}{1+\epsilon_s}\Big)p_1 + \frac{\rho_m a^2}{\omega^2}\frac{d}{dx}\Big(\frac{1-f_\nu}{\rho_m}\frac{dp_1}{dx}\Big) - \beta\frac{a^2}{\omega^2}\frac{f_\kappa - f_\nu}{(1-Pr)(1+\epsilon_s)}\frac{dT_m}{dx}\frac{dp_1}{dx} = 0 \tag{2.26}$$

Energy flux in the regenerator is derived by integrating the energy flux density expressed in equation (2.20) with respect to y from y=0 to y'=0 and expanding it to second order. The resulting energy flux in the regenerator is

$$\begin{aligned} \dot{H} &= \frac{\Pi y_0}{2\omega\rho_m}\mathrm{Im}\Big[\frac{d\tilde{p}_1}{dx}p_1(1-\tilde{f}_\nu - \frac{T_m\beta(f_\kappa - \tilde{f}_\nu)}{(1+\epsilon)(1+Pr)}\Big] + \frac{\Pi y_0 c_p}{2\omega^3\rho_m(1-Pr)}\frac{dT_m}{dx}\frac{dp_1}{dx}\frac{d\tilde{p}_1}{dx} \\ &\times\mathrm{Im}\Big[\tilde{f}_\nu + \frac{(f_\kappa - \tilde{f}_\nu)(1+\epsilon_s f_\nu/f_\kappa)}{(1+\epsilon_s)(1+Pr)}\Big] - \Pi(y_0 K + l_0 K_s)\frac{dT_m}{dx} \end{aligned} \tag{2.27}$$

where ˜ denotes complex conjugation, Im[ ] denote the imaginary part and Π is the perimeter of the plate.

It must be noted again that the energy flux is a sum of work and heat fluxes. Work flux alone is estimated by integrating the time-averaged product of pressure and velocity amplitude, with respect to y between the plates. The resulting equation is

$$\dot{W}_2 = \Pi y_0 \mathrm{Re}\frac{i\tilde{p}_1 dp_1/dx}{2\omega\rho_m}(1-f_\nu). \tag{2.28}$$

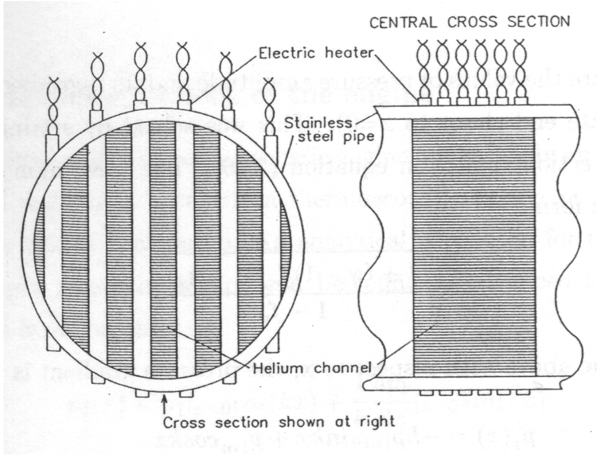

Figure 2.6: Schematic of a hot heat exchanger in a Thermoacoustic engine. (Source:Fig.2. of Swift, 1992)

2.2.2 Heat exchangers

The functions of heat exchangers are to remove heat from or input heat to the ends of the regenerator. The types of heat exchangers that have been used to date are parallel plates, porous materials and, more recently a tube-in-shell geometry. The latter was tested successfully by Swift (1997).

For parallel plate type heat exchangers, the thickness of the plates is generally of the order of the thermal penetration depth in the plate material. The plate spacings are generally of the order of the thermal penetration depth in the gas. Heat exchangers are placed almost touching at either end of the regenerator. The width of the heat exchanger plates in the direction of sound propagation is conventionally chosen as a peak to peak displacement amplitude of the gas parcel traveling from the edge of the regenerator. The plate temperature of the heat exchanger is usually kept constant by passing pipes, in which there is a heating element or a constant stream of cold fluid, through the stack of plates. An example of a hot-end heat exchanger is shown in figure 2.6.

The analytical expressions shown in this section are those for the parallel plate type heat exchangers. These are directly applicable to the thermoacoustic couples that are maintained at a constant temperature.

Thermoacoustic couples and heat exchangers have different natures because of the fact that heat exchangers have a regenerator placed next to them. The analytical expressions described by Swift (1988) do not include plate end effects. Particularly for the temperature, this model is not considered appropriate for heat exchangers, as described later in this section.

The pressure distribution in a thermoacoustic couple or a heat exchanger with a parallel plate geometry, is given as follows.

$$p_1(x) = p_{1in} coskx + (\frac{p'_{1in}}{k}) sinkx, \tag{2.29}$$

where p_{1in} and p'_{1in} are the values of pressure amplitude and its x-gradient at the beginning of the plate (the plate end closer to x=0). This was solved by setting the temperature gradient in the x-direction to zero in equation (2.26). The wave number k is a complex number and is of the form,

$$k = \frac{\omega}{a}\sqrt{\frac{1+(\gamma-1)f_\kappa/(1+\epsilon_s)}{1-f_\nu}}. \tag{2.30}$$

Differentiating the above with respect to x, the pressure gradient is

$$p'_1(x) = -kp_{1in}sinkx + p'_{1in}coskx. \tag{2.31}$$

The velocity profiles in heat exchangers and thermoacoustic couples are the same as given by equation (2.21).

The temperature amplitude in a thermoacoustic couple is obtained by setting the temperature gradient in the x-direction and ϵ_s to zero in equation (2.22). Setting ϵ_s to zero is an appropriate assumption for an isothermal plate.

$$T_1 = \frac{T_m\beta p_1}{\rho_m c_p}\Big(1 - \frac{cosh[(1+i)y/\delta_\kappa]}{cosh[(1+i)y_0/\delta_\kappa]}\Big) \tag{2.32}$$

This expression is used for the gas near a thermoacoustic couple plate but not for a heat exchanger plate. As Swift (1992) indicated, equation (2.32) is not appropriate for heat exchangers because it does not contain a mean temperature gradient in the y-direction even though there is a time-averaged heat flux over a cycle between the plates and the gas.

To date, as described by Swift (1992), the temperature of a heat exchanger plate is calculated by applying Fourier's law of heat conduction for the time- and the space-averaged heat flux through the heat exchanger plate.

Given the heat flux, $\dot{Q}$, coming into or out of the heat exchanger region, the time-averaged temperature difference between the gas and the heat exchanger plate can be given as follows.

$$< \delta T >= \frac{\dot{Q}\delta_\kappa}{AK}, \tag{2.33}$$

where A is the total surface area of the heat exchanger plate in contact with gas. δ_K appears because a linear temperature gradient is assumed within the thermal penetration depth. The time-averaged heat flux $\dot{Q}$ leaving or entering the regenerator section can be calculated from the 1st order model or merely can be set as the value of the input heat flux.

The steady state heat conduction assumption is often a very poor assumption in the developing or the oscillating flows. This is discussed in more detail in section 2.6.

This method only gives the approximate time averaged temperature difference between the heat exchanger plate surface and the gas in the domain while the temperature profile remains unknown. This is one of the main motivations for the current work.

2.2.3 The remaining sections of the engine

The remaining sections of the thermoacoustic engine are basically an empty resonator tube with closed rigid ends for a heat driven thermoacoustic engine or a speaker and a rigid end for a speaker driven heat pump. An analytical expression for the pressure along the tube for the empty resonator section can be found in advanced acoustic texts such as Pierce(1989) and is of the form;

$$p_1(x) = p_1|_{x=0}cos(kx) + \frac{1}{k}\frac{dp_1}{dx}|_{x=0}sin(kx) \tag{2.34}$$

where

$$k = \frac{\omega}{a}\left(1 + \frac{1-i}{2}\frac{\delta_\nu}{R} + \frac{1-i}{i}(\gamma - 1)\frac{\delta_\kappa}{R}\right). \tag{2.35}$$

Here, $p_1|_{x=0}$ and $\frac{dp_1}{dx}|_{x=0}$ are the pressure amplitude and the pressure gradient at the beginning of the tube. When there is a rigid end at x=0 then the maximum pressure amplitude (and assuming it is not a complex number) is expected to be at x=0.

2.2.4 Method of calculation

The way the set of equations shown in sections 2.2.1 to 2.2.3 is used to predict the performance of thermoacoustic engines is described in this section. As an example, we consider a simple half wavelength prime mover, as shown in figure 2.7.

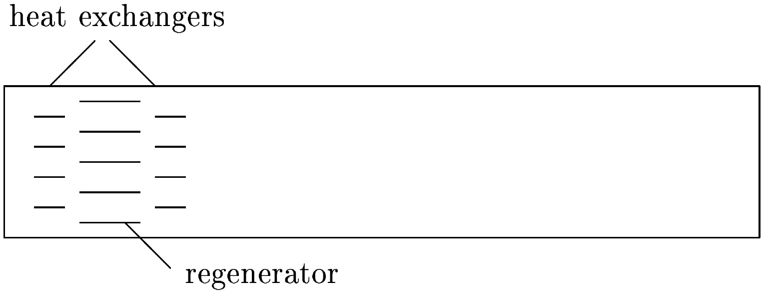

Figure 2.7: Cross section of the simplified half wavelength prime mover.

The calculation should start from x=0, the closed end of the tube with guessed values of frequency and pressure and temperature amplitudes at the closed end. First the pressure and its gradient at the empty section just ahead of the heat exchanger, are calculated using equation (2.34) and its derivative. Temperature variation is not considered in the empty section of the tube.

To find the pressure and its gradient at the beginning of the heat exchanger plate, continuity of pressure and of volumetric velocity are used at the joint. Then, equation (2.29) and (2.31) are used to calculate the pressure and its gradient at the end of the heat exchanger. Again, the mean temperature is assumed to be the same as at the hot end of the tube. The temperature of the heat exchanger plate is assumed from the input heat and the mean temperature in the gas.

Entering into the regenerator section, again continuity of pressure and volumetric flow are used. The pressure wave equation in the regenerator section is solved using the Runge-Kutta method. Once the pressure amplitudes are found, temperature and velocity amplitudes and energy and work fluxes can be found using equations (2.21) to (2.28).

Going from the regenerator to the heat exchanger section, again the continuity conditions are imposed to find the pressure and its gradient. The plate temperature of the heat exchangers is found from the mean temperature and heat flux at the end of the regenerator. If it is required to be at a certain temperature, and the temperature calculated does not match, the initially guessed temperature amplitude at x=0 needs to be changed.

The pressure and its gradient at the other end of the resonator can be computed in the same way as the first empty section. Impedance at the closed end is known and, if the calculation does not match, the initial assumption of the pressure and the frequency are not appropriate. Calculations must be restarted with new initial values and continued until these values match.

2.3 Short engine model

The first order analytical model described in section 2.2 requires a good initial estimate of the pressure and temperature amplitudes at x=0. In order to quickly calculate these values, a so called 'short engine model' is used. This model is known to give only a rough indication of performance with errors in heat flux or temperature differences across the stack of up to 40% (Swift 1992).

In the short engine model, the following assumptions, in addition to those for the first order model (described in section 2.2), are made.

- The plates are short enough that they do not perturb the standing wave.
- The plates are short enough that the pressure and the velocity can be assumed not to be x-dependent over the plate.
- The plate spacing and the thickness is much larger than the thermal penetration depth in the gas and plate respectively. This is called a 'boundary layer approximation'.

The third assumption is quite reasonable as, in most practical devices, the plate spacing in the regenerator is approximately $\delta_k \leq y_0 \leq 2\delta_k$ and the plate thickness is $\delta_s \leq l_0 \leq 2\delta_s$. There are two types of short engine model. One includes and the other ignores the viscosity of the gas. These will be described in order.

2.3.1 Arbitrary viscosity

In the short engine model with viscosity, the pressure and the velocity are expressed as in equations (2.1) and (2.21), respectively. However, the phase shift between the pressure and y-averaged velocity is assumed to be that of a standing wave.

Based on the above-mentioned assumptions, energy flux and work flux are given as follows.

$$\begin{aligned}\dot{H} = &-\frac{1}{4}\Pi\delta_\kappa \frac{T_m \beta p_1^s < u_1^s >}{(1+\epsilon_s)(1+Pr)(1-\delta_\nu/y_0+\delta_\nu^2/2y_0^2)} \\ &\times \Big[\Gamma\frac{1+\sqrt{Pr}+Pr+Pr\epsilon_s}{1+\sqrt{Pr}} - \big(1+\sqrt{Pr}-\frac{\delta_\nu}{y_0}\big)\Big] - \Pi(y_0 K + l_0 K_s)\frac{dT_m}{dx}, \qquad (2.36)\end{aligned}$$

where $\Gamma = \nabla T_m / \nabla T_{crit}$ is the ratio of the temperature gradient to the critical mean temperature gradient. The subscript 's' for pressure and velocity indicates the standing wave value. The critical temperature gradient is defined as $T_m \beta \omega p_1^s / \rho_m c_p u_1^s$ (see section 2.4 for more details). With the boundary layer approximation, ϵ_s is reduced to

$$\epsilon_s = \rho_m c_p \delta_\kappa / \rho_s c_{ps} \delta_{ks}. \qquad (2.37)$$

The work flux is simplified to

$$\begin{aligned}\dot{W}_2 = &\frac{1}{4}\Pi\delta_\kappa L\frac{(\gamma-1)\omega(p_1^s)^2}{\rho_m a^2(1+\epsilon_s)} \times \Big(\frac{\Gamma}{(1+\sqrt{Pr})(1-\delta_\nu/y_0+\delta_\nu^2/2y_0^2)} - 1\Big) \\ &-\frac{1}{4}\Pi\delta_\nu L\frac{\omega\rho_m < u_1^s >^2}{1-\delta_\nu/y_0+\delta_\nu^2/2y_0^2} \qquad (2.38)\end{aligned}$$

These equations can be re-arranged to predict quantities such as the temperatures of the hot and the cold ends of the regenerator.

With the short engine model, it is possible to estimate the losses at the resonator. By setting the temperature gradient in equation (2.38), the power absorbed at the plate can be found. Noting that in the resonator section, $y_0 \gg \delta_\kappa$ and taking the area average (by the surface area of the plate) yields

$$\dot{e}_{diss} = \frac{1}{4}\frac{(p_1^s)^2}{\rho_m a^2}\delta_\kappa\frac{\gamma-1}{1+\epsilon_s}\omega + \frac{1}{4}\rho_m(u_1^s)^2\delta_\nu\omega \qquad (2.39)$$

where $\dot{e}_{diss}$ is defined as the energy dissipation per unit surface area of the resonator.

2.3.2 Zero viscosity

This model assumes zero viscosity. This assumption has obvious limitations however Swift (1988) introduced this model to help more clearly describe the concepts of the thermoacoustic engine. When the viscosity is set to zero, Pr=0 and f_ν=0, and the velocity is that of the standing wave. As a consequence, the energy flux reduces to

$$\dot{H} = -\frac{1}{4}\Pi\delta_\kappa\frac{T_m\beta}{1+\epsilon_s}p_1^s u_1^s(\Gamma-1) - \Pi(y_0 K + l_0 K_s)\frac{dT_m}{dx} \qquad (2.40)$$

and the work flux reduces to

$$\dot{W}_2 = \frac{1}{4}\Pi\delta_\kappa L\frac{(\gamma-1)\omega}{\rho_m a^2(1+\epsilon_s)}(p_1^s)^2(\Gamma-1). \tag{2.41}$$

With these equations, it is simpler to describe the contribution of each term. The energy flux given in equation (2.40) does not contain work flux and can be considered as a heat flux only. Then the first term is the heat flux carried by the oscillatory compressible flow and the second term is the heat flux due to conduction in the gas and in the plate. The direction of the heat and work flux is determined by the magnitude of Γ. Work flux is proportional to the square of the pressure amplitude.

2.4 The single plate model

Another simplified model described in Swift (1988) is the single plate model which was used to describe the thermoacoustic effect. Here, in addition to presenting the model, some basic concepts of thermoacoustic engines that are useful for later chapters are described.

Additional to the assumptions made for the short engine model without viscosity, it is assumed that the thermal conductivity in the x-direction in gas is negligible. It is also assumed that the plate has a large enough heat capacity that its temperature does not fluctuate at the acoustic frequency. (This will set ϵ_s to zero.) Temperature dependence of thermal properties in the gas and the plate is also ignored.

Under these assumptions, the temperature amplitude over a plate which was derived from the linearized energy equations is as simple as:

$$T_1 = \Big(\frac{T_m\beta p_1^s}{\rho_m c_p} - \frac{\nabla T_m u_1^s}{\omega}\Big)(1 - e^{-(1+i)(y-y_0)/\delta_k}). \tag{2.42}$$

(For the convenience of the later chapters, the expression shown here was derived using a different y-coordinate than that used by Swift. The plate surface is located at y=y_0 and the mid point between consecutive plates at y=0.)

With this simpler expression, it is easy to define the critical temperature gradient. The magnitude of the temperature gradient on the plate relative to the critical temperature gradient determines the operating mode of the regenerator, i.e. whether it operates as a heat pump or a prime mover.

The critical temperature gradient is given by equating the first bracket of equation (2.42) to zero which gives

$$\nabla T_{crit} = \frac{T_m\beta\omega p_1^s}{\rho_m c_p u_1^s}. \tag{2.43}$$

When $\nabla T_m = \nabla T_{crit}$, there is no temperature oscillation as the temperature change due to the pressure oscillations cancels those due to the displacement of the gas. For efficient engine performance, the temperature gradient applied to the regenerator plate should be near the critical temperature as shown in Wheatley *et al.* (1986). However, when the engine operates at such conditions, the power output or heat transfer rate of the device approaches zero while the efficiency approaches that of the Carnot cycle. For a more generalized case (in which the viscosity and finite specific heat of the solid are considered), it is not possible to define the critical temperature gradient clearly.

The energy flux in this model can be given as

$$\dot{Q}_2 = -\frac{1}{4}\Pi\delta_k T_m \beta p_1^s u_1^s (\Gamma - 1). \tag{2.44}$$

Notation $\dot{Q}_2$ is used instead of $\dot{H}_2$ as equation (2.44) does not include work flux.

Equation (2.44) shows that when $\nabla T_m = \nabla T_{crit}$, there is no heat flux. When $\nabla T_m > \nabla T_{crit}$, $\dot{Q}_2$ is positive and heat flows from the higher temperature end to the lower temperature end, towards the pressure node (i.e. operating as a prime mover). The opposite occurs when $\nabla T_m < \nabla T_{crit}$. (i.e. operating as a heat pump). It also shows the positioning effect on heat flux of the position of the regenerator in the standing wave.

The work flux in this model simplifies to

$$\dot{W}_2 = -\frac{1}{4}\Pi\delta_\kappa L \frac{T_m \beta^2 \omega}{\rho_m c_p}(p_1^s)^2 (\Gamma - 1). \tag{2.45}$$

2.5 Previous work in thermoacoustics

2.5.1 Analytical work in general

In the early 1980s, the study of thermoacoustic engines was still in the stages of the demonstration of thermoacoustic effects and testing the validity of the application of Rott's theory (Rott 1969, 1973, 1974, 1975, 1980). Rott's is the first linear theoretical investigation of heat driven oscillations and was originally developed to investigate the Taconis Oscillation. Rott's work involves the calculation of pressure, velocity and temperature amplitudes and the condition of onset of acoustic oscillation in the tube with wide and narrow cross sections with a non-uniform temperature distribution (Rott 1969), the relation between the temperature gradient in a tube and the onset of the oscillation (Rott 1973), and heat flux along the tube (Rott 1974,1975). All of his work related to thermoacoustic theory is summarized in Rott (1980). Merkli and Thomann (1975) also developed an analytical expression for heat flux in resonant tubes and tested its validity with experiment for laminar flow cases only.

Although Rott's and Merkli and Thomann's works did not consider stacks of plates inside the tube, they provided the foundation for understanding thermoacoustic phenomena.

Wheatley (1983) constructed a thermoacoustic couple consisting of a few parallel plates. He then developed thermoacoustic formulations for ideal gases (which is equivalent to the most general model from Swift (1988) as described in section 2.2, but ignoring temperature fluctuations at the plate surface). Wheatley's formulation was based on Rott's theory but for parallel plate geometries. Later, they were modified by Swift *et al.* (1985) for application to liquid media.

Hofler (1990) reports that he has carried out calculations of the performance of short thermoacoustic stacks with arbitrary plate separation and arbitrary acoustic phasing. Arnott (1991) focuses on the development of the formulation of energy flow along a stack having arbitrarily shaped pore cross sections.

By the early 1990s, most of the linear theory had been established but at the same time, its deficiencies had also been shown experimentally.

2.5.2 Experimental work

Many experiments carried out after the 1980s attempted to improve the understanding of thermoacoustic phenomena and to improve the first order theory without re-solving the governing equations.

Wheatley *et al.* (1983) were convinced that some day a useful device could be built, when they demonstrated a thermoacoustic heat pump with a few plates and produced a large temperature gradient along the plates. Wheatley *et al.* (1985) also demonstrated a thermally driven oscillator and acoustically driven refrigerator along with a thermoacoustic couple to explain the mechanism of the thermoacoustic engine in a heuristic manner for the first time.

Wheatley *et al.* (1985, 1986, 1989) built another device, nicknamed the Beer cooler, which was a heat operated heat pump (details of the beer cooler is given in section 1.1). The intention of the invention was to design a refrigerator having no moving parts. The performance of the device was poor since the regenerators for the heat pump and the prime mover were not placed at the optimum positions in the resonator.

An acoustically driven refrigerator was built by Hofler (1986) for the first time as a speaker-driven cooling apparatus. It consisted of an acoustic driver attached to a 33cm long, 38mm i.d. tube which contained helium and layers of 82.4mm long Kapton sheet. Although it was built purely for demonstration, the cold end of the regenerator reached close to -40°C, with a refrigeration power of 0.6-0.8W after 200 minutes, driven at a 'drive ratio' of 3.5%. The 'drive ratio' is the ratio of the amplitude of the pressure fluctuations to the mean pressure. A later device by Hofler (1986, 1988), named the 'Thermoacoustic refrigerator', without a cooling load, achieved -78°C when the ambient temperature was 23°C.

Wheatley (1986) *et al.* built a demonstration prime mover using liquid sodium as the working fluid. The reason liquid sodium is chosen is that it has less viscous loss, and high electrical conductivity which make it possible to convert acoustic to electric energy using magnetohydrodynamic effects. However, the deficiencies of the liquid are that it has a very low adiabatic compressiblity and larger longitudinal thermal conductivity than a gas, and that it must be driven by greater pressure than when the gas is the medium. The power density also dropped as liquid sodium has a larger heat capacity. Migliori and Swift (1988a, b) built a liquid sodium thermoacoustic engine but its prime mover efficiency was only 1.8% at the highest heat input when it was driven with a drive ratio as high as 50%.

Soon after such demonstration devices were built, the fact that the experimental results and the first order linear analytical solution disagree became notable, especially at higher pressure amplitudes. Disagreement between the first order theory and the experimental data was first discussed by Migliori and Swift (1988a, b) from their measurements of the performance of the liquid sodium thermoacoustic prime mover. When the working fluid is liquid, the drive ratio that can produce a high enough heat pumping effect needs to be about 10 times larger than that of the gas-filled device. In Migliori's device, the drive ratio was 15%. This is well in the region of second order acoustic theory (Swift 1992). Their experimental data showed very poor agreement with linear theory when comparing the heat flux as a function of the amplitudes of the pressure fluctuations, even after they took into account the resonator losses and the temperature drop at the heat exchanger.

Atchley (1988, 1989) made extensive measurements to investigate this disagreement using helium or argon filled thermoacoustic prime movers at drive ratios between 0.1% and 1%. His work showed that when the drive ratio exceeds 0.4%, the data start to deviate from the theory. For drive ratios greater than approximately 1%, the discrepancy from the linear theory remains almost constant.

Atchley *et al.* (1990) observed the distortion of the acoustic pressure wave form from a sinusoidal pattern as the drive ratio was increased from 1 to 8 %. They investigated how the nonlinear generation of higher harmonics increases as the drive ratio is raised. As higher harmonics are generated, the energy from the fundamental mode is reduced which is unfavorable to the performance of thermoacoustic engines. Their measurements agreed only qualitatively with the analysis of Coppens and Sanders (1968) which gives analytical expression for the ratios of the pressure amplitudes of the second to fundamental and third to second harmonics.

Swift (1992) measured the heat flux and the temperature at heat exchangers and again showed deviations from first order analytical solutions. The temperature differed more from the linear theory than did the heat fluxes. One of the main causes of this was the use of steady state heat transfer correlation due to poor understanding of the heat transfer mechanisms at heat exchangers. Other causes for disagreement are the existence of higher harmonics and turbulence. These can be used to explain the discrepancies to some extent, but further theoretical work is needed.

These facts lead to detailed investigations of the flow field inside thermoacoustic engines by many researchers, as described in the following section.

2.5.3 Further investigation of the flow field inside thermoacoustic engines

The study of the flow field in a thermoacoustic engine has been carried out for further understanding of the thermoacoustic effect beyond the level of the first order analytical model.

Earlier, investigation of the flow field was carried out by Merkli and Thomann (1975). They investigated transition to turbulence in an oscillating flow in a resonator filled with air (but without regenerators or heat exchangers), when testing at frequencies up to to 130 Hz. They found that turbulence occurs when the critical Reynolds number is approximately 400. The critical Reynolds number is defined as

$$Re = \frac{2u_1}{\sqrt{(\nu\omega)}} = \sqrt{2}\frac{u_1\delta_\nu}{\nu} \tag{2.46}$$

Where ν is the kinematic viscosity, δ_ν is the viscous penetration depth and u_1 is the amplitude of the velocity in the x-direction.

Olson and Swift (1996) measured energy dissipation in straight and coiled pipes (again without regenerators and heat exchangers) for a wider range of Reynolds and Womersely numbers. Their investigation was aimed at verifying the existing analytical model of dissipation.

Gaitan *et al.* (1994) visualized and measured fluid velocity inside and near the regenerator using a stroboscopic lamp and a laser Doppler velocimeter.

Herman *et al.* (1994) started investigating alternative visualization techniques for thermoacoustic engines in order to improve the understanding of heat transfer and fluid flow structure in thermoacoustic engines. They used on-line holographic interferometry combined with high-speed cinematography to measure the unsteady oscillating temperature fields. For the visualization of flow fields, they used smoke injection and for the visualization of the temperature distribution on the regenerator plates, they used thermochromatic liquid crystals. Details of the measurements were not given in Herman *et al.* (1994).

Using these techniques, Wetzel and Herman (1996) and Herman *et al.* (1998) investigated the temperature and the flow field at the plate edge of the regenerator. The purpose of their investigation was to improve the understanding of the heat transfer mechanisms at heat exchangers. They observed vortex formation at the corner of the plate. Their instantaneous temperature fields in between and outside two plates were asymmetric and they suggest that this may be due to buoyancy effects. As they increased the drive ratio, the temperature field became more complex but detailed analysis was not given.

Mozukewich (1995) investigated relations between the flow field and heat transfer experimentally. Mozukewich measured the heat transfer from wire screens of various diameters located at a velocity antinode in an acoustic standing wave at resonant frequencies from 141 to 2391 Hz over a wide range of Reynolds numbers. The tube contained helium. Although his experimental equipment does not exactly reproduce those at a heat exchanger in a thermoacoustic engine (because it does not have the regenerator adjacent to the wire screens), his findings are to be noted.

His intention was to investigate whether steady flow heat transfer correlations for wire screens or reticulated foam in a cylinder can be applied to heat exchangers in a thermoacoustic engine with such geometries. His experimental result showed that at a high velocity

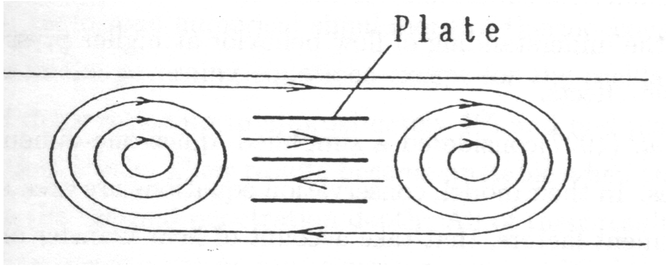

Figure 2.8: Flow pattern of acoustic streaming. (Source:Fig.6. of Ozawa, 1998)

amplitude, Nu follows the steady flow forced convection correlation, time-averaged over an acoustic cycle, while at low amplitude, Nu has a constant value determined by natural convection. He found that the transition between these two regimes occurs abruptly when the streaming Reynolds number is 88. The streaming Reynolds number is defined as

$$Re_s = u_1^2 d/\omega\nu \tag{2.47}$$

where d is the diameter of the wire and u_1 is evaluated at the location of the wire, calculated from the measured pressure amplitude p_1 using $w_1 = p_1/\rho c$. He suggested that this sudden transition is due to the occurrence of acoustic streaming. His results show that with increasing frequency, the transition occurs at a larger Reynolds number.

Many types of acoustic streaming have been identified in pulse tube engines and some types of streaming can be eliminated by the appropriate design of the resonator (Olson and Swift 1997). (A General reference on acoustic streaming is given by Nyborg (1965).) There have also been investigations into acoustic streaming in the resonator mainly at higher pressure amplitudes (Gopinath 1992, Kawahashi and Arakawa 1996). However, little work has been carried out to investigate acoustic streaming in resonators with regenerators or heat exchangers inside. Ozawa *et al.* (1999) visualized acoustic streaming inside a resonator with a regenerator. They tested the case when the spacing of the plates in the regenerator is much larger than the thermal penetration depth. They observed vortices at both edges of the plates and also a larger scale circulation of flow that surrounds the stack of plates as indicated in figure 2.8.

Kawamoto (1997) *et al.* modified the first order analytical model of Swift (1988) to include the effect of the mean flow through the stack due to acoustic streaming. This improved the agreement between experimental results and the analytically calculated temperature distribution at the plate surface when the appropriate magnitude of mean velocity is chosen. However, they suggest that this model still requires further experimental investigations into the vortex structure.

2.5.4 Numerical work

Various types of numerical simulations of thermoacoustic engines have been considered in order to improve the understanding of flow behavior at higher pressure amplitudes and to study the plate end effects.

Watanabe *et al.* (1997) considered a simplified 'quasi-one-dimensional model' of thermoacoustic devices. In their model, conservation equations are area averaged over the cross section yet adjustment factors, that take account of heat transfer and drag effects, are incorporated into the model. Their purpose was to find a model that is relatively simple but approximately valid in the non-linear regime. Their model was crude and only agreed with the experimental results qualitatively. (Yuan *et al.* 1997)

Worlikar and Knio (1996) developed a simplified model (the method of which is not detailed) for a low-Mach number compressible unsteady flow developing in the neighborhood of solid boundaries. The modeling is based on the assumption that the length of the thermoacoustic regenerator is much smaller than that of the wavelength of the driving standing wave. Their intention was to overcome the the stiff scale complexity, which is characterized by large differences in acoustic wavelength, stack geometry and relevant viscous and dynamic length scales.

They intended to simulate a regenerator stack enclosed in a resonator with one end closed and the other end driven by an acoustic driver. Their simulation domain surrounded two plates in the regenerator. In the direction of plate spacing, the domain started from half the plate thickness and ended at half the plate spacing of the other side. Their simulation did not include heat exchangers. Their purpose was to examine fundamental features of the flow and the dependence of the results on the ratio of plate thickness to plate spacing, the ratio of plate length to plate spacing, Kinetic Reynolds numbers and stack positions. They covered drive ratios from 0.2 to 1.0%. All plate spacings they tested were at least 10 times larger than the thermal penetration defined by Swift (1988). The ratio of plate length to the particle displacement distance was a maximum of 0.5. Plates were located near the velocity antinode.

However, they only presented instantaneous stream functions; no comment was made on its effect on heat transfer to the regenerator. An interesting flow feature drawn from their work is that there is a vortex at the edge and outside of the plates.

In 1998, Worlikar *et al.* extended their work by including the energy equation in the plate and investigated temperature contours and the time averaged 'energy flux density'. (The energy flux density is the total energy flux per unit area; it is a vector quantity.) The energy vectors they calculated neglected energy due to dissipation. They only displayed energy vectors at the corner of the plate for small and large drive ratios. They point out that at a smaller drive ratio, the energy vectors leaving the cold end of the plate rapidly curve around the corner and then follow straight paths towards the hot end. But at the higher drive ratio, the energy leaves from the corner and moves into a recirculation region before returning to the plate. However, they showed energy vectors in only a small part of the flow field near the plate edge, which has made it difficult to draw more conclusions.

Cao *et al.* (1996) performed numerical simulations of thermoacoustic couples without making assumptions in the governing equations except for the oscillatory boundary conditions. They tested drive ratios up to approximately 1% and had plate spacings close to the thermal penetration depth. Their results became unstable when the plate spacing was set to less than twice the thermal penetration depth. All of their results were presented in terms of an energy flux density but no investigations were made of the flow field.

2.5.5 Heat exchangers

Although heat exchangers are crucial parts in thermoacoustic engines, not many investigations that focus on heat exchangers have been made, let alone finding a method to design efficient heat exchangers. Swift (1992) showed that 25% of the power produced by the regenerator was dissipated at the heat exchanger by viscous processes. The preferred geometry for heat exchangers described in section 2.2.2 is very crude.

Whereas it has been conventional to consider that heat exchanger plates should be approximately the length of the particle displacement distance and that the plate spacing should be almost the thermal penetration depth, Hofler (Swift 1994) observed better performance of thermoacoustic devices when the heat exchanger plate lengths and spacings were smaller than these values. Swift's (1992) experiment, using a large thermoacoustic engine, also showed that reducing the length of the heat exchanger plates to half particle displacement length did not affect the performance of the heat exchanger.

This is an indication that the heat transfer mechanism in the heat exchanger, which is the shortest component in a thermoacoustic engine, is strongly dependent on plate end effects. Analysis of such effects are well beyond the current first order analytical models.

Hardly any detailed investigations of heat exchangers have been carried out. However, there are some experiments and the focus of which was to find the temperature profile at the heat exchanger.

Swift (1992) measured the temperature of the heat exchanger plates and the mean temperature of the gas near the plate over a wide range of pressure amplitudes. In linear theory, it is expected that, as the pressure amplitude is increases, the mean temperature of the gas should linearly increase. However, he observed that, as the pressure amplitude was increased, the measured temperature deviated from that calculated from the linear theory.

Swift was unable to measure temperature profiles over the heat exchanger plates because the actual plate spacings were so small that it was not possible to locate thermocouples between the plates without touching both plates. He assumed that the temperature measured is equivalent to approximately the spatial- and the time-average of the gas temperature.

As suggested by Swift (1992) the analytical solution shown in section 2.2.2 was derived by assuming a steady state solution of the form in equation (2.13) which does not have a mean temperature gradient in the y-direction. Therefore, when the solution is time-averaged, it will not have a time-averaged mean temperature gradient in the y-direction while there is a time-averaged heat flux in that direction.

Hofler (1994) developed a numerical code to design more efficient, larger scale and low temperature span thermoacoustic refrigerators. The code contains improved solutions for the heat exchangers. Details of the code are not given in the paper. Hofler claims that the width of the heat exchangers and the spacing of the plates should be much less than previously proposed (Swift 1994).

Xiao (1995a, b) analytically solved the sets of equations for the isothermal plate case claiming its equivalence to a heat exchanger. This was similar to Swift's (1988) analysis but included the effect of heat transfer between the tube and the surrounding environment. However, like Swift's analysis, it required appropriate boundary conditions at the start of the domain. There was no discussion of the appropriate boundary conditions for the heat exchanger simulation in his work.

Smith (1993) attempted to obtain the first order analytical temperature profile in the gas near the heat exchanger plate by assuming the steady state solution as follows

$$T(x,y,t) = T_m(x) + T_1(x,y)e^{i\omega t} + \delta T(x,y) \tag{2.48}$$

instead of equation (2.13).

Inconsistencies were found in his analysis, since the mean entropy and the density were left to be constant in the y-direction. However, following his analysis, the general energy equation of heat transfer to the first order is of the following form:

$$i\omega\rho_m c_p T_1 - K\frac{\partial^2 T_1}{\partial y^2} = K\frac{\partial^2 T_m}{\partial y^2}e^{-i\omega t} + i\omega T_m \beta p_1 - \rho_m u_1 c_p \frac{\partial T_m}{\partial x} \tag{2.49}$$

Solving the above equation, T_1 is,

$$T_1 = (\frac{K}{i\omega\rho_m c_p}\frac{\partial^2 T_m}{\partial y^2}e^{-i\omega t} + \frac{T_m\beta}{\rho_m c_p}p_1 - \frac{u_1}{i\omega}\frac{\partial T_m}{\partial x})(1 - e^{-(1+i)y/\delta_k}) \tag{2.50}$$

Since there is a time dependent part in the expression, it conflicts with the assumed solution pattern. For it to be consistent with the form of the initially assumed solution, one needs to assume a linear mean temperature gradient in the y-direction which is the same as the previously mentioned steady state heat transfer assumption by Swift (1992). If one was also to assume the mean of the entropy and the density are y-dependent near the heat exchanger plate, there will be the same consequence.

Using second law analysis, Hobson and Ishikawa (1996) developed a single indicator of optimum heat exchanger spacing given the position, thickness, and width (in the direction of the sound propagation) of the plates and the operating condition of the engine. Details of this are described in chapter 3.

The accuracy of the analysis for the viscous terms is the same as that of the first order theory, but the heat transfer term, which involves oscillating heat transfer, is crude. The analysis has not been tested experimentally.

2.6 Previous work in other reciprocating devices

The differences and similarities of the mechanisms of regenerators in thermoacoustic engines and in other reciprocating devices have been described in section 2.1.2. In this section, we look at investigations into Stirling engines to understand and characterize heat transfer in an oscillating flow. It must be noted that under most operating conditions in the Stirling engine, the flow field is transitional or turbulent (Koehler *et al.* 1990, Ibrahim and Kannapareddy 1991, Ahn and Ibrahim 1991). In most work on thermoacoustic devices, the flow is assumed to be laminar, however, it is important to survey heat transfer studies in a complex flows such as in Stirling engines. This type of work is scarce in other devices.

In the development of the Stirling engine, the necessity to investigate oscillating heat transfer grew from the fact that the predicted power output and efficiency disagreed with experimental results. It has generally been considered that the inability to predict wall heat loss under conditions of oscillating pressure and flow has limited the development of the Stirling engine and its range of applications.

It has been suggested (Simon and Seume 1988) that steady state correlations for pressure drop and heat transfer rate should be replaced by correlations that account for the effect of oscillation. Many have emphasized (e.g. Koehler *et al.* 1990, Devalba and Rispoli 1991, Smith *et al.* 1992) the importance of accurate simulation of the oscillating fluid flow and heat transfer to improve techniques for optimizing heat exchanger designs. In the Stirling engine, the cooler, heater and regenerator are regarded as a group of heat exchangers.

For this reason NASA and other U.S. government agencies have provided funding for analytical, numerical and experimental research to investigate the characteristics of oscillating heat transfer (Tew *et al.* 1989, Tew and Geng 1992).

In oscillating flows, velocity and temperature profiles, the friction factor and heat transfer coefficients are considerably different from those for steady flow (Ibrahim *et al.* 1989, 1992). The heat transfer rate between the solid and the fluid is much higher than in a steady flow. It has also been observed that the characteristics of the turbulence structure (as described by Hino *et al.* 1983, Koehler *et al.* 1990) differ greatly from those in steady flows.

Ohmi *et al.* (1982) observed that the turbulence structure in an oscillating flow is different from that in a non-oscillating flow. They investigated the transition to turbulence in an oscillating flow in a pipe over a wide range of Reynolds number (600 $\sim$ 6500) with dimensionless frequencies, in the form of Womersely number ($\sqrt{\omega'}=2d\sqrt{\omega/\nu}$), from 2.6 to 41. (The actual frequencies ranged from 0.0527 to 6.24 Hz and, at these low frequencies, the compressibility of the fluid is regarded as negligible).

The definition for the Reynolds number they used is

$$Re = u_{m1}d/\nu \tag{2.51}$$

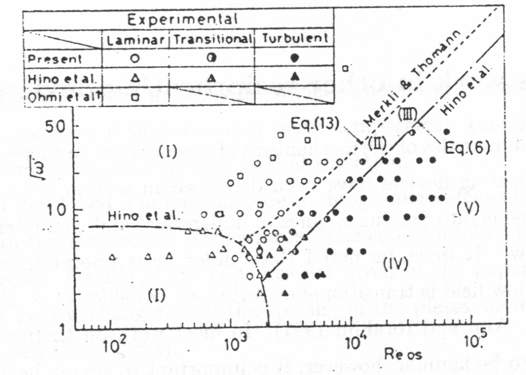

Figure 2.9: Flow characteristic in an oscillating flow. (Source: Ohmi and Iguchi 1982)

where u_{m1} is the cross sectional mean velocity amplitude and d is the diameter of the tube. They have characterized the flows into five types with respect to the Reynolds number and Womersely number as follows:

I laminar

II small amplitude perturbations in the early stage of the accelerating phase at the central portion of the pipe

III small amplitude perturbations in the phase of higher velocities

IV turbulence bursts in the decelerating phase

V turbulence bursts in the decelerating and accelerating phases

The laminar flow region is limited to where $\sqrt{\omega'} < 7$ and $Re < 2 \times 10^3$. Ohmi *et al.* summarized their experimental results as in figure 2.9.

Therefore there are a few critical points to separate one flow regime from another. Some experimental results are not clear on this point. Sergeev (1966) obtained the critical Reynolds number as $Re_{\delta c} = 500$ from visual observation and the power measurement of the oscillator. $Re_{\delta c}$ is expressed as

$$Re_{\delta c} = \frac{|u_m|\delta_\nu}{\nu} \tag{2.52}$$

where δ_ν is the same as the thermal penetration depth described in section 2.2 and $|u_m|$ is the cross sectional mean velocity amplitude. $Re_{\delta c}$ differs from the critical Reynolds number for transition to turbulence in a standing wave in a tube defined by Merkli and Thomann (1975) in equation (2.46), by a factor of $\sqrt{2}$. Hino *et al.* (1976) detected three different regimes of turbulent flow in their experiment using hot wires. They are weakly turbulent flow, conditionally turbulent flow and fully turbulent flow. The conditionally turbulent flow is where the turbulence is generated suddenly in the decelerating phase and in the accelerating phase, the flow recovers to laminar. They found that the critical Reynolds number for the conditionally turbulent flow is $Re_{\delta c} = 550$ when the Stokes parameter, defined as $\frac{d}{2}\sqrt{\frac{\omega}{2\nu}}$, is greater than 1.6. Both experiments were conducted in a straight circular tube.

In order to correlate the oscillating temperature and the heat transfer, use of a complex notation commonly used in AC electric circuits and acoustics, was first proposed by Pfriem (1940). He also suggested the introduction of a complex heat transfer coefficient to express the phase difference between the oscillating gas and the temperature. The analogy to the complex heat transfer is the complex impedance in an AC circuit. He solved a simplified one dimensional energy equation for an ideal gas exposed to an oscillating pressure. By assuming that the temperature can be expressed in terms of a complex exponential, he attained a complex heat flux. Then the complex Nusselt number was found by dividing the complex heat flux by the complex temperature difference, where the temperature difference was taken between the gas in the center of the tube and the wall.

Many variations of expressing the oscillating heat transfer using complex notation followed. Lee (1983) calculated the complex heat transfer coefficient with a differently simplified energy equation. He took the temperature difference between a mixed mean gas value (instead of the center line value) and the wall. Gedeon (1986) introduced a complex Nusselt number for incompressible oscillating flows, Kornhauser and Smith (1989) for oscillating pressure and flow and Jeong (1995) for oscillating pressure and flow with a temperature gradient applied along the cylinder wall.

Kornhauser and Smith (1988, 1989, 1994) put the complex temperature (fluctuation to the first order), heat transfer rate and complex Nusselt number (at this stage unknown) into Newton's law of cooling in order to predict heat flow in a flow with oscillating pressure and velocity as

$$\dot{q}_c = \frac{K}{D_h} Nu_c (T_c - T_w). \tag{2.53}$$

Subscript c denotes complex and T_c is the mixed mean complex temperature of the gas, T_w is the wall temperature of the wall and D_h is the hydraulic diameter. Taking the real part of equation (2.53),

$$\dot{q} = \frac{K}{D_h}[Nu_r(T - T_w) + Nu_i T] \tag{2.54}$$

where T is the actual mixed mean gas temperature in Kornhauser and Smith (1988 and 1994) but it is the center line temperature of the tube in Kornhauser and Smith (1989).

Most experiments to measure oscillating heat transfer in Stirling engines have been made in tubes with one end driven by a piston (Kornhauser and Smith 1989). Several have pistons at both ends (eg. Dean et al. 1993). The tube wall temperature is kept constant and purely real.

Kornhauser and Smith (1989) calculated a complex Nusselt number and correlated it with the oscillating Peclet number

$$Pe_\omega = \frac{\omega D_h^2}{4\alpha} \tag{2.55}$$

where α is the thermal diffusivity. Their experiments showed that the Nusselt number was dependent on the axial location of the position along the tube. However, the operating conditions they tested in 1989, where Pe_ω is less than 100, were later found to be in the region where the correlation breaks down (Kornhauser and Smith 1994).

The experimental results shown in 1988 and 1994 were carried out for a wider range of operating conditions, with frequencies ranging from 0.034 to 16.8 Hz and mean pressures from 100 to 1800 kPa at volume ratios of 2.0, 4.0 and 8.0. The volume ratio is defined as the ratio of maximum volume to minimum volume of the gas. The correlation between Nu_c and Pe_ω breaks down for open cylinders with Peclet numbers in the range $10 < Pe_\omega < 100$ and fails as the volume ratio increase. The experiments also showed that very poor correlation was obtained for heavier gases. They suggest that this break down is due to compressibility effects.

Yagyu and Smith (1991) used Fourier transforms to extend the method of correlating oscillating heat transfer to cases when pressure fluctuations are very non-sinusoidal. In their method they assumed that the total heat flux could be calculated when the complex Nusselt number for each of the harmonics and the complex temperature difference are given. They conducted experiments by driving a piston periodical but non-sinusoidally. The mean pressures used in the experiment ranged from 0.26 to 1.72 MPa and the volume ratio was 1.78. The piston speeds used ranged from 0.042 to 0.33Hz and the gases used were helium and argon. The mean temperature of the gas was calculated using the ideal gas law.

They found that the magnitude of the complex Nusselt number correlated well with Pe_ω multiplied by the speed ratio rather than Pe_ω only. The speed ratio is defined as

$$\gamma_s = \frac{v_p}{v_t} \tag{2.56}$$

where $v_p = \sqrt{\gamma R T_w}$ is the speed of sound in the gas based on the wall temperature and $v_t = \sqrt{2\omega\alpha_w}$ is the speed of the temperature wave in the cylinder wall. The latter is equivalent to the thermal penetration depth divided by the angular frequency.

Jeong and Smith (1992) pointed out that the application of an AC circuit analogy to oscillating heat transfer is not valid when there is a significant change in density during the cycle. They developed a semi-analytical model for heat transfer with oscillating pressure which is appropriate even when the density change is large. They solved the temperature profile in the y-direction for a gas contained in a tube that has pistons at both ends moving in phase. The expression for the heat flux they derived does not contain a complex Nusselt number like coefficient. Instead, the coefficients that correlated the temperature change and the heat transfer were time dependent. They show that only when the density change in the gas is very small, a constant complex Nusselt number is valid.

Tang and Cheng (1993) applied a multivariate statistical analysis to obtain a correlation equation for the cycle averaged Nusselt number. The time averaged Nusselt number is calculated by time averaging the instantaneous Nusselt number which is determined from

$$Nu = qD/K(T_W - T_b) \tag{2.57}$$

where q is the instantaneous heat flux between the wall and the fluid, D is the diameter of the tube and T_b is the instantaneous bulk temperature of the fluid in the heated tube. T_b is the average of the instantaneous bulk temperatures at the inlet and the outlet of the heated tube and the bulk temperature of the fluid associated with energy stored inside the heated tube. The instantaneous heat flux q through the tube wall was constant in the experiment.

Tang and Cheng correlated the time averaged Nusselt number with three parameters: Re, Re_ω and A_ω, where Re_ω is a kinetic Reynolds number, $\rho\omega D^2/\mu$, and A_ω is the dimensionless fluid displacement in an incompressible pipe flow driven by an oscillating piston in a sinusoidal motion which is defined as

$$A_\omega = X_{max}/L = \pi U/\omega L = (D/L)(Re/Re_\omega). \tag{2.58}$$

Here X_{max} is the fluid displacement, L is the length of the heated area and U is the cycle averaged velocity. The latter should be the amplitude of the oscillatory velocity. A_ω correlated well at the operating conditions they tested.

Yuan and Dybbs (1992) determined an instantaneous Nusselt number inside a porous metal regenerator from measurements of the instantaneous temperature as a function of axial location. The Nusselt number was calculated from a simplified 1-D energy equation that was rearranged to express the heat transfer coefficient. The operational pressure in their experiment ranged from 2 to 10MPa at operating frequencies from 20 to 100Hz in helium. The temperature difference between the cold and hot end ranged up to approximately 300K. The kinetic Reynolds number, defined as $Re_\omega = \omega d^2/4\nu$, was between 0.035 and 0.759, where d is the mean pore size of the porous medium. Yuan and Dybbs (1992) found that the transient Nusselt number increases with frequency, but drops when the frequency is as high as 100Hz at lower working pressures. The cause of this was not discussed. At the cold end, the transient Nusselt number was found to decrease as the frequency increased for all operating pressures. They also confirmed that Nusselt numbers were much higher than those measured for a unidirectional flow.

2.7 Further investigations needed

The focus of the current work is to understand the mechanisms of oscillatory heat transfer in thermoacoustic engines with the goal of improving the design of heat exchangers in thermoacoustic engines. However, the literature survey in sections 2.5 to 2.6 indicates that many investigations are required at fundamental levels. What is lacking in the research of thermoacoustic engines before being able to actually look into the improvement of heat exchangers are:

- systematic investigations into the flow behavior at the plates (of heat exchangers and regenerators).
- systematic investigations of plate end effects
- an appropriate method of presenting results

These investigation are needed at various operating conditions starting from low pressure amplitude. In the current work, turbulence is not considered in the simulation domain. These data are required in order to correlate oscillating heat transfer at heat exchangers in thermoacoustic engines and to optimize heat exchanger design. The details of an optimization method are presented in chapter 3.

Chapter 3

The optimization of heat exchanger design using second law analysis

3.1 Introduction

As has been described in chapter 2, significant advances have been made towards producing analyses of the interaction of the regenerator plates with the working fluid in oscillatory flows. These advances have made possible the design and construction of a number of practical thermoacoustic devices. However, to date, relatively little research has been directed towards developing appropriate techniques for the design of efficient heat exchangers in thermoacoustic devices, despite the fact that up to 25% of the power produced by a thermoacoustic engine can be dissipated in the heat exchangers (Swift 1992).

It is necessary to determine the geometry (spacing, thickness and length) of the heat exchanger given the location of the heat exchanger plates and the operating conditions of the thermoacoustic engine in order to improve the overall efficiency of the engine. It is also important to take account of constraints that exist when determining the heat exchanger geometries within the closed volume.

This chapter begins by giving a general introduction to second law analysis, in which a thermal system is optimized in terms of entropy generation. The analysis is then applied to heat exchangers of thermoacoustic engines. The relation between a first law efficiency and second law efficiency for a thermoacoustic engine operating as a heat pump or prime mover is also shown.

A new procedure is presented for establishing a thermodynamically optimum surface area for a heat exchanger in an acoustic standing wave by minimizing entropy generation at the heat exchangers due to the thermodynamic irreversibilities produced by heat exchange and by viscous losses. Although the analysis relies on a steady state heat transfer correlation at the heat exchanger, should an improved correlation become available, the analysis can be easily adapted.

3.2 Second law analysis

3.2.1 Introduction

Conventionally, the so called first law efficiency, which is the ratio of the output of useful energy (in the form of work or heat) to the total energy input, has been used to determine designs of machinery or systems that convert energy into useful output in various applications. However, with the growing concern for the limitation of energy resources and the environmental impact of energy use in recent years, attention has re-focused on second law analysis as it indicates how efficiently the available energy is utilized.

Second law analysis is a method of optimizing a system's geometry or operating conditions in terms of minimizing the entropy generation in the system. The expression for entropy generation can be derived by combining the second law and the first law of thermodynamics in a non-equilibrium state. This is not the same as the mere calculation of irreversibility or availability. The differences are, as discussed in Alefeld (1989, 1990), that the calculation of irreversibility or availability only shows how much potential work of the maximum work available is lost. However, from a practical point of view, it is more informative and helpful in designing systems to quantify the loss in product output caused by individual irreversibilities or to quantify the additional input required to run a process at a given output level. By applying second law analysis, these quantities can be calculated without assuming a reference state.

The method of applying second law analysis to various machinery and systems is thoroughly discussed and summarized in Bejan (1982a, 1982b). Typically, second law analysis is applied to the design of devices such as heat exchanger networks, mixers, turbines, compressors and solar collectors. Examples of relating the individual irreversibilities and the system's overall system efficiencies can be found in Alefeld (1987, 1989, 1990) or Carmody and Shelton (1993).

3.2.2 Entropy generation in the convective medium and second law analysis

A general expression for entropy generation in a flow is derived by the following steps. This procedure can be found in general fluid mechanics text books (such as Landau and Lifshitz, 1959 p186; Bird *et al.* 1960, p350).

General expressions for the conservation of mass and energy (first law) are given respectively by

$$\frac{D\rho}{Dt} = -\rho(\nabla \cdot \mathbf{v}) \tag{3.1}$$

$$\rho\frac{De_i}{Dt} = -(\nabla \cdot \mathbf{q}) - p(\nabla \cdot \mathbf{v}) + \Phi \tag{3.2}$$

where e_i is the internal energy (e is used for internal energy so that it is not confused with the x-component of velocity, u), $\mathbf{q}$ is the heat flux vector and Φ is the dissipation function given in equation (2.8).

When the system is not in thermodynamic equilibrium, due to the existence of velocity and temperature gradients, strictly speaking, definitions of thermodynamic quantities are no longer meaningful. However, within a small volume of fluid, the thermodynamic state of the fluid inside the volume can be regarded as uniform and in localized equilibrium (Oshida and Fujishiro, 1991, p168). When considering the entropy balance in the small volume, the entropy change in a volume should equal the sum of the net entropy flow that enters and the entropy generated in the volume (Bird *et al.* 1960). As the volume approaches zero, the entropy balance can be expressed as follows:

$$\rho\frac{DS}{Dt} = -(\nabla\cdot\mathbf{s}) + \dot{s}_{gen} \tag{3.3}$$

where S is the entropy per unit mass, $\mathbf{s}$ is the entropy flux vector, which is measured with respect to fluid velocity, and $\dot{s}_{gen}$ is the rate of entropy generation per unit volume.

Taking the substantial derivative of the canonical expression $de_i = TdS - pd(1/\rho)$,

$$\rho\frac{DS}{Dt} = \frac{\rho}{T}\frac{De_i}{Dt} - \frac{p}{\rho T}\frac{D\rho}{Dt} \tag{3.4}$$

Substituting equation (3.3) on the left hand side and equations (3.1) and (3.2) on the right hand side of the equation (3.4) yields

$$-(\nabla\cdot\mathbf{s}) + \dot{s}_{gen} = -\frac{\nabla\cdot\mathbf{q}}{T} + \frac{\Phi}{T}. \tag{3.5}$$

Noting that the local entropy flux is equal to the local heat flux divided by the local temperature - that is, $\mathbf{s}=\mathbf{q}/\mathrm{T}$, after some algebraic manipulation, the entropy generation per unit volume is expressed as

$$\dot{s}_{gen} = -\frac{\mathbf{q}\cdot\nabla T}{T^2} + \frac{\Phi}{T} \tag{3.6}$$

and further substituting $\mathbf{q} = -K\nabla T$

$$\dot{s}_{gen} = \frac{1}{T^2}K(\nabla T)^2 + \frac{\Phi}{T}. \tag{3.7}$$

For a two dimensional system in cartesian coordinates, equation (3.7) can be written as

$$\dot{s}_{gen} = \frac{K}{T^2}\left[(\frac{\partial T}{\partial x})^2+(\frac{\partial T}{\partial y})^2\right]+\frac{\mu}{T}\left\{-\frac{2}{3}(\frac{\partial v_x}{\partial x}+\frac{\partial v_y}{\partial y})^2+2(\frac{\partial v_x}{\partial x})^2+2(\frac{\partial v_y}{\partial y})^2+(\frac{\partial v_y}{\partial x}+\frac{\partial v_x}{\partial y})^2\right\} \tag{3.8}$$

where T is the mean temperature of the small control volume.

When considering the entropy generation in the whole domain, equation (3.8) can be integrated over the domain. If the temperature T varies only slightly through the fluid and differs little from the reference temperature, T can be taken outside the integral. Landau (1959) justifies the appropriateness of integrating the entropy generation rate over the whole domain, however, in the current work, taking the view of the 'local equilibrium', entropy generation was evaluated at each cell.

Entropy generation can be directly associated with dissipation of energy in a sound wave as described by Landau (1959, p298). In the following, the derivation is modified to a volume averaged form because Landau integrates the entropy generation over a control volume extended to infinity.

Using Landau's notation, the mechanical energy is the maximum amount of work that can be done in passing from a given non-equilibrium state to one of thermodynamic equilibrium. The work obtained is the maximum when the process is reversible (i.e. without change of entropy) and it is then

$$e_{mech} = e_0 - e(s), \tag{3.9}$$

where e_0 is the initial value of the energy per unit volume and $e(s)$ is the energy at the equilibrium state assuming that the entropy did not change from its initial value. Then the change in the entropy during the process causes e_{mech} to differ from its maximum. Differentiating equation (3.9) with respect to time we have

$$\dot{e}_{mech} = -\dot{e}(s) = -\frac{\partial e}{\partial s}\dot{s}. \tag{3.10}$$

The derivative of the energy with respect to the entropy is the temperature and this is the temperature that the system would have if it were in thermodynamic equilibrium at that entropy. Denoting the temperature as T_0,

$$\dot{e}_{mech} = -T_0 \dot{s}_{gen}. \tag{3.11}$$

Here, as the time rate of change of entropy is the entropy generation rate and, to be consistent with the notations used in this chapter, $\dot{s}$ is replaced by $\dot{s}_{gen}$. $\dot{e}_{mech}$ is the energy dissipation as it is proportional to the rate of entropy change.

3.3 Second law analysis for thermoacoustic engine heat exchangers

3.3.1 Relation between first law and second law efficiencies in thermoacoustic engines

When designing a system based on a second law analysis, the system design is said to be optimized when it generates the least entropy. However, in order to minimize the entropy generation, one must keep the process as reversible as possible. This could be a very time consuming process or involve some geometries that are not practical to build. For thermoacoustic engines, as the device reaches the Carnot efficiency, power output diminishes.

The optimum designs are also influenced by economical and environmental aspects which are outside the scope of this thesis.

Still, second law analysis has come into more common use as, not only does it indicate the quality of energy conversion in the system, but also the quantity consumed. First law efficiency, as stated by H. Hevert and S. Hevert (1980), is silent on the effectiveness with which availability is consumed and is based on the philosophy that energy resources are best conserved by not using them. However, Hevert mentions that second law efficiency is not as explicit as first law efficiency when making decisions in design.

This is not the case when the entropy generation is converted into required additional input or lost output as discussed by Alefeld (1990). Alefeld (1987) shows the expression of the COP of heat pumps and refrigerators as a function of the entropy generation. This can be applied to a thermoacoustic engine operating in heat pump mode. Alefeld applies the first law and the second law to a control volume which contains a heat pump. The first law for the whole heat pump system, can be written as

$$\dot{Q}_H - \dot{Q}_C - \dot{W} = 0 \tag{3.12}$$

Where $\dot{Q}_H$ is the heat rejected by the system, $\dot{Q}_C$ is the heat absorbed by the system and $\dot{W}$ is the work input to the system. The second law of the system can be written as

$$\frac{\dot{Q}_H}{T_H} - \frac{\dot{Q}_C}{T_C} = \sum_i \dot{S}_{gen_i} \tag{3.13}$$

where $\sum_i \dot{S}_{gen} i$ is the sum of all the entropy generation for the irreversible process in each of the i steps in the system, according to Alefeld. In the current work the right hand side of equation (3.13) is interpreted as the entropy generation at each section i of a thermoacoustic device. T_H and T_C are the temperatures of the hot and cold reservoirs respectively. The COP of a heat pump is defined as $COP{=}\dot{Q}_C/\dot{W}$. Therefore, by combining equations (3.12) and (3.13), and eliminating $\dot{Q}_H$, COP can be written as

$$COP = \frac{\frac{T_C}{T_H - T_C}}{1 + \frac{T_H T_C}{T_H - T_C} \frac{\sum_i \dot{S}_{gen} i}{\dot{Q}_C}} \tag{3.14}$$

where the numerator of the above equation is the Carnot efficiency of the heat pump. Considering the first law and the second law for prime movers and knowing that the efficiency of the prime mover is defined as $\eta = \dot{W}/\dot{Q}_H$, the following can be derived,

$$\eta = \frac{\left(\frac{T_H - T_C}{T_H}\right)}{\left(1 + \frac{T_C \sum_i \dot{S}_{gen} i}{\dot{W}}\right)}. \tag{3.15}$$

It is clear from these expressions that reducing entropy generation in a process is the key to improving overall efficiency of the device. The same statement can be inferred from equation (3.11) which associates entropy generation and energy dissipation, but not as explicitly as this. The equation also indicates that the overall efficiency is only affected by the magnitude of the total entropy generation. It must be noted that as the efficiency reaches that of the Carnot cycle, the thermoacoustic effect diminishes as mentioned in section 2.4. Entropy generation in the regenerator section is necessary for the thermoacoustic engine to function. At the plate surface of the heat exchangers, heat is transferred to a plate from the gas by conduction. In such a process entropy generation is unavoidable. The effort to eliminate entropy generation in the heat exchangers competes against the practical and the economical aspects of the design, yet minimizing it will be beneficial in terms of the efficiency. Second law analysis gives an indication of the best geometries for heat exchangers, given the practical constraints.

Entropy generation in a sound wave with viscosity and heat transfer can generally be expressed using equation (3.8), which can be applied anywhere inside the thermoacoustic engine. The equation shows that entropy generation is due to temperature and velocity gradients within the gas. These two components have counteracting effects on the entropy generation. For example, when the gas passes through a narrow channel, entropy generation due to the velocity gradient is dominant, and for a wide channel, temperature gradient terms become dominant. This would lead to finding a compromising optimum channel width that would generate least entropy.

In section 3.3.2, a simplified method of calculating entropy generation in the heat exchanger region and a method of optimizing heat exchanger design based on that is developed.

3.3.2 Development of second law analysis

The concept of expressing both the heat transfer and flow loss irreversibilities in steady flow heat exchangers as summed components of a single entropy generation term and optimizing this with respect to area or flow conditions was pioneered by Bejan in the late 1970s and early 1980s. A comprehensive review of this and related work is given in Bejan (1987) with a more detailed treatment of the basic principles and techniques in Bejan (1982a).

In designing an effective heat exchanger, it is important to minimize both the temperature difference between the working fluid and heat exchanger surface (for a given heat transfer rate) and the flow losses due to viscous and thermoacoustic effects. For given fluid properties and operating conditions, the former design criterion is best met by choosing a large heat exchange surface area, whereas flow losses are reduced by minimizing the contact area between fluid and solid surfaces. These competing sources of thermodynamic irreversibility suggest the existence of an optimum heat exchanger area.

In this section, second law analysis is carried out analytically using a simplified expression for viscous dissipation and the temperature difference between the gas and the heat exchanger plate.

The analysis follows closely the approach taken for conventional steady flow heat exchangers by Bejan (1987), but entropy generation terms pertinent to oscillating flow heat

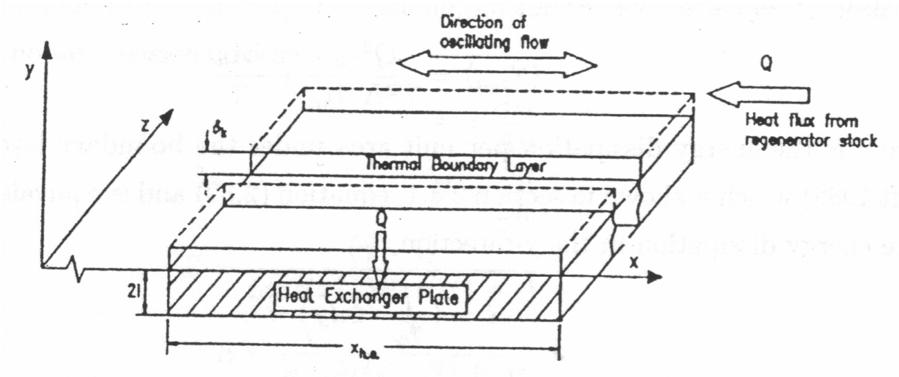

Figure 3.1: Schematic representation of a section of heat exchanger plates.

transfer and flow losses are developed using Swift's (1992) first order solutions where they are available. Consider now a single heat exchanger plate with the geometry and heat flux indicated in figure 3.1. Several simplifying assumptions may be made which enable an expression to be determined for the entropy generation rate within the gas above the plate. The acoustic wave is incident on the y-z plane, and the width in the z-direction $\Pi/2$ experiences the same flow and temperature field (the latter flow and temperature assumptions are conditional on $x_{he} << \lambda$). Denoting Q as the heat flux entering or leaving the heat exchanger section over a cycle, and ΔT as the time averaged temperature difference between the temperature of the plate surface and that of the gas outside the thermal boundary layer, then $q_z \partial T/\partial z \sim 0$, $q_y \partial T/\partial y \sim Q\Delta T/\delta_k$ and $q_x \partial T/\partial x \sim Q\Delta T/x_{he}$. Typically, $\delta_k \sim 0.1$ mm and $x_{he} \sim 10$ mm so that, $q_x \partial T/\partial x << q_y \partial T/\partial y$. With these simplifications, together with the short stack approximation (Swift 1988) that since $x_{he} << \lambda$ then the acoustic pressure (and therefore the rate of power dissipation) is constant over the width x_{he} of the heat exchanger, equation (3.6) becomes

$$S_{gen} = -\frac{x_{he}\Pi}{T^2}\int_0^{y_0} q_y \frac{\partial T}{\partial y} dy + \frac{x_{he}\Pi}{T}\int_0^{y_0} \Phi dy. \tag{3.16}$$

The temperatures in equation (3.16) have been taken outside the integral since variations between the plate ($y = 0$) and free stream ($y = y_0$) fluid temperatures are assumed to be small relative to their absolute values (the implied assumption being that we are designing an efficient heat exchanger).

In order to obtain the correct scaling for the heat transfer term in equation (3.16), the following approach based on that presented by Swift (1992) has been adopted.

$$\text{For } y_0 > \delta_k,\ \left\langle -\int_0^{y_0} q_y \frac{\partial T}{\partial y} dy \right\rangle \sim \frac{Q^2 \delta_k}{A_{he}^2 K} \text{ and } \left\langle -\int_{\delta_k}^{y_0} q_y \frac{\partial T}{\partial y} dy \right\rangle \sim 0 \tag{3.17}$$

where $\langle\rangle$ denotes time averaging. Equation (3.16) becomes after time averaging both the heat transfer and fluid loss terms,

$$\langle \dot{S}_{gen} \rangle = \frac{Q^2 \delta_k}{T^2 K A_{he}} + \frac{\dot{e} A_{he}}{T} \tag{3.18}$$

where $\dot{e}$ is the energy dissipation per unit area under the boundary layer approximation (Swift 1988) which is shown in section 2.3.1, equation (2.39) and is equivalent to the integral of the energy dissipation in the y-direction,

$$\dot{e} = \left\langle \int_0^{y_0} \Phi dy \right\rangle \tag{3.19}$$

with the boundary layer assumption. Substituting equation (2.39) into equation (3.18) gives for the entropy generation,

$$\langle \dot{S}_{gen} \rangle = \frac{Q^2 \delta_k}{T^2 K A_{he}} + \frac{A_{he}\omega}{4T}\left[\frac{p_1^2 \delta_k (\gamma - 1)}{\rho_m a^2 (1+\epsilon)} + \rho_m u_1^2 \delta_v\right] \tag{3.20}$$

Equation (3.20) shows clearly the competing effects of area on the heat transfer (first term) and flow loss (second term) components of the total entropy generation. In order to determine the area which results in the minimum entropy generation (or minimum destruction of exergy), equation (3.20) is differentiated with respect to the heat exchanger area and equated to zero to give, after some algebraic manipulation,

$$\frac{3(\omega l_0)^2 A_{he}^4}{A_R^2} + \frac{8u_R \omega l_0 A_{he}^3}{A_R} + 4u_R^2\left[\frac{(\gamma-1)}{tan^2(x/\bar{\lambda})Pr^{1/2}(1+\epsilon)} + 1\right]A_{he}^2 - \frac{16Q^2}{\rho_m \omega Pr^{1/2} TK} = 0 \tag{3.21}$$

In going from equation (3.20) to (3.21), equation (2.2) and equation (2.1) were used for u_R and p_1 respectively. The velocity amplitude u_1 inside the heat exchanger, which is a function of A_{he} for a fixed resonator cross-sectional area A_R, is eliminated by (i) using mass flow continuity across the interface between the heat exchanger and open resonator ($u_i = (1 + l_0/y_0)u_R$) and (ii) setting the heat exchanger width equal to the local displacement amplitude within the heat exchanger (ie. $x_{he} = 2u_i/\omega$). The velocity amplitude in the heat exchanger domain was assumed to be constant since the heat exchanger plate is very short in comparison with the acoustic wave length. Therefore, the velocity amplitude at the entrance to the heat exchanger is considered to represent the velocity amplitude inside the heat exchanger region and the same applies to the pressure amplitude in the heat exchanger domain.

These conditions give

$$u_i = u_R(1 + \frac{l_0}{y_0}) = u_R + \frac{A_{he}\omega l_0}{2A_R n}$$

where $A_{he} = x_{he}\pi R^2/(y_0 + l_0)$. Also by assuming lossless acoustics in the open resonator section before the heat exchanger, and that the presence of a short heat exchanger (ie. $x_{he} << \lambda$) would not produce any significant wave effects, p_1 is eliminated using

$$\frac{p_1}{\rho_m a} = \frac{u_R}{tan(x/\bar{\lambda})} \tag{3.22}$$

by combining equation (2.1) and (2.2). Further simplification of equation (3.21) is achieved by defining the non-dimensional terms,

$$A = \frac{A_{he}}{A_R} \tag{3.23}$$

$$U = \frac{u_R}{\omega l_0} \tag{3.24}$$

$$Z = \frac{(\gamma - 1)}{tan^2(x/\bar{\lambda})Pr^{1/2}(1+\epsilon)} \tag{3.25}$$

$$E = \frac{Q^2}{\rho_m \omega^3 l_0^2 Pr^{1/2} TKA_R^2} \tag{3.26}$$

Where A is the non-dimensional heat exchanger area, U, the non-dimensional velocity which is the velocity ratio in the y and x directions multiplied by the plate spacing thickness ratio. The non-dimensional parameter Z can be considered as an indicator of the positioning effect given the thermal properties of the gas. E indicates the heat flux going through the heat exchanger plate given the geometry, gas properties and operating conditions.

Multiplying equation (3.21) by $1/(A_R \omega l_0)^2$ and substituting equations (3.22) to (3.26), gives the following implicit expression for the dimensionless optimum heat exchanger area in terms of the other three dimensionless parameters,

$$3A^4 + 8A^3U + 4U^2(Z+1)A^2 - 16E = 0 \tag{3.27}$$

A more useful but still implicit expression for A of the form,

$$U = \frac{-A \pm \left[\frac{A^2}{4}(1-3Z) + \frac{4(Z+1)E}{A^2}\right]^{1/2}}{Z+1} \tag{3.28}$$

can be determined from equation (3.27). Once A has been determined implicitly from equation (3.28) then, by using similar arguments to those used in determining equation (3.22) (eliminating u_i of $u_R = u_i/(1 + l_0/y_0)$), an expression for the optimum heat exchanger plate spacing,

$$y_0 = 2l_0 \frac{U}{A} \tag{3.29}$$

can be derived.

3.3.3 Application of analysis to existing devices

In this section, the preceding analysis is applied to two existing devices and a proposed thermally driven heat pump. The analysis finds the optimum plate spacings for the existing devices given their operating conditions and the heat exchanger plate thickness and lengths.

The three devices are:

1. A quarter wavelength, thermally driven heat pump in which the prime-mover and the heat pump regenerators are placed adjacent in the resonator, built by Wheatley *et al.* (1989) and hereafter referred to as the WE;

2. A large scale thermoacoustic prime-mover built by Swift (1992) to test existing first order thermoacoustic theory, and hereafter referred to as the SE;

3. A thermally-driven half wavelength thermoacoustic heat pump which provides combined domestic heating and cooling, designed by Hobson in 1993. (Ishikawa and Hobson 1996), and hereafter referred to as the IE.

The operating conditions and relevant engine geometry details are listed in table 3.1. In all three devices, the heat exchangers serving the hotter ends of both the prime mover and heat pump regenerator plates, were positioned closer to the pressure antinode than were the cold heat exchangers. δ_{km} in table 3.1 indicate the approximate thermal penetration depth evaluated at the temperature of each heat exchanger. Also shown in table 3.1 is the new plate spacing calculated from the current analysis (denoted as $y_0(new)$). It is interesting to note that the spacings used for the hot heat exchanger of the prime mover in the WE and the cold heat exchanger of the SE are close to the optimum plate spacing calculated from the present analysis. However, the values used for the cold heat exchanger of the WE and the hot heat exchanger of the SE are much smaller than the optimum values indicated by the analysis. It is also interesting to note that most of the values of y_0(new) violate

	IE				WE		SE	
	Heat pump		Prime mover		Heat pump		Prime mover	
Operating conditions	P_m=1.e5N/m^2				P_m=3.e5N/m^2		P_m=1.4e6N/m^2	
	P_A=4.6e4				P_A=1.9e4		P_A=9.4e4	
	f=533.4Hz				f=590Hz		f=121Hz	
	R=5.0cm				R=1.9cm		R=6.4cm	
H.E.	Cold	Hot	Cold	Hot	Cold	Hot	Cold	Hot
y_0 [mm]	N.A.	N.A.	N.A.	N.A.	0.5	0.5	0.41	0.48
l_0 [mm]	0.25	0.25	0.25	0.25	0.25	0.25	0.13	0.23
x_{he} [mm]	6.11	4.05	8.60	5.97	10.0	7.60	5.10	6.00
x [cm]	39.6	42.3	37.4	42.7	20.0	31.0	154.2	185.0
Q [W]	105.0	144.0	1057.0	1163.0	10.0	280.0	5903.8	6533.8
T [K]	264.0	298.0	333.0	673.0	267.0	553.0	308.0	973.0
material	copper	copper	copper	copper	copper	nickel	copper	nickel
δ_{km}[mm]	0.30	0.33	0.36	0.63	0.16	0.30	0.19	0.45
y_0(new)	1.6	0.9	0.3	0.4	6.0	0.4	0.5	1.3

Table 3.1: Operating conditions and geometry of three engines. (Operating conditions for the WE and SW are measured values. Heat flux for the Cold end heat exchanger of the prime mover and the hot end heat exchanger of the heat pump for the WE are not available. H.E. stands for heat exchangers.)

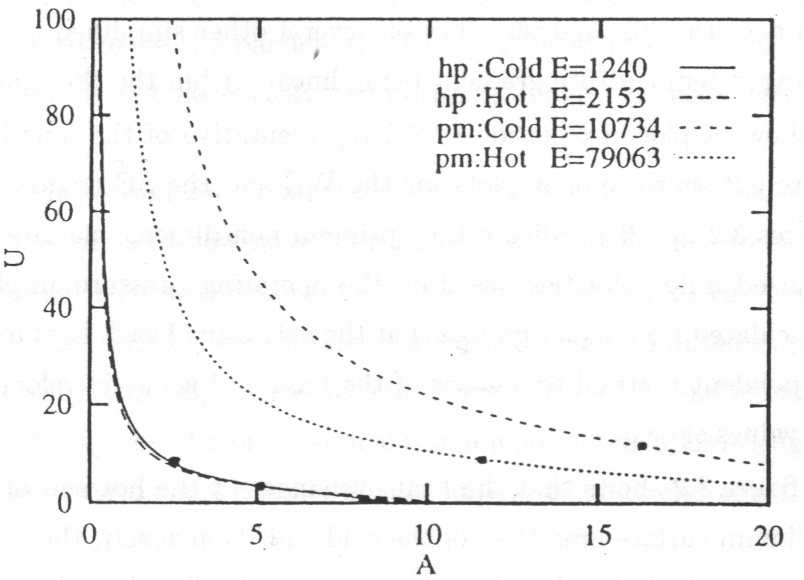

Figure 3.2: Non-dimensionalized velocity U versus non-dimensionalized optimum surface area A of the IE.

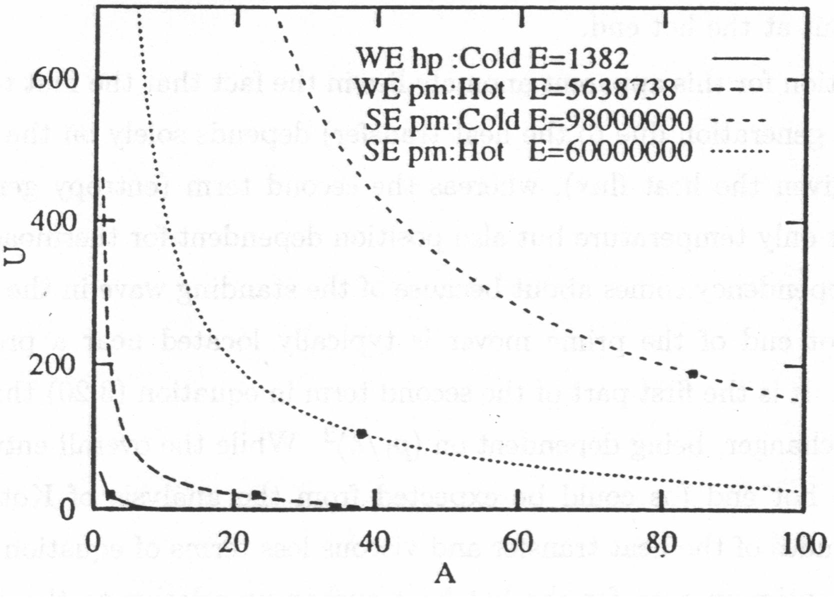

Figure 3.3: Non-dimensionalized velocity U versus non-dimensionalized optimum surface area A of the SE and the WE. (hp and pm stand for heat pump and prime mover.)

the boundary layer approximation on which the analysis is based. However, this is not a serious problem because this analysis relies on several other simplified assumptions (such as the time averaged temperature gradient being linear within the thermal boundary).

Figure 3.2 shows a plot of equation (3.28) representative of the four heat exchangers of the IE. Figure 3.3 shows similar plots for the WE and the SE devices. The boxes on the lines in figures 3.2 and 3.3 indicate the optimum non-dimensional areas for the given non-dimensionalized fluid velocities based on the operating pressure amplitudes given in table 3.1 and calculated from equation (3.24) at the entrance of each heat exchanger. Local temperature dependent thermal properties of the fluid and acoustic velocity were used in calculating the values shown.

For the IE, figure 3.2 shows that the heat exchanger at the hot end of the heat pump has a larger optimum surface area than of the cold end. Conversely, the optimum area for the heat exchanger at the hot end of the prime mover is smaller than that for the cold end.

From figures 3.2 and 3.3, it is evident that the optimum area for the hot heat exchanger is substantially less than that for the cold heat exchanger for the prime mover components of both the IE and the SE. This is an important result for heat exchanger design in thermoacoustic prime movers and, at first inspection, may seem counterintuitive. The hot heat exchangers carry higher thermal loads than the cold heat exchangers (see table 3.1) and one might expect that a larger area for the hot end would be suitable. However the hot end of the heat exchanger being closer to a velocity node (therefore leading to a lower magnitude of oscillating velocity) might lead to the expectation that viscous losses would be less important at the hot end.

An explanation for this apparent anomaly lies in the fact that the first term of equation (3.20) (entropy generation due to the heat transfer) depends solely on the heat exchanger temperature (given the heat flux), whereas the second term (entropy generation due to viscosity) is not only temperature but also position dependent for thermoacoustic engines. The position dependency comes about because of the standing wave in the thermoacoustic device. The hot end of the prime mover is typically located near a pressure antinode (velocity node). It is the first part of the second term in equation (3.20) that dominates at the hot heat exchanger, being dependent on $(p_1/a)^2$. While the overall entropy generation is lower at the hot end (as could be expected from the analysis of Kotas (1986)), the relative magnitudes of the heat transfer and viscous loss terms of equation (3.20) are such that a smaller optimum area for the hot heat exchanger relative to the area of the cold heat exchanger is favored.

3.4 Discussion

Second law analysis applied to heat exchangers in thermoacoustic engines gives a good indication of geometries for designing heat exchangers. However, the heat transfer correlation used when developing the analysis was a steady state one. Also, the heat exchanger width was assumed to be the particle displacement length $x_{he}=2u_1/\omega$. However there is evidence that this is not necessarily the optimum length for heat exchanger plates (see section 2.5.5).

As discussed in section 2.6, detailed numerical studies of heat transfer under conditions of oscillating pressure and flow have been carried out, but do not provide a suitable heat transfer correlation that would permit an analytical solution to the first (heat transfer) integral in equation (3.16). Most studies are verified using a limited number of operating conditions and they also neglect the investigations of the plate end effect.

For this analysis to be of more practical use, a more detailed knowledge of the flow field and heat transfer over a short plate, which is subject to plate end effect, is required.

Chapter 4

On the simulation of thermoacoustic effects using PHOENICS

4.1 Introduction

In this chapter, the general introduction and suitability of using a commercial CFD package (PHOENICS) to simulate sound waves and thermoacoustic effects is discussed. All notation when describing PHOENICS and its numerical schemes are consistent with PHOENICS manuals TR100 (Spalding 1991), 140, 141, 200a,b (CHAM Development Team 1991a,b,c,d) unless otherwise specified.

4.2 Numerical scheme used in PHOENICS

PHOENICS is a computer code which was developed by CHAM Ltd. for simulating fluid flow, heat transfer, chemical reactions and related phenomena (Spalding 1991). The acronym stands for Parabolic Hyperbolic Or Elliptic Numerical Integration Code Series. It is a general purpose code to predict the distribution of any variables obeying conservation laws. PHOENICS solves the governing equations using a finite volume method.

The main components of PHOENICS are a pre-processor called SATELLITE and a processor called EARTH. It also has post processors called PHOTON (to display computational grids and flow patterns graphically), AUTOPLOT (to plot numerical data in 2-D graphs), and PINTO (to transfer PHOENICS data from one grid to another of different coarseness).

SATELLITE interprets the instructions provided by the user in the form of a Q1 file and creates a file containing instructions which EARTH can interpret. In a Q1 file, the user specifies the type of problem and its geometry, the thermal properties, boundary conditions, some options for the solution methods, required output information, etc. Instructions are written in PHOENICS Input Language (PIL) and FORTRAN. (However, not all FORTRAN command can be used in Q1 files.)

EARTH generates solutions according to instructions from the SATELLITE and writes output files that are readily used in post processing. EARTH possesses FORTRAN subroutines which are accessible to the user. One of the important collections of subroutines is called GROUND. The main function of GROUND is to supply boundary conditions, sources, fluid properties, iteration control and output control. Extra subroutines can be written in FORTRAN and added to a GROUND file if features that are available do not meet the user's requirements.

The laws of conservation of mass, momentum, energy, chemical species, etc. for each phase and species can all be expressed in a differential equation of the form,

$$\frac{\partial(r\rho\varphi)}{\partial t} + \nabla \cdot (r\rho\mathbf{v}\varphi - r\Gamma_{\varphi}\nabla\varphi) = rS_{\varphi}. \tag{4.1}$$

The notation in equation (4.1) is as listed below.

r : volume fraction of phase
ρ : density
φ : any conserved property of phase such as enthalpy, momentum per unit mass, etc.
Γ_{φ} : exchange coefficient of the entity φ, such as viscosity or thermal conductivity
S_{φ} : source of φ per unit phase volume, such as viscous dissipation or heat source

For a single phase flow (r=1), the momentum equations can be expressed by setting φ to each of u, v and w and S_{φ} will contains terms such as the pressure gradient in the relevant direction, friction in the fluid, etc. Conservation of Energy can be expressed when $\varphi = h$, the enthalpy, and S_{φ} contain terms such as pressure variation with time, heat sources, etc. The continuity equation can be expressed when $\varphi = 1$ and S_{φ} expresses the mass flow rate.

The governing differential equation (4.1) is integrated over the finite volume of a computational cell and over a finite time. Then the resulting volume, area and time averages are approximated by way of a variety of interpolation assumptions that can be chosen by users. Options that are available for the convection terms are upwind, hybrid interpolation schemes, central differencing schemes and the quadratic upwind differencing scheme. The scheme used for discretizing the equations in time are implicit, explicit, Crank-Nickolson and Courant-number dependent formulations. By default, the fully implicit hybrid set is used in PHOENICS (Spalding 1991).

It is generally considered that the fully implicit formulation, unlike explicit methods, is unconditionally stable for any size of time step (Spalding 1991, Versteeg and Malalasekera 1995). However, Tomiyama *et al.* (1990, 1991), indicate that, although the scheme itself is unconditionally stable for any time step sizes, linear iteration solvers for the discretized equations can only take time steps a little larger than those constrained by the CFL (Courant-Friedrichs-Levy) condition. They showed this only for a 1D problem.

Generally the size of time steps that can be used for all the explicit methods for solving the compressible 2-D Navier Stokes equations, as well as the implicit MacCormack scheme, are limited by the CFL condition (Anderson *et al.* 1984),

$$\Delta t \leq \frac{1}{(|v_x|/\Delta x) + (|v_y|/\Delta y) + a\sqrt{[1/(\Delta x)^2] + [1/(\Delta y)^2]}}. \tag{4.2}$$

In addition, small time steps are needed for higher accuracy as the numerical scheme used is only first order in time.

Whatever iteration scheme is chosen, equation (4.1) is re-arranged to a set of the finite volume equations generally having the form,

$$a_P \varphi_p = a_N \varphi_N + a_S \varphi_S + a_E \varphi_E + a_W \varphi_W + a_H \varphi_H + a_L \varphi_L + a_T \varphi_T + b, \tag{4.3}$$

where a_P, a_N, etc. are coefficients expressing convection and diffusion. a_T is a coefficient which represents the influence of the past on the present. b represents the source appropriate to φ for the cell. A cell with four of its neighbors is shown in figure 4.1. Lower case characters at cell walls indicate where velocities are stored. For the 3-D case, the cells are 'topologically Cartesian', having six sides and eight corners. The center of the cell is regarded as a typical point called a 'grid node'. A staggered grid arrangement is used for velocities. In equation (4.3), the subscripts indicate the location in the cell. The notation is

P : typical point within cell;
N : north neighbor node, in positive y direction;
S : south neighbor node, in negative y direction;
E : east neighbor node, in positive x direction;
W : west neighbor node, in negative x direction;
H : high neighbor node, in positive z direction;
L : low neighbor node, in negative z direction; and
T : grid node at earlier time.

In PHOENICS iterative methods such as the Jacobi and Gauss-Seidel point by point methods or the tri-diagonal matrix algorithm (TDMA) can be used when solving sets of linear algebraic equations having the form of equation (4.3).

In order to couple the momentum and continuity equations, PHOENICS uses the SIMPLEST (SIMPLE ShorTend) algorithm suggested by Spalding (1981) which is a variant of the SIMPLE (Semi-Implicit Method for Pressure-Linked Equations) method (Patankar and Spalding 1972).

The basic idea of the algorithm is that first the pressure field is guessed, then the corresponding velocity fields are computed using the momentum equation and the resulting errors in the continuity equation are computed. Based on these errors, corrections that are needed to be made to pressure and velocities are computed. This process is iterated until negligible correction is necessary (i.e. until the imbalances in the conservation equations at each cell are within the convergence criteria set by the user).

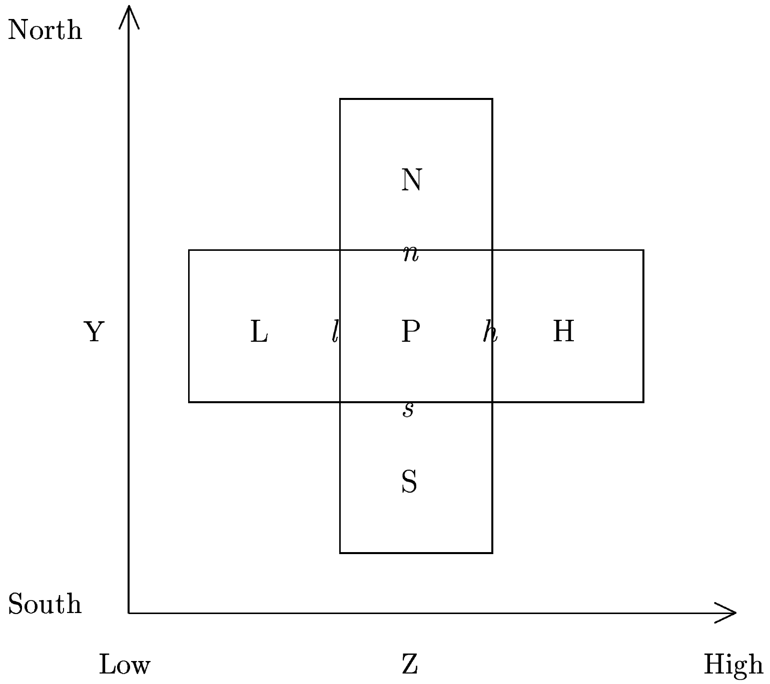

Figure 4.1: A cell arrangement.

4.2.1 Boundary conditions

In PHOENICS, boundary conditions are treated as linearized sources in the differential equation. Therefore an extra term, $C(V - \varphi)$, is added to equation (4.3) and it can be re-written as

$$a_P \varphi_p = \sum_{F=W,E,S,N,H,L} a_F \varphi_F + a_T \varphi_T + b + vol.\ C(V - \varphi_p). \tag{4.4}$$

Here V is a quantity which has the same dimensions as φ and C is a coefficient to match the dimensions of this extra term with other terms in the differential equation. *vol.* is the cell volume.

To set boundary conditions, the user must specify values of C and V and the location of the boundary. Three types of boundary conditions can be set by the user. These are fixed flux, fixed value and wall type boundary conditions.

A fixed value boundary condition is chosen when the user wants to fix variables such as pressure, velocity and temperature directly at the boundary. This can be done by setting V to the desired value for that variable at the boundary and C to a very large value so that when all terms in equation (4.4) are divided by C, only the last term is significant, thus setting $V = \varphi_p$. The default value of C for a fixed value boundary condition is 2.0E10.

Fixed flux boundary conditions are used to specify heat flux or mass flux at the boundary. This can be done by setting V to a desired value for flux and C to a very small value. When a fixed flux boundary condition option is chosen, PHOENICS automatically divides the value of the flux V by C. Therefore, the last term in equation (4.4) becomes V itself.

The default value of C is 2.E-10.

When a wall type boundary condition is chosen, the velocity on the wall is set to zero automatically. When the variable being solved is velocity, the coefficient C at the boundary is set to $\mu A/d$ so that the last term in equation (4.4) becomes $\mu A(V_W - V_n)/d$, where A is the wall area at a cell and d is the distance between the wall face and the cell center. V_W and V_n are the velocities at the wall and the cell that is attached to the wall respectively. When the enthalpy is being solved, the coefficient is automatically set to $\mu A/Prd$ so that the last term of equation (4.4) becomes $KA(T_W - T_n)/d$ where T_W and T_n are the temperatures at the wall and the cell adjacent to it.

When the boundary condition is not set by the user, PHOENICS, by default, assumes that all boundaries of the domain are impervious to the flow. This default boundary condition can be used to specify a plane of symmetry in the domain.

4.2.2 Stopping criteria

PHOENICS has three levels of iteration in order to solve systems of linear equations. The most inner level of iteration is the linear equation solver, the second level is the SIMPLEST algorithm and finally the sweep. The first iteration level solves the NX (the total number of cell in x direction) by NY (the total number of cell in y direction) system of equations for a variable φ using a choice of linear equation solvers at each 'slab', where a slab is an x-y array of cells at each z. At the second iteration level, the SIMPLE algorithm is used. Usually one iteration suffices if the problem is elliptic since the slab is going to be visited many times. At the third iteration level, the solution algorithm proceeds slab by slab sweeping across all Z cells. The iteration stops when the sum of the absolute values of the imbalances in the finite volume equation after each sweep fall below a user set reference value. In PHOENICS, users specify the residual criteria for all levels of the iterations. A tighter residual criteria means that the simulation requires longer to complete.

For the most outer iteration, the residual criteria can be set by specifying constants or using the SELREF option in PHOENICS. The latter involves automatically setting the residual criteria for each variable at each time step as follows,

$$\mathrm{RESREF}(\varphi) = \mathrm{RESFAC} \times \mathrm{TOTFLO}(\varphi)/(\mathrm{NX} \times \mathrm{NY} \times \mathrm{NZ}) \tag{4.5}$$

where TOTFLO(φ) is the sum of all sources for variable φ, including sources associated with convection and diffusion transport. It is the net sum of flux of the variable. It is updated at the end of each sweep for all quantities at each time step. (Note, that the z-component velocities are updated at IZ=NZ-1). RESFAC is a small fraction which the user can specify according to their required accuracy of solution.

PHOENICS allows the user to control the rate of convergence to avoid instabilities. This can be done by specifying linear or false time step relaxation factors. This changes the speed of iteration but not the ultimate solutions that are obtained. To avoid divergence, one can also specify maximum and minimum allowable values for each variable.

Although z was chosen as the direction of sound propagation when using PHOENICS in the current work, hereafter the direction of propagation will be the x-axis to be consistent with conventional thermoacoustic notation.

4.3 Errors in numerical simulations

4.3.1 General Errors expected in numerical simulations

Numerical errors are caused mainly from

- discretization of the governing equations,
- incomplete iteration,
- approximation of boundary conditions, and
- round off errors.

Discretization errors can usually be estimated from the numerical scheme chosen and grid dependency tests. The user has limited control over this type of error when using commercial software (although the grid can be refined). Errors introduced by boundary conditions depend on how closely the physical boundary conditions can be represented in the computer model and how boundary conditions are discretized. Round off errors that are introduced by the limited arithmetic precision of computers are usually much smaller than the other errors mentioned.

An error from incomplete iteration is called a convergence error. This is the difference between the solution at the current iteration and the exact solution. The magnitude of this error depends on the residual criteria chosen. Barrett *et al.* (1994) suggest that a good stopping criterion should

- identify when the error (the difference between the analytical and numerical solutions) is small enough to stop
- stop if the error is no longer decreasing or is decreasing too slowly, and
- limit the maximum amount of time spent iterating.

Barrett *et al.* describe a method to estimate the error in terms of the residual criteria set. However, it was not possible to calculate this error using PHOENICS as some information necessary was not accessible. A more general method for estimating convergence error is described in section 4.5.3.

4.3.2 Additional Errors expected when simulating thermoacoustic effects

In addition to the errors mentioned in section 4.3, there may also be errors due to loss of significant figures.

Thermoacoustic problems are characterized by having very stiff dimensions. For example, a thermoacoustic effect occurs between the regenerator or heat exchanger plates that are placed apart a distance of the order of the thermal penetration depth, δ_k. On the other hand, tube lengths are of the order of the acoustic wave length. For a thermoacoustic engine operating under typical condition, the ratio δ_k/λ is approximately 10^{-4}.

In addition to stiff dimensional problems, variables of interest in simulating thermoacoustic effects are second order quantities. The second order quantities are derived from the first order variables. The thermoacoustic heat flux and the work flux are caused by the fluctuating pressure, velocity, temperature and density. If you take the difference between two temperatures that have very similar magnitude, to calculate the heat flux at the plate surface, there may be some loss of accuracy due to the limited number of significant figures being used. (Loss also will depend on the grid sizes and the geometry.) If you consider the fact that the temperature amplitudes in conventional thermoacoustic devices are approximately 1/100th of the mean temperature, a limited number of significant figures could have a severe effect on the heat flux.

For all simulations from chapters 6 to 8, the convergence rate of the temperature was larger than the convergence rate of other variables. At its maximum, it was approximately 0.1% of the fluctuating amplitude of the temperature. (It must be noted that for all operating conditions tested, the amplitude of the temperature fluctuations was less than 5% of the mean temperature.)

When the convergence rate of the temperature is 0.1% of the temperature amplitude, the fourth digit of temperature amplitude will have some uncertainties, which makes the number of significant figures of the temperature amplitude three. Consider a case to calculate heat flux between a plate surface and a gas with the temperature having three significant figures using Fourier's law of heat conduction. In that case, one would take a temperature difference between the gas in the closest cell to the plate surface and the plate, divide the difference by the distance between the cell center and the plate surface and multiply it by the conductivity of the gas.

When we take the difference between two temperature amplitudes of 3 significant figures, the difference must be at least 1% of the temperature amplitude because any smaller difference would be redundant. When the difference is 1%, the number of significant figures of the difference reduce to one. As a consequence, heat flux calculated based on this temperature difference would have one significant figure. Although this is the worst example, generally the number of significant figures in heat flux is one to two in the current work. Therefore, 10% difference in heat flux can be considered insignificant.

The number of significant figures is crucial to the calculation of the second order quantities such as heat or work flux in thermoacoustic effects.

4.4 Limitations of PHOENICS2.1 when simulating thermoacoustic effects

PHOENICS2.1 is a code written in single precision (the number of the significant figure is eight with Fortran 77 on the Silicon Graphics, Origin 2000). This is proven to be sufficient for most problems (Spalding 1991). However, codes written in single precision generally can not meet as strict a residual criteria, even after many iterations, as can those written in double precision.

The PHOENICS manual (Spalding 1991 p5.17) suggests that when modeling involves extremely small quantities, problem should be non-dimensionalized or should be solved for carefully chosen dimensions.

If the problem was normalized in a standard way, for example, normalizing x and y by the same characteristic length and normalizing the x and y components of the velocity vector, v_x and v_y, by the same reference velocity for 2-D problems, the non-dimensional governing equation can be re-written so that there is just one extra coefficient appearing in these equations which, in PHOENICS, can be adjusted by changing the thermal properties.

As described in section 2.5, most problems involving thermoacoustic effects have stiff dimensions. Then it is more appropriate to normalize each variable by a different characteristic value in order to keep all quantities of the same order of magnitude. When using different characteristic values to normalize the governing equations, non-dimensional coefficients appear in front of almost all terms. However, each term of the governing equations solved in PHOENICS could not be multiplied by such non-dimensional variables as they are not accessible. (Even if one could run the simulation of normalized governing equations, the relative magnitude of cycle averaged energy flux to its fluctuating amplitude will not change, i.e., the simulation of second order effects still requires more significant figures.)

The units used were changed in order to avoid the use of small grid sizes and small time steps. (Note that the y grid dimensions are extremely small if SI units are used.) The PHOENICS manual suggests that one should avoid the use of cells for which any of the lengths, face areas or volumes are less than 1.E-8 (Spalding 1991). Typical operating conditions, geometries and some important variables from Swift (1992) are listed in SI units and in units using cm, g and cs (centi second) in table A.1 in appendix A, although this alone does not solve the stiff dimension problem.

Double precision Fortran codes were written for calculating the thermal properties, boundary conditions and for all post processing. (The post processing involves time and space averaging of many data in the GROUND file.) It was noticed when taking averages of small fluctuating quantities, in some extreme cases, (for example, internal energy change from cycle to cycle), that variations were undetectable when calculated in single precision.

When calculating a fluctuation which is small relative to its mean value, PHOENICS offsets the mean values of pressure and enthalpy. However, mean values (pressure and enthalpy) are added back, when calculating densities and temperatures.

Therefore for the calculation of temperature, density and compressiblity[1], the built-in PHOENICS subroutines were not used but double precision Fortran codes in the GROUND file were written for the current work. However, as the PHOENICS solver operates in single precision, the thermal properties and boundary conditions have to be converted back to single precision when they are passed to EARTH.

It also was found during running the cyclic simulations that the so called ‘re-start facility’ in PHOENICS should not be used for the current simulation. The re-start facility enables the user to take the results of one simulation as initial conditions for another simulation. It originally seemed a suitable option for the current simulation since the boundary conditions are oscillating, and for the simulation to reach steady state, it was necessary to compute over many cycles. The flow and temperature fields of the last time step of one cycle were the initial conditions for the next cycle. However, it was noticed that the re-start facility apparently did not transfer all the results from the generated file since every time a new cycle was simulated using the re-start facility, there was a glitch in plots of pressure, velocity and temperature versus time. This appeared at the first time step of every new run.

4.5 Additional Post-processing features developed for thermoacoustic simulations

4.5.1 Calculation of energy flux density

It is quite common to look at pressure and temperature fields etc. in CFD studies. The PHOENICS post processors are capable of visualizing contours and vector fields of each variable being solved without manipulating data output by the EARTH. However, the variables of interest, in thermoacoustic problems are the heat and work flux. Then the display of the energy density flux may be more useful for understanding the physics of the flow.

In order to visualize the direction of the heat flux, temperature contours generally are sufficient for steady heat transfer problems but they are not suitable when convection is involved. In Cao *et al.* (1996), the total of the work and heat fluxes is presented in terms of an energy density flux which is given by equation (2.20). Cao *et al.* describe that for periodic problems like thermoacoustics, the cycle average of the energy flux density is a conserved quantity because at steady state, the cycle averaged total energy is constant. As this is a conserved quantity, it can be displayed using an ’energy line’. An example of such

---

[1] The definition of compressibility used in PHOENICS is $\frac{1 \delta \rho}{\rho \delta p}$

energy lines taken from Cao *et al.* is shown in figure 4.2. An energy line is an analogue to the stream line in steady flow. The intensity of the energy density flux is indicated by the spacing between consecutive lines when the energy flux between consecutive lines is constant. Arrows on the lines indicate the direction of the energy flux density.

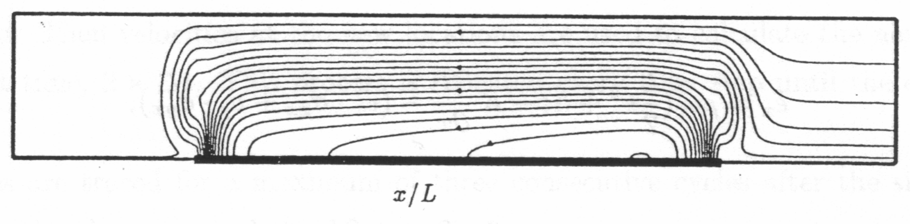

Figure 4.2: Energy lines over an isothermal plate in a standing wave. (Source: Fig.2 (b) of Cao *et al.* 1996)

It must be noted that the visualization of energy flux density is useful for describing the physics of the thermoacoustic effect but work and heat flux are not separable except where energy lines terminate at solid boundaries. (because the energy can flow though the plate only in the form of heat flux). In addition, energy flux can not easily be measured experimentally.

Some considerations can be given to visualizing the heat flux and the work flux separately by appreciating the so called 'Heat line' originally proposed by Kimura and Bejan (1983). The heat line was proposed as a tool for visualizing convective heat transfer and was developed from an analogy to the steam line. It has been used to visualize the heat flux in systems with natural convection and radiation (Draoui *et al.* 1991) and the heat flux in unsteady buoyancy driven flows (Aggarwal and Manhapra 1989).

The heat line is derived from a heat function that satisfies the steady state energy equation. There is no net energy flow across a heat line. Kimura and Bejan define the heat function Φ_H for an incompressible inviscid 2-D flow,

$$\frac{\partial \Phi_H}{\partial y} = \rho c_p v_x T - k\frac{\partial T}{\partial x} \tag{4.6}$$

$$-\frac{\partial \Phi_H}{\partial x} = \rho c_p v_y T - k\frac{\partial T}{\partial y}. \tag{4.7}$$

Then they find the heat line numerically, by combining equations (4.6) and (4.7) with the energy equation for incompressible inviscid 2-D flow.

The right hand sides of equation (4.6) and (4.7) are same as the x and y-components of equation (2.20) except that the kinetic and dissipation terms are not included. It is not possible to derive a heat function analytically for 2-dimensional viscous compressible flow.

Therefore, in the current work, energy lines must be used. Energy lines are drawn by always taking the tangential to vectors of energy flux density, i.e.

$$\dot{e}_x dy - \dot{e}_y dx = 0 \tag{4.8}$$

where $\dot{e}_x$ and $\dot{e}_y$ are the x and y-components of energy flux density which can be written as follows,

$$\dot{e}_x = \rho v_x(\frac{1}{2}\mathbf{v}^2 + h) - K\frac{\partial T}{\partial x} - (v_x \cdot \sigma_{xx} + v_y \cdot \sigma_{yx}), \tag{4.9}$$

where

$$\sigma_{xx} = \mu\frac{2}{3}[2\frac{\partial v_x}{\partial x} - \frac{\partial v_y}{\partial y}] \tag{4.10}$$

and

$$\sigma_{yx} = \mu[\frac{\partial v_x}{\partial y} + \frac{\partial v_y}{\partial x}], \tag{4.11}$$

and

$$\dot{e}_y = \rho v_y(\frac{1}{2}\mathbf{v}^2 + h) - K\frac{\partial T}{\partial y} - (v_x \cdot \sigma_{xy} + v_y \cdot \sigma_{yy}), \tag{4.12}$$

where $\sigma_{xy} = \sigma_{yx}$ and

$$\sigma_{yy} = \mu\frac{2}{3}[2\frac{\partial v_y}{\partial y} - \frac{\partial v_x}{\partial x}]. \tag{4.13}$$

In order to calculate the energy density flux, a block of code was added to GROUND.F. Each term in equation (4.9) and (4.12) was evaluated at the cell center and the differential terms were calculated using central differencing for all cells in the x and y directions. For the enthalpy, H, equation (5.2) was used. Velocities for each direction had to be averaged using the values stored at the cell faces. Velocities at the cell faces on the symmetrical boundary (BC15,23) were calculated by fitting a quadratic curve near the boundary.

$\dot{E}_{BC34}$ was evaluated at the boundary cell center and both backward and central differencing were tested. When using the central differencing, an analytical value was used for values at the cell outside BC34. $\dot{E}_{BC34}$ calculated using both methods did not differ greatly, therefore the central differencing scheme was used because of the convenience of the algorithm.

The spacing between energy lines was determined by first finding the total x-component of energy flux through a y-face at a x-coordinate where the heat flux through a plate surface changes its direction. Then the energy line spacing, ΔE can be determined depending on how many energy lines are required.

4.5.2 Particle tracking for the current work

In the current work, a simple subroutine to track particles in the gas near the plate (for thermoacoustic couple and heat exchanger simulations) was written. The initial locations of nine particles are shown in figure 4.3. The initial x-locations are at each end of the plate and at the middle of the plate. The initial y-locations are at the cell above plate surface, at a quarter of the inter plate spacing and near the middle of the interspacing.

The locations of nine particles after a short time increment Δt are calculated by multiplying velocities (in both x and y directions) at the initial particle location with the time step size Δt. Then velocities at the new locations are used to calculate the next particle locations at time, $2 \times \Delta t$. This process is repeated every time step until the end of the cycle.

Particles are traced for a maximum of three consecutive cycles after the simulations are considered to have reached steady state.

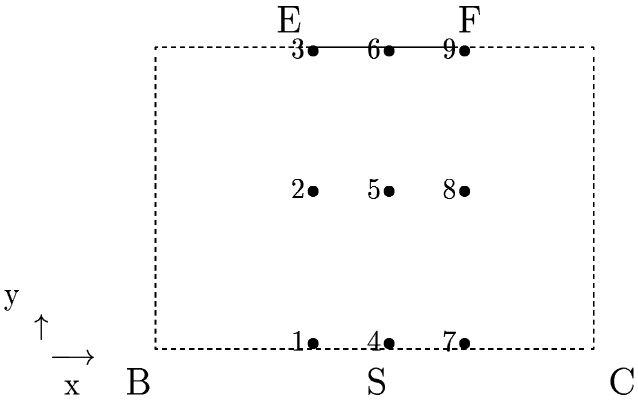

Figure 4.3: 9 particle starting positions in the simulation domain.

Results of particle tracking from one of the test cases from chapter 7, case 1 of table 7.1, are shown in figure 4.4. Particle tracks were calculated for two different time step sizes Δt=0.28% and 0.21% of the duration of a cycle in order to estimate the sensitivity of the particle traces to time step size, x-x_E is the distance from the inner plate edge. Particle 8 was chosen as it had the largest movement in the y-direction, and the particle did not return to its initial position at the end of each cycle. In fact for this case, the difference in y location from the start to the end of a cycle is about 5% of the half plate spacing. This may seem like an error however, the difference between locations at the start and end of a cycle for the two different time step sizes was less than 0.1% of the half plate spacing y_0. This indicates that particle 8 is gradually moving away from the plate and a detail discussion of this is made in section 7.7.

4.5.3 Convergence monitoring for the current work

In the current work, RESFAC in equation (4.5) was set near zero for all simulations, knowing it will never satisfy the criteria. It was set near zero to ensure that the equation solving process for any variables was not switched off. This allowed the minimum achievable error to be monitored. It was not possible to set an appropriate residual criteria that was strict enough or that could ensure a small enough error for all variables at all time steps for the reasons mentioned in section 4.3.

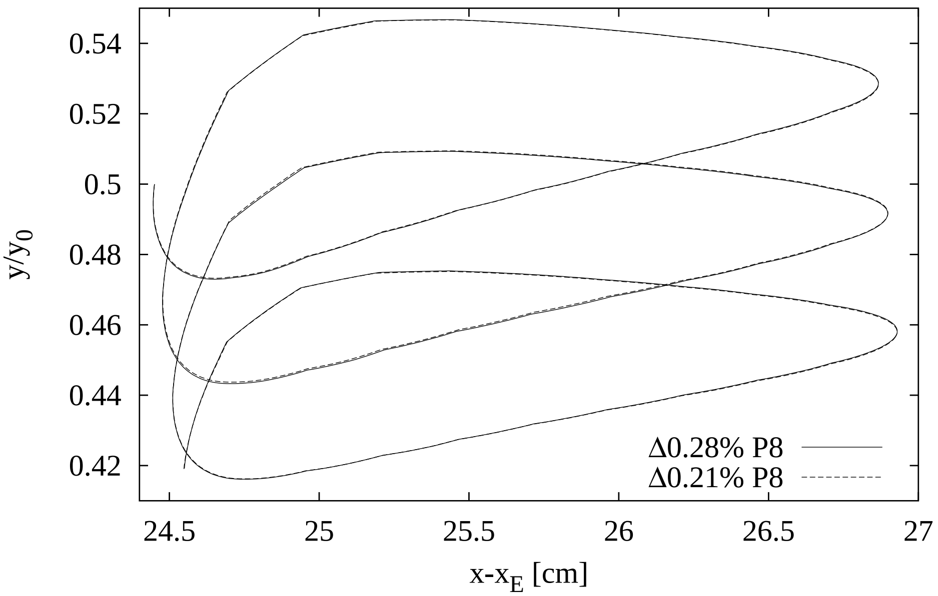

Figure 4.4: Particle trace of particle 2 for two different time steps. Case 1 of section 7.3.

Extra coding was required to stop the iteration if the change in 'spot values' (the values of all variables at each cell at each time step) from the previous sweep to the current sweep was smaller than a specified value. This value was set to 1.E-8 times the spot value. In a single precision code any fractional change smaller than this can not be detected. In current work, simulations were run until the residual for each variable reached a minimum and plateaued.

An expression for the error at step n is

$$\|\epsilon^{\mathbf{n}}\| \approx \frac{\|\delta^{\mathbf{n-1}}\|\|\delta^{\mathbf{n}}\|}{\|\delta^{\mathbf{n}}\| - \|\delta^{\mathbf{n-1}}\|} \tag{4.14}$$

where $\epsilon^{\mathbf{n}}$ is the error matrix at the n^{th} iteration and $\delta^{\mathbf{n}}$ is the matrix of the difference between solutions at iterations n+1 and n. $\|\epsilon^{\mathbf{n}}\|$ is the norm of $\epsilon^{\mathbf{n}}$. In the current work, the maximum magnitude norm was used. The derivation of equation (4.14) is described in Ferziger and Perić (1997) .

Calculation of the error using equation (4.14) showed some instability in the simulations reported in chapter 6 to 8. This was because, in most cases, the convergence rate never reached zero but rather plateaued to a constant value. When this happens, the denominator of equation (4.14) approaches zero and the error rapidly increases. Therefore, in the current work, this method of calculating the error was not used.

The residual and the spot value changes from sweep to sweep for all simulations were calculated to monitor convergence. Since the current simulation is cyclic, the spot value changes from one cycle to the next were also monitored to ensure that the simulation reached steady state. In the current work, it was chosen that when the convergence rate from cycle to cycle no longer changed, even though it has not reached zero, the simulations were considered to have reached steady state. The cycle at which this occurs is referred to as the 'cut off cycle'.

The physical nature of the problem is also used to check convergence. An energy balance over the whole domain should be achieved at steady state. Details of this are described for each of the test cases.

Chapter 5

Methods for simulating heat exchangers using PHOENICS

5.1 Introduction

As discussed in Chapter 2, there have been far fewer analytical and numerical studies of heat exchangers in thermoacoustic devices than of regenerators, despite the fact that efficient design of heat exchangers is crucial to improve the efficiency of thermoacoustic devices. The paucity of studies on heat exchangers is due to the complexity of the conditions that must be specified at the boundary, when one tries to isolate the heat exchanger section to study it analytically or numerically. The operating conditions inside a thermoacoustic engine can be found only after the geometries of all the components have been determined and the components have been placed within the resonator. All variables are interrelated. Therefore isolating the heat exchanger section and carrying out simulations of it involves making some simplifying assumptions.

When considering how to model the heat exchangers in a thermoacoustic device, the primary objective was to make the model as applicable as possible to the heat exchangers in an operational device.

5.2 Heat exchanger model

In this section, the method used to simulate heat exchangers in thermoacoustic devices using PHOENICS and a discussion of its validity is presented. Any interference with the resonator tube wall is neglected.

5.2.1 Description of the model

Figure 5.1 shows part of a basic thermoacoustic engine which consists of hot and cold heat exchangers and a regenerator. (This could be either a heat pump or a prime mover). The simulation domain is indicated by a dotted line. As shown in Figure 5.2, the model consists of an arbitrary plate of the heat exchanger inside the resonator. Due to symmetry, only half of the spacing between the plates is simulated. The thickness of the plate is not included in the domain. The right-hand side of the simulation domain, just outside the heat exchanger plate, is usually where the regenerator end rests. The left hand side of the domain is the closed end of the resonator (a rigid end). The choice of this domain is made to save computation time, and to focus on the oscillating heat transfer mechanisms occurring within the heat exchanger of the thermoacoustic engine. Therefore, the model only applies to the hotter heat exchangers of prime mover or heat pump.

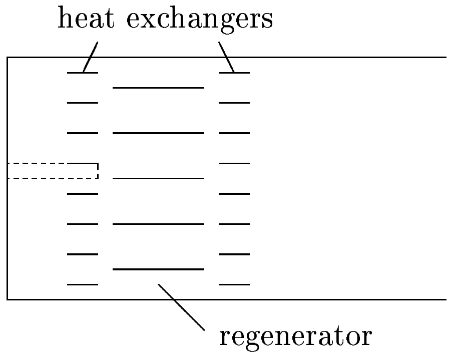

Figure 5.1: Cross section of simplified Thermoacoustic engine.

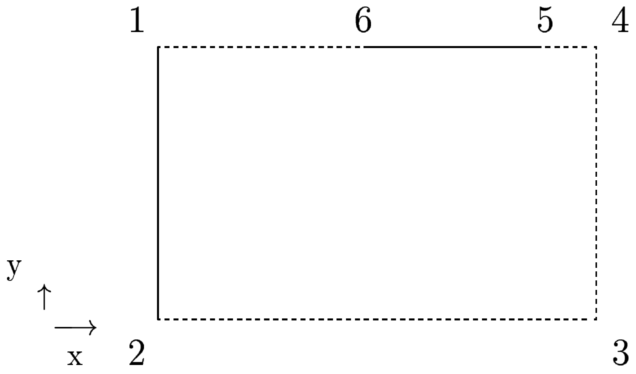

Figure 5.2: The computational domain .

In order to model cold heat exchangers of heat pumps and prime movers, one must replace the close end of the tube with conditions at the center of the resonator but this requires extra assumption which are different from those made at the closed end. This should be considered in future work.

Although it may seem more economical to choose a domain that surrounds just the heat exchanger plate, one end was chosen as the closed end of the resonator to reduce the number of approximations needed to be made when specifying the boundary conditions.

The boundary conditions used are described in section 5.2.3.

Although most thermoacoustic engines are circular cross section, the domain of the present simulation is two dimensional. This is satisfactory for most cases where the ratio of plate spacing to resonator diameter is very small. Also, the fact that a symmetrical boundary condition is applied to the boundary parallel to the plate means that the effects of the resonator tube walls are neglected. The consequence of this is that the resonator tube diameter is not a parameter in the modeling. Thus, the results will be applicable to thermoacoustic engines with arbitrary resonator tube diameters but will not include tube wall effects.

The flow in both the heat exchanger section and the empty section of the tube are assumed to be laminar in the present simulations. For all operating conditions considered in the present study, $Re_{m\&t}(=2u_1/\sqrt{\nu\omega}$, as described in section 2.5.3) is less than 400. (It must be noted that this does not ensure that there is no turbulence in the empty section, where the diameter is much larger than the plate spacing.)

The flow leaving the regenerator and entering the simulation domain is also assumed to be free from acoustic streaming. This assumption is based on the investigation of Hiramastu *et al.* (1991). They numerically investigated the heat transfer to three plates that are aligned in the same direction, as shown in figure 5.3, and are subject to a high speed compressible laminar flow. They found that as the distance between the plates increased, heat transfer at the left edges of second and third plates increased due to the flow disturbance. Their results showed that as the plates are placed closer together, disturbance to the flow at the edge of second and third plates diminished. They also found that if the plates are not aligned horizontally, more disturbances are observed between the first, second and third plates. However, there are no reported studies of the influence of axial spacing between plates subject to the oscillatory flow. Suzuki *et al.*'s (1994) and Majumdar and Amon (1991) studied heat transfer to axially aligned plates subject to oscillatory flow. However, they focussed on increasing the heat transfer at the plate edges due to the disturbance of the gas and did not investigate cases when the plates are placed closer.

Although Hiramatsu *et al.* did not make heat transfer measurements in an oscillatory flow, the way the heat transfer increased due to the disturbed flow in Suzuki *et al.* (1994) and in Majumdar and Amon (1991) were similar to that of Hiramatsu *et al.*. This suggests that, should the plates be placed closer to each other in the axial direction, the disturbance of the flow would reduce. For the current work, when the boundary conditions are specified very close to the plate in order to model the regenerator edge, the flow could be speculated to be laminar.

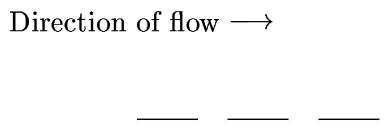

Figure 5.3: Plate alignment used in Hiramatsu *et al.* (1991).

5.2.2 Governing equations

The continuity, momentum and energy equations for a 2-D compressible ideal gas at low Mach number (equations (2.4) to 2.7)) are the governing equations of the current simulations. As discussed in section 5.2.1 the flow is assumed to be laminar. The source terms in each of the governing equations expressed in the form of equation (4.1), are chosen so that each would correspond to equation (2.4), (2.5) and (2.6) respectively. PHOENICS solves the energy equations in terms of enthalpy while equation (2.7) is written in terms of temperature. Constant specific heats are assumed so conversion from enthalpy to temperature is straight forward. In order to close the equation set, auxiliary equations for thermodynamic properties, transport properties and boundary conditions are required. The boundary conditions are described separately in the section 5.2.3.

In the current work, the gas used for the simulations is Helium. The equation of state for an ideal gas,

$$p = \rho R T \tag{5.1}$$

is used to calculate the density. For a calorically perfect gas (constant specific heats), the enthalpy may be written as

$$h = c_p (T - T'). \tag{5.2}$$

where T' is the reference temperature which can be set to the mean gas temperature. (Equation (5.2) makes the enthalpy at the reference temperature zero. This choice is made because in the current work, one is concerned with the relatively small fluctuation of temperature around its mean temperature.) The transport properties required in the current model are the viscosity and the thermal conductivity of the gas. A power law model is used for the variation of viscosity with temperature,

$$\mu = \mu' (\frac{T}{T'})^s \tag{5.3}$$

where s is a constant, and μ' is the dynamic viscosity at the reference temperature T'. This has been found to be suitable for ideal monotonic gases (Chapman and Cowling, 1970) and was chosen over other approximations for its simplicity.

The constant s for typical monoatomic gases that are used in the thermoacoustic engines such as Helium, Argon, Neon etc, ranges from 0.6 to 0.9. The maximum disagreement of the model with Helium, which has an s value of 0.647, is 2 % between the above expression and the measurement of viscosity in the temperature range between 15K and 460K (For T=43-1073K, s=0.657 is preferable (Chapman and Cowling, 1970)). The kinematic viscosity is calculated by dividing equation (5.3) by the temperature dependent density of the gas. The Prandtl number is assumed to be constant over the temperature range of the simulations. This, along with the assumption of constant specific heats, leads to the variation of thermal conductivity with temperature having the same form as equation (5.3) with the same exponent.

5.2.3 Initial and boundary conditions

At the start of the simulations all variables throughout the simulation domain were set at their mean values as follows.

$$\left.\begin{array}{l} u = 0 \\ v = 0 \\ T = T_m \end{array}\right\} \text{at t=0 at all x and y cells} \tag{5.4}$$

The conditions imposed on each boundary, except for the oscillatory boundary conditions at BC34 (refer to figure 5.2), are as follows,

$$\left.\begin{array}{l} u = 0 \\ v = 0 \\ \frac{dT}{dx} = 0 \end{array}\right\} \text{BC12} \tag{5.5}$$

$$\left.\begin{array}{l} v = 0 \\ \frac{dT}{dy} = 0 \end{array}\right\} \text{BC23, 45 and 61} \tag{5.6}$$

$$\left.\begin{array}{l} u = 0 \\ v = 0 \\ T = T_{he} \end{array}\right\} \text{BC56} \tag{5.7}$$

Here, BC12 is the rigid wall boundary at the end of the tube and BC23 is the symetrical boundary mid-way between the heat exchanger plates. BC56 is the surface of the heat exchanger plate. T_{he} is the temperature of the plate at the surface in contact with the gas.

In an operational device the plates (BC56) are kept at a constant temperature with heating elements (see figure 2.6) or a cooling refrigerant. If the plate thickness and the thermal contact between the heat exchanger plates and the heating element or cooling refrigerant are to be considered, additional complexity of simulation is required.

When the temperature of BC56 is kept constant, pipes and the heat exchanger plates are assumed be in perfect thermal contact. Plate thickness was not included in the current simulations. The additional complexity involved in simulating the plates was not considered necessary to achieve the goals of the present study and was not taken any futher.

Special considerations were required for BC34. For the plate in the domain to function as a heat exchanger within a thermoacoustic engine, BC34 must impose conditions consistent with there being a regenerator operating as a heat pump or a prime mover just outside the boundary. One can consider that if the pressure, velocity and temperature that are expected at the regenerator are imposed at BC34, the plate in the domain functions as a heat exchanger.

Simpler modelling of the boundary conditions would be possible of the whole devices was simulated, but this would come at the expense of greatly increased computational time and memory requirements. For example, with a speaker driven heat pump, the condition of resonance is to have pressure and the volumetric velocity in phase at the face of the speaker no matter what geometry the rest of the components have. However, by choosing another point in the tube as a boundary, one must specify the boundary conditions for the flow and temperature fields that would exist at that point in an operating device.

Cao *et al.* (1996) have carried out a computational simulation of a thermoacoustic couple. (A thermoacoustic couple is described in section 2.1.) In their simulation the plate thickness is neglected and the plate's temperature is kept uniform. Although their simulation is not for a heat exchanger plate, careful inspection of their boundary condition is useful for the current work.

Their simulation domain is similar to the current work except that it does not extend to the tube wall; instead it encompasses just the region near the plate, to save computation time. The domain is similar to that in figure 5.2 except that BC12 is moved closer to the inner plate edge, 6, and BC12 is not the rigid end but an oscillating boundary condition is specified.

Cao *et al.* imposed oscillating boundary conditions at the left and right ends of their domain where they specify the following x-component of velocity,

$$u_{left} = -u_A[sin(2\pi x_{left}/\lambda)cos(\omega t)] + \alpha cos(2\pi x_{left}/\lambda)sin(\omega t)] \tag{5.8}$$

$$u_{right} = -u_A[sin(2\pi x_{right}/\lambda)cos(\omega t)] + \alpha cos(2\pi x_{right}/\lambda)sin(\omega t)]. \tag{5.9}$$

This is a summation of the progressive wave (subscript +) and the regressive wave (subscript -),

$$u_+ = u_A\frac{(1+\alpha)}{2}sin(\omega t - kx) \tag{5.10}$$

and

$$u_- = -u_A\frac{(1-\alpha)}{2}sin(\omega t + kx). \tag{5.11}$$

When coefficient $\alpha = 0$, the equation is that of an ideal resonant standing wave which has a velocity node at $x = 0$ (although they do not simulate the region near $x = 0$). In such a case, for all x, the pressure and velocity are 90° out of phase. Their sound source is assumed to be outside the domain on the right hand side.

When the plate is introduced within the domain, the resonant standing wave phasing is perturbed near the plate and there is energy loss through the isothermal plate due to action of the viscosity.

Cao *et al.*, adjust the amplitude of the regressive and progressive waves by changing α. This does not change the phase between the incident and the reflected pressure or velocity at the tube end as α is a real number, i.e. resonance is maintained even when α is changed. It changes only the temporal phase between the pressure and the velocity as a function of x.

If one assumes a relationship between the velocity and the pressure derived from the plane wave equation, as can be found in general acoustics text books (such as Kinsler and Frey, 1962), pressures associated with the progressive and the regressive wave are

$$u_+ = \frac{P_+}{\rho a} \qquad u_- = -\frac{P_-}{\rho a}. \tag{5.12}$$

Superposition of these pressures is after some manipulation of trigonometirc functions

$$p = \rho a u_A \sqrt{cos^2(-kx) + \alpha^2 sin^2(-kx)}cos(\omega t - \theta_1), \tag{5.13}$$

where θ_1 is $tan^{-1}\alpha cos(-kx)/sin(-kx)$ while the super position of velocities is

$$u = u_A \sqrt{\alpha^2 cos^2(-kx) + sin^2(-kx)}cos(\omega t - \theta_2) \tag{5.14}$$

where θ_2 is $tan^{-1}cos(-kx)/\alpha sin(-kx)$. The the temporal phase difference between the pressure and the velocity is

$$\theta_1 + \theta_2 = tan^{-1}\frac{\alpha cos(-kx)}{sin(-kx)} + tan^{-1}\frac{cos(-kx)}{\alpha sin(-kx)}$$

In the analysis of Cao *et al.*, α is adjusted to ensure that the phase shift between the pressure and the velocity is 90° at the inner plate edge so that there is no average energy flux crossing the left end of the plate.

When the plate is short in comparison with the acoustic wave length, their boundary conditions are appropriate. However, for longer plates and plates of finite thickness, a refinement of the boundary condition is required. The first point is that viscous effects will lead to a small shift in the resonant frequency. The resonant frequency will also be shifted when the plate thickness is included. The presence of the plate changes the volume of the hollow section in the tube and, therefore, it will change the resonant frequency. The other point is that the amplitudes of the regressive and the progressive waves are fixed in the x-direction, whereas, in reality, they should decrease by a small amount along the plate. However, at steady state, summation of both waves is correct although the amplitude of each wave is not accurately expressed.

In the current work, to avoid such ambiguity, the simulation domain was stretched up to the closed end of the resonator and an oscillatory boundary was used only on one side of the plate. The oscillatory boundary specified at the open end of the simulation domain is calculated from analytical values. Forcing boundary conditions which are not exactly those which would occur for a thermoacoustic couple at the boundary locations will cause the computed flow field to deviate from that for an ideal thermoacoustic couple and, in the worst case, the solution may not converge.

The pressure, the velocity and the temperature at BC34 can be expressed using complex notation as follows,

$$p = p_m + Re\left\{p_1 e^{(i\omega t)}\right\} \tag{5.15}$$

$$u = Re\left\{u_1 e^{i(\omega t + \alpha_{reg-u} + \alpha_{pu})}\right\} \tag{5.16}$$

$$T = T_m + Re\left\{T_1 e^{i(\omega t + \alpha_{reg-T} + \alpha_{pT})}\right\}, \tag{5.17}$$

where p_1, u_1 and T_1 are the complex amplitudes (either y-dependent or not dependent) of pressure, x-component of velocity and temperature, respectively, around their mean values. α_{pu} is the quantity used to manually control the temporal phase shift between velocity and pressure from those of an ideal standing wave. α_{pT} is the quantity used to control the temporal phase shift between temperature and pressure from those of the ideal solution for the temperature distribution in the regenerator section. α_{reg-u} and α_{reg-T} are, respectively, the phase shifts between velocity and pressure and temperature and pressure at the regenerator plate.

In order to simulate a 2-D standing wave with these boundary conditions, equation (2.1) should be used for p_1. For T_1, the first term inside the first brackets of equation (2.42) should be used. And for u_1,

$$u_1 = i\frac{-P_A}{\rho_m a} sin(kx), \tag{5.18}$$

which is equation (2.2) multiplied by the unit complex number, i, to impose a 90° temporal phase shift between the pressure and the velocity. Temporal phase shifts α_{pu}, α_{pT}, α_{reg-u} and α_{reg-T} should be set to zero. The standing wave simulated using these conditions is consistent with a tube with a closed end (a velocity node or a pressure antinode) at x=0.

In order to simulate the heat exchangers of a thermoacoustic engine, a number of options are considered for u_1 and T_1 but for p_1, the pressure amplitude of a standing wave is used.

To obtain expressions for T_1 and α_{reg-T}, equation (2.42), which is an expression for the temperature amplitude over the regenerator plate of the single plate model, was space averaged in the y-direction. This was done because in a practical device, often, the heat exchanger plates and the regenerator plates are not aligned with one another so that it is hard to predict the exact temperature profile entering the heat exchanger section. The y-averaged complex temperature amplitude, T_1, is of the form,

$$T_1 = \Big(\frac{p_1^s}{\rho_m C_p} - \frac{\nabla T_m u_1^s}{\omega}\Big)\Big(1 - \frac{\delta_k}{y_0(1+i)}(1 - e^{-(1+i)\frac{y_0}{\delta_k}})\Big) \tag{5.19}$$

where ∇T_m, is the temperature gradient developed over the regenerator stack (which is outside the domain of the present simulation). By space averaging, the phase shift of the temperature from the pressure is made constant in the y-direction.

By rearranging inside the second bracket in the second term of equation (5.19) and separating it into real and imaginary parts, then normalizing both terms by the magnitude of the real part, the phase shift can be expressed as

$$\alpha_{reg-T} = tan^{-1}\frac{\text{Imaginary part}}{\text{Real part}}. \tag{5.20}$$

If the imaginary part and the real part are both negative or the real part positive and the imaginary part is negative, α_{reg-T} is set to be negative ($-\pi < \alpha_{reg-T} < 0$) and for all other cases, α_{reg-T} is set positive ($0 < \alpha_{reg-T} < \pi$).

Complex notation in acoustics can also be re-written in the following manner as shown in Morse and Ingard (1989). The temperature at BC34 can be expressed as

$$T = T_m + Re\{\sqrt{Real^2 + Imaginary^2}e^{i(\omega t + \alpha_{reg-T})}\}, \tag{5.21}$$

where the temperature amplitude is now a real number, $\sqrt{Real^2 + Imaginary^2}$, and the temporal phase shift of temperature is α_{reg-T}.

The amplitudes of pressure and velocity used in equation (5.15) and (5.16) are those for an ideal standing wave. For the temperature distribution the solution for an ideal regenerator is chosen. In reality, the amplitudes and the phases of all three quantities will differ slightly from the simple analytical solution due to the viscosity of the gas, the thermal interaction between the plate and the gas and the change in the open cross section of the tube due to the plates.

Other oscillatory boundary conditions, based on analytical expression with various degree of complexity, are also considered.

When the velocity amplitude from the first order analytical model, given in equation (2.21), is y-averaged, it leaves

$$u_1 = \frac{i}{\omega \rho_m}\frac{dp_1}{dx}\Big(1 - f_\nu\Big). \tag{5.22}$$

When the temperature amplitude from the first order analytical model given in equation (2.22) is y-direction, it leaves

$$\begin{aligned} T_1 = {} & \frac{T_m \beta p_1}{\rho_m c_p} - \frac{1}{\rho_m \omega^2}\Big(1 - \frac{Pr}{(Pr-1)}f_\nu\Big)\frac{dp_1}{dx}\frac{dT_m}{dx} \\ & -\Big[\frac{T_m \beta p_1}{\rho_m c_p} + \frac{(dp_1/dx)(dT_m/dx)}{(Pr-1)\rho_m \omega^2}\Big)\Big] f_k \end{aligned} \tag{5.23}$$

Noting that the plate is infinitesimally thin and isothermal, ϵ_s was set to zero in equation (2.22). The combinations of temperature and velocity amplitude for BC34 shown in table 5.1 were considered. When y-dependent velocity or temperature profiles are used, the regenerator and heat exchanger plates are assumed to be aligned. When y-averaged, the phase shift calculated from equation (5.20) is dependent on the plate space y_0. Averaging in the y-direction may not be suitable for large plate spacings as the phase shift occurs only within the thermal penetration depth near the plate surfaces.

	T_1	u_1
BC34-1	eq.(5.19)	eq.(2.2)
BC34-2		eq.(5.22)
BC34-3	eq.(2.42)	eq.(2.2)
BC34-4		eq.(5.22)
BC34-5	eq.(5.23)	eq.(5.22)
BC34-6	eq.(2.22)	eq.(2.21)

Table 5.1: Possible combination of T_1 and u_1 at BC34.

Some equations listed in the table 5.1 for u_1 require dp_1/dx, the pressure gradient at the exit of regenerator, (i.e., at BC34). As the pressure boundary condition at BC34 is given by equation (5.15), dp_1/dx was found by differentiating equation (5.15). Again, the heat exchanger and regenerator plates were assumed to be aligned. The cross section change in going from the regenerator to the heat exchanger section can be taken into account by applying continuity of volumetric flow using the short engine model.

However for the realistic case, dp_1/dx at the exit of regenerator should be complex as can be seen from equation (2.31). The complex part is assumed to be small. Therefore the effect of imposing only the real value will appear as a slight error in amplitude and the temporal phase of the velocity. (The effects of this assumption on u_1 can be checked by changing the temporal phase of u_1, α_{pu} and its amplitude.)

If one is to avoid the ambiguity of the effects of interactions between the heat exchanger plate edges and the regenerator plates, it is possible to extend the simulation domain further to include up to the center of regenerator plate. There, one can apply the first order analytical solution which agrees well with experiments at the center of the regenerator plate but only for limited operating conditions as mentioned in section 2.5.2. This boundary condition would also preclude acoustic streaming. In addition, it will then be necessary to assume some distribution of the mean temperature over the plate surface. (Some test runs in the current work showed that the results were too dependent on the temperature distribution assumed on the plates of the regenerator and for one to produce useful results, the temperature of the regenerator plates must be specified accurately.)

When simulating hot heat exchangers, sometimes the temperature difference between the heat exchanger region and the empty section of the resonator tube is of the order of 10^2 K. In such a case, the resonant frequency evaluated at each temperature differs greatly. However, Rott (1976) shows analytically that the resonant frequency when there is a large temperature difference within a tube is very close to the resonant frequency evaluated at the temperature of the colder portion of the tube. This is also shown in Swift's experiment (Swift 1992) with a large thermoacoustic prime mover. In that prime mover, the small section of the resonator is at nearly 900K and the gas temperature in the rest of the tube is near 300K. The reason for this can be explained by considering a half wavelength closed resonator as a moving mass bouncing against two springs, with the moving mass being the mass of the gas in the central third of the resonator, and the two spring being the compressiblity of the gas in the outer thirds of the resonator. The resonance frequency of a mass on a spring is $\sqrt{k/m}$. The frequency would depend on the temperature because the density of the moving gas that contributes to m depends on the temperature while the spring constant is independent of temperature because gas compressiblity causing it is independent of temperature. It is only in the outer third of the resonator of the thermoacoustic engine where the temperature differs greatly from ambient temperature. Thus the resonant frequency is governed primarily by the ambient temperature. Resonance can be checked by observing the pressure amplitude at the tube wall. The operating frequency should be constant throughout the tube but thermal properties will still be temperature dependent. As a consequence, the wave vector differs in each section at a different temperature.

Analytical boundary conditions were also specified in cells immediately to the right of BC34 (see figure 5.2) to enforce the condition at BC34. Analytical values imposed there, were calculated from the first order theory at the regenerator plate (shown in section 2.2). The last row of cells in the x-direction was not used as one can not specify the value of velocity there due to the staggered grid arrangement. The extra cell after BC34 did not affect the results of the simulation much but the last cell of the domain should not be used to specify the standing wave conditions.

Chapter 6

Simulation of a standing wave

6.1 Introduction

Since there are no analytical, experimental or numerical data which to compare with results from the heat exchanger model, care has been taken to justify the validity of the modeling in the current work. As a first step, simulation of a standing wave was carried out as there have not been any previous examples where PHOENICS has been used to simulate transient sound waves.

The suitability of using PHOENICS to simulate sound waves is investigated by simulating standing waves in a Helium filled 2-D duct, away from the tube wall. The results are compared with 1-D first order analytical solutions for various operating conditions. Conditions were chosen to cover typical operating conditions of existing thermoacoustic engines.

6.2 Method of simulation and test cases

The standing wave can be simulated using the boundary conditions described in section (5.2.3) with the same simulation domain as in figure 5.2 except there is no plate. The oscillating pressure and temperature specified at BC34 are in phase and the velocity is 90° out of phase.

Since symmetrical conditions are imposed for BC14 and BC23, the gas in the solution domain is unaffected by the resonator tube wall. Therefore the model can be compared to the standard first order analytical solution for a 1-D standing wave in a quarter wave length resonator as shown in equations (2.1), (2.2) and (2.3) for pressure, velocity and temperature. The standing wave is in resonance if the pressure amplitudes at the closed end of the tube are maximum.

In order to make comparisons, Helium at a mean pressure of 100kPa and a mean temperature of 300K was chosen and tested at drive ratios[1] of 1.0 and 10 %. These drive

---

[1] The drive ratio is the ratio between pressure amplitude at the pressure antinode and the mean pressure,

ratios correspond to Mach numbers of 6.e-3 and 6.e-2 respectively. The Mach numbers calculated here are based on the velocity amplitude at the velocity antinode and the speed of sound based on the mean temperature, following Cao *et al.* (1996). Operating frequencies of 100Hz and 500Hz were tested. The domain length in the x-direction is 1/16 of the acoustic wave length and in the y-direction is three times the thermal penetration depth evaluated at the mean temperature. These conditions, listed in table 6.1, were chosen to cover typical operating conditions of thermoacoustic engines. Tests were carried out for selected cases to investigate the dependence of the numerical results on grid size and uniformity (sections 6.3.1 to 6.3.3) and on other variables other, such as frequency, drive ratio and simulation domain length (sections 6.4.1 to 6.4.3).

Case	Freq.[Hz]	Drive rat.[%]	Mach no.	λ[m]	δ_{km}[mm]
1	100	1	6.0e-3	1.0e0	2.4e-2
2	100	3	1.8e-2	1.0e0	2.4e-2
3	100	5	3.0e-2	1.0e0	2.4e-2
4	100	8	4.8e-2	1.0e0	2.4e-2
5	100	10	6.0e-2	1.0e0	2.4e-2
6	500	1	6.0e-3	2.0e0	1.1e-2

Table 6.1: Operating conditions for the standing wave simulations, Pm=1.E6Pa, Tm=300K, Helium, Pr=0.71, Domain length=1/16λ, Domain height $y_0 = 3\delta_{km}$.

Grid size tests were done by varying the size of Δt, the Courant number and the aspect ratio of the grid ($\Delta x/\Delta y$). The definition of Courant number ($= u\Delta t/\Delta x$) used here is the one dimensional form of equation (4.2) except the sound speed is omitted. Sound speed was neglected as the speed of particle oscillation in an standing wave is a small fraction of the sound speed. Courant number was evaluated at BC34 where the velocity amplitude is a maximum as long as the domain length is less than the quarter wave length. Courant number here is used only as an indicator of grid sizes since the CFL condition is generally considered unimportant for the numerical scheme used in PHOENICS (as discussed in section 4.2).

The dependence of the results on the frequency of the sound wave can be checked by comparing the simulation results for cases 1 and 6. For the dependence on the drive ratio, cases 1 to 5 were compared. For all cases, the following results were checked and listed in tables.

1. Space and time averaged difference between spot values for the current cycle and the previous cycle. The values are expressed as a percentage of the fluctuating amplitude of the variable concerned. ($\Delta p_{cy}/P_A$, $\Delta u_{cy}/u_A$, $\Delta T_{cy}/T_A$ and $\Delta \rho_{cy}/\rho_A$) Hereafter referred to as the convergence rate.

---

as described in section 2.5.2

2. Change in averaged bulk temperature from the previous to the current cycle. ($\Delta Tb_{cy}/T_A$)
3. Time and space averaged differences from the 1-D analytical solution. (p_{err}/P_A, u_{err}/u_A and T_{err}/T_A) Hereafter referred as the error.
4. Time averaged energy flux (x-component) E_x at the center of the resonator. ($\dot{E}x_{cen}$)
5. Time averaged energy flux E_x at BC34. ($\dot{E}x_{BC34}$)
6. Area averaged amplitude of E_x at BC34. (ex_{ABC34})
7. Cycle averaged energy dissipation in the domain calculated using equation (3.11). ($\dot{S}_{gen}T_0$)
8. Difference between the analytical and numerical pressure amplitude at the closed end monitored at NY/2. ($\Delta P_A/P_A$)
9. Number of cycles required to reach steady state (Cycles)

The area averaged bulk temperature was calculated using

$$T_b = \frac{\sum_{i=1}^{NX}\sum_{j=1}^{NY}\rho_{i,j}\Delta x(i,j)\Delta y(i,j)T(i,j)}{\sum_{i=1}^{NX}\sum_{j=1}^{NY}\rho_{i,j}\Delta x(i,j)\Delta y(i,j)} \tag{6.1}$$

at all time steps and at the end of a cycle it is time averaged by dividing by the number of time steps (since a uniform time step is used).

E_x is the total of the x-component of energy flux through the y-face of the cell ($\Delta y\times$ unit length in the z-direction) which is calculated using equation (4.9) and e_x is the area average of E_x.

Items 1 to 3 and 8 are expressed as percentages and are normalized by the amplitude of the relevant variable (p, u or T) for an ideal standing wave. (The convergence rate of the enthalpy, H, is the same as that of temperature since for an ideal gas, PHOENICS calculates the temperature from equation (5.2) and c_p is constant.) Item 9, the number of cycles to reach steady state, varies slightly depending on the setting of the relaxation factor and the maximum number of iteration specified by the user. This is due to the fact that the iteration never meets the residual criteria as discussed in section 4.5.3. Unless otherwise stated, each series of tests used the same relaxation factor and maximum number of iterations.

The amplitude of the x-component of energy density flux at BC34, ex_{ABC34}, is the maximum instantaneous energy density flux which was chosen out of all time steps and all y cells at x-location, BC34. As this is an area averaged quantity, when comparing its magnitude to the total cycle averaged energy flux through BC34 or the mid-resonator section ($\dot{E}_{BC34}$ or $\dot{E}_{cen}$), in the current work it was decided to multiply ex_{ABC34} by the domain height y_0 and the unit length in the z-direction.

When presenting the numerical and analytical results in the same figure, solid lines are used for analytical solutions and points or points with lines are used for the numerical results.

6.3 Grid dependency tests

6.3.1 Tests on time step

The sensitivity of the solution to the time step size was tested for case 1. The Courant number and the aspect ratio were fixed at 0.01 and 200 respectively. Other operating conditions are listed in Table 6.1. The time step sizes tested were 0.83, 0.42, 0.28, 0.21 and 0.17% of the duration of the cycle. A complete table of results is given in table 6.2. All the results listed in the table are those at the 'cut off cycle' which is described in section 4.5.3.

Run		1	2	3	4	5	6
Δt	[%]	0.83	0.42	0.28	0.21	0.17	0.14
$\Delta p_{cy}/P_A$	[%]	8.8e-4	1.7e-3	2.8e-3	5.4e-3	1.6e-2	1.5e-2
$\Delta u_{cy}/u_A$	[%]	8.0e-4	1.6e-3	2.9e-3	5.6e-3	1.5e-2	1.5e-2
$\Delta T_{cy}/T_A$	[%]	4.4e-2	2.2e-2	7.7e-3	7.2e-3	1.8e-2	1.7e-2
$\Delta \rho_{cy}/\rho_A$	[%]	2.9e-2	1.5e-2	5.9e-3	6.1e-3	1.8e-2	1.6e-2
$\Delta Tb_{cy}/T_A$	[%]	4.2e-2	2.2e-2	6.6e-3	6.0e-3	4.3e-3	8.9e-3
p_{err}/P_A	[%]	2.4e-1	1.2e-1	9.3e-2	7.9e-2	6.8e-2	6.5e-2
u_{err}/u_A	[%]	3.5e-1	1.8e-1	1.2e-1	1.0e-1	9.7e-2	9.0e-2
T_{err}/T_A	[%]	4.8e-1	3.8e-1	3.0e-1	2.9e-1	2.6e-1	3.0e-1
$\dot{E}x_{cen}$	[W]	-1.1e-1	-5.6e-2	-3.8e-2	-2.9e-2	-2.1e-2	-1.8e-2
$\dot{E}x_{BC34}$	[W]	-1.1e-1	-5.5e-2	-3.7e-2	-2.9e-2	-2.1e-2	-1.8e-2
ex_{ABC34}	[W/m^2]	2.1e4	2.2e4	2.2e4	2.2e4	2.2e4	2.2e4
$\dot{S}_{gen}T_0$	[W]	8.7E-8	8.6e-8	8.6e-8	8.6e-8	8.6e-8	8.6e-8
$\Delta P_A/P_A$	[%]	-1.0e-1	-1.1e-1	-1.9e-1	-4.7e-1	-1.6e-1	-2.1e-1
Cycles		10	14	18	18	21	20
$\Delta x/\lambda$		2.0e-3	9.6e-4	6.4e-4	4.8e-4	3.8e-4	3.2e-4
$\Delta y/\delta_{km}$		4.3e-1	2.1e-1	1.4e-1	1.0e-1	8.3e-2	7.0e-2

Table 6.2: Results of simulations for case 1 with various time step sizes, Courant no.=0.01, $\Delta x/\Delta y \simeq 200$.

The convergence rate and the time and space averaged error versus number of cycles for p_1, u_1 and T_1 are plotted in figures 6.1 to 6.3 for simulations with Δt=0.83, 0.42, 0.28 and 0.14%.

Figures 6.1 to 6.3 show that the convergence rate drops rapidly (especially for coarse

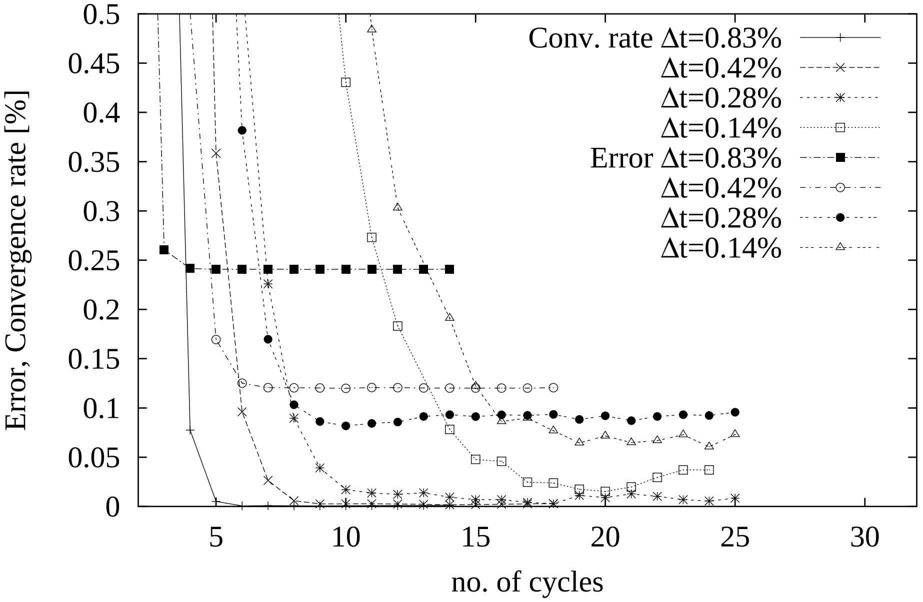

Figure 6.1: Convergence rate and error of the pressure versus number of cycles for case 1.

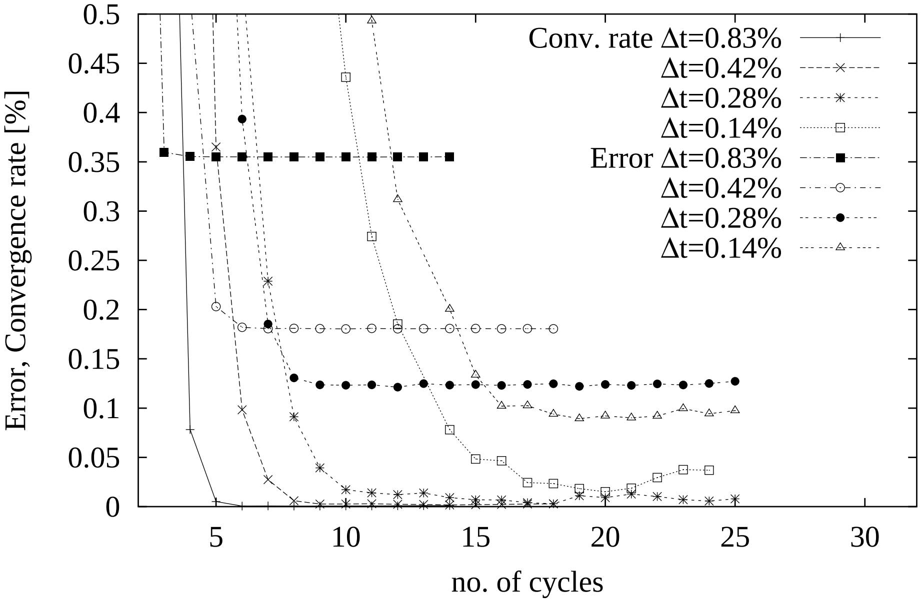

Figure 6.2: Convergence rate and error versus number of cycle for the velocity amplitude for case 1.

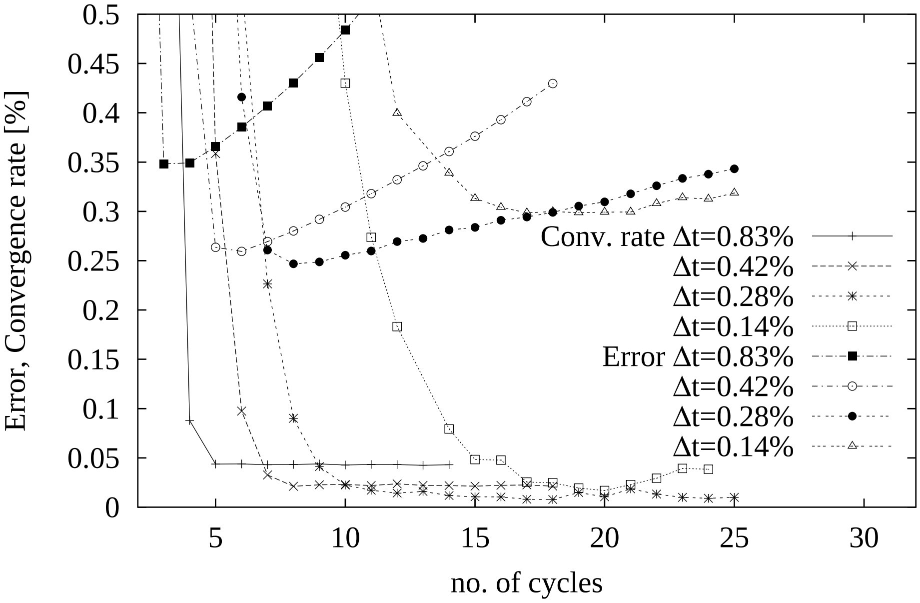

Figure 6.3: Convergence rate and error versus number of cycle for the temperature amplitude for case 1.

time step sizes) but once it reaches a certain value, it stays constant. The magnitude of this convergence rate was smaller at the 'cut off cycle' when the time step size was smaller. It is expected that errors would decrease further if PHOENICS was run in double precision.

Although the convergence rates for temperature are larger than those for pressure and velocity amplitude, for all time steps tested (except when Δt=0.14%), simulating for more cycles does not improve the convergence rate of the temperature and in fact the convergence rate of the other variables becomes worse.

The error in temperature starts to increase almost linearly at half the number of cut off cycles for all time step sizes. The error gradually increases, if further iterations beyond the cut-off cycle were made.

When using large time steps (Δt=0.42% and 0.28%), the convergence rate of temperature is approximately ten times that of pressure and velocity. In that case, the rate of increase in error (between the analytical and numerical values) coincides with the convergence rate (i.e., because the convergence rate does not further improve, the averaged temperature of the domain can change at the rate of the convergence rate and therefore deviate from that for a true standing wave where there is no temperature drift). However, at finer time step sizes (Δt =0.21%, 0.17% and 0.14%), the convergence rates are of similar order to that of pressure and velocity, while the error of temperature linearly increases but at a slower rate than those for the larger Δt. Considering that the magnitude of the error is normalized by the temperature amplitude, which is approximately 1/100 of the mean temperature, the error increase for test cases with smaller time steps are negligible. However, it is suggested that the iteration of the simulation is stopped as soon as the convergence rate plateaus.

As noted in section 4.4, the units for the simulations were chosen to avoid the use of small grid dimensions and time steps. In order to test if use of such dimensions affected the magnitude of the convergence rate of the temperature, the same standing wave simulations were carried out with SI units. Results are listed in table 6.3. The results show that the temperature still has the largest convergence rate.

Run		7	8	9	10	11
Δt	[%]	0.42	0.28	0.21	0.17	0.14
$\Delta p_{cy}/P_A$	[%]	1.7e-3	3.0e-3	3.7e-3	1.1e-2	1.3e-2
$\Delta u_{cy}/u_A$	[%]	1.6e-3	3.1e-3	3.4e-3	1.1e-2	1.4e-2
$\Delta T_{cy}/T_A$	[%]	2.1e-2	2.3e-2	1.2e-2	1.2e-2	1.4e-2
$\Delta \rho_{cy}/\rho_A$	[%]	1.4e-2	1.5e-2	8.0e-3	1.1e-2	1.3e-2
$\Delta Tb_{cy}/T_A$	[%]	2.0e-2	2.3e-2	1.1e-2	7.1e-4	2.4e-3
p_{err}/P_A	[%]	1.2e-1	8.6e-2	6.7e-2	8.0e-2	8.8e-2
u_{err}/u_A	[%]	1.8e-1	1.4e-1	1.1e-1	1.0e-1	1.0e-1
T_{err}/T_A	[%]	3.1e-1	3.1e-1	2.7e-1	3.1e-1	2.2e-1
$\dot{E}x_{cen}$	[W]	-5.6e-2	-3.8e-2	-2.8e-2	-2.1e-2	-2.0e-2
$\dot{E}x_{BC34}$	[W]	-5.5e-2	-3.7e-2	-2.8e-2	-2.2e-2	-2.0e-2
ex_{ABC34}	[W/m^2]	2.2e4	2.2e4	2.2e4	2.2e4	2.2e4
$\dot{S}_{gen}T_0$	[W]	8.6e-8	8.6e-8	8.6e-8	8.6e-8	8.6e-8
$\Delta P_A/P_A$	[%]	-1.0e-1	-4.6e-2	-1.2e-1	-3.1e-1	3.6e-1
Cycles		11	15	17	21	18
$\Delta x/\lambda$		9.6e-4	6.4e-4	4.8e-4	3.8e-4	3.2e-4
$\Delta y/\delta_{km}$		2.1e-1	1.4e-1	1.0e-1	8.3e-2	7.0e-2

Table 6.3: Results of simulations for case 1 with various time step sizes. SI units. Courant no.=0.01. $\Delta x/\Delta y \simeq 200$.

In order to compare how results are influenced by changing the units, errors for pressure, velocity and temperature versus size of time steps are shown for both cases in figure 6.4. The figure shows that the overall errors reduce with the size of Δt when using either units and there are very small differences between the results of simulations using the different units except at $\Delta t < 0.21\%$. At these smaller values of Δt, the errors using SI units start to increase or become unstable. This is expected due to the round off errors (see discussion in section 4.4). Use of non SI units seems more effective for smaller time steps.

For all time step sizes tested, the simulation agreed with the analytical solution to within 0.5% for case 1 at steady state and, from the magnitude $\Delta P_A/P_A$, all test cases are resonant. However, these are time and space averaged errors. In order to show that the magnitudes of the errors are evenly spread in time and space, the numerical results and

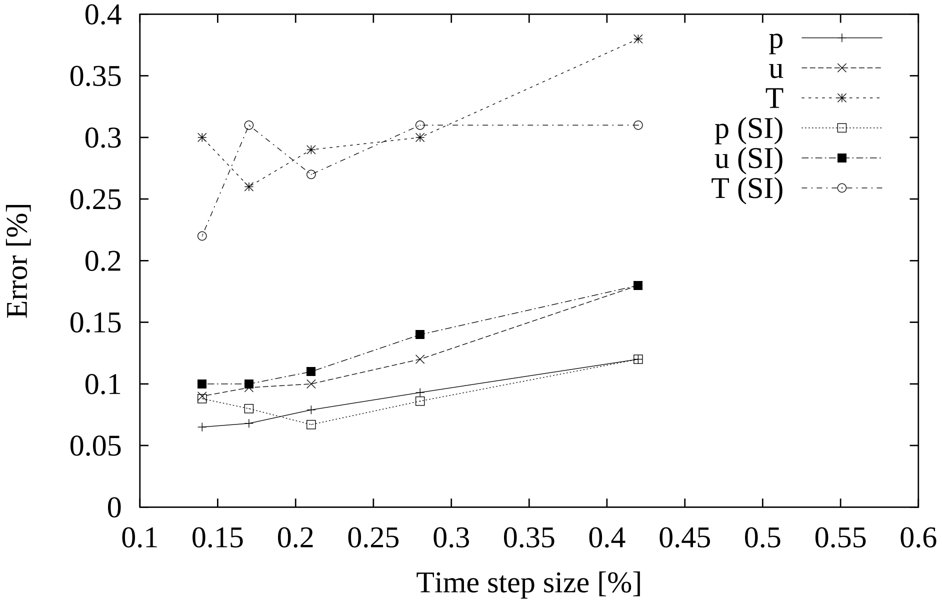

Figure 6.4: Error versus time step size for case 1 using two different units.

the analytical solutions for pressure, velocity and temperature at the center of the domain (in the y-direction) as a function of the x-coordinate at time steps every 1/8 of a cycle for the simulation with $\Delta t = 0.42\%$ are shown in figures 6.5 to 6.7. τ is the duration of a cycle.

Figures 6.5 to 6.7 show that the simulations agree well at every 1/8th of a cycle at all x-locations and it can be considered that the time and space averaged error will give a good indication of the error in the simulation.

Simulations with the smallest time step are very time consuming and, are unnecessary if the required agreement with the analytical solution is of the order of 1%. Therefore, further tests for special grid dependency using case 1 were carried out either with time step sizes of 0.42% or larger.

Since the convergence rate for the bulk temperature is almost equal to the convergence rate of temperature at steady state, it will not be displayed in further results listed in this chapter. The convergence rates of the bulk temperature when Δt=0.17 or 0.14% do not agree with those of temperature, and this could be an indication of round off error.

In both table 6.2 and 6.3, the x-component of time averaged energy flux through BC34, $\dot{E}x_{BC34}$ and that at the center of the simulation domain, $\dot{E}x_{cen}$, were finite negative values. This means that the energy is flowing into the simulation domain. However, the magnitudes of $\dot{E}x_{BC34}$ and $\dot{E}x_{cen}$ are at the maximum, 0.05% of amplitude of energy flux. Considering the accuracy limitation discussed in section 4.3.2, 0.05% of the energy flux is negligible.

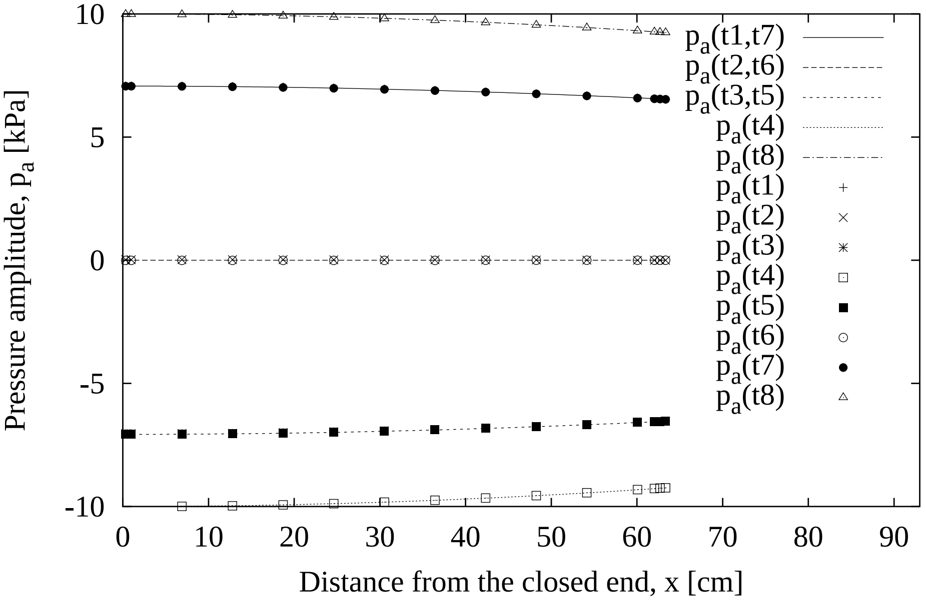

Figure 6.5: Comparison of pressure amplitude with the analytical solution at 8 time steps in a cycle for case 1, $\Delta t = 0.42\%$, Domain height= $3\delta_{km}$. t1=$\tau/8$, t2=$2\tau/8$ ..... t8 =τ.

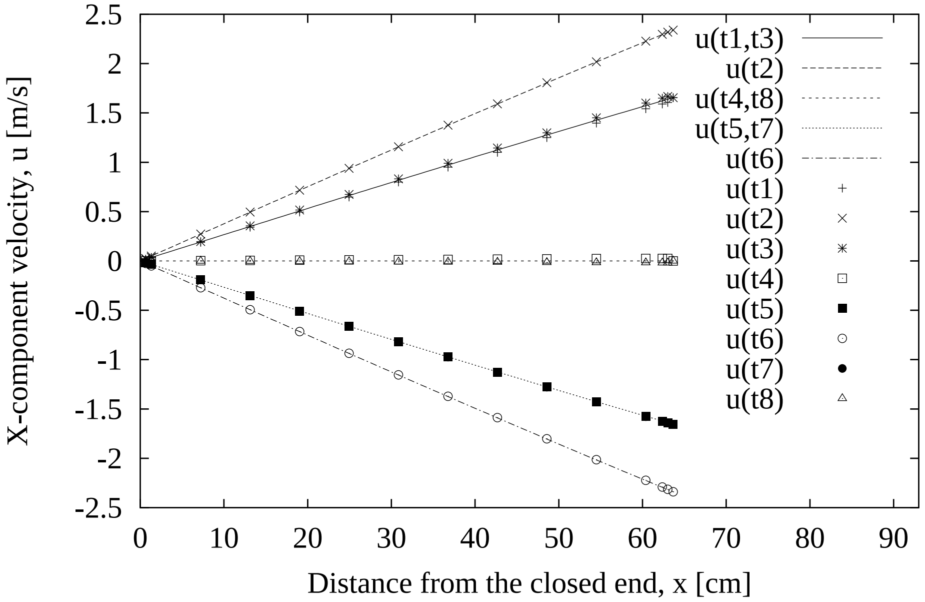

Figure 6.6: Comparison of velocity amplitude with the analytical solution at 8 time steps in a cycle for case 1, $\Delta t = 0.42\%$, Domain height $=3\delta_{km}$.

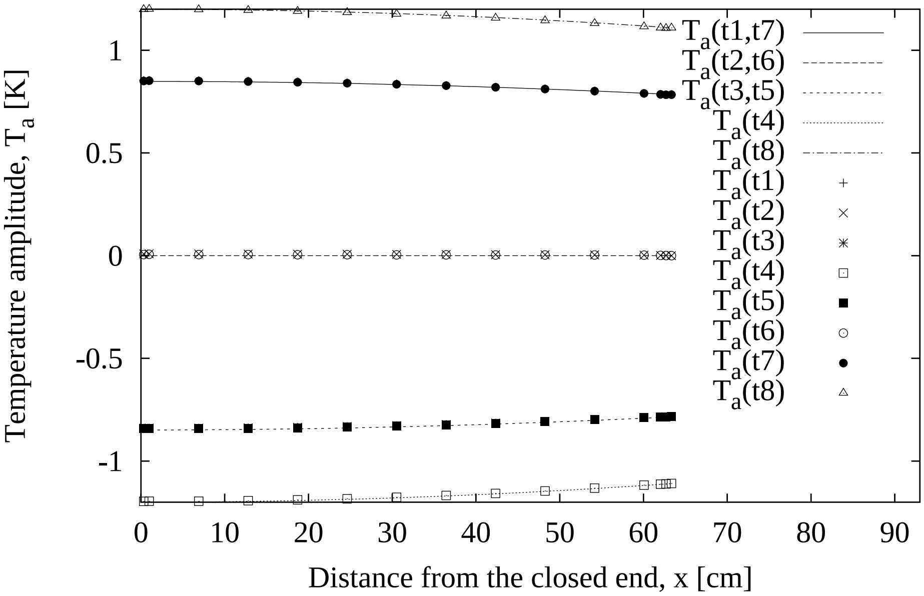

Figure 6.7: Comparison of temperature amplitude with the analytical solution at 8 time steps in a cycle for case 1, $\Delta t = 0.42\%$, Domain height $=3\delta_{km}$.

6.3.2 Spatial grid dependence tests

The aspect ratios ($\Delta x/\Delta y$) of the grids used in the simulations (shown in table 6.2) are of the order of 10^2 larger than the conventionally suggested value for stability of near 1. In order to test the dependence of the simulation results on grid resolution in the y-direction, the Courant number was kept constant and the aspect ratio was changed to unity by stretching the domain in the y-direction by 600 times for case 1. The rest of the conditions were the same as for case 1 and the time step used was 0.42% of the duration of a cycle. The results are listed in the table 6.4. The results were not largely affected by the aspect ratio since the simulation is nominally 1-D and the domain does not include any of the tube walls except at the rigid end.

The dependence of the simulation results on grid resolution in the x-direction was tested by varying the Courant number while keeping Δy constant. Courant numbers tested were 0.005, 0.01, 0.02 and 0.04. For all cases the time step size was 0.278 % of the duration of a cycle. The results are listed in table 6.5. The results show that the error did not significantly reduce as Δx was reduced.

Uniformly spaced grids in time and space were used for all simulations presented in this section. For the standing wave simulation, it is appropriate to use uniform Δy as the problem is nearly one dimensional. Uniform Δt is also appropriate since the fluctuating velocities, temperatures and pressures are phase shifted (i.e. when the velocity amplitude is at its peak, the pressure and temperature amplitudes are near zero).

Run		2	12
$\Delta x/\Delta y$		1.9e2	9.7e-1
$\Delta p_{cy}/P_A$	[%]	1.7e-3	1.5e-3
$\Delta u_{cy}/u_A$	[%]	1.6e-3	1.3e-3
$\Delta T_{cy}/T_A$	[%]	2.2e-2	2.1e-2
$\Delta \rho_{cy}/\rho_A$	[%]	1.5e-2	1.4e-2
p_{err}/P_A	[%]	1.2e-1	1.2e-1
u_{err}/u_A	[%]	1.8e-1	1.8e-1
T_{err}/T_A	[%]	3.8e-1	3.6e-1
$\dot{E}x_{cen}$	[W]	-5.6e-2	-1.1e1
$\dot{E}x_{BC34}$	[W]	-5.6e-2	-1.1e1
ex_{ABC34}	[W/m^2]	2.2e4	2.2e4
$\dot{S}_{gen}T_0$	[W]	8.6e-8	1.7e-5
$\Delta P_A/P_A$	[%]	-1.1e-1	-9.8e-2
Cycles		14	11
$\Delta y/\delta_{km}$		2.1e-1	4.3e1

Table 6.4: Aspect ratio test. Courant no.=0.01, case 1, Δt=4.2%, $\Delta x/\lambda$=9.6e-4.

Run		13	3	14	15
Courant no		0.005	0.01	0.02	0.04
$\Delta p_{cy}/P_A$	[%]	7.2e-3	3.0e-3	8.3e-3	1.7e-3
$\Delta u_{cy}/u_A$	[%]	7.0e-3	3.3e-3	8.1e-3	1.7e-3
$\Delta T_{cy}/T_A$	[%]	1.3e-2	2.1e-2	1.5e-2	1.5e-2
$\Delta \rho_{cy}/\rho_A$	[%]	1.0e-2	1.4e-2	1.1e-2	1.0e-2
p_{err}/P_A	[%]	1.3e-1	8.6e-2	6.6e-2	6.4e-2
u_{err}/u_A	[%]	1.2e-1	1.4e-1	1.2e-1	1.3e-1
T_{err}/T_A	[%]	3.2e-1	3.8e-1	3.0e-1	3.2e-1
$\dot{E}x_{cen}$	[W]	-3.6e-2	-3.8e-2	-3.7e-2	-3.7e-2
$\dot{E}x_{BC34}$	[W]	-3.6e-2	-3.7e-2	-3.6e-2	-3.7e-2
ex_{ABC34}	[W/m^2]	2.1e4	2.2e4	2.2e4	2.2e4
$\dot{S}_{gen}T_0$	[W]	8.5e-8	8.6e-8	8.7e-8	9.0e-8
$\Delta P_A/P_A$	[%]	-1.5e-1	-3.3e-2	-1.2e-1	-1.2e-1
Cycles		15	19	17	19
$\Delta x/\lambda$		1.3e-3	6.4e-4	3.2e-4	1.6e-4

Table 6.5: Results with different Courant number in the x-direction for case 1. Δt=0.28%, $\Delta y/\delta_{km}$=1.4e-1.

6.3.3 Variable grid size in the x-direction

For most simulations of thermoacoustic devices, the domain length in the x-direction is at least 10^2 times larger than it is in the y-direction and it may be more economical to have fine grids only near the regions where rapid changes occur. Fine grids are required near the oscillatory boundary for simulations of thermoacoustic couples and heat exchangers in chapters 7 and 8, when a single plate is located near the oscillatory boundary. In those simulations, a gird arrangement as shown in figure 6.8 is suitable. (This is because the energy dissipation at the closed end is negligible and fine grids were not considered there.) In figure 6.8, the grid spacing in the x-direction gradually expands towards the closed end of the tube.

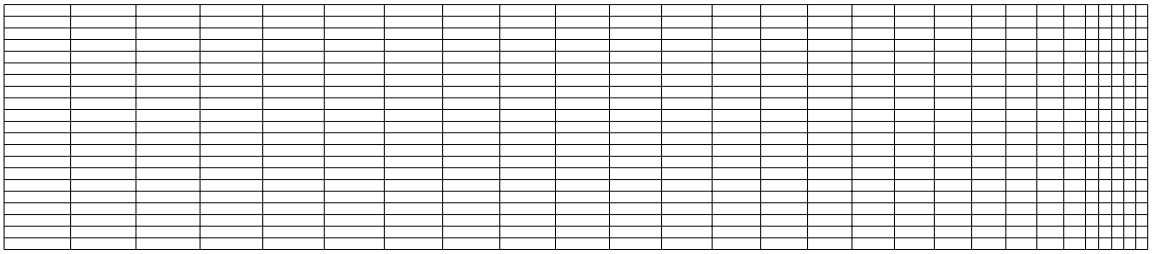

Figure 6.8: Variable grid in x-direction.

In a standing wave, the gas oscillates in the x-direction throughout the simulation domain. In order to test if a grid with varying Δx can be used for standing wave simulations, this grid arrangement was tested with various degree of expansion of the x-grid.

In PHOENICS, the grid size in the x-direction at the i^{th} grid is determined by multiplying the x-domain length by XFRAC(i)-XFRAC(i-1). Where XFRAC(i) is given by

$$\mathrm{XFRAC(i)} = 1.0 - (\frac{\mathrm{NX} - \mathrm{i}}{\mathrm{NX}})^{\alpha_x}. \tag{6.2}$$

NX is the last x grid in the domain and i = 1 corresponds to the grid point closest to the closed end of the tube. α_x is a constant specified by the user. α_x determines the degree of expansion of Δx. In the current work, given α_x, the total number of x-grid points is adjusted so that the grid size at the cell where oscillating boundary conditions are specified satisfies the Courant number chosen.

The operating conditions and geometry of case 1 was used and α_x=1.2, 1.4, 1.9 and 2.3 were tested. The results of simulations with these grids are presented in table 6.6. The last column is a re-listing of the results in table 6.2 with time step size 0.28%.

The errors in pressure slightly decrease as α_x increases while the errors in velocity and temperature slightly increase with α_x. The results show that it is not necessary to have a fine grid even at the rigid end where the acoustic wave is reflected. In terms of errors, a uniform grid or grid arrangement 1 with α_x ranging from 1.2 to 1.9 are preferable.

Overall, the sensitivity to the spatial grid size is not high since the numerical scheme used is second order with respect to the spacial grid. Thus in order to reduce computation time, the grid arrangement shown in figure 6.8 would be the best choice.

Run		16	17	18	19	3
Arrangement		1				uniform
α_x		1.2e0	1.4e0	1.9e0	2.3e0	1.0
$\Delta p_{cy}/P_A$	[%]	4.8e-3	7.1e-3	6.2e-3	8.0e-2	2.8e-3
$\Delta u_{cy}/u_A$	[%]	5.7e-3	9.0e-3	9.6e-3	1.6e-2	2.9e-3
$\Delta T_{cy}/T_A$	[%]	9.2e-3	1.3e-2	1.5e-2	1.6e-2	7.7e-3
$\Delta \rho_{cy}/\rho_A$	[%]	7.2e-3	9.7e-3	1.1e-2	1.2e-2	5.9e-3
p_{err}/P_A	[%]	9.4e-2	8.3e-2	7.6e-2	6.9e-2	9.3e-2
u_{err}/u_A	[%]	1.3e-1	1.5e-1	1.6e-1	1.9e-1	1.2e-1
T_{err}/T_A	[%]	2.4e-1	2.4e-1	2.2e-1	2.8e-1	3.0e-1
$\dot{E}x_{cen}$	[W]	-3.8e-2	-3.9e-2	-4.1e-2	-3.1e-2	-3.7e-2
$\dot{E}x_{BC34}$	[W]	-3.7e-2	-3.7e-2	-3.7e-2	-3.7e-2	-3.7e-2
ex_{ABC34}	[W/m^2]	2.2e5	2.2e5	2.2e5	2.2e5	2.2e5
$\dot{S}_{gen}T_0$	[W]	8.6e-8	8.6e-8	8.6e-8	8.6e-8	8.6e-8
$\Delta P_A/P_A$	[%]	-1.4e-1	-8.8e-2	-2.1e-1	2.4e-4	-1.9e-1
Cycles		12	12	12	11	18
$\Delta x/\lambda$		6.6e-4	6.6e-4	6.6e-4	6.7e-4	6.4e-4

Table 6.6: Results with different grid arrangement in the x-direction for case 1 with Δt=0.28% and $\Delta y/\delta_{km}$=1.4e-1.

6.4 Dependence on other variables

6.4.1 Dependence on frequency

The simulation for the higher frequency condition, case 6, was tested with 3 different time step sizes. The results are in table 6.7. Although the time step sizes expressed as a percentage of the duration of a cycle are the same as those for case 1, the actual time step size is only 20% of that for the lower frequency cases as the duration of the cycle is shorter when the frequency is higher. The magnitude of error is similar for all simulations when the time step size is expressed as a percentage of the duration of a cycle. The last column of table 6.7 shows the results with a Courant number of 0.02 (which reduced the size of Δx by 1/5th) and the aspect ratio, $\Delta x/\Delta y$, is 0.002. While reduction of Δt by 1/3rd reduced errors, reduction of Δx by 1/5th slightly increased the error when tested with $\Delta t = 0.28\%$.

6.4.2 Dependence on drive ratio

In order to test the accuracy of the simulations for different drive ratios, Cases 2 to 5 were run. In order to have a reasonable number of grids points within the domain, the Courant

Run		22	23	24	25
Δt	[%]	0.83	0.42	0.28	0.28
$\Delta p_{cy}/P_A$	[%]	6.0e-4	2.9e-3	5.4e-3	9.0e-3
$\Delta u_{cy}/u_A$	[%]	6.1e-3	2.0e-3	5.5e-3	9.1e-3
$\Delta T_{cy}/T_A$	[%]	4.3e-2	2.0e-2	1.3e-2	1.6e-2
$\Delta \rho_{cy}/\rho_A$	[%]	2.9e-2	1.4e-2	9.0e-3	1.3e-2
p_{err}/P_A	[%]	2.4e-1	1.2e-1	8.8e-2	2.7e-1
u_{err}/u_A	[%]	3.6e-1	1.8e-1	1.3e-1	1.3e-1
T_{err}/T_A	[%]	4.8e-1	3.5e-1	2.6e-1	4.1e-1
$\dot{E}x_{cen}$	[W]	-4.8e-2	-2.5e-2	-1.7e-2	-1.6e-2
$\dot{E}x_{BC34}$	[W]	-4.8e-2	-2.5e-2	-1.7e-2	-1.5e-2
ex_{ABC34}	[W/m^2]	2.1e5	2.2e5	2.2e5	2.1e5
$\dot{S}_{gen}T_0$	[W]	1.9e-7	1.9e-7	1.9e-7	1.9e-7
$\Delta P_A/P_A$	[%]	-1.0e-1	-1.1e-1	-1.2e-1	-1.6e-1
Cycles		10	13	14	11
$\Delta x/\lambda$		2.0e-3	9.6e-4	6.4e-4	3.3e-3

Table 6.7: Results of case 6 (500Hz) with various time step sizes. Courant no.=0.01 except for the last column. $\Delta y/\delta_{km}$=1.4e-1.

number had to be increased from 0.01 to 0.02 for Cases 4 and 5. Results of these simulation are in table 6.8. (Cases 2 to 6 are numbered as runs 26 to 29 in the table.)

The table shows that although errors of the pressure and the velocity remain less than 1% for all drive ratios, errors of the temperature increased by 20 times at the highest drive ratios. Although $\Delta P_A/P_A$, when the drive ratio is 10%, is of the order of 1%, the fact that it is 10 times that of lowest drive ratio indicates that the standing wave is less resonant.

At higher drive ratios (over 5%), the cut off cycle was not as clear, particularly for the temperature. Once the convergence rate reduced to a certain value, it started to reduce linearly at a much slower rate as shown in figure 6.9. Changes in convergence rates are more significant for drive ratios over 5% and a linear drift of convergence rate continued even after 40 cycles. On the other hand, the convergence rates for drive ratios of 1% and 3 % platue after less than 20 cycles. Drifts in convergence rate were not significant for pressure and velocity for all drive ratios.

While the convergence rate of temperature slowly reduces as the number of cycles simulated is increased, the error linearly increases as shown in figure 6.10. Figure 6.11 shows the magnitude of errors as a function of drive ratio at cycles between 15 and 20.

The magnitudes of the error and the convergence rate of temperature at a drive ratio of 1% and those for a drive ratio of 10% differ by ten times at the 25th cycle. The fact that the convergence rate is normalized by amplitudes that are proportional to each drive ratio

Run		3	26	27	28	29
Drive ratio	[%]	1	3	5	8	10
$\Delta p_{cy}/P_A$	[%]	2.8e-3	2.6e-3	1.7e-3	1.1e-3	1.0e-2
$\Delta u_{cy}/u_A$	[%]	2.9e-3	2.5e-3	1.6e-3	1.0e-3	1.0e-2
$\Delta T_{cy}/T_A$	[%]	7.7e-2	3.8e-2	5.2e-2	5.9e-2	5.4e-2
$\Delta \rho_{cy}/\rho_A$	[%]	5.6e-3	2.6e-2	3.5e-2	3.9e-2	3.6e-2
p_{err}/P_A	[%]	9.3e-2	2.2e-1	3.6e-1	4.2e-1	5.2e-1
u_{err}/u_A	[%]	1.2e-1	2.5e-1	3.8e-1	6.2e-1	7.6e-1
T_{err}/T_A	[%]	2.9e-1	7.7e-1	1.6e0	5.4e0	5.2e0
$\dot{E}x_{cen}$	[W]	-3.7e-2	-3.2e-1	-9.4e-1	-2.5e0	-3.8e0
$\dot{E}x_{BC34}$	[W]	-3.7e-2	-3.3e-1	-8.8e-1	-2.3e0	-3.5e0
ex_{ABC34}	[W/m^2]	2.2e5	1.9e6	5.3e6	1.4e7	2.1e7
$\dot{S}_{gen}T_0$	[W]	8.6e-8	7.7e-7	2.2e-6	6.3e-6	9.9e-6
$\Delta P_A/P_A$	[%]	-1.9e-1	-3.4e-1	-5.4e-1	-9.2e-1	-1.2e0
Cycles		18	16	24	64	53
$\Delta x/\lambda$		6.4e-4	2.0e-3	3.3e-3	2.6e-3	3.3e-3

Table 6.8: Drive ratio = 1 to 10%, Δt=0.28%, $\Delta y/\delta_{km}$=1.4e-1, Courant no.=0.01 except for runs 28 and 29.

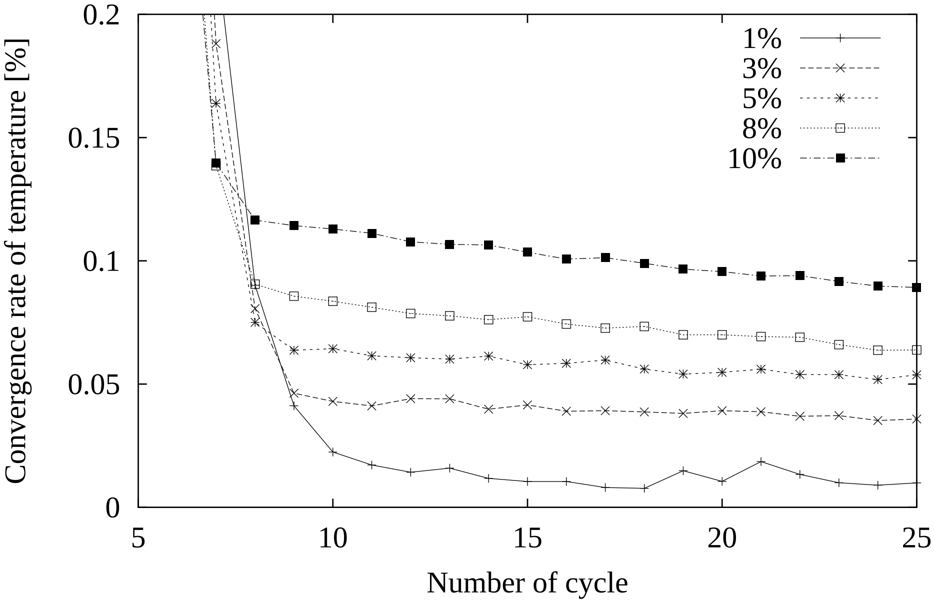

Figure 6.9: Convergence rate for temperature versus number of cycles for drive ratios 1 to 10% . (See table 6.8 for run numbers)

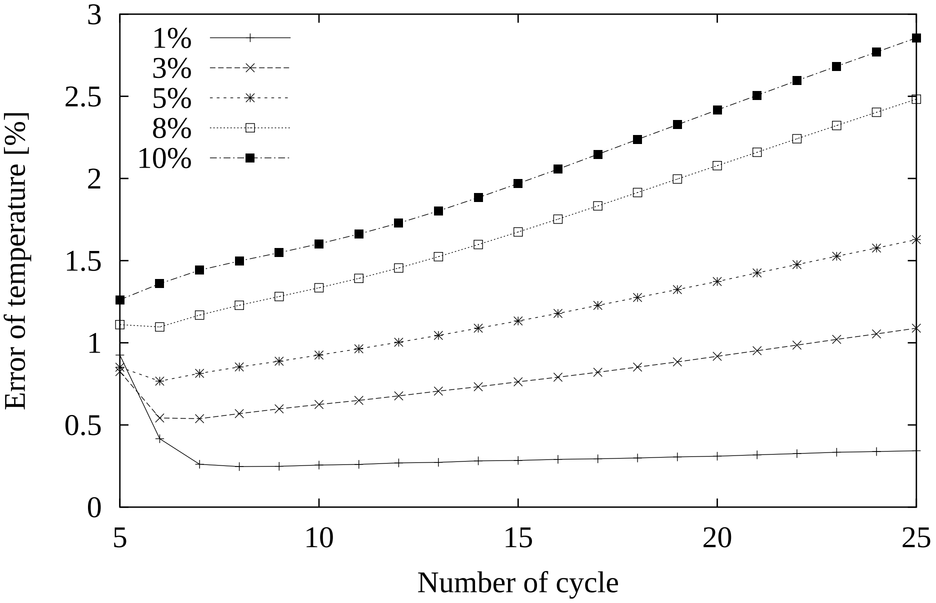

Figure 6.10: Errors in temperature versus number of cycles for drive ratios of 1 to 10% . (See table 6.8 for run numbers)

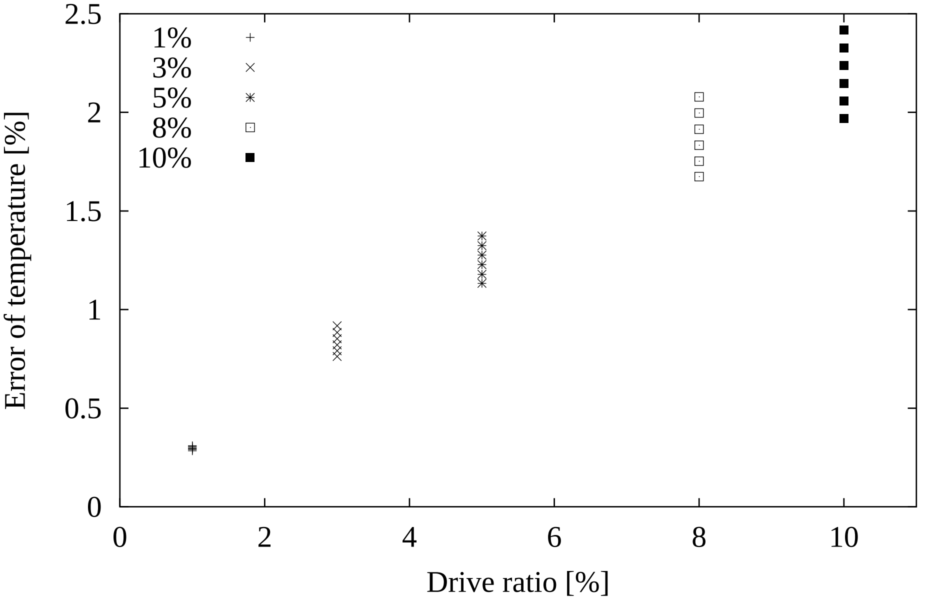

Figure 6.11: Errors in temperature versus drive ratios for cycles 15 to 20. (See table 6.8 for run numbers)

indicates that the actual convergence rate is larger by ten times. The convergence rate of the temperature at a drive ratio of 10% eventually reaches similar levels to those when the drive ratio is 1%. (However, it must be noted that the error in temperature keeps increasing). This suggests that the higher order terms becomes significant as the drive ratio is increased and the boundary conditions applied at BC34 are no longer appropriate and the simulation takes longer to converge to reach steady state. Although wall effects are not included in the current simulation, higher harmonics become more significant at higher drive ratios.

These results also suggest the importance of an appropriate residual criteria in order to know when to stop the iteration. For the current work, if the convergence of the simulation is slow, the iteration was terminated when the convergence rate of temperature reached approximately 0.05%.

In order to visualize how the numerical simulations deviate from the analytical solutions, the distributions of pressure, velocity and temperature at NY/2 as a function of x are plotted for every 1/8th of a cycle for the case where errors were largest, i.e. when the drive ratio is 10%. Results are shown in figures 6.12 to 6.14. Errors are largest at locations where each variable oscillates at maximum amplitude. Errors in pressure and temperature are larger at x=0cm while velocity errors are largest at BC34. One may consider that by changing the temporal phase shift of pressure and velocity at BC34 from that of ideal standing wave, these errors would improve. However, according to figure 6.13, the temporal phase shift is not equal at each time step. At t1, the phase is delayed in comparison to the analytical solutions while at t3, t5, and t7 the phase is advanced and at t2, t4 and

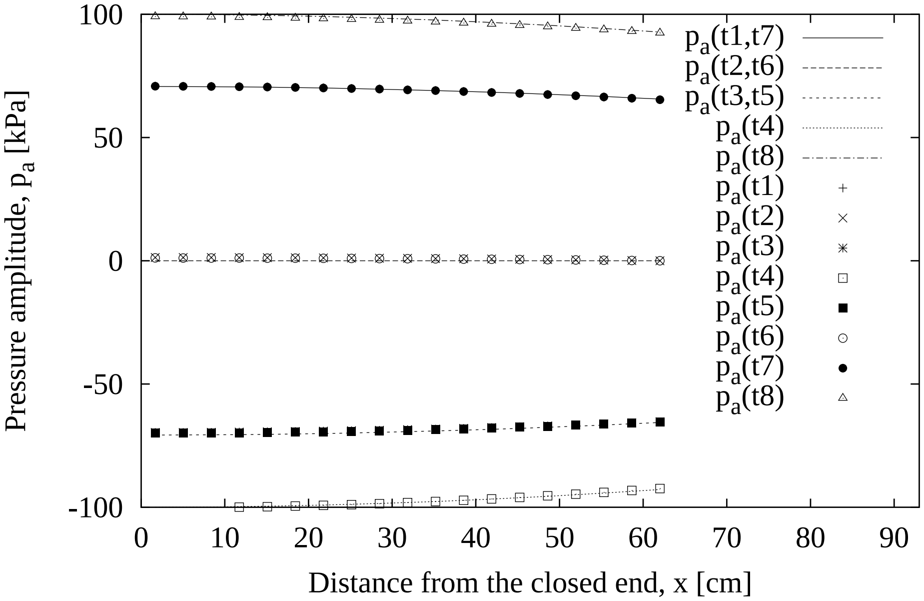

Figure 6.12: Comparison of pressure amplitude with the analytical solution at 8 time steps in a cycle for case 5, $\Delta t = 0.28\%$, Domain height $=3\delta_{km}$. t1=$\tau/8$, t2=$2\tau/8$ ..... t8 =τ.

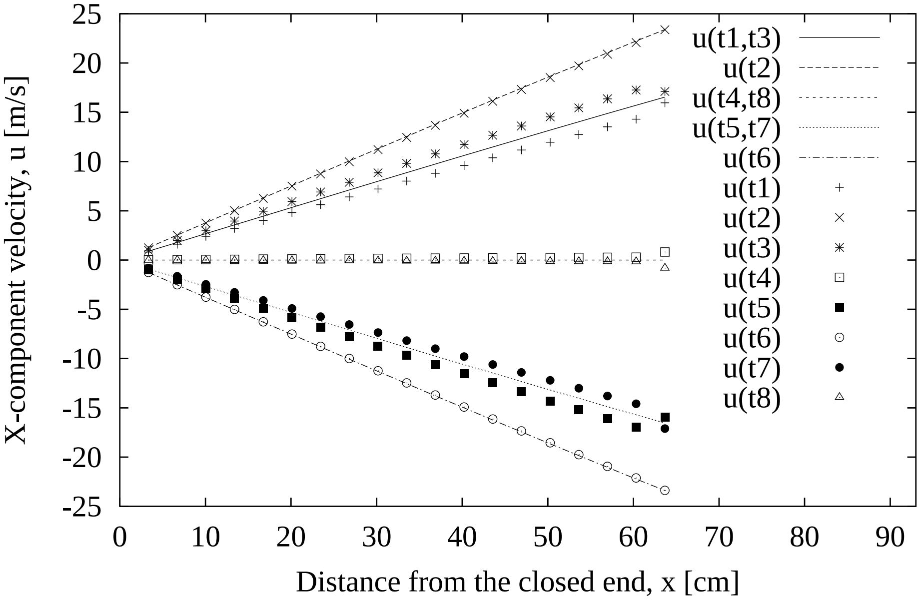

Figure 6.13: Comparison of velocity amplitude with the analytical solution at 8 time steps in a cycle for case 5, $\Delta t = 0.28\%$, Domain height $=3\delta_{km}$.

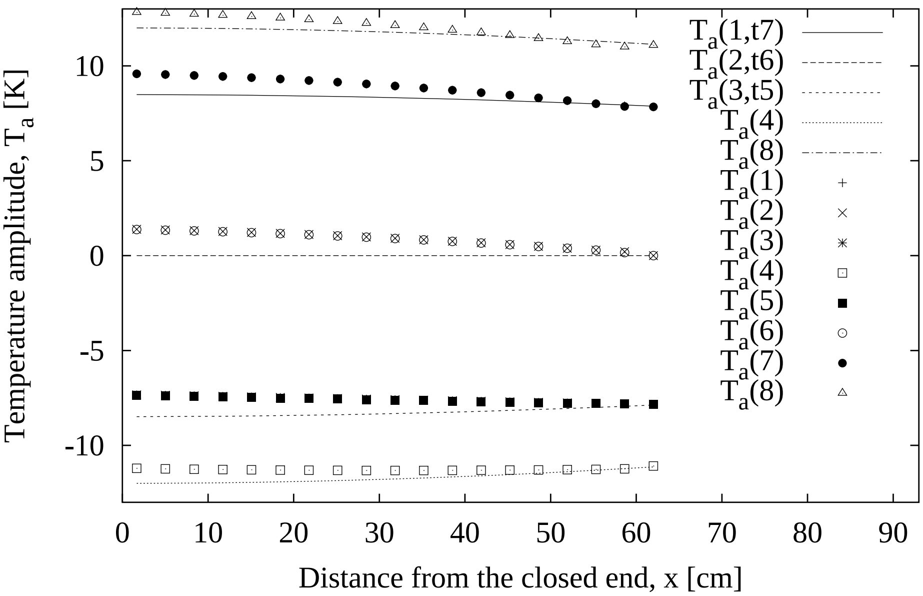

Figure 6.14: Comparison of temperature amplitude with the analytical solution at 8 time steps in a cycle for case 5, $\Delta t = 0.28\%$, Domain height $=3\delta_{km}$.

t8 the phase is equal. As expected, changing the temporal phase of the velocity from the pressure did not improve the results. Simulation results with finer time step sizes showed the same tendency. Dependence of the phase shift on the sizes of Δt and Δx was tested separately for case 5 but the results did not show significant dependence on the time step and grid sizes.

Figure 6.15 shows a time dependence of velocity at the center of the domain. A purely sinusoidal curve is shown as a visual guide. The pressure and the temperature were purely sinusoidal while the velocity was slightly distorted as shown in figure 6.15.

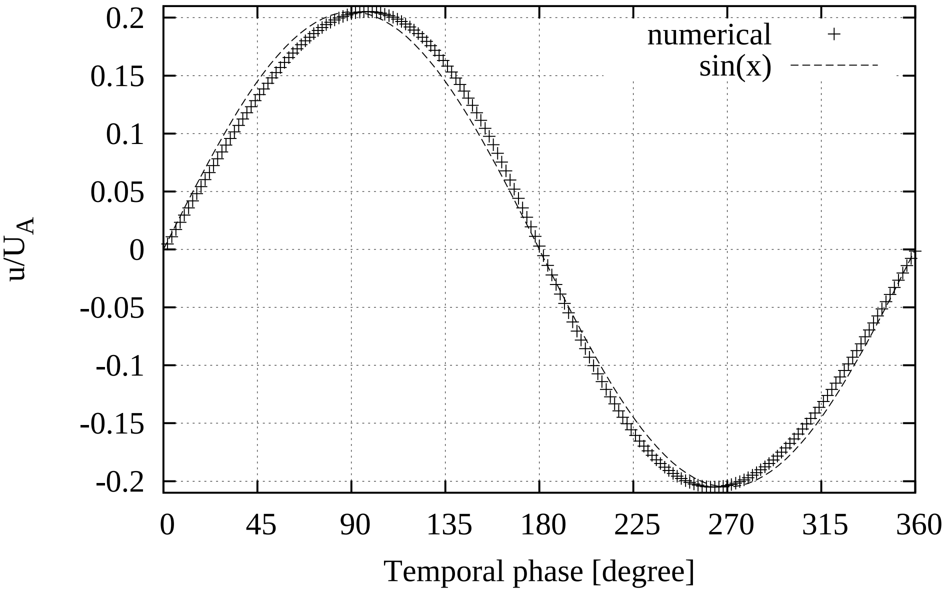

Figure 6.15: Time dependency of velocity at center of the simulation domain. case 5

Therefore, at drive ratio greater than 5%, the ideal standing wave conditions are not very accurate for the operating condition and geometries tested. However, although specifying idealistic boundary conditions takes longer to converge, a steady state is eventually reached, after responding to the boundary conditions imposed.

6.4.3 Dependence on the domain length

Dependence of the computed solutions on the length of the domain in the x-direction is tested for case 1. Various domain lengths between $\lambda/24$ and $6\lambda/32$, were tested. Further extension of the domain was considered un-necessary since the heat exchangers in thermoacoustic engines are generally placed less than $6\lambda/32$ from the closed end of the resonator. The time step size used was 0.42%.

The size of Δx was calculated by evaluating the Courant number at BC34. The Courant number used was 0.01, the same as for the simulations in table 6.2 where the time step size was 0.28%. Δy, was kept constant for all simulations. Results are listed in tables 6.9 and 6.10.

Run		30	2	31	32	33	34
x		$\frac{\lambda}{24}$(b)	$\frac{\lambda}{16}$	$\frac{3\lambda}{32}$	$\frac{3.5\lambda}{32}$	$\frac{3.75\lambda}{32}$	$\frac{\lambda}{8}(b)$
$\Delta p_{cy}/P_A$	[%]	1.8e-3	1.7e-3	7.4e-3	1.3e-2	8.5e-3	1.5e-2
$\Delta u_{cy}/u_A$	[%]	1.8e-3	1.6e-3	7.5e-3	1.2e-2	8.0e-3	1.4e-2
$\Delta T_{cy}/T_A$	[%]	2.2e-2	2.2e-2	1.9e-2	2.2e-2	1.8e-2	1.9e-2
$\Delta \rho_{cy}/\rho_A$	[%]	1.5e-2	1.5e-2	1.4e-2	1.6e-2	1.3e-2	1.6e-2
p_{err}/P_A	[%]	5.3e-2	1.2e-1	2.9e-1	4.7e-1	7.6e-1	1.9e0
u_{err}/u_A	[%]	1.1e-1	1.8e-1	3.2e-1	4.9e-1	7.9e-1	1.9e0
T_{err}/T_A	[%]	3.2e-1	3.8e-1	5.4e-1	7.0e-1	1.0e0	2.0e0
$\dot{E}x_{cen}$	[W]	-3.8e-2	-5.6e-2	-8.2e-2	-9.9e-2	-1.1e-1	-1.1e-1
$\dot{E}x_{BC34}$	[W]	-3.7e-2	-5.5e-2	-8.4e-2	-9.6e-2	-1.0e-1	-1.1e-1
ex_{ABC34}	[W/m^2]	1.5e5	2.1e5	2.8e5	3.0e5	3.1e5	3.1e5
$\dot{S}_{gen}T_0$	[W]	5.8e-8	8.6e-8	1.3e-7	1.5e-7	1.6e-7	2.1e-7
$\Delta P_A/P_A$	[%]	-3.9e-2	-1.1e-1	-5.2e-2	-1.4e0	-2.8e0	-1.9e0
Cycles		13	14	18	23	31	27
$\Delta x/\lambda$		6.5e-4	9.6e-4	1.4e-3	1.6e-3	1.7e-3	1.8e-3

Table 6.9: Results with different domain lengths (up to $\lambda/8$) for case 1 (Drive ratio = 1%) with Δt=0.42%, Courant no.=0.01, $\Delta y/\delta_{km}$=2.1e-1.

Run		35	36	37	38	39	40
x		$\frac{4.25\lambda}{32}$	$\frac{4.5\lambda}{32}$	$\frac{4.75\lambda}{32}$	$\frac{5\lambda}{32}$	$\frac{5.5\lambda}{32}$	$\frac{6\lambda}{32}$
$\Delta p_{cy}/P_A$	[%]	6.9e-3	6.8e-3	1.2e-2	1.3e-2	1.4e-2	3.6e-2
$\Delta u_{cy}/u_A$	[%]	8.5e-3	6.4e-3	1.2e-2	1.5e-2	1.4e-2	3.3e-2
$\Delta T_{cy}/T_A$	[%]	1.1e-2	2.3e-2	2.2e-2	2.1e-2	1.5e-2	3.4e-2
$\Delta \rho_{cy}/\rho_A$	[%]	9.5e-3	1.6e-2	1.9e-2	1.9e-2	1.8e-2	4.0e-2
p_{err}/P_A	[%]	1.1e0	8.0e-1	8.6e-1	9.7e-1	1.3e0	1.7e0
u_{err}/u_A	[%]	9.9e-1	7.5e-1	8.0e-1	9.0e-1	1.2e0	1.6e0
T_{err}/T_A	[%]	1.1e0	1.1e0	1.2e0	1.2e0	1.5e0	1.9e0
$\dot{E}x_{cen}$	[W]	-1.2e-1	-1.3e-1	-1.3e-1	-1.4e-1	-1.5e-1	-1.6e-1
$\dot{E}x_{BC34}$	[W]	-1.2e-1	-1.2e-1	-1.3e-1	-1.4e-1	-1.5e-1	-1.6e-1
ex_{ABC34}	[W/m^2]	3.1e5	3.0e5	2.9e5	2.8e5	2.5e5	2.2e5
$\dot{S}_{gen}T_0$	[W]	1.9e-7	1.9e-7	2.0e-7	2.1e-7	2.3e-7	2.5e-7
$\Delta P_A/P_A$	[%]	4.4e0	+2.7e0	2.1e0	1.7e0	1.4e0	1.2e0
Cycles		39	36	41	40	54	65
$\Delta x/\lambda$		1.9e-3	2.0e-3	2.0e-3	2.1e-3	2.2e-3	2.3e-3

Table 6.10: Results with different domain lengths (up to $3\lambda/16$) for case 1 (Drive ratio=1%) with Δt=0.42%, Courant no.=0.01, $\Delta y/\delta_{km}$=2.1e-1.

The convergence rates versus the number of cycles for all domain lengths tested are shown in figure 6.16.

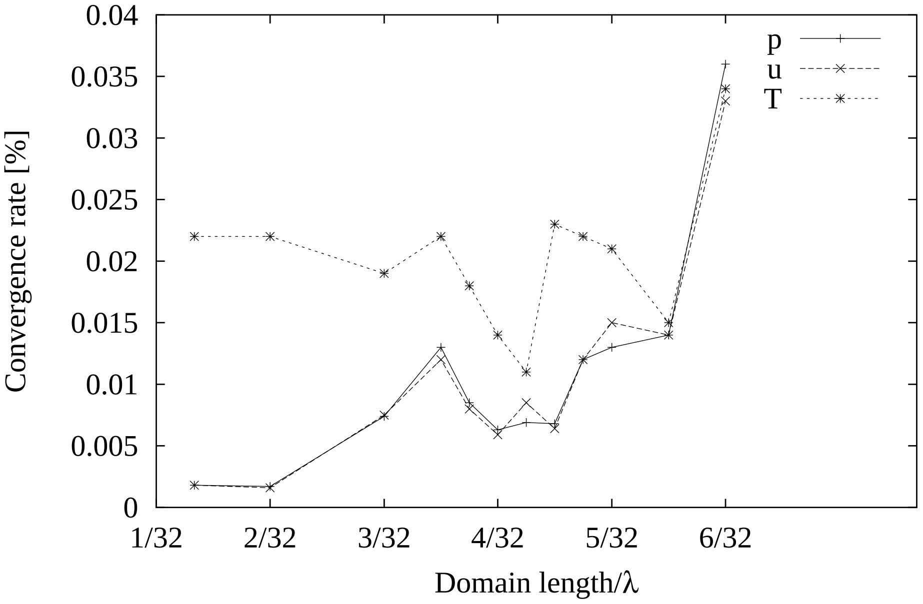

Figure 6.16: Convergence rate versus Domain length. Courant no.=0.01 $\Delta t = 0.42\%$.

Time and space averaged errors are plotted as a function of domain length in figure 6.17.

Slower convergence rates were observed as the domain length increased. The magnitude of the error grew as the domain length increased and the peak was observed when $\lambda/8$. These results were repeatable. $\Delta P_A/P_A$ also increases with the domain length and was highest when the domain length was $4.5\lambda/32$.

In order to see how the numerical solution deviates from the analytical solution when the domain length is $\lambda/8$, both numerically and analytically calculated pressure, velocity and temperature amplitudes are plotted as a function of x at the center of the simulation domain in the y-direction in figures 6.18 to 6.20.

The deviation from the analytical solution is largest at the location where variables have maximum fluctuating amplitude at their maximum and the way they deviate as a function of x-location was the same for all domain lengths tested.

At first inspection of table 6.9, this location dependence of error seems to be associated with the amplitude of energy flux at the boundary. However, the last column of the table, which shows results for the longest domain, does not follow the trend.

In order to find if the errors are associated with the difference between the relative magnitudes of pressure, velocity and temperature at the starting time of the simulation, the same simulations were carried out starting at a different phase during a cycle. The offset starting phases tested were $\pi/4$, $\pi/2$ and π. The results are listed in table B.1 in appendix B. These results show that the simulation results were not largely affected by

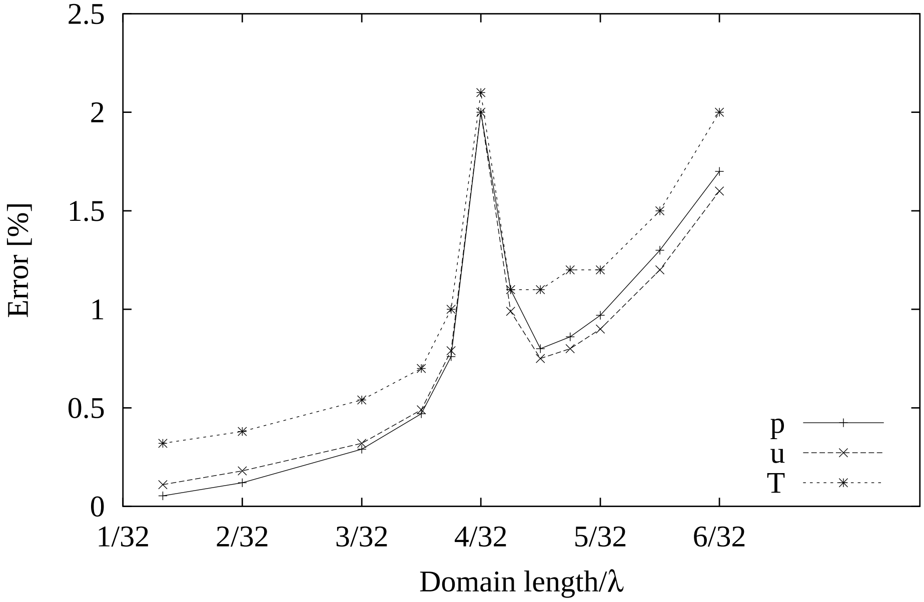

Figure 6.17: Errors for P, u and T versus domain length.

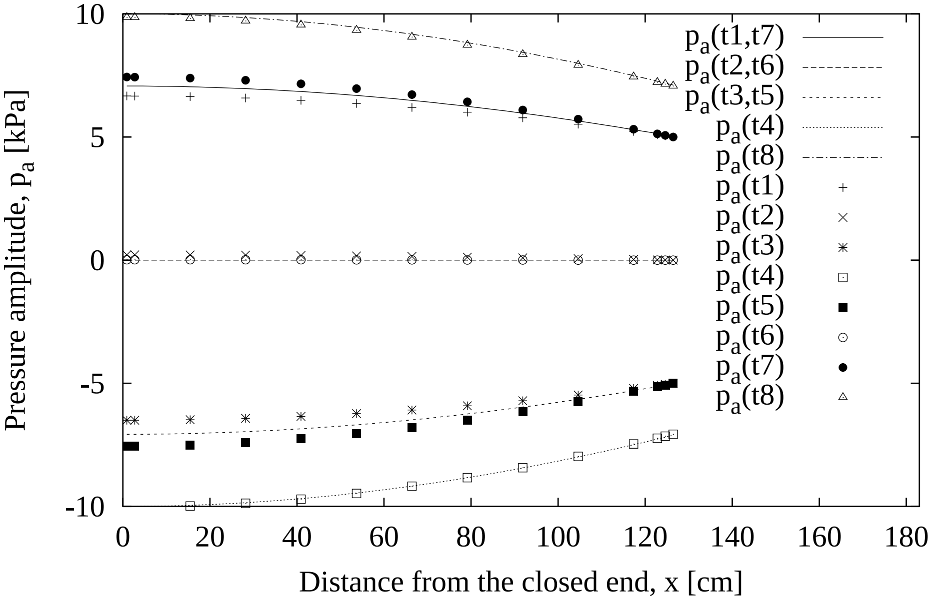

Figure 6.18: Comparison of pressure amplitude with the analytical solution at eight time steps during a cycle with $\Delta t = 0.42\%$, Domain length $= \lambda/8$. t1$=\tau/8$, t2$=2\tau/8$ ..... t8 $=\tau$. Other operating conditions are the same as for case 1.

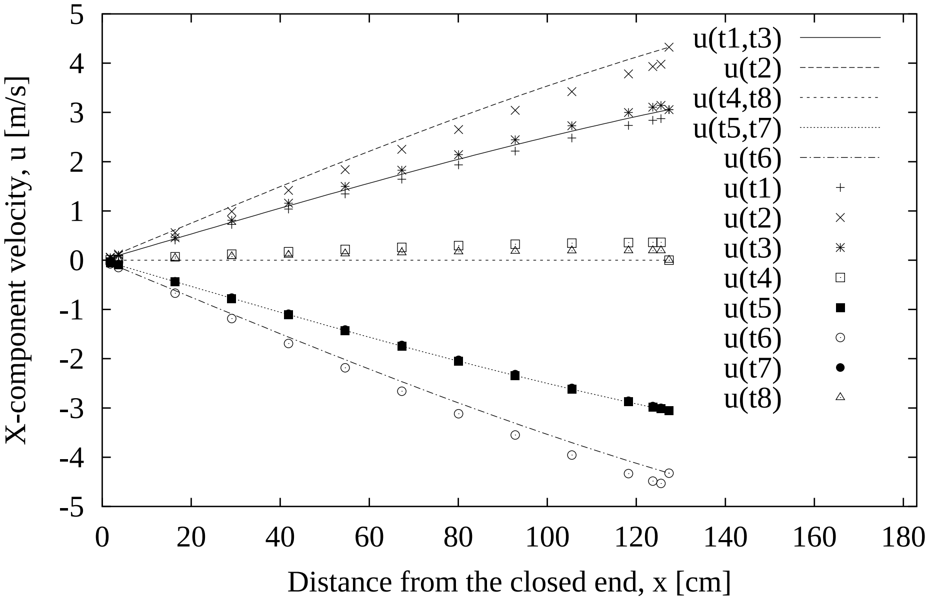

Figure 6.19: Comparison of velocity amplitude with the analytical solution at eight time steps in a cycle with $\Delta t = 0.42\%$, Domain length $= \lambda/8$. t1=$\tau/8$, t2=$2\tau/8$ ..... t8 =τ. Other operating conditions are same as case 1.

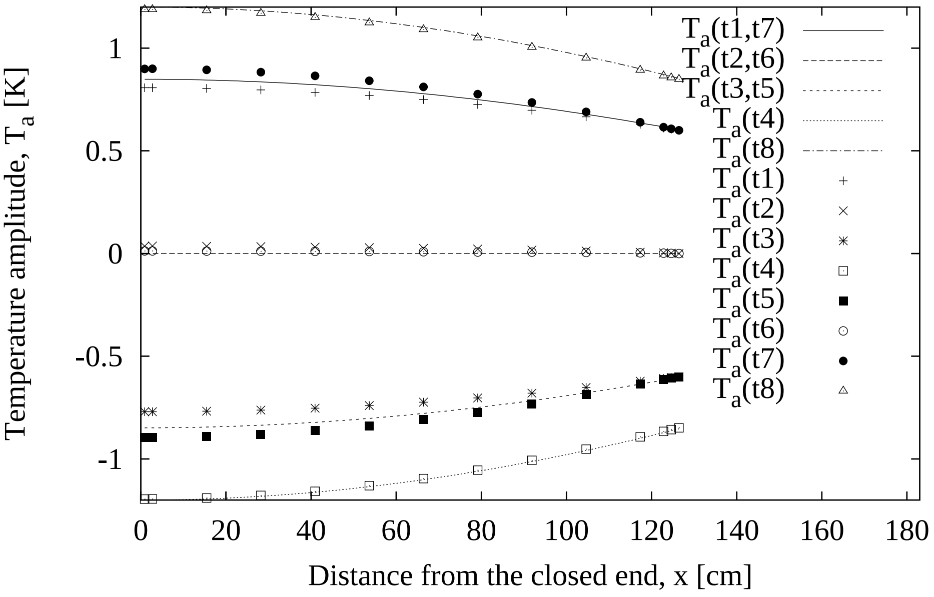

Figure 6.20: Comparison of temperature amplitude with the analytical solution at eight time steps in a cycle with $\Delta t = 0.42\%$, Domain length=$\lambda/8$. t1=$\tau/8$, t2=$2\tau/8$ ..... t8 =τ. Other operating conditions are same as case 1.

the relative magnitudes of each of the variables at the start of the simulations.

Dependence of the results on the aspect ratio $\Delta x/\Delta y$ was also tested but, as expected, changing the aspect ratio did not alter the results.

6.5 Summary

The current work demonstrated that it is possible to simulate 2-D standing waves using the commercial software PHOENICS.

Agreement between the numerical simulation results and the 1-D analytical solutions were less than 1% (normalized by amplitudes of the pressure and the velocity) for the pressure and the velocity for all test cases. Temperature had larger errors but at lower drive ratio, again the agreement was less than 1% in comparison to its fluctuating amplitude.

Since the continuously oscillating boundary condition is discretized as a function of time and the numerical scheme is first order with respect to the time step, the accuracy of the simulation largely depends on the size of the time step as mentioned in the section 4.2. The results were not largely affected by changing the aspect ratio or Courant number.

Although the agreement with the analytical solution was of the order of a few percent or less, a gradual rise in the time and space averaged bulk temperature within the domain was observed as the number of cycle increases. Two possible reasons were considered to explain the temperature rise.

Tables 6.2 to 6.7 show that the temperature rise gradually decreased as the time step was refined but it was not eliminated completely. Further refinement of the time step did not improve the agreement with the analytical solution or the drift in the time and space averaged temperature. These are considered to result from non physical effects such as numerical diffusion or drift as discussed in section 4.3. These could be improved by using a code written in double precision so that each iteration can meet stricter residual criteria.

The other possible reason for a temperature increase in the domain could be energy dissipation at the rigid end. However, the numerically calculated energy dissipation shows that the energy dissipated at the rigid end is almost negligible. The approximate temperature rise estimated from dissipation at the rigid end is condition dependent. However, for runs 1 to 6, for example, the temperature rise estimated from the energy dissipation calculated using equation (2.39) is of the order of 0.01% of the temperature amplitude over a cycle which is one hundredth of the temperature drift due to incomplete convergence.

At higher drive ratios, agreement with the analytical solution was poorer. This is not surprising as the 1-D standing wave analytical solution is only suitable for small oscillations. Although the tube wall is not included in the simulation domain and the viscosity of Helium is low, at the higher drive ratio, higher harmonics become significant. This was reflected in a non-sinusoidal velocity.

The dependence of the solutions on the domain length was unexpected. Various reasons for this were proposed but the actual cause of the disagreement with the analytical solutions has not been finalized.

The current work also clearly shows the importance of selecting the appropriate residual criteria when simulating transient acoustic phenomena.

Overall, the energy dissipation at the rigid end due to viscosity calculated using equation (2.39) did not agree with the energy dissipation calculated using equation (3.16). This was due to insufficient grid resolution near the solid boundary. It will be seen in chapter 7 and 8 that when plates are introduced to the simulation domain, dissipation at the solid boundary is insignificant compared to that which occurs near the plates. Therefore, it is not necessary to increase grid resolution to capture this effect.

Chapter 7

Simulation of thermoacoustic couples

7.1 Introduction

In this chapter, the addition of an array of thin plates (that are maintained at a constant temperature) to the simulation domain is considered. By applying the same oscillatory boundary conditions at the open end of the simulation domain as those used in the standing wave simulations, a thermoacoustic couple that is connected to a heat source or sink can be simulated. Again, only part of the complete device is simulated.

The purpose of this chapter is to test the suitability of PHOENICS for simulating thermoacoustic effects. In order to check if the thermoacoustic effect is simulated correctly, the results from the simulations are compared with the first order analytical model of a thermoacoustic couple and with the results of numerical simulations carried out by Cao *et al.* (1996). There are limits to which agreement can be expected because of simplifying assumptions made in the analytical model and the difference between the simulation methodologies of the current work and that of Cao *et al.*. These limitations are discussed thoroughly. Within these limitations, the validity of the PHOENICS simulation is demonstrated.

After justifying the validity of the simulation in the current work, further investigations, such as the investigation of flow fields, particle traces, and entropy generation, were carried out for thermoacoustic couple simulations with various plate spacings and Mach numbers. Plate spacings that were tested in the current work include Hofler's preferred plate spacing for heat exchangers (see section 2.5.5) that are as small as the thermal penetration depth. Such simulations have not been tested in previous studies.

7.2 Method of simulating thermoacoustic couples

In the current work, thermoacoustic couples were simulated by applying standing wave conditions at the open end of the simulation domain (BC34 of figure 5.2) and setting the plate temperature to a constant value. As described in Cao *et al.* (1996), it is appropriate to use standing wave conditions if the oscillatory boundary is specified far enough away from the plate and the other end of the simulation domain is chosen as the closed end of the tube.

Cao *et al.* chose a smaller simulation domain than that used in the current work in order to save computation time. Their simulation domain is shown in figure 7.1. Locations that are the same as those used in the current simulations are indicated in brackets by the numbers used in figure 5.2. Point S in figure 7.1 is midway between E and F but on the symmetrical boundary BC. In the current work, plate edge F is referred to as the outer edge of the plate and plate edge E as the inner edge of the plate.

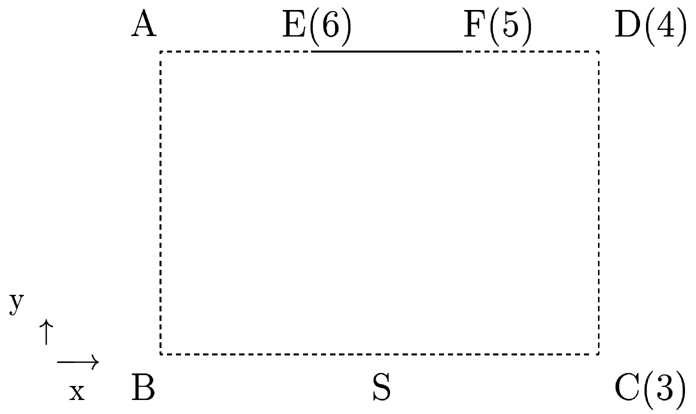

Figure 7.1: The computational domain of Cao *et al.* (1996). Numbers in brackets are those from figure 5.2.

Because their oscillatory boundaries on both sides are located relatively close to the plate, under some operating conditions they could not specify boundary conditions which accurately represented a plate in a standing wave. In the current work tests are carried out to determine the appropriate locations of the open end of the domain which is necessary for simulation of a plate in a standing wave (see section 7.5.2).

7.3 Selection of test cases

Because the validity of simulations in the current work are evaluated by comparing results with analytical solutions and with the simulation results of Cao *et al.* (1996), the test cases chosen are mostly the same as those of Cao *et al.*. The test cases selected are listed in table 7.1. Case numbers in brackets are 'run numbers' from Cao *et al.* (1996).

x_E is the distance from the closed end of the tube, x=0, to the inner plate edge, point E in figure 7.1. ϕ_E and ϕ_S are, respectively, the phase difference from 90° between the pressure and the velocity at points E and S in figure 7.1.

Case	δ_{km}/y_0	x_E/λ	M	Re	$Re_{m\&t}$	Re_{wo}	ϕ_E	ϕ_S
1 (2)	0.30	0.10	0.01	131.5	23.0	32.7	2°	11°
2 (×)	0.30	0.10	0.02	262.5	46.0	32.7	NA	NA
3 (5)	0.30	0.10	0.03	394.4	69.0	32.7	0°	NA
4 (×)	0.30	0.10	0.04	525.9	92.0	32.7	NA	NA
5 (7)	0.30	0.10	0.05	657.4	115.0	32.7	0°	NA
6 (9)	0.60	0.10	0.03	197.1	69.0	8.17	0°	30°
7 (×)	1.00	0.10	0.03	118.3	69.0	2.94	NA	NA
8 (10)	1.20	0.10	0.03	98.61	69.0	2.04	0°	69°
9 (×)	1.60	0.10	0.03	73.96	69.0	1.15	NA	NA
10 (×)	1.80	0.10	0.03	65.74	69.0	0.91	NA	NA
11 (16)	0.30	0.037	0.03	394.4	69.0	32.67	0°	NA
12 (17)	1.20	0.037	0.03	98.57	69.0	2.04	0°	NA

Table 7.1: Thermoacoustic couple test cases. Case numbers in brackets are the run numbers of Cao *et al.* (1996). An '×' indicates a condition not tested by Cao *et al.*. Plate length is 0.024λ, the cyclic boundary condition is specified 0.0085λ away from the right edge of the plate for all cases, the test gas is Helium, $\gamma = 5/3$, $Pr = 0.68$, $p_m = 1.E4Pa$.

The Reynolds numbers are presented in table 7.1. For all cases, the kinematic viscosity is based on the mean temperature and density in the tube. $Re = 2y_0u_a/\nu$, where u_a is the velocity amplitude at the velocity antinode (in the standing wave) and y_0 is the half plate spacing. $Re_{m\&t} = 2u_a/(\nu\omega)^{1/2}$, where ω is the frequency of the standing wave, was used by Merkli and Thoman (1975a) in their experiments. $Re_{wo} = \omega y_0^2/\nu$ was used by Worlikar and Knio (1996) in their study.

The plate length used in Cao *et al.* (1996) was $L = 0.024\lambda$ and their oscillatory boundary conditions on each side of the plate were specified 0.0085λ away from the plate edges. In the current work, oscillatory boundary conditions were specified only on one side and they also were specified 0.0085λ from the edge of the plate.

For most of the test cases run by Cao *et al.*, BC34 was located at a distance of $\lambda/8$ from the closed end (x=0) of the tube. It must be noted that for the standing wave simulations in the current work, the agreement between analytical solutions and simulation results when BC34 was set at this location was not as good as when the boundary was specified at other locations (see section 6.4.3).

In order to replicate the test cases of Cao *et al.* (1996) from the parameters given in their paper, the mean temperature and the frequency had to be assumed in order to determine the operating conditions and geometries. In the current work, they were chosen to be 300K and 100Hz respectively.

The grid sizes were made approximately equal to those used by Cao *et al.*. However, the time step size, Δt, and frequency were not specified in their paper. In the current work Δt was chosen to be 0.28% of the duration of a cycle. (Some grid dependency tests to check the suitability of this time step are reported in section 7.5.1.)

Additional items that are listed in the results tables for thermoacoustic couple simulations are

- The time averaged total heat flux at the surface of the plate ($\dot{Q}_{pl}$)
- The time averaged total energy flux at the surface of the plate ($\dot{E}_{ypl}$)
- The area averaged amplitude of heat flux (q_A)
- The area averaged amplitude of the x-component of energy flux density calculated using equation (7.4) described in section 7.6.1. (H_x)
- The area averaged amplitude of the y-component of energy flux density calculated using equation (7.5) described in section 7.6.1. (H_y)
- The normalized time averaged energy balance error. ($\dot{Q}_{Error}/(MAX(e_{ABC34}, H_x) \times$ $y_0 \times$ unit length in the z-direction))
- The energy dissipation at the surface of the plate calculated using equation (2.39) ($\dot{E}_{diss}pl$)

Comparisons with analytical solutions are made only across the passage at the middle of the plate. The values shown are averaged in the y-direction. In some series of test cases, additional items are listed as required.

Test cases selected in the current section can be grouped to investigate the dependence of results on

- the drive ratio (or Mach number),
- the plate spacing,
- the plate location, and
- combinations of the above.

7.4 Convergence monitoring of the thermoacoustic couple model

When the plate was introduced into the simulation domain for thermoacoustic couple simulations, it was noticed that the simulations required more cycles to reach a steady state than do the standing wave simulations. The major difference between the two cases is that for a standing wave simulation, the domain is adiabatic whereas for thermoacoustic couple simulations, there is an isothermal region. (Slow convergence was also noticed by Worlikar *et al.* (1996) in their simulation of a thermoacoustic couple in a duct. However, their simulation included plate thickness which considered heat transfer within the plate.)

Since the convergence of temperature in some thermoacoustic couple simulations is extremely slow, other criteria to stop the iterations were also considered based on an important quantity in the thermoacoustic effect. This is the time averaged heat flux or the y-component of the energy flux at the surface of the plate. Monitoring the convergence rate of either quantity is appropriate as the y-component of energy flux at the plate surface should be equal to the heat flux in to the plate (since the x and y-components of velocity, u and v, are zero on the plate). The ratio of the time averaged heat flux to its maximum amplitude, $\dot{Q}_{pl}/Q_A$, and the ratio of the time averaged y-component of energy flux density to its amplitude, $\dot{Ey}_{pl}/Ey_A$, are both of the order of 10^{-2} for thermoacoustic couple simulations. In the current work, a simulation was considered to have converged when the relative change in the time and area averaged heat and energy fluxes are of the order of 0.1% for four consecutive cycles. In some cases, the convergence rate of heat flux did not reach this value while the convergence rate of the temperature is acceptable in comparison to other test cases. (This was because the heat flux itself was near zero.) In such a case, the iteration was stopped by limiting the value of the convergence rate of the temperature to 0.05%.

Once the solutions converged, an energy balance of the domain was checked at each cycle in order to test if the converged solutions were valid. At steady state, the x-component of energy flux at BC34, $\dot{E}_{BC34}$, should equal the heat flux at the plate, $\dot{Q}_{pl}$. The same balance should also exist for the cycle averaged values and therefore any differences between these two quantities can be considered to be an error, $\dot{Q}_{Error}$, given by

$$\dot{E}_{xBC34} + \dot{Q}_{pl} = \dot{Q}_{Error}. \tag{7.1}$$

This error is caused from numerical error (see section 4.3) and from incomplete convergence. The incomplete convergence is partly due to the limitation that the software works only in single precision. The number of significant figures is very important for the simulation of thermoacoustic effects.

When $\dot{E}_{BC34}$ is positive, energy flows in the direction of increasing x. $\dot{Q}_{pl}$ is negative when it enters the domain through the isothermal plate and positive when it is going out of the domain.

$\dot{E}_{xBC34}$ for a thermoacoustic couple model should be equal to the energy dissipation, $\dot{E}_{diss}$, caused by the action of viscosity and the temperature gradients in the gas. At steady state, any energy dissipated within the simulation domain should leave through the isothermal plate and the same amount of energy should enter the domain through BC34. The fact that the amplitudes of p_1, u_1 and T_1 are maintained constant at BC34 even though energy is being lost from the domain, means that this boundary condition can compensate for any energy dissipation in the domain, i.e. BC34 can act as an energy source. Although at the cell face the values for p_1, u_1 and T_1 are fixed, the energy flux, $\dot{E}_{BC34}$, will be affected by the results within the simulation domain as the calculation of $\dot{E}_{BC34}$ requires values at one cell before the boundary cell to calculate gradients in quantities, such as temperature and velocities, as described in section 4.5.1. The magnitude of $\dot{E}_{diss}$ can be calculated from the numerical results by applying the equation (3.11) over the whole domain.

In the current work, $\dot{Q}_{Error}$ was normalized by Q_A, the larger of the amplitudes of the x-component of energy flux either at boundary DC (BC34) or at point S in figure 7.1, ex_{ABC34} or H_x respectively.

Noting that the magnitude of the cycle averaged value of $\dot{Q}_{pl}$ is only of the order of 1% or less of that of its fluctuating amplitude, simulations are considered to be valid if the normalized error is less than 10%. The software limitations (see section 4.3.2) contribute to setting this as the acceptable magnitude of $\dot{Q}_{Error}$.

7.5 Preliminary tests

Before simulating all test cases, first, some of the grid dependency tests carried out in the current work by varying grid sizes around those used by Cao *et al.* (1996) are shown. Then the appropriateness of using the same location for the oscillatory boundary conditions as that specified in Cao's work is considered.

Case 1 was used for the grid dependency tests in section 7.5.1 and cases 1, 3 and 5 are used to test the location of the oscillatory boundary conditions in section 7.5.2.

7.5.1 Grid dependency and convergence tests for Run 1

The grid arrangement used for thermoacoustic couple simulations is shown in figure 7.2 where the plate is indicated by a bold line. The grid spacings in the y-direction and in time are uniform. In the x-direction the grid spacing is only uniform near the plate and near BC34. X grids in the remaining section are gradually enlarged towards the closed end by using equation (6.2). Having a uniform grid in the empty section did not significantly

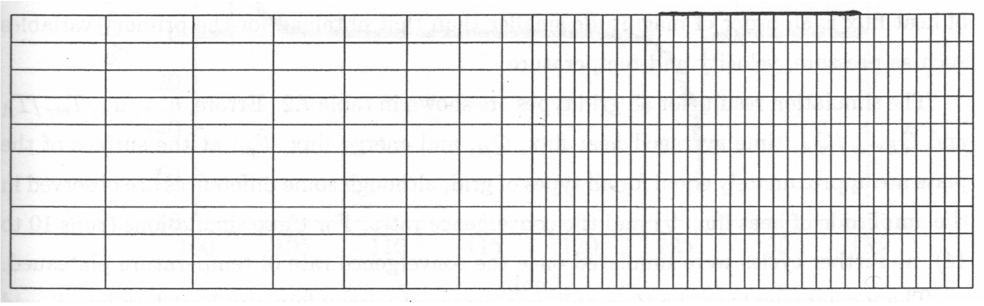

Figure 7.2: Typical grid arrangement used for thermoacoustic couple simulations. (Not to scale)

change the results but made the simulations more time consuming. A uniform grid spacing was used in the y-direction as a relatively small number of grids are required for the results to be independent of the y-grid size. Physically one would not expect a non-uniform grid in the y-direction to be required because the spacing between the plates is of the order of the viscous penetration depth, and the viscous and thermal penetration depths are similar in a gas with a Prandtl number close to unity.

Case 1 of Cao *et al.* (1996) (see table 7.1) was used as the datum condition for grid dependency tests. This case is referred to here as grid 1 and the grid and time step sizes are referred to as Δx_1, Δy_1, and Δt_1 respectively (Note $\Delta t_1 = 0.278\%$). The variations from these datum conditions are as follows

- Grid 2 : $\Delta t = 0.75\Delta t_1$
- Grid 3 : $\Delta y = 0.50\Delta y_1$
- Grid 4 : $\Delta x = 0.80\Delta x_1$
- Grid 5 : $\Delta x = 0.70\Delta x_1$

Here, Δt is expressed as a percentage of the duration of the cycle and Δx is the size of the grid in the x-direction in the finely meshed region around the plate. (see figure 7.2.)

To reach steady state, a thermoacoustic couple simulation requires many more cycles than does a simulation of a standing wave at the same drive ratio. In order to assess when a steady state is reached for the thermoacoustic couple simulations, the convergence rate of the time averaged heat flux was monitored in the way described in section 7.4. The convergence rates of $\dot{Q}_{pl}$, p, u and T as a function of the number of cycles for Grid type 1 (run 10) are plotted in figure 7.3. The convergence rate of heat flux is normalized by the amplitude of the heat flux to the plate. As described in section 4.3.2, the convergence rate of heat flux is an order of magnitude smaller than that obtained for the primary variables such as pressure, velocity and temperature.

The simulation results for all grid types are shown in table 7.2. Errors, u_{err}/u_A, T_{err}/T_A and $\dot{Q}_{Error}/Q_A$, time averaged heat flux, $\dot{Q}_{pl}$, and energy flux, $\dot{E}_{pl}$, at the surface of the plate are approximately equal for all types of grid, although some differences are observed in the amplitude of heat flux, q_A and the convergence rates. For these simulations (runs 10 to 14), no further cycles were simulated once the convergence rate of temperature plateaued.

The y-components of the time and area averaged energy flux and heat flux for all grid types are shown in figures 7.4 and 7.5 respectively. In these and subsequent figures, short vertical lines are used to indicate the location of the inner and the outer edges of the plates. The shapes of the curves are almost identical for all grid types in both figures but the differences are largest near the outer edge of the plate. The differences in the heights of the peaks at each end of the plate are more dependent on the size of Δx than on those of Δy and Δt. This is because the x-coordinates of the cell center in some simulations

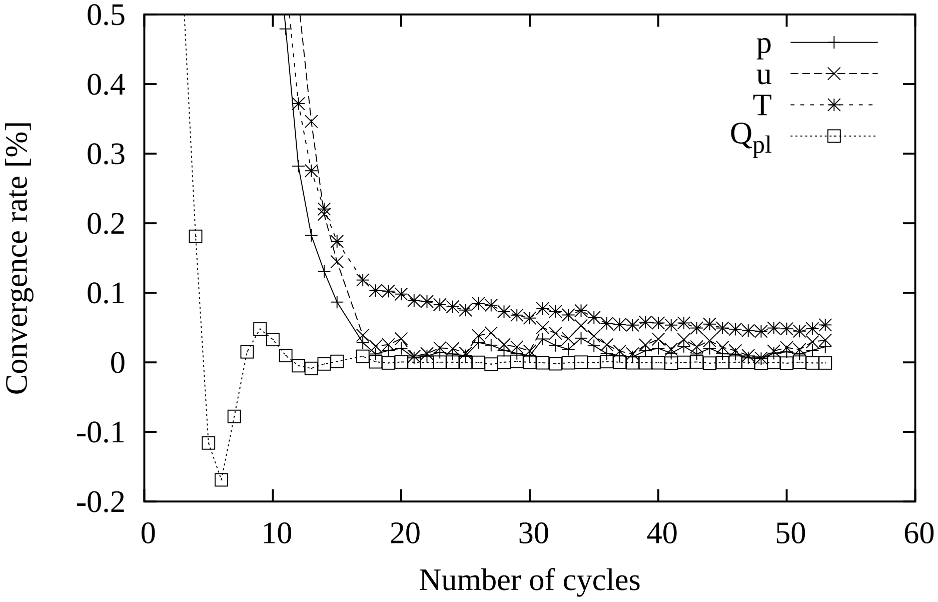

Figure 7.3: Convergence rate of pressure, p, velocity, u, temperature, T, and heat flux, $\dot{Q}_{pl}$ versus number of cycles. Case 1 with Grid type 1 (run 10).

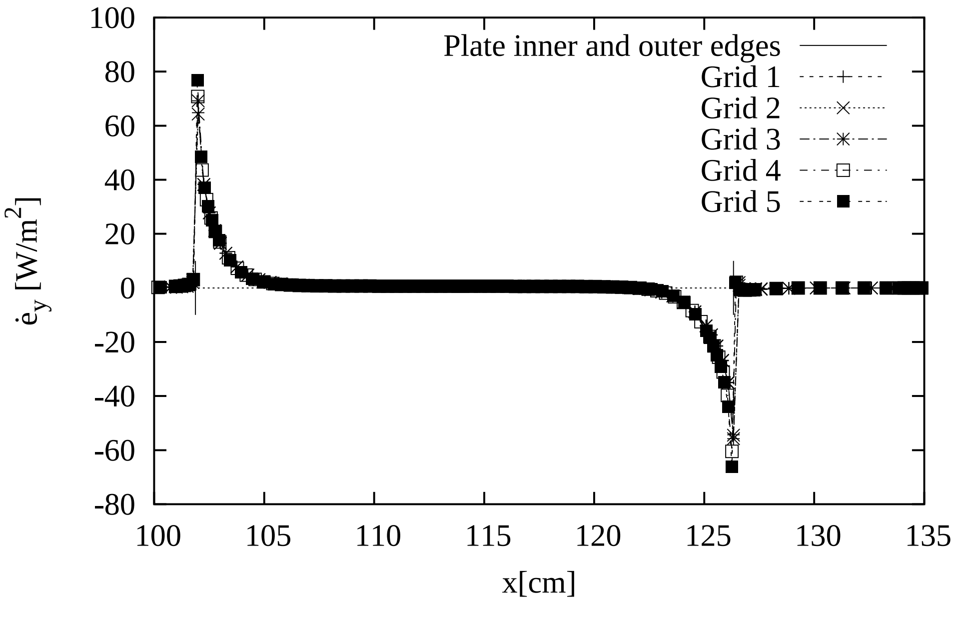

Figure 7.4: Time averaged energy flux density in the y-direction at the surface of the plate for case 1 with various grid sizes. Vertical lines at $x \simeq 102$ cm and $x \simeq 127$ indicate the plate inner and outer edges respectively. (Note: Grid 1: datum, Grid 2:$\Delta t = 0.75\Delta t_1$, Grid 3:$\Delta y = 0.50\Delta y_1$, Grid 4:$\Delta x = 0.80\Delta x_1$, Grid 5:$\Delta x = 0.70\Delta x_1$)

Run		10	11	12	13	14
Grid type		Grid 1	Grid 2	Grid 3	Grid 4	Grid 5
$\Delta p_{cy}/P_A$	[%]	5.2e-3	1.0e-2	9.8e-3	5.6e-3	1.0e-2
$\Delta u_{cy}/u_A$	[%]	6.0e-3	1.4e-2	1.2e-2	7.7e-3	1.7e-2
$\Delta T_{cy}/T_A$	[%]	4.5e-2	5.4e-2	5.2e-2	5.4e-2	5.4e-2
$\Delta \rho_{cy}/\rho_A$	[%]	3.1e-2	3.8e-2	3.5e-2	3.7e-2	3.6e-2
$\Delta Tb_{cy}/T_A$	[%]	3.2e-2	3.2e-2	3.8e-2	3.2e-2	3.5e-2
u_{err}/u_A	[%]	3.2e0	3.1e0	3.2e0	3.2e0	3.2e0
T_{err}/T_A	[%]	5.7e-1	5.6e-1	5.7e-1	5.8e-1	5.8e-1
$\dot{Q}_{pl}$	[W]	1.5e-1	1.5e-1	1.5e-1	1.4e-1	1.4e-1
$\dot{E}_{pl}$	[W]	1.3e-1	1.2e-1	1.3e-1	1.2e-1	1.2e-1
$\dot{E}x_{cen}$	[W]	-2.0e-2	-2.1e-2	-2.0e-2	-2.0e-2	-2.0e-2
$\dot{E}x_{BC34}$	[W]	-1.0e-1	-1.3e-1	-1.0e-1	-9.9e-2	-1.0e-1
q_A	[W/m^2]	3.0e2	3.0e2	3.0e2	3.2e2	3.5e2
ex_{ABC34}	[W/m^2]	8.9e2	8.9e2	8.9e2	8.9e2	8.9e2
H_x	[W/m^2]	-9.5e2	-9.5e2	-9.5e2	-9.5e2	-9.5e2
H_y	[W/m^2]	-6.2e1	-6.2e1	-6.2e1	-6.2e1	-6.2e1
$\dot{Q}_{Error}/Q_A$	[%]	3.9e-1	1.3e-1	3.9e-1	2.7e-1	2.6e-1
$\dot{E}_{diss}pl$	[W]	1.1e-1	1.1e-1	1.1e-1	1.1e-1	1.1e-1
$\dot{S}_{gen}T_0$	[W]	1.3e-1	1.3e-1	1.3e-1	1.3e-1	1.3e-1
$\Delta P_A/P_A$	[%]	5.7e0	6.0e0	5.7e0	5.7e0	5.7e0
Cycles		48	37	40	36	43
$\Delta x/\lambda$		2.5e-4	2.5e-4	2.5e-4	2.0e-4	1.6e-4
$\Delta y/\delta_{km}$		8.3e-2	8.3e-2	4.2e-2	8.3e-2	8.3e-2

Table 7.2: Simulation results of case 1 with five grid types.

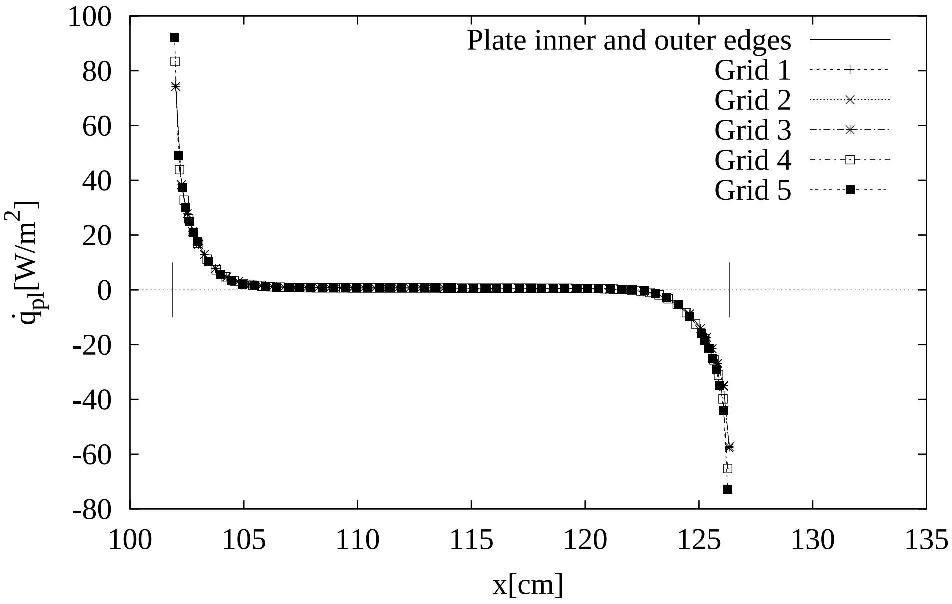

Figure 7.5: Time averaged heat flux at the surface of the plate for Run 1 with various grid sizes. (Note: Grid 1: datum, Grid 2:$\Delta t = 0.75\Delta t_1$, Grid 3:$\Delta y = 0.50\Delta y_1$, Grid 4:$\Delta x = 0.80\Delta x_1$, Grid 5:$\Delta x = 0.70\Delta x_1$)

are slightly offset due to the differences in grid sizes and when the peak is very sharp, the offset will result in a different peak height. This can be proved by the fact that the curves for Grids 1, 2 and 3 coincide. However, these differences in peak height do not affect the net amount of energy or heat flux at the plate significantly, as shown in table 7.2.

The integration of curves in figure 7.4 and 7.5 over the plate surface yields $\dot{E}_{pl}$ and $\dot{Q}_{pl}$. The difference between the net heat flux, $\dot{Q}_{pl}$ and the energy flux, $\dot{E}_{pl}$ at the plate surface is 10%. This difference is due to the difference in the ways $\dot{E}_{pl}$ and $\dot{Q}_{pl}$ are calculated. Both quantities are evaluated at cell centers, i.e. a distance $\Delta y/2$ away from the plate surface. $\dot{E}_{pl}$, calculated using equation (2.20) that is the total energy flux which consist of convection of total enthalpy, heat conduction and energy dissipation. The way equation (2.20) is calculated is described in section 4.5.1. $\dot{Q}_{pl}$ is calculated using Fourier's law of heat conduction with the temperature gradient being based on the temperature of plate and that of the gas at $\Delta y/2$ cell away from the surface.

Considering the fact that the magnitude of $\dot{Q}_{pl}$ and $\dot{E}_{pl}$ are approximately 1% of the maximum amplitude of the energy flux in the simulation domain and the accuracy limitation discussed in section 4.3, this difference is not considered to be significant.

Most items listed in table 7.2 are similar for all grid types. H_x and H_y calculated using equation (7.4) and (7.5) remain constant for all grid types. Differences in q_A occur for the same reason as that described for peak height differences. The energy balance error, $\dot{Q}_{Error}/Q_A$, decreased when Δt was reduced but reducing the size of Δx from that used for Grid 4 did not reduce the error any further.

The phase shifts, computed both numerically and analytically, are listed in table 7.3. Values are negative because of the sign convention used in the current work. The current work shows the actual phase shift rather than taking 90° off from the phase shift as in Cao *et al.* (1996).

Run	ϕ_{E_C}	ϕ_{F_C}	ϕ_{S_C}	$\phi_{S_{AN}}$	ϕ_{SP_C}	$\phi_{SP_{AN}}$
Grid1	-74.0	-59.0	-98.0	-98.0	-49.0	-53.0
Grid2	-73.5	-59.3	-97.5	-98.0	-48.8	-53.0
Grid3	-75.0	-59.0	-99.0	-98.0	-51.0	-53.0
Grid4	-75.0	-59.0	-99.0	-98.0	-51.0	-53.0
Grid5	-75.0	-59.0	-99.0	-98.0	-50.0	-53.0

Table 7.3: Grid dependent test for Run 1. (Note: Grid 1: datum, Grid 2:$\Delta t = 0.75\Delta t_1$, Grid 3:$\Delta y = 0.50\Delta y_1$, Grid 4:$\Delta x = 0.80\Delta x_1$, Grid 5:$\Delta x = 0.70\Delta x_1$)

Subscript $_C$ denotes the current simulation, $_{AN}$ the first order analytical solution and SP the center of the plate surface. S is at the same location as SP but on the symmetrical boundary as indicated in figure 7.1. E is the inner edge of the plate and F is the plate outer edge as shown in figure 7.1. For example, ϕ_{F_C} is the phase shift calculated from the current simulation at the edge of the plate and $\phi_{SP_{AN}}$ is the analytically calculated phase shift at the center of the plate surface.

Reducing the time step size, Δt by 25% (Grid 1 to 2) had little effect (maximum of 0.3°) on the phase shift. Reducing the size of Δy by 50% (Grid 1 to 3) changed the phase shift by a maximum of 2°, which is only 0.5% of 360°. Reducing the size of Δx by 50% (Grid 1 to 4 and 5) also had only a small effect on the results.

Overall, grid size tests in this section showed that Grid 1 is sufficient for thermoacoustic couple simulations for case 1.

7.5.2 Boundary specification location test

The oscillatory boundary conditions used to simulate thermoacoustic couples in the current work are the same as those used for the standing waves reported in chapter 6. The suitability of applying standing wave boundary conditions very close to the plate when trying to simulate a thermoacoustic couple could be called into question because one would expect the presence of the plate to cause gas conditions close to the plates to deviate from those in an ideal standing wave. However, if ideal standing wave conditions are applied at an oscillatory boundary further away from the plate (to the right in figure 7.1), then a suitable thermoacoustic couple simulation may be possible. In this section, the influence of the location of the oscillatory boundary on the simulations is tested.

The first case tested is case 1 of table 7.1 which is run 2 of Cao *et al.* (1996). Cao *et al.* specified the oscillatory boundary conditions approximately four times the particle displacement distance (evaluated at BC34 when M=0.01) away from the edge of the plate.

In the current simulation, in order to test whether this location is far enough away from the plate outer edge, the distance was stretched by both two and four times. Two distances that are shorter than that used by Cao *et al.*, were also tested. One is approximately twice and the other is 1/10th of the particle displacement distance. This latter case, is equivalent to specifying the oscillatory boundary conditions one cell away from the plate outer edge.

If it is far enough away from the plates, then changing the location of the oscillatory boundary conditions should not change the results near the plate. Since the heat transfer to and from the plate is of primary interest, this has been compared for different locations of the oscillatory boundary.

The results of these tests are shown in table 7.4. The items listed as $x_5 - x_4/2u_1\omega$ in the second row of the table are the distances between the outer plate edge and the location of the oscillatory boundary (5 and 4 in figure 7.1) normalized by the particle displacement distance evaluated at BC34. The first two columns in table 7.4 are, respectively, cases when the oscillatory boundary conditions are specified one cell away from the plate outer edge (run 1) and approximately two times the particle displacement distance (run 2). The third column (run 3), is case 1 of table 7.1. This has the oscillatory boundary specified at the same location as used by Cao *et al.*. Runs 4 and 5 are cases in which the distance $x_4 - x_5$ has been stretched by two and three times that of run 3. For all test runs in the table, iteration was stopped when the convergence rate of the temperature no longer improved.

The energy flux across the passage at the x-location mid-way between the closed end and the inner edge of the plate, $\dot{E}_{cen}$, in table 7.4 should ideally be zero at the steady state since energy cannot accumulate in the simulation domain. However, $\dot{E}_{cen}$ is finite at values that are only approximately 0.3% of maximum energy flux $(MAX(e_{ABC34}, H_x) \times y_0 \times$ unit length in z-direction) for all cases, and hence are not considered to be significant.

Table 7.4 shows that most quantities are similar for all runs 1 to 5 except for the energy flux at the surface of the plate, $\dot{E}_{pl}$ and errors, u_{err}/u_A, $Terr/T_A$ and $\dot{Q}_{Error}$.

Errors u_{err}/u_A and $Terr/T_A$ are approximately equal for runs 2 to 5 but $\dot{Q}_{Error}$ gradually increases as the oscillatory boundary is moved closer to the plate outer edge. Time averaged energy fluxes at the plate surface, $\dot{E}_y$, also increase when the boundary is closest to the plates and it is highest for run 1.

In order to visualize the effect of different locations of the oscillatory boundary on the time averaged y-component of energy flux density at the plate surface, the results for runs 1 to 3 and 3 to 5 are shown in figures 7.6 and 7.7 respectively.

The results indicate that in terms of the energy flux density at the surface of the plate, the oscillatory boundary could have been specified closer (run 2) than the distance used by Cao *et al.* (run 3) when M=0.01. However, when the Mach number is increased, the particle displacement distance will increase. Then the relative distances that are used for

Run		1	2	3	4	5
$\frac{x_4-x_5}{2u_1/\omega}$		1.1e-1(1 cell)	1.9e0	3.8e0	7.6e0	1.5e1
$\Delta p_{cy}/P_A$	[%]	7.7e-3	1.3e-2	5.2e-3	1.2e-2	8.5e-3
$\Delta u_{cy}/u_A$	[%]	9.4e-3	1.9e-2	6.0e-3	2.1e-2	1.1e-2
$\Delta T_{cy}/T_A$	[%]	7.4e-2	5.6e-2	4.5e-2	5.5e-2	6.0e-2
$\Delta \rho_{cy}/\rho_A$	[%]	5.1e-2	4.1e-2	3.1e-2	4.1e-2	4.3e-2
$\Delta Tb_{cy}/T_A$	[%]	5.0e-2	4.0e-2	3.2e-2	2.1e-2	1.3e-2
u_{err}/u_A	[%]	4.3e0	3.3e0	3.2e0	3.2e0	3.6e0
T_{err}/T_A	[%]	2.1e0	5.6e-1	5.7e-1	6.7e-1	1.1e0
$\dot{E}_{pl}$	[W]	4.1e-1	1.7e-1	1.3e-1	1.2e-1	1.2e-1
$\dot{E}x_{cen}$	[W]	-2.0e-2	-2.0e-2	-2.0e-2	-2.0e-2	-2.0e-2
$\dot{E}x_{BC34}$	[W]	-1.3e-1	-1.1e-1	-1.0e-1	-9.7e-2	-1.0e-1
q_A	[W/m^2]	2.7e2	3.0e2	3.0e2	3.0e2	3.0e2
ex_{ABC34}	[W/m^2]	9.7e2	8.9e2	8.9e2	8.7e2	8.03e2
H_x	[W/m^2]	-9.5e2	-9.5e2	-9.5e2	-9.5e2	-9.5e2
H_y	[W/m^2]	-6.2e1	-6.2e1	-6.2e1	-6.2e1	-6.2e1
$\dot{Q}_{Error}/Q_A$	[%]	3.6e0	8.0e-1	4.0-1	3.0e-1	2.6e-1
$\dot{E}_{diss}pl$	[W]	1.1e-1	1.1e-1	1.1e-1	1.1e-1	1.1e-1
$\dot{S}_{gen}T_0$	[W]	1.2e-1	1.3e-1	1.3e-1	1.3e-1	1.3e-1
$\Delta P_A/P_A$	[%]	3.8e0	6.6e0	5.7e0	4.0e0	2.8e-1
Cycles		19	36	48	60	42

Table 7.4: Simulation results with various locations of the oscillatory boundary when M=0.01. $2u_1/\omega$=2.28cm when evaluated at x_5, the plate outer edge. Plate length L=24.5 cm, domain height y_0=0.806 cm, $\Delta x/\lambda$=2.5e-4, $\Delta y/\delta_{km}$=8.3e-2.

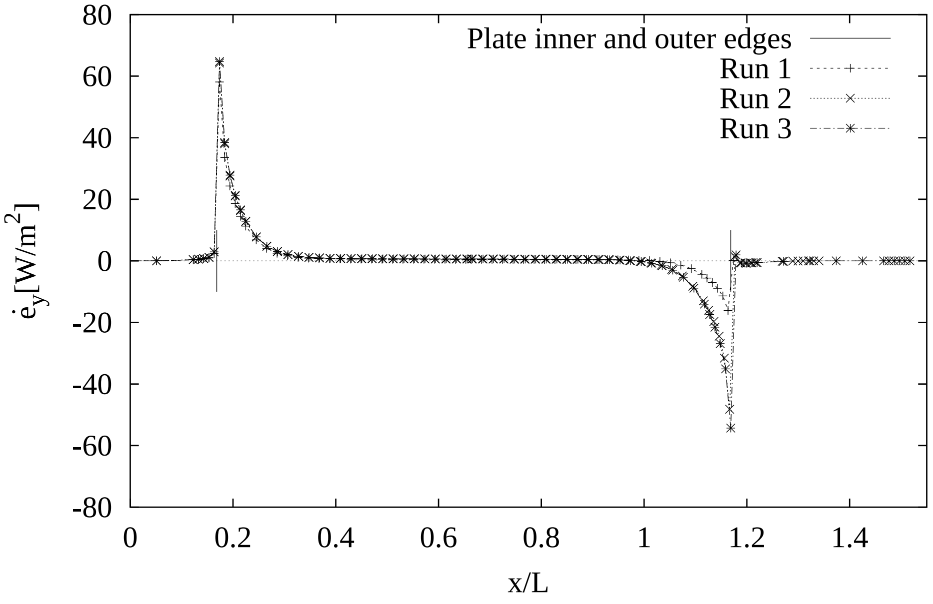

Figure 7.6: Time averaged energy flux density in the y-direction at the surface of the plate for run 1 to 3. M=0.01, plate length, $L = 24.5$cm, domain height, $y_0 = 0.81$ cm. Note that the oscillatory boundary is progressively further from the plates as run numbers increases.

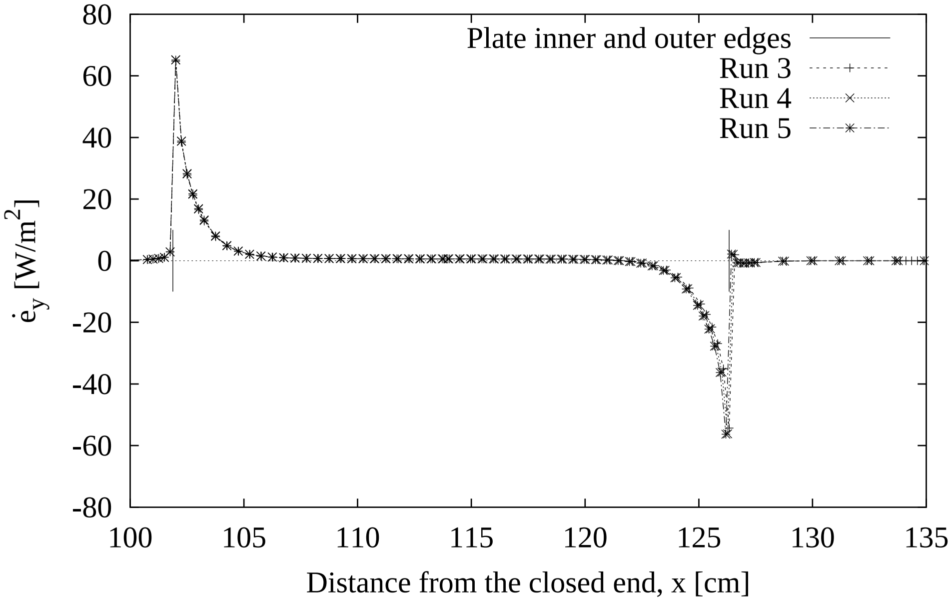

Figure 7.7: Time averaged energy flux density in the y-direction at the surface of the plate for run 3 to 5. M=0.01, plate length, $L = 24.5$cm, domain height, $y_0 = 0.81$ cm. Note that the oscillatory boundary is progressively further from the plates as run numbers increases.

test cases when M=0.01, must be re-evaluated.

When Cao *et al.* (1996) varied the Mach number of their test cases, they did not change the location of the oscillatory boundary. In order to test the dependence of the results on the locations of the oscillatory boundary at different Mach numbers, case 3 (M=0.03) from the table 7.1 was tested with the boundary specified at 4 different locations. The results are presented in table 7.5. In run 6, the oscillatory boundary conditions are specified one cell away from the plate outer edge. In run 7, the oscillatory boundary is located at the same location as that used by Cao *et al.*. The oscillatory boundary conditions for runs 8 and 9 are specified at twice and three times that of run 7.

Run		6	7	8	9
$\frac{x_4-x_5}{2u_1/\omega}$		0.036(1 cell)	1.27	2.53	3.80
$\Delta p_{cy}/P_A$	[%]	2.8e-3	4.0e-3	2.7e-2	5.3e-3
$\Delta u_{cy}/u_A$	[%]	4.6e-3	6.6e-3	4.4e-3	6.4e-3
$\Delta T_{cy}/T_A$	[%]	1.3e-1	9.1e-2	6.8e-2	8.4e-2
$\Delta \rho_{cy}/\rho_A$	[%]	8.7e-2	6.0e-2	4.5e-2	5.7e-2
$\Delta Tb_{cy}/T_A$	[%]	1.1e-1	9.0e-2	7.8e-2	7.4e-2
u_{err}/u_A	[%]	9.8e0	5.4e0	3.7e0	3.7e0
T_{err}/T_A	[%]	2.3e0	1.1e0	9.5e-1	8.6e-1
$\dot{E}_{pl}$	[W]	3.9e0	1.6e0	1.1e0	9.3e-1
$\dot{E}x_{cen}$	[W]	-1.9e-1	-1.8e-1	-1.8e-1	-1.8e-1
$\dot{E}x_{BC34}$	[W]	-1.2e0	-9.0e-1	-8.9e-1	-9.2e-1
q_A	[W/m^2]	1.5e3	1.6e3	1.5e3	1.5e3
ex_{ABC34}	[W/m^2]	8.8e3	8.4e3	8.1e3	7.8e3
H_x	[W/m^2]	-8.5e3	-8.5e3	-8.5e3	-8.5e3
H_y	[W/m^2]	-1.8e2	-1.8e2	-1.8e2	-1.8e-2
$\dot{Q}_{Error}/Q_A$	[%]	3.9e0	1.0e0	3.4e-1	1.9e-1
$\dot{E}_{diss}pl$	[W]	1.0e0	1.0e0	1.0e0	1.0e0
$\dot{S}_{gen}T_0$	[W]	1.1e0	1.2e0	1.2e0	1.1e0
$\Delta P_A/P_A$	[%]	9.1e0	1.6e1	1.2e1	9.5e0
Cycles		32	51	67	46

Table 7.5: Simulation results with various locations of the oscillatory boundary when M=0.03. $2u_1/\omega$=6.84cm when evaluated at x_5, the plate outer edge. Plate length L =24.5cm, domain height y_0=0.806cm, $\Delta x/\lambda$=2.5e-4, $\Delta y/\delta_{km}$=8.3e-2.

The results in table 7.5 show again that, as the oscillatory boundary is moved closer to the plates, u_{err}/u_A, T_{err}/T_A and $\dot{Q}_{Error}/Q_A$ increase.

In figure 7.8, the energy flux density at the plate surface for runs 6 to 9 are shown to visualize the influence of the location of the oscillatory boundary.

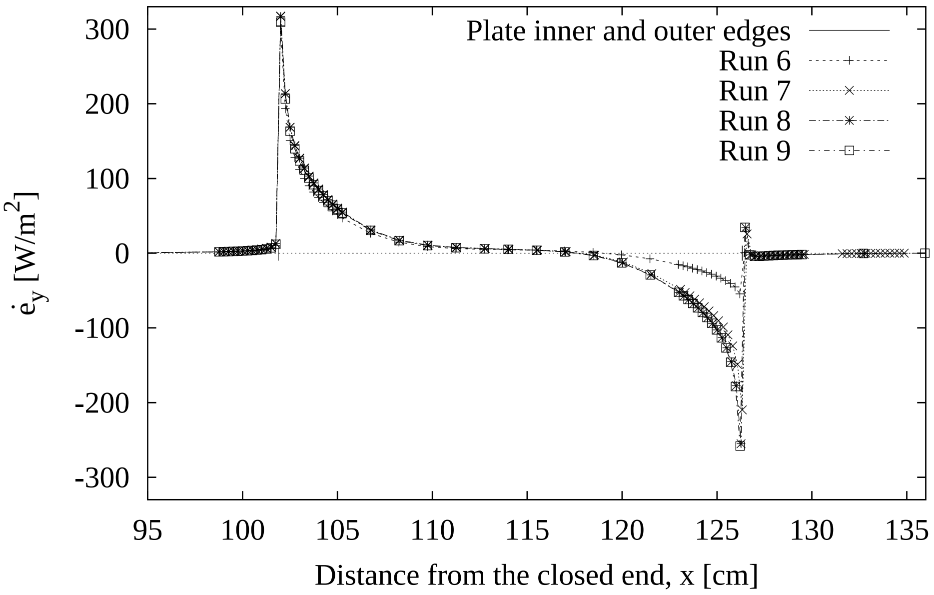

Figure 7.8: Time averaged energy flux density in the y-direction at the surface of the plate for run 6 to 9. M=0.03, plate length, L=24.5cm, domain height, y_0=0.81cm. Note that the oscillatory boundary is progressively further from the plates as run numbers increases.

Figure 7.8 indicates that the location of the oscillatory boundary used by Cao *et al.* (run 7 in the current work) for the simulation with M=0.03 is satisfactory.

Figure 7.9 shows how the errors u_{err}/u_A, T_{err}/T_A and $\dot{Q}_{Error}/Q_A$ vary with the location of the oscillatory boundary for different Mach numbers. Figure 7.9 indicates that as the oscillatory boundary conditions are moved further away, all errors reduce and eventually reach similar values for Mach numbers from 0.01 to 0.05. (One exception to this is the errors in temperature when M=0.05. The cause of the larger errors in temperature but not in velocity is not clear at this point and further investigation is suggested for the future.) Therefore, if the location of the oscillatory boundary is set at a few particle displacement distances away from the edge of the plate for a lower Mach number condition, errors will increase as Mach number is raised unless the location of the oscillatory boundary is not suitably adjusted.

It must be noted here that all simulations in this section are considered to be valid because the magnitude of the energy balance error, $\dot{Q}_{Error}$ is at the maximum, just under 5%. This only suggests that when the oscillatory boundary is specified closer, the nature of the simulation changes. When the ideal standing wave condition is specified far enough away, the simulation is that of an isothermal plate in a standing wave, and the flow field around the plate is representative of that in the ideal thermoacoustic couple. As the oscillatory boundary is moved closer to the plate outer edge, ideal standing wave conditions are forced near the plate. Then the simulation models how the thermoacoustic effect over

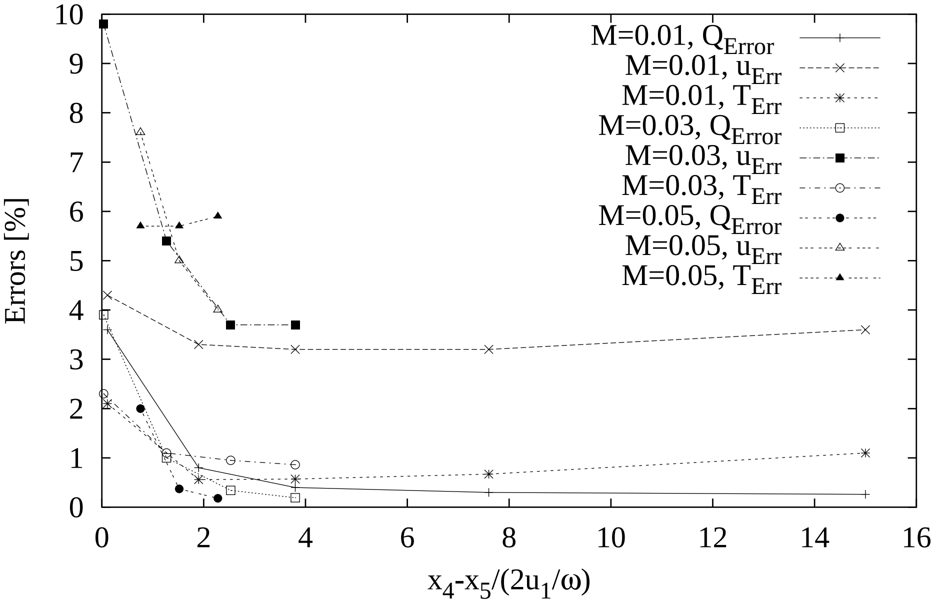

Figure 7.9: Errors versus distance between the outer plate edge and the oscillatory boundary normalized by the particle displacement distance at various Mach numbers.

the plate is modified when the plate is subject to forced standing wave conditions near the plate. (It is believed that this forcing of standing wave boundary conditions at every cycle caused a slightly larger energy balance error, $\dot{Q}_{Error}$ when the oscillatory boundary was close to plate outer edge.)

This also suggests that Cao *et al.* (1996) are not exactly simulating the isothermal plate in a standing wave, especially at higher Mach numbers. As described in section 5.2.3, they compensate for having the oscillatory boundary too close to the plate by adjusting the left and right going waves. However, their oscillatory boundaries are uniform in the y-direction despite the fact that the flow profile near the plate outer edge is strongly y-dependent.

In order to demonstrate how the pressure, temperature and velocity fluctuations differ from those in a pure standing wave near to the plate edge, simulation results in which the oscillatory boundary was specified sufficiently far from the plate are examined in the next section.

7.5.3 The y-dependence of flow field near the plate

The y- and the time dependency of the pressure, the velocity and the temperature near the plate can be shown by comparing each variable with those of the ideal standing wave one cell away from the plate outer edge. In figures 7.10 and 7.11, each variable is compared at three y-locations, at a cell away from the symmetrical boundary (labeled as $y = \Delta y$), at half way between the symmetrical boundary and the plate surface (labeled as $y = y_0/2$), and at the plate surface (labeled as $y = y_0$). Each variable is normalized by its amplitude at antinodes. S.W. stands for standing wave. The test case used in these figures is run 2 of table 7.4, the case in which the standing wave boundary conditions are specified far away enough for a thermoacoustic couple simulation as shown in figure 7.6.

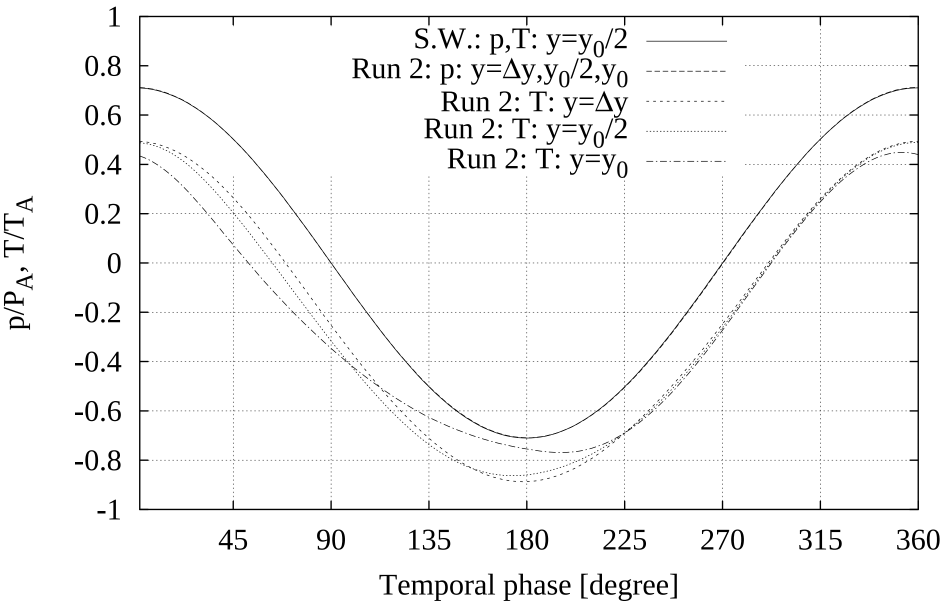

Figure 7.10: Pressure and temperature of run 2 and those of the standing wave (S.W.) as a function of time one cell away from the outer plate edge. M=0.01, $y_0 = 3\delta_{km}$.

In figure 7.10 the pressure and the temperature for run 2 are shown along with plots for the ideal standing wave. The pressure does not show y-dependence and it was exactly the same as that of the ideal standing wave. However, temperature does show some small y-dependence and the mean temperature is lower by approximately 20% of T_A, the amplitude of the temperature fluctuations. This offset is not due to a temperature drift but to a thermoacoustic effect near the plate (Results show that, even after 36 cycles, the mean temperature drift in the simulation domain is less than 1% of the fluctuating temperature amplitudes.) The figure also shows that the temperature fluctuation is not purely sinusoidal close to the plate surface.

Figure 7.11 shows that the amplitude of the velocity fluctuations vary with y-location (even though the x-location check point is one cell beyond the plate outer edge). The velocity closest to the plate surface is not purely sinusoidal. Velocities away from the plate surface are still 90° out of phase with the pressure.

The same comparisons are shown in figures 7.12 and 7.13 when $y_0 = \delta_{km}/2$ but all other operating conditions are the same as for run 2. The results for small plate spacings are shown in table B.2 in appendix B. (Table B.2 also contains simulation results for cases when the oscillatory boundary conditions were specified one cell away (as in run 1) and $x_4 - x_5/(2u_1/\omega)$=3.8 away (as in run 3) when y_0=$\delta_{km}/2$.)

When the plate spacing is reduced to the thermal penetration depth, quantities show less y-dependence but there are clear phase shifts both in the temperature and the velocity.

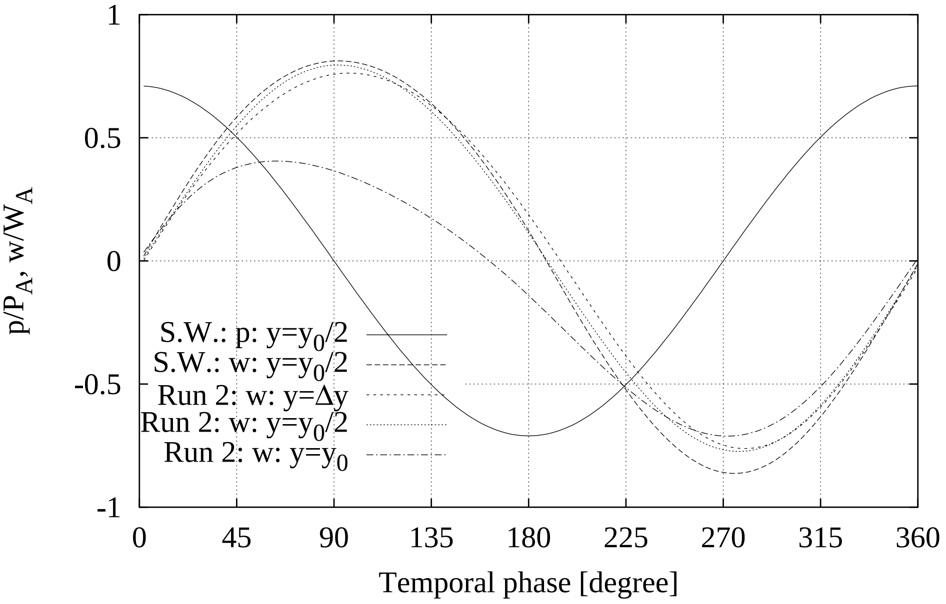

Figure 7.11: Pressure and velocity (x-component) of run 2 and those of the standing wave (S.W.) as a function of time one cell away from the outer plate edge. M=0.01, $y_0 = 3\delta_{km}$.

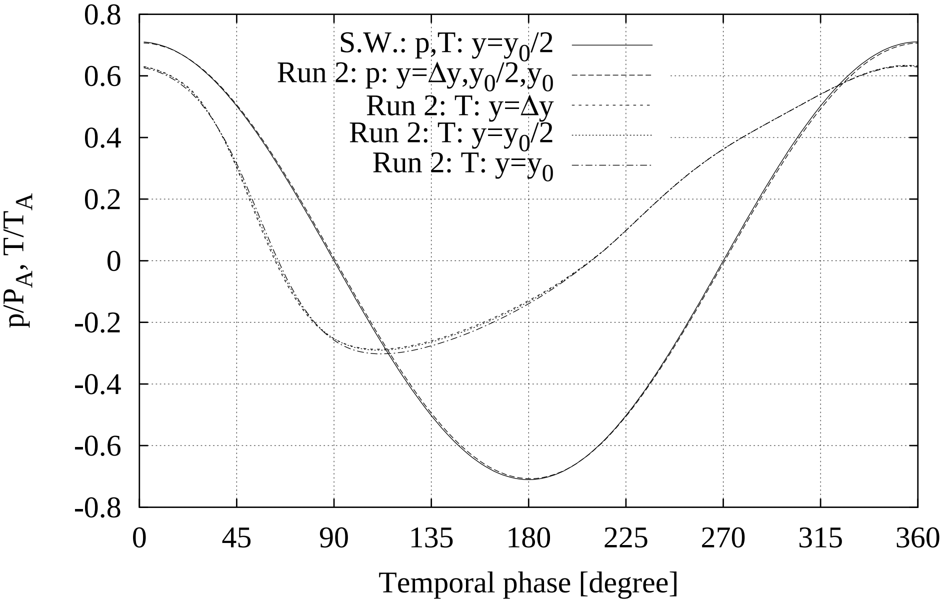

Figure 7.12: Pressure and temperature of run 2 and those of the standing wave (S.W.) as a function of time at one cell away from the outer plate edge. M=0.01, $y_0 = \delta_{km}/2$.

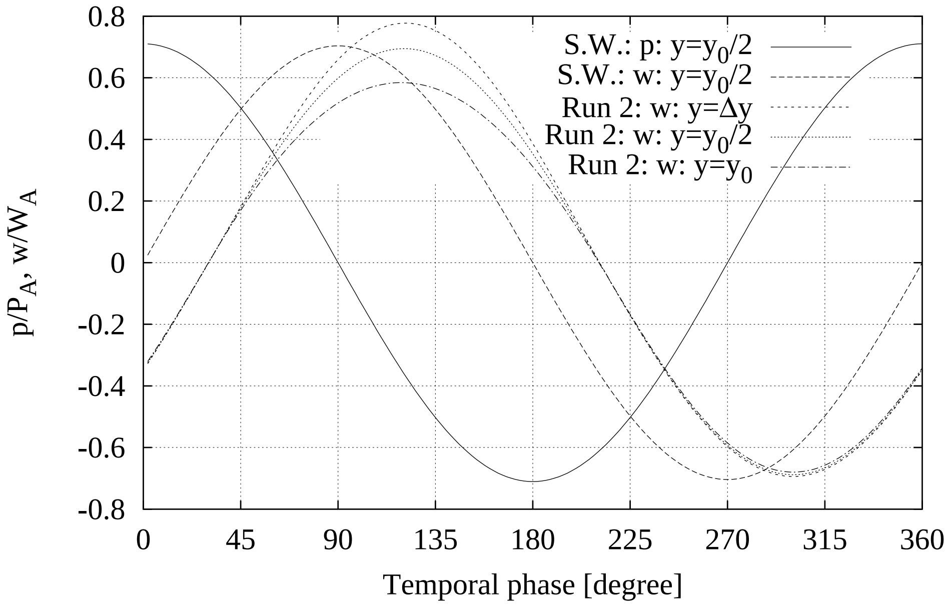

Figure 7.13: Pressure and velocity (x-component) of run 2 and those of the standing wave (S.W.) as a function of time at one cell away from the outer plate edge. M=0.01, $y_0 = \delta_{km}/2$.

The temperature is very distorted from a pure sinusoid and this time, the mean temperature has shifted higher by 20% of the amplitude. The rise in mean temperature corresponds to the fact that the energy dissipation is dominant at this plate spacing.

Overall, not only the y-dependency but also the non-sinusoidal temperature and velocities near the plate makes the simulation model of Cao *et al.* unclear, particularly when they adjust the phase without taking account of the y-dependence and the non-sinusoidal form of the temperatures and the velocities. The current model is clearer in the physical situation of the simulation in both cases when a standing wave boundary condition is far away and close to the plate.

In order to see the differences between the method of simulations of the current work and that of Cao *et al.*, the oscillatory boundary conditions were specified at the same location as used by Cao *et al.* for test cases with a higher Mach number but the caveat that using this location will lead to deviations from true thermoacoustic couple behavior over the plate at higher Mach numbers must be borne in mind.

7.6 Comparisons of the current simulations with analytical solutions and with the results of Cao *et al.*

7.6.1 Methods of comparisons

This section describes the methods of comparing the results of the current work with the first order analytical solution and with the simulation results of Cao *et al.* (1996). Some expected disagreements are also discussed.

The existing first order analytical solutions of thermoacoustic couples that predict the pressure, temperature and the velocity over a plate, are expected to agree well only near the plate center as they do not include plate end effects (see section 2.2). Therefore, the comparisons between the current work and the analytical solutions were made at the plate center only. In the current work, values of the temperature and the x-component of velocity are compared with the analytical solutions.

The temperature amplitude, given by equation (2.32), is a function of the pressure as given by equation (2.29). The x-component of the velocity given by equation (2.21) is a function of pressure gradient as given by equation (2.31). The pressure and the pressure gradient expressed in equations (2.29) and (2.31) require the amplitude of the pressure and the pressure gradient at the inner edge of the plate in order to calculate those at the plate center.

In order to find the pressure and the pressure gradient at the inner edge of the plate, equations (2.29) and (2.31) can be rearranged so that, from the pressure and pressure gradient specified at BC34, those at the inner edge of the plate can be found. (Both the pressure and its gradient are assumed not to be y-dependent.)

The pressure at the plate outer edge is approximated by that of a standing wave whether the oscillatory boundary conditions are specified very close to or far away from the plate outer edge. (This is a reasonable assumption, as the results of the current work showed that in most test cases the pressure (in contrast to the velocity and temperature) at the plate outer edge was very similar to that in an ideal standing wave.) The pressure gradient was calculated by differentiating equation (5.15) with respect to x and applying the continuity of volumetric velocity at the plate outer edge. For the velocity in the empty resonator section, the velocity in an ideal standing wave was used and for the velocity between the plates, equation (2.21) was used. As a result, the pressure gradient at the plate outer edge is

$$\frac{dp_1}{dx}|_{plate} = -\kappa P_A sin(\kappa x_{BC34}) \frac{1}{1 - f_\nu}. \tag{7.2}$$

Cao *et al.* (1996), avoided calculating the amplitude and the gradient of the pressure at the plate edge analytically by using values from the results of their numerical simulations. In fact they have directly matched the phase and amplitudes of the temperature and the velocity at point S in figure 7.1.

In the current work, such a fit was not used. Instead the analytical values of the temperature and the velocity at the center of the plate were calculated based on the boundary conditions specified at BC34.

The phase shifts between pressure and velocity, between velocity and temperature and between temperature and pressure were calculated from equations (2.10), (2.29), the x-component of (2.12), (2.21), (2.13) and (2.32). Because of the way analytical solutions are calculated, the results of simulations are expected to agree at operating conditions where plate end effects do not influence the results at the plate center. These conditions can be discovered after the series of comparisons in section 7.6.2 and 7.6.3. It is also expected that as the drive ratio is increased, the agreement will be poorer since only first order analytical solutions are used.

The reason that the results of Cao *et al.* were chosen to be compared with the current work is that the investigation of Cao *et al.* (1996) is one of only a few numerical studies of thermoacoustic couples that solve the full, 2-D Navier Stokes equations. The way that Cao *et al.* chose the extent of the simulation domain in order to reduce its size and the way that boundary conditions are specified is also closest to the current work.

However, it must be noted that in Cao's work, oscillatory boundary conditions are specified outside both edges of the plate (boundary AB and DC in figure 7.1) as described in the section 5.2.3. In the current work, the boundary is located further away from the plate, at the closed end of the tube. It must also be noted that the boundary conditions for all simulations of Cao *et al.* (1996) are adjusted so that the phase shift between the pressure and the velocity at point E is 90°. These phase adjustments were not made in the present study because the current work indicated that the phase shift varied significantly in the y-direction and it was difficult to adjust the phase only at point E. As a consequence, agreement between Cao *et al.* and the current work is expected at operating conditions where Cao *et al.* made only small phase adjustments at point E. Tests in section 7.6.3 indicate these conditions. Details of this are discussed in section 7.5.2.

Cao *et al.* presented their simulation results in terms of x and y-components of energy flux density (rather than the primary variables such as velocity and temperature), in order to better show the physics of the thermoacoustic effect at the thermoacoustic couple. They used equations (4.9) and (4.12) to calculate the components of the energy flux density numerically. To obtain an analytical value for the cycle averaged x-component of energy flux density at the middle of the plate, they used the expression

$$h_x = \rho_m c_P \overline{Tu}. \tag{7.3}$$

Thus they used only the second term in equation (4.9). This term is assumed to be dominant at point S in figure 7.1, because at the plate center, the mean temperature gradients in both the x and y-directions and the y-components of velocity are very small. In the current work, the x-component of the energy flux density at the center of the plate is calculated from equation (7.3) using T and u calculated by the method described previously in this section. When presenting x- and y-components of energy flux, Cao *et al.* normalized them by approximate maximum amplitudes H_x and H_y. These amplitudes are defined in equations (23) and (29) in Cao *et al.* (1996). Equation (23) of Cao *et al.* is

$$H_x = -\rho_m C_p |T_{1,S}||u_{1,S}| \tag{7.4}$$

where $|T_{1,S}|$ and $|u_{1,S}|$ are the magnitudes of the complex amplitudes of the fundamental components of temperature and velocity at point S in figure 7.1. This is the same as equation (7.3), evaluated at point S. Cao *et al.* obtained $|T_{1,S}|$ and $|u_{1,S}|$ from the results of their numerical simulations. In the current work, both $|T_{1,S}|$ and $|u_{1,S}|$ were calculated analytically. To determine $|u_{1,S}|$ and $|T_{1,S}|$, equations (2.21) and (2.32) were evaluated respectively at point S.

In order to determine H_y, Cao *et al.* assumed that the integral of the x-component of energy flux with respect to y at the center of the plate should be equal to the total energy flux into the plate, 'near' its edge (at the end of the plate where the energy flow is into the plate). They chose the 'near plate edge' region to be the size of the particle displacement distance.

When the pressure and the velocity have the same phasing as that of a standing wave at point S, they obtained

$$H_y = \frac{y_0 \omega |P_{1,E}|}{2(1+Pr)} Im \frac{f_\kappa - \widetilde{f_v}}{1 - \widetilde{f_v}} \tag{7.5}$$

and when the phasing at point E is not that of a standing wave,

$$H_y = \frac{y_0 \omega |P_{1,E}|}{2(1+Pr)} Im \Big(e^{i\phi_E} \frac{f_\kappa - \widetilde{f_v}}{1 - \widetilde{f_v}} \Big) \tag{7.6}$$

where $P_{1,E}$, is the pressure amplitude at the inner edge of the plate and ϕ_E is the difference from 90° of the phase shift between pressure and velocity at the inner edge of the plate. Since point E is at the edge of the plate, using the analytical solution for $P_{1,E}$ was considered inappropriate. Therefore in the present work, $P_{1,E}$ was found from the numerical solution as in Cao *et al.* (1996).

However, equation (7.6) seems incorrect and $|P_{1,E}|$ and $e^{i\phi_E}$ should be $|P_{1,S}|$ and $e^{i\phi_S}$ if they have derived it as described above (i.e. they equate the total energy flux at the plate center to the heat flux into the plate at its inner edge). This would not contribute to significant errors if $|P_{1,E}|$ and ϕ_E do not differ greatly from $|P_{1,S}|$ and ϕ_S. (Later tests in this chapter revealed that in some cases both the phase and the amplitudes differ by approximately 20°.) In the current work, H_x and H_y were used only when required in order to compare with the results of Cao *et al.*.

When Cao *et al.* displayed their results of energy flux density, they normalized the x-coordinate with either the plate length or the particle displacement distance and the y-coordinate with the plate half spacing, in the expectation that they might reduce the dependency of the energy flux density on other variables.

7.6.2 Results of test cases and comparison with analytical solutions

In this section, the results of comparisons with analytical solutions for all test cases are discussed. As described in section 7.3, test cases can be grouped to investigate the dependency of results on the drive ratio, plate spacing and plate locations.

Although further investigations of these dependencies are left until section 7.7, the results for each group listed in tables 7.6 to 7.9 are shown in separate sections from 7.6.2.1 to 7.6.2.3 respectively. This section focuses on the dependence of errors on each variable.

The phase shifts between pressures and velocities at various locations on the plate for all test cases are shown in table 7.7.

7.6.2.1 Test with various Mach numbers

RUN		15	16	17	18	19
M		0.01	0.02	0.03	0.04	0.05
$\frac{x_4-x_5}{2u_1/\omega}$		3.8e0	1.9e0	1.3e0	9.5e-1	7.6e-1
$\Delta p_{cy}/P_A$	[%]	5.2e-3	1.1e-2	4.0e-3	1.6e-3	1.3e-3
$\Delta u_{cy}/u_A$	[%]	6.0e-3	1.9e-2	6.6e-3	2.4e-3	2.0e-3
$\Delta T_{cy}/T_A$	[%]	4.5e-2	6.3e-2	9.1e-2	1.2e-1	1.5e-1
$\Delta \rho_{cy}/\rho_A$	[%]	3.1e-2	4.5e-2	6.0e-2	7.2e-2	9.7e-2
$\Delta Tb_{cy}/T_A$	[%]	3.2e-2	5.7e-2	9.0e-2	1.2e-1	1.5e-1
u_{err}/u_A	[%]	3.2e0	4.0e0	5.4e0	6.9e0	8.3e0
T_{err}/T_A	[%]	5.7e-1	8.4e-1	1.1e0	2.2e0	5.4e0
$\dot{E}_{pl}$	[W]	1.3e-1	6.0e-1	1.6e0	3.7e0	7.2e0
$\dot{E}x_{cen}$	[W]	-2.0e-2	-8.0e-2	-1.8e-1	-3.3e-1	-5.4e-1
$\dot{E}x_{BC34}$	[W]	-1.0e-1	-4.0e-1	-9.0e-1	-1.5e0	-2.8e0
q_A	[W/m^2]	3.0e2	8.3e2	1.6e3	2.4e3	3.5e3
ex_{ABC34}	[W/m^2]	8.9e2	3.7e3	8.4e3	1.5e4	2.5e4
H_x	[W/m^2]	-9.5e2	-3.8e3	-8.5e3	-1.5e4	-2.4e4
H_y	[W/m^2]	-6.2e1	-1.2e2	-1.8e2	-2.4e2	-3.0e2
$\dot{Q}_{Error}/Q_A$	[%]	3.3e-1	6.7e-1	1.0e0	1.8e0	2.3e0
$\dot{E}_{diss}pl$	[W]	1.1e-1	4.5e-1	1.0e0	1.8e0	2.8e0
$\dot{S}_{gen}T_0$	[W]	1.3e-1	5.2e-1	1.2e0	2.1e0	3.3e0
$\Delta P_A/P_A$	[%]	5.7e0	1.1e1	1.6e1	2.1e1	2.6e1
Cycles		48	67	51	41	33

Table 7.6: Simulation results for Case 1 - 5, $x_4 - x_5$ = 8.66 cm, y_0=0.806 cm, $\Delta x/\lambda$ = 2.5e-4, $\Delta y/\delta_{km}$ = 8.3e-2.

Table 7.6 shows that as the Mach number is increased, the simulations take longer to converge which was also the case in the standing wave simulations in chapter 6. Therefore, runs 17 to 19 were stopped when the time averaged heat flux at the plate surface no longer changed by 0.1% of its magnitude, as described in section 7.4.

Errors u_{err}/U_A, T_{err}/T_A and $\dot{Q}_{Error}/Q_A$ increase as the Mach number increases. This is because the location of oscillatory boundary conditions is fixed at all Mach numbers (as described in section 7.5.2). This makes it harder to identify the error increase due to the increase in the Mach number.

In order to see whether this increase in errors is due to having a smaller $x_4 - x_5/(2u_1/\omega)$ or due to having a higher Mach number, the errors in table 7.6 are shown as a function of $x_4 - x_5/(2u_1/\omega)$ in figure 7.14, with the data from figure 7.9 when the oscillatory boundary locations were varied at M=0.01 and 0.03.

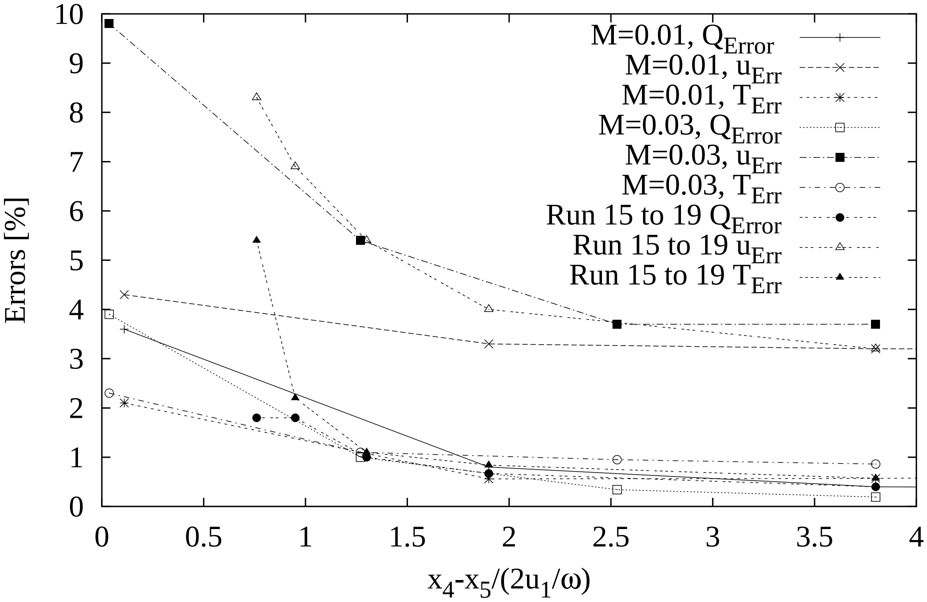

Figure 7.14: Errors versus distance between the outer plate edge and the oscillatory boundary normalized by the particle displacement distance with various Mach numbers.

Figure 7.14 shows that u_{err} and, more so, T_{err} increase more rapidly when $x_4 - x_5/(2u_1/\omega)$ is reduced by increasing the Mach number rather than by changing the actual location of the oscillatory boundary. This fact indicates that at a Mach number around 0.05 (this corresponds to a drive ratio of approximately 8%) the first order analytical solution becomes less valid (i.e. error increase in not just due to the oscillatory boundary being close). It must also be noted that the increase in $\Delta P_A/P_A$ indicates that as the distance between the plate outer edge and the oscillatory boundary is reduced, the standing wave is less resonant. It becomes less resonant more rapidly when the distance is reduced by an increasing Mach number.

Energy dissipation calculated over the whole domain, $\dot{S}_{gen}T_0$ agrees well with the analytically calculated energy dissipation at the plate surface, $\dot{E}_{diss}pl$ at all Mach numbers when $y_0 \simeq 3\delta_{km}$. This shows that energy is dissipated mainly near the plate surface.

At lower Mach numbers, numerically calculated phase differences between the pressure and the velocity at plate center ϕ_{SP_C} and ϕ_{S_C} agree well with the analytically calculated $\phi_{SP_{AN}}$ and $\phi_{S_{AN}}$. They gradually deviate as the Mach number is increased and at the highest Mach number tested, they differ by approximately 16°. The difference between ϕ_{E_C}

Run	Case	ϕ_{E_C}	ϕ_{F_C}	ϕ_{S_C}	$\phi_{S_{AN}}$	ϕ_{SP_C}	$\phi_{SP_{AN}}$
15	1	-74.0	-59.0	-98.0	-98.0	-49.0	-53.0
16	2	-72.0	-54.0	-95.0	-98.0	-45.0	-52.0
17	3	-67.0	-50.0	-91.0	-98.0	-40.0	-52.0
18	4	-63.0	-47.0	-88.0	-98.0	-37.0	-52.0
19	5	-60.0	-44.0	-86.0	-98.0	-36.0	-52.0
20	6	-78.0	-60.0	-94.0	-95.0	-58.0	-63.0
21	7	-86.0	-86.0	-96.0	-87.0	-81.0	-74.0
22	8	-88.0	-94.0	-97.0	-85.0	-87.0	-76.0
23	9	-90.0	-106.0	-100.0	-81.0	-95.0	-75.0
24	10	-90.0	-111.0	-102.0	-77.0	-98.0	-73.0
25	11	-84.0	-68.0	-106.0	-98.0	-61.0	-52.0
26	12	-92.0	-95.0	-101.0	-86.0	-92.0	-76.0

Table 7.7: Phase shifts between pressure and velocity at various locations (runs 15 to 26).

and ϕ_{F_C} is always 16°. Analytical calculations of phase at plate edges are not available.

It is expected that the energy flux which is calculated from the numerical results using equation (7.3), will deviate from the analytically calculated energy flux in the same manner as u_{err} and T_{err}. Plots of energy flux density are shown in section 7.6.3.

7.6.2.2 Test with various plate spacings

Dependence of errors on plate spacings can be investigated from the results of run 17 and runs 20 to 24. Iterations of runs 20 to 24 (table 7.8) were also stopped by monitoring the convergence rate of $\dot{Q}_{pl}$. When the simulations are run over many cycles, $\dot{Q}_{Error}/Q_A$ slowly increases for most cases. Although run 17 was simulated for over 50 cycles, it has a smaller $\dot{Q}_{Error}/Q_A$ than do runs 20 to 24. All iterations are considered valid based on the small magnitudes of $\dot{Q}_{Error}/Q_A$.

While T_{err}/T_A is almost constant at all y_0, u_{err}/u_A is considerably dependent on y_0 despite the fact that the first order analytical solutions used are applicable to spacings that are smaller than the thermal penetration depth. It must be noted here that it is not necessary to consider the effect of the location of the oscillatory boundary, because M=0.03 for all runs and, based on results in section 7.5.2, the boundary location is appropriate for a valid thermoacoustic couple simulation. Therefore, larger u_{err} at the smaller plate spacings is due to the poor estimation of the pressure gradient while the pressure is relatively well estimated by that of the standing wave. This suggests that in order to compare the numerical results with the first order analytical solution in the plate region, better agreement is obtained by using the numerically calculated amplitude and phase of pressure

Run		20	21	22	23	24
y_0		$1.7\delta_{km}$	δ_{km}	$0.83\delta_{km}$	$0.63\delta_{km}$	$0.56\delta_{km}$
$\Delta p_{cy}/P_A$	[%]	2.2e-3	7.2e-3	2.6e-3	2.0e-3	2.4e-3
$\Delta u_{cy}/u_A$	[%]	2.8e-3	9.2e-3	3.3e-3	2.1e-3	2.4e-3
$\Delta T_{cy}/T_A$	[%]	1.3e-1	1.5e-1	1.4e-1	1.5e-1	1.3e-1
$\Delta \rho_{cy}/\rho_A$	[%]	8.7e-2	1.0e-1	9.3e-2	9.9e-2	9.0e-2
$\Delta Tb_{cy}/T_A$	[%]	1.1e-1	1.2e-1	1.1e-1	1.1e-1	1.0e-1
u_{err}/u_A	[%]	6.1e0	1.0e1	1.3e1	1.8e1	2.1e1
T_{err}/T_A	[%]	1.1e0	1.2e0	1.2e0	1.3e0	1.3e0
$\dot{E}_{pl}$	[W]	1.8e0	2.0e0	2.0e0	2.0e0	2.1e0
$\dot{E}x_{cen}$	[W]	-9.2e-2	-5.4e-2	-4.4e-2	-3.0e-2	-2.4e-2
$\dot{E}x_{BC34}$	[W]	-8.9e-1	-1.0e0	-1.1e0	-1.1e0	-1.1e0
q_A	[W/m^2]	1.3e3	9.4e2	8.7e2	8.9e2	9.5e-2
ex_{ABC34}	[W/m^2]	8.4e3	8.3e3	8.2e3	7.9e3	7.7e3
H_x	[W/m^2]	-9.4e3	-1.2e4	-1.4e4	-2.1e4	-2.6e4
H_y	[W/m^2]	-2.0e2	-1.6e2	-1.2e2	-6.0e1	-4.5e1
$\dot{Q}_{Error}/Q_A$	[%]	2.4e0	3.4e0	3.5e0	3.2e0	2.8e0
$\dot{E}_{diss}pl$	[W]	1.0e0	1.0e0	9.3e-1	7.0e-1	6.3e-1
$\dot{S}_{gen}T_0$	[W]	1.4e0	1.8e0	1.9e0	2.1e0	2.2e0
$\Delta P_A/P_A$	[%]	1.2e1	7.3e0	5.6e0	3.7e0	3.2e0
Cycles		28	26	26	21	22
$\Delta y/\delta_{km}$		4.2e-2	4.2e-2	4.2e-2	2.8e-2	2.8e-2

Table 7.8: Simulation results for cases 6 - 10. M=0.03, δ_{km}=0.24cm $x_4 - x_5/(2u_1/\omega)$=1.3e0, $\Delta x/\lambda$ =2.5e-4.

and pressure gradient at the plate edge as input to the analytical model. This is similar to the way Cao *et al.* match the phase and amplitude of numerical and analytical solutions at point S in figure 7.1.

The resonance of the standing wave is better at smaller plate spacings which indicates that the agreement between the analytical and numerical solutions is not influenced by the resonance.

Numerically calculated energy dissipation over the whole domain and analytically calculated energy dissipation at the plate surface start to disagree as the plate spacings are reduced. This is expected as the analytical expression for energy dissipation at the plate surface was derived, based on the assumption that the plate spacings are much larger than the thermal penetration depth. Further discussion on energy dissipation is presented in section 7.7.2.

Phase differences, ϕ_{E_C}, ϕ_{F_C}, ϕ_{S_C} and ϕ_{SP_C}, for runs 20 to 24 in table 7.7 indicate that the variance of the phase shift in the y-direction becomes small as the plate spacings are reduced. Agreement between the analytical solutions and the numerical results at the plate center becomes poorer as the plate spacings are reduced.

7.6.2.3 Test of the plate location in the domain

Dependence of errors on domain lengths and plate spacings can be investigated from the results in table 7.9. All simulations were stopped by monitoring the magnitude of the convergence rate of the heat flux at the plate surface.

Errors u_{err}/U_A and T_{err}/T_A are smaller when the domain length is shorter (runs 25 and 26). Shorter domain lengths also showed better agreement between numerical and analytical results in the standing wave simulations in chapter 6. However, it must be noted that the better agreement is also due to the fact that $x_4 - x_5/(2u_1/\omega)$ is larger, as described in section 7.5.2. (The particle displacement distance is smaller at a smaller x-coordinate.)

When the simulation domain is short, the analytically calculated $\dot{E}_{diss}pl$ agrees better with $\dot{S}_{gen}T_0$ even at small plate spacing.

Errors in energy balance of the simulation domain, $\dot{Q}_{Error}/Q_A$, are larger for both domain lengths when plate spacings are small. Agreement between the analytically and numerically calculated phase shifts at the plate center (ϕ_{S_C} and $\phi_{S_{AN}}$, ϕ_{SP_C} and $\phi_{SP_{AN}}$) for both simulation domains are poor but slightly better when the plate spacing is large.

The phase difference between the inner and the outer edge of the plate are similar for runs 17 and 25, and 22 and 26 although the actual values of the phase differ.

RUN		17	22	25	26
$\frac{x_4-x_5}{2u_1/\omega}$		1.3	1.3	2.4	2.4
x_E/λ		0.10	0.10	0.037	0.037
y_0		$3.33\delta_{km}$	$0.83\delta_{km}$	$3.33\delta_{km}$	$0.83\delta_{km}$
$\Delta p_{cy}/P_A$	[%]	4.0e-3	2.6e-3	1.0e-3	9.5e-4
$\Delta u_{cy}/u_A$	[%]	6.6e-3	3.3e-3	1.2e-3	9.6e-4
$\Delta T_{cy}/T_A$	[%]	9.1e-2	1.4e-1	8.3e-2	1.2e-1
$\Delta \rho_{cy}/\rho_A$	[%]	6.0e-2	9.3e-2	5.5e-2	7.9e-2
$\Delta Tb_{cy}/T_A$	[%]	9.0e-2	1.1e-1	8.2e-2	1.1e-1
u_{err}/u_A	[%]	5.4e0	1.3e1	1.9e0	6.6e0
T_{err}/T_A	[%]	1.1e0	1.2e0	1.6e0	8.3e-1
$\dot{E}_{pl}$	[W]	1.6e0	2.0e0	1.2e0	9.6e-1
$\dot{E}x_{cen}$	[W]	-1.8e-1	-4.4e-2	-6.8e-2	-1.7e-2
$\dot{E}x_{BC34}$	[W]	-9.0e-1	-1.1e0	-6.4e-1	-5.1e-1
q_A	[W/m^2]	1.6e3	8.7e2	1.1e3	1.1e3
ex_{ABC34}	[W/m^2]	8.4e3	8.2e3	6.0e3	6.4e3
H_x	[W/m^2]	-8.5e3	-1.4e4	-4.9e3	-7.5e3
H_y	[W/m^2]	-1.8e2	-1.2e2	-2.2e2	-1.4e2
$\dot{Q}_{Error}/Q_A$	[%]	1.0e0	3.5e0	1.1e0	3.0e0
$\dot{E}_{diss}pl$	[W]	1.0e0	9.3e-1	9.5e-1	8.1e-1
$\dot{S}_{gen}T_0$	[W]	1.2e0	1.9e0	9.4e-1	9.0e-1
$\Delta P_A/P_A$	[%]	1.6e1	5.6e0	8.3e-1	6.0e-1
Cycles		51	26	49	29
$\Delta y/\delta_{km}$		8.3e-2	4.2e-2	8.3e-2	4.2e-2

Table 7.9: Simulation results for run 25, 26. Results of Run 17 and 22 are re-listed. $\Delta x/\lambda$=2.5e-4, δ_{km}=0.24cm.

7.6.3 Comparison with the results of Cao *et al.* (1996)

In this section, some of the results of the test cases in tables 7.6, 7.8 and 7.9 are compared with the simulation results of Cao *et al.* (1996). The order of presentation of the results follows that of Cao *et al.*.

First, the energy lines of run 15 are shown in figure 7.15. The y-coordinate in the figure has been inverted to compare with equivalent figures of Cao *et al.*. Run 15 is a test case with a large plate spacing at low Mach number ($y_0 = 3.3\delta_{km}$, M=0.01). Run 15 is the test case equivalent to run 1 of Cao *et al.* (1996) where they applied standing wave boundary conditions and did not adjust the phase shift of the pressure and the velocity at the plate inner edge. Therefore the results of the current work are expected to agree well with the results of Cao *et al.*.

The energy lines of runs 1 and 2 from Cao *et al.* (Fig.2 (a), (b) of Cao *et al.* (1996)) are displayed in figure 7.16 (a) and (b) respectively. Run 2 of Cao *et al.* is very similar to run 1 but the boundary conditions were adjusted to alter the phase shift between the pressure and the velocity at the plate inner edge from 92° to 90°. As the adjustment is small, it can be seen that the energy lines of run 2 are very similar to these of run 1.

The energy lines in figures 7.15 and 7.16(a) and (b) indicate that there is energy transfer from the outer edge of the plate to the inner edge of the plate.

The obvious difference between the three results is in the energy lines passing towards the left boundary of the simulation domain. Since the domain to the left of the plate is enclosed within nominally adiabatic boundaries, any energy flux passing in from the right boundary and not entering the plate will lead to an accumulation of energy in the tube to the left of the plate. If the flux of energy between consecutive energy lines is the same for results in figure 7.16 (a) and (b), (this is not discussed in Cao *et al.*.) then the total amount of energy accumulating in the domain to the left of the plate is larger for run 1 than for run 2. However, based on the present simulations, the magnitude of this energy flux is very small compared with the energy flux transferred through the ends of plates. And more importantly, as shown in the table 7.6, the amount of energy flux flowing towards the closed end $\dot{E}_{cen}$ is approximately 20% of cycle averaged energy flux at the oscillatory boundary $\dot{E}x_{BC34}$, while $\dot{E}x_{BC34}$ is 1.3% of the instantaneous maximum fluctuation amplitude of energy flux. Therefore, the energy flux flowing towards the closed end is negligible in comparison with the amount of energy flux caused by thermoacoustic effects at the plate. Taking this to be the main difference between runs 1 and 2 and noting that in any case, the differences are small at this condition, run 15 of the present simulation is compared with run 2 of Cao *et al.*.

Although the energy lines and the phase shift between the pressure and the velocity at point S in figure 7.1 agreed well with those of Cao *et al.*, the phase shift at the plate inner edge, ϕ_{E_C} (shown in table 7.7) did not agree. The current work has also shown a strong variation of phase shift in the y-direction and it is evident that if the phase shift at point

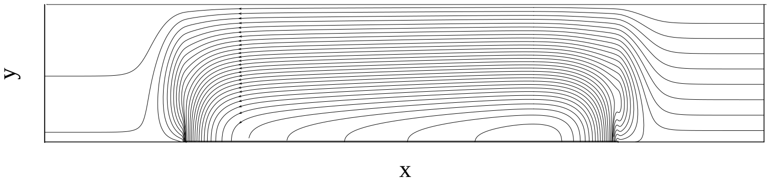

Figure 7.15: Energy lines for Run 15 of the current work. The vertical scale is stretched by a factor of 10.

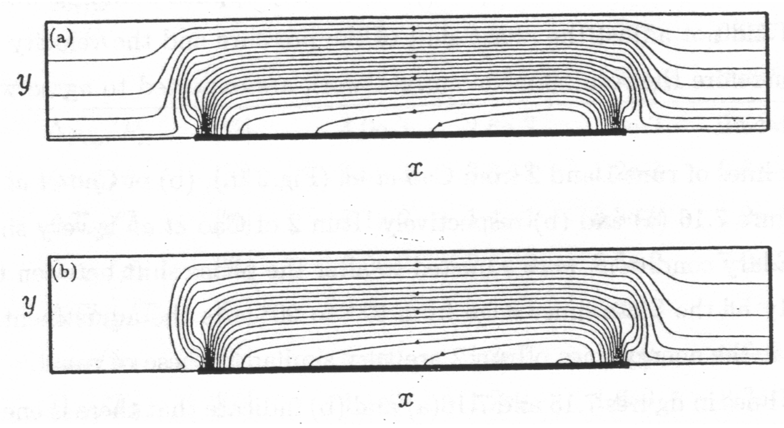

Figure 7.16: Energy lines pattern for Run 1 (above) and 2 (bottom) from Cao *et al.* (1996). The vertical scale is stretched by a factor of 10.

E is adjusted to 90°, the phase shift away from the point E at the same x-location, would not be 90°.

Energy flow towards the closed end is inevitable since most simulations are stopped before they reach true steady state to save computation time and also to avoid the accumulation of numerical errors. If we were able to ignore the numerical errors and let the simulations run for a few hundreds cycles, one would expect initially to observe the energy flux that flows towards the closed end gradually accumulate then at the true steady state, any excess energy should constantly leave from the plate so that there is no accumulation of energy in the domain.

The time averaged y-component of energy flux density at plate surface for run 15 of the current work and run 2 of Cao's simulation are shown in figure 7.17.

The data from Cao's work were read from Fig.4 of their paper and will contain a read off error estimated to be ± 3% in both e_y/H_y and x/L.

Overall agreement of the curve is sound and differences in the curves can be considered to be within the limitation of the accuracies of the simulations. The peak heights differ by approximately 8%. However, this was not considered significant as the peak is very narrow and sharp and its height depends on the grid resolution as discussed in section 7.5.1.

The time averaged energy flux at the surface of the plate shows that most of the net heat transfer occurs at the edges of the plate. For run 15 the particle displacement distance

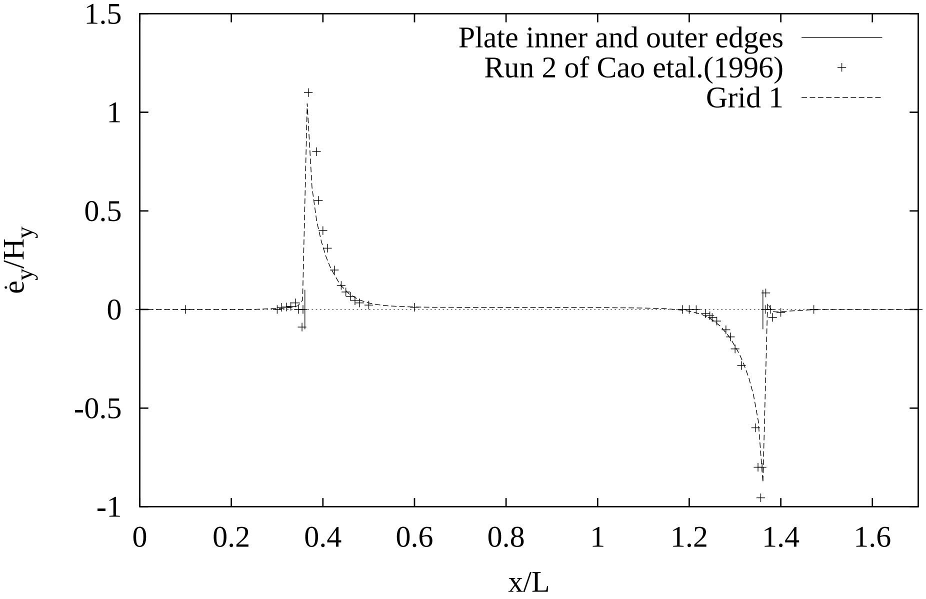

Figure 7.17: Time averaged normalized energy flux density in the y-direction at the surface of the plate (run 15). The crosses represent the results of Cao *et al.*.

is L/11. It can be seen from figure 7.17 that it is only in regions within approximately the particle displacement distance of the ends of the plate that significant heat transfer to or from the plate occurs.

Both the current work and Cao's simulations show that the peak height of the time averaged y-component of energy flux is larger at the inner edge of the plate than at the outer edge. In Cao's results, small spikes (which are numerical errors as they do not reflect the physical situation) appear just outside of both plate edges which, in the current work, only appear on the outer plate edge. This difference and the cause of these spikes are investigated in appendix C.

The instantaneous normalized y-component of energy flux for run 15 is plotted in figure 7.18. The same plot from Cao *et al.*(1996) is shown in figure 7.19. There is a difference of 180° in the starting time of the oscillatory boundary conditions, therefore, time $5\tau/8$, t5, in the current work corresponds to the time $\tau/8$ in Cao's work.

The amplitudes agree better further away from the inner plate edge. This is due to the fact that in Cao's work, oscillatory boundary conditions are also specified at the inner plate edge. Although the amplitudes are not exactly the same, the overall shape and the time dependency of the curves are similar.

All comparisons made so far relate to run 15 which has a large y_0 and small M. Results from this condition was expected to agree with the results of Cao *et al.*. The next comparison shows how the current work and the results of Cao *et al.* differ when the half plate spacing, y_0, is varied.

Cao *et al.* (1996, Fig. 3) presented the normalized x-component of energy flux, e_x/H_x,

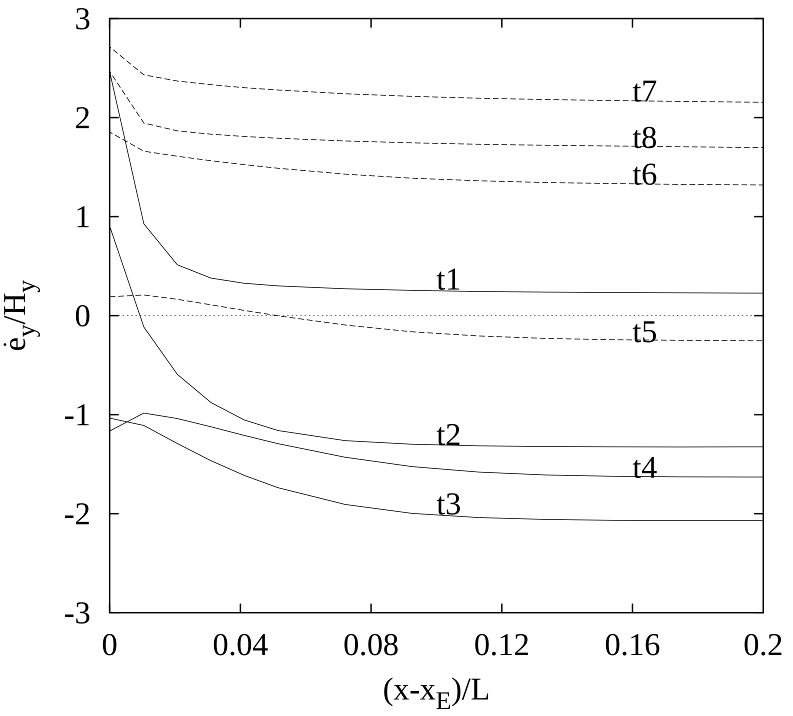

Figure 7.18: Instantaneous normalized energy flux density in the y-direction at the surface of the plate (run 15). (Note t1=$\tau/8$, t2=$2\tau/8$ ..... t8 =τ)

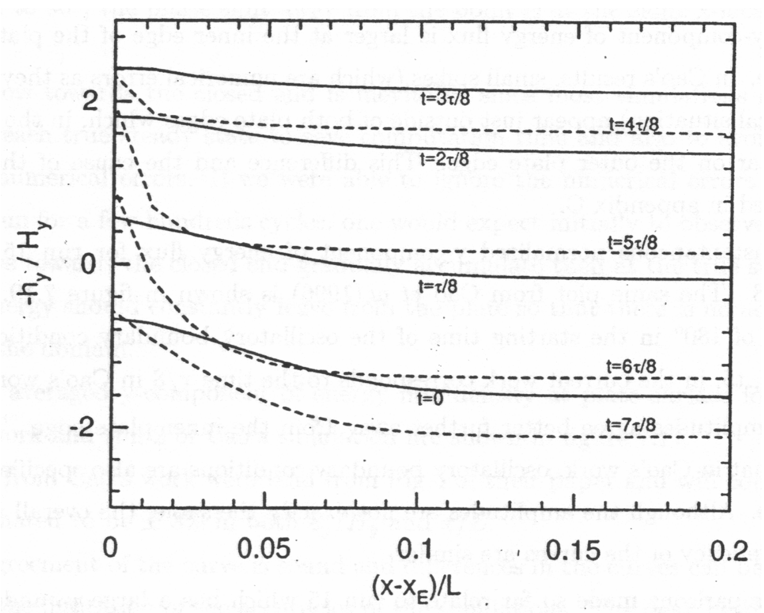

Figure 7.19: Instantaneous normalized energy flux density in the y-direction at the surface of the plate, Fig. 5 of Cao *et al.*.

at the middle of a thermoacoustic couple versus normalized y-location for various plate spacings at M=0.03 (the same as case 3 of table 7.1). In figure 7.20, e_x/H_x of runs 17 and 20 to 24 are displayed along with Cao's data from Fig. 2 of Cao *et al.* (1996). In Cao's simulation, the normalized energy flux at the middle of the plate became larger as the spacing became smaller. However, in the current work, the magnitude of e_x/H_x starts to decrease when δ_{km}/y_0 exceeds 0.6. This may be caused by the fact that the phase shift at plate inner edge, ϕ_E in the current work, is not adjusted to 90°. Dependence of various properties on plate spacings is further investigated in section 7.7.

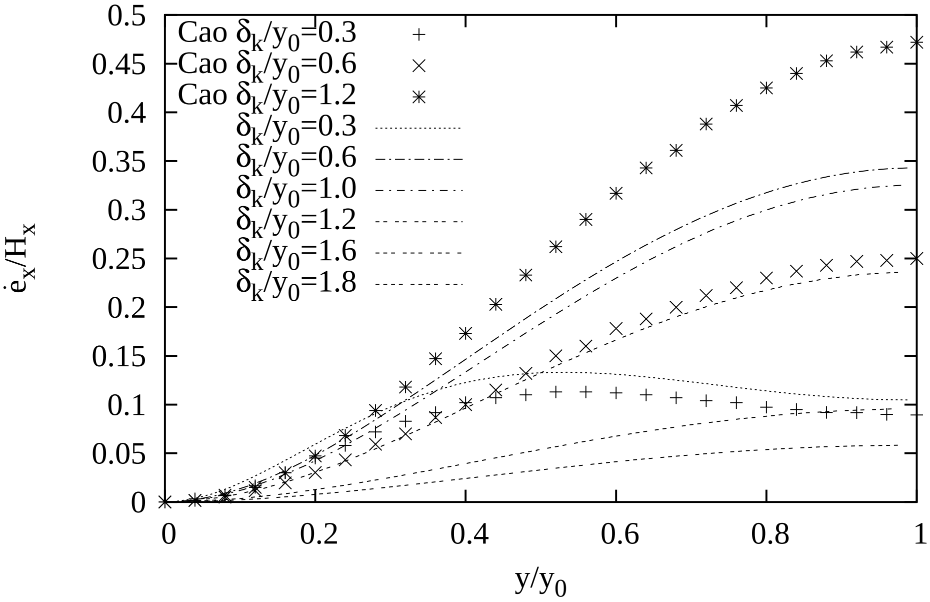

Figure 7.20: Plate spacing dependency of the time averaged normalized energy flux in the x-direction at the center of the plate. (run 17; δ_k/y_0=0.3, run 20; δ_k/y_0=0.6, run 21; δ_k/y_0=1.0, run 22; δ_k/y_0=1.2, run 23; δ_k/y_0=1.6, run 24; δ_k/y_0=1.8) M=0.03. The symbols show the results of Cao *et al.* (1996) while the lines are from the present work.

Plots of normalized energy flux density in the y-direction at the surface of the plate for runs 17 and 20 to 24 are shown in figure 7.21. This figure is enlarged around the inner edge of the plate and is shown in figure 7.22 with the results from Fig.7 of Cao *et al.* for $\delta_{km}/y_0 = 1.2$, as a guide. Fig.7 of Cao *et al.*, reproduced here as figure 7.23, shows the normalized energy flux only near the inner edge of the plate.

The results of the current work (figure 7.22) show a similar trend to that of Cao *et al.* (figure 7.23) but the actual quantities differ by 20% to 30%. An interesting feature is observed in the present results with e_y/H_y at the outer plate edge being inverted when the plate spacing is smaller than $\delta_{km}/y_0 = 1.0$. This was not identified in Cao *et al.* (1996) and is further investigated in section 7.7.

When y_0 was varied, considerable disagreement in phase shift between the current work and the results of Cao *et al.* were observed. When normalizing e_y by H_y calculated using

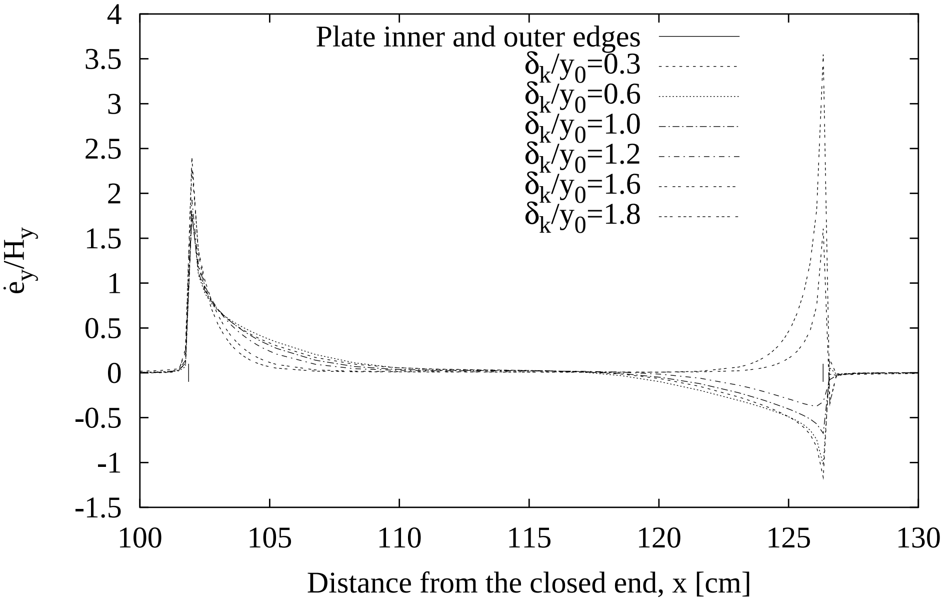

Figure 7.21: Normalized time averaged y-component of energy flux density at the plate surface for different plate spacings. (run 17; δ_k/y_0=0.3, run 20; δ_k/y_0=0.6, run 21; δ_k/y_0=1.0, run 22; δ_k/y_0=1.2, run 23; δ_k/y_0=1.6, run 24; δ_k/y_0=1.8)

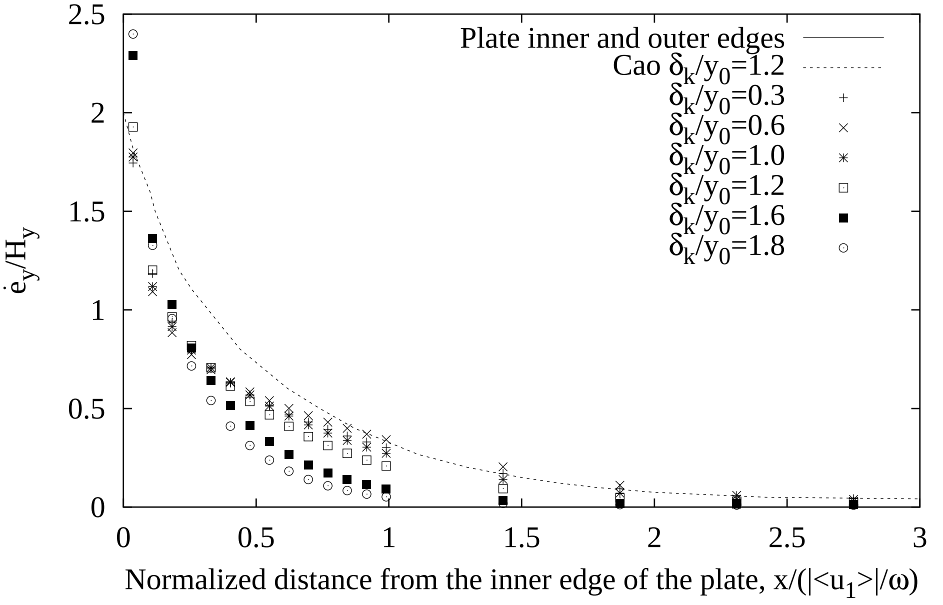

Figure 7.22: Normalized time averaged y-component of energy flux density near the plate inner edge for different plate spacings. (run 17; δ_k/y_0=0.3, run 20; δ_k/y_0=0.6, run 21; δ_k/y_0=1.0, run 22; δ_k/y_0=1.2, run 23; δ_k/y_0=1.6, run 24; δ_k/y_0=1.8)

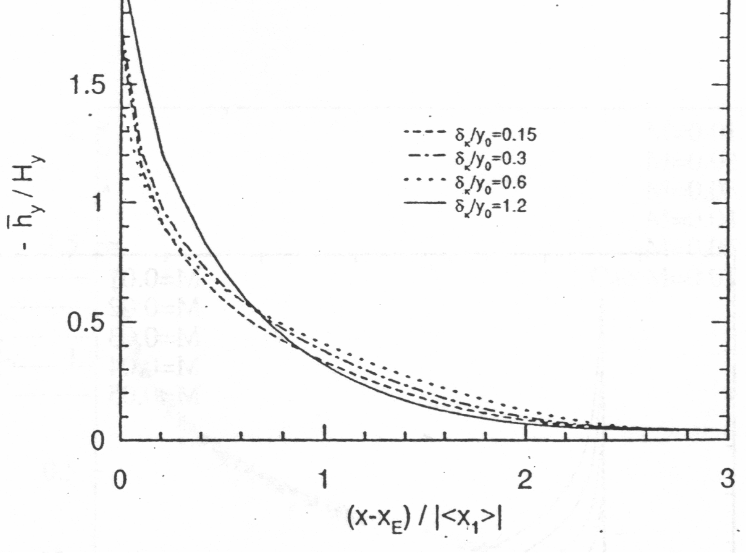

Figure 7.23: Normalized time averaged y-component of energy flux density near the plate inner edge for different plate spacings (Fig.7 of Cao *et al.* (1996)).

equations (7.5) and (7.6), agreement was poor in both cases. It is likely that Cao *et al.* had to significantly adjust the oscillatory boundary conditions to change the phase shift at the inner plate edge ϕ_E to 90°. In this case, there is poor agreement with the current work.

Next, the comparison of the results of the current work and the results of Cao *et al.* at various Mach numbers are made by looking at the y-component of time averaged energy flux density, e_y versus x.

In figure 7.24, both e_y, calculated from the current work, and x are not normalized. The width of the peak in the figure shows the increase of the particle displacement distance with the increase of Mach number.

Fig. 6 of Cao *et al.* (1996) is reproduced in figure 7.25. This shows the y-component of the time averaged energy flux, e_y normalized by H_y. The x-coordinate in the figure is normalized by the amplitude of the particle displacement $| < u_1 > |/\omega$. Cao *et al.* only display the energy flux near the inner edge of the plate.

Figure 7.24 was re-scaled after normalizing e_y and x and results are shown in figure 7.26 along with Cao's results (taken from their Fig.6) when M=0.01. After normalization, all curves fall approximately on the same line, which agrees with the tendency seen in Fig.6 of Cao *et al.*. Slight offsets of the curves and differences in amplitudes are due to the small differences in plate locations and the magnitudes of H_y. They are also due to the fact that the oscillatory boundary conditions are not specified at the inner edge of the plate in the present work. This suggests that at $y_0 = 3\delta_{km}$, Cao *et al.* did not significantly adjust the phase shift for all Mach numbers. It is interesting to note that as the Mach number is increased the resonance becomes poorer while the agreement between the results of Cao *et al.* and those of the current work are good for all Mach numbers.

Finally, the influence of the plate location in the domain on e_y in the current work and the work of Cao *et al.* are compared. Figure 7.27 shows e_y and the x-location without

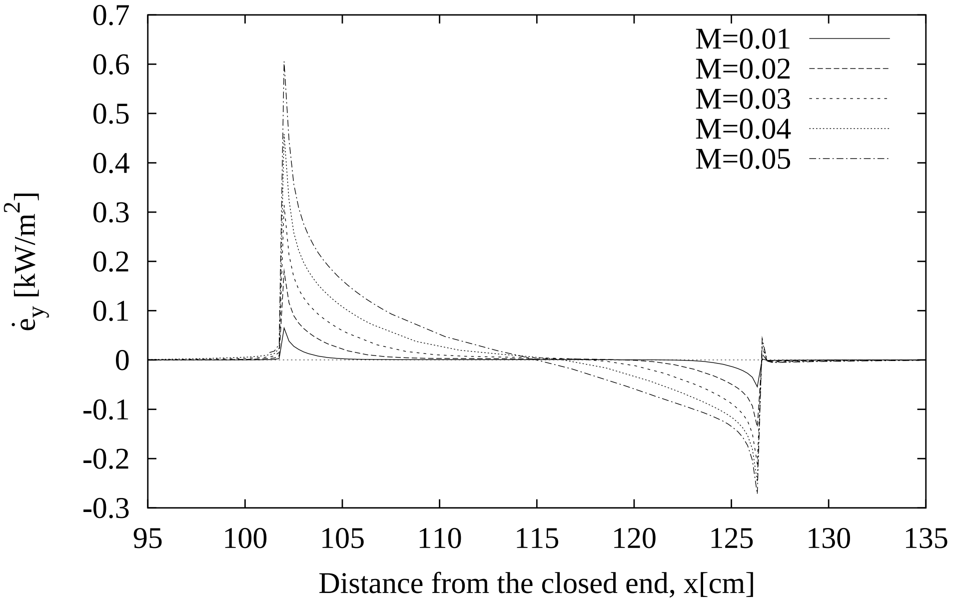

Figure 7.24: The y-component of time averaged energy flux density at the surface of the plate for various Mach numbers (run 15; M=0.01, run 16; M=0.02, run 17; M=0.03, run 18; M=0.04, run 19; M=0.05)

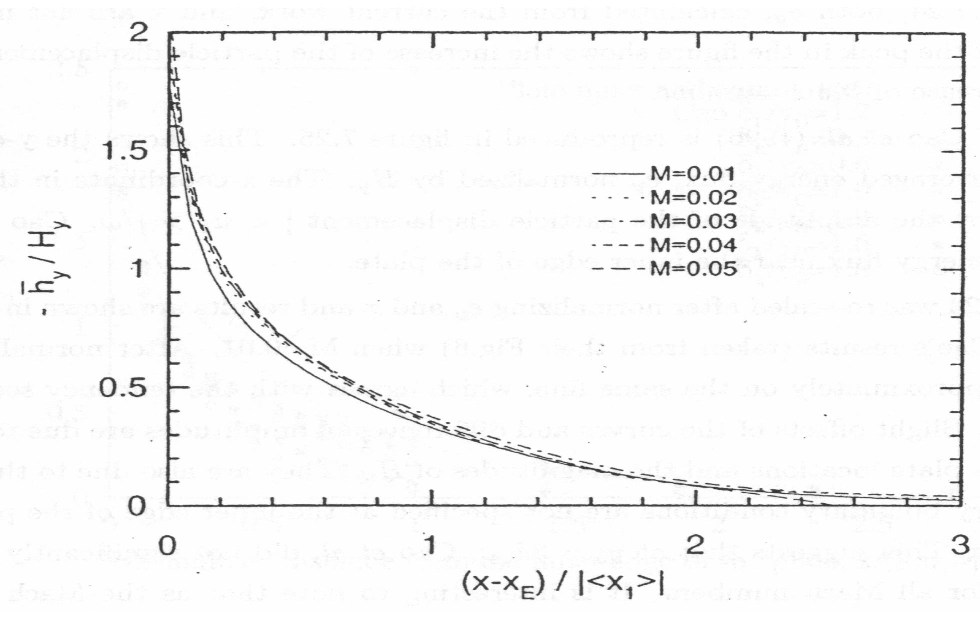

Figure 7.25: Fig. 6 of Cao *et al.* (1996).

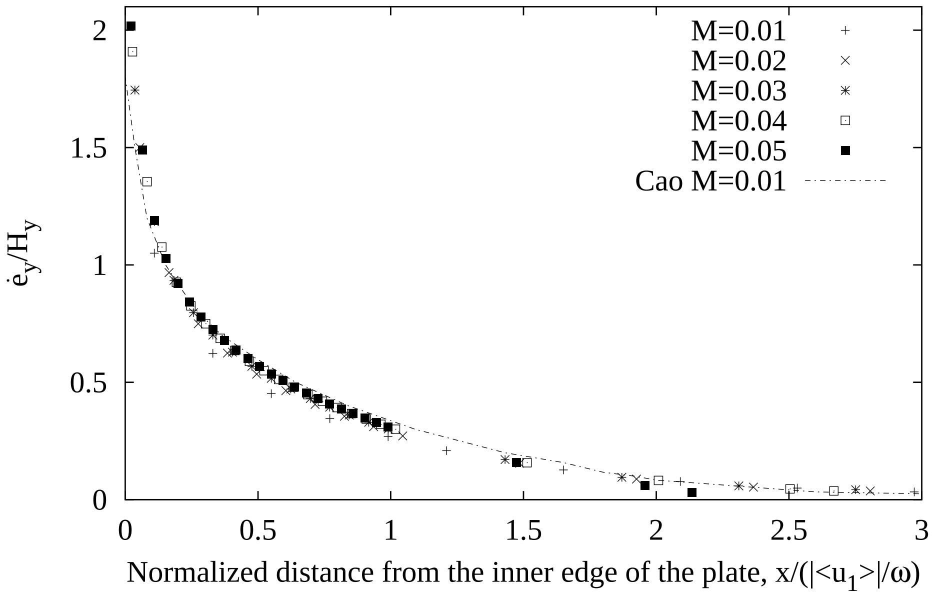

Figure 7.26: The y-component of time averaged energy flux density at the surface of the plate for various Mach numbers (run 15; M=0.01, run 16; M=0.02, run 17; M=0.03, run 18; M=0.04, run 19; M=0.05). The line represent the results from Fig. 6 of Cao *et al.* (1996) when M=0.01.

normalization. e_y for a smaller simulation domain (25 and 26) shows narrower peaks at both edges of the plate, demonstrating that the particle displacement distance at a lower x-coordinate is smaller than for runs 17 and 22.

In order to compare the present results with Fig. 9 of Cao *et al.*, which is shown in figure 7.28, results from figure 7.27 are normalized and are shown only near the inner edge of the plate in figure 7.29. The chained line in figure 7.29 represents the data from Fig.9 of Cao *et al.* (1996) when $y_0 = 1.2$. Although all curves fell almost on the same line as in Cao's Fig.9, their magnitudes differ from Cao's results. However the way four lines cross when $x/|u_1|/\omega < 1$ is similar to Cao's Fig.9. These differences could be caused by the combination of reasons previously discussed (i.e., no oscillatory boundary condition specified near inner plate edge, phase adjustment by Cao *et al.*.)

7.6.4 Summary of comparisons

Comparisons in sections 7.6.2 and 7.6.3 were carried out in order to justify the simulations of the current work. In terms of the energy balance of the simulation domain, all simulation results in both sections are valid based on the criterion proposed in section 4.3.2.

The results of the current work, analytical calculations and the results of Cao *et al.* do not agree in all cases. This was expected due to the way the analytical solutions are calculated and also due to the fact that Cao *et al.* specified the oscillatory boundary on both sides of the plate edge and the fact that they adjusted the boundary conditions so

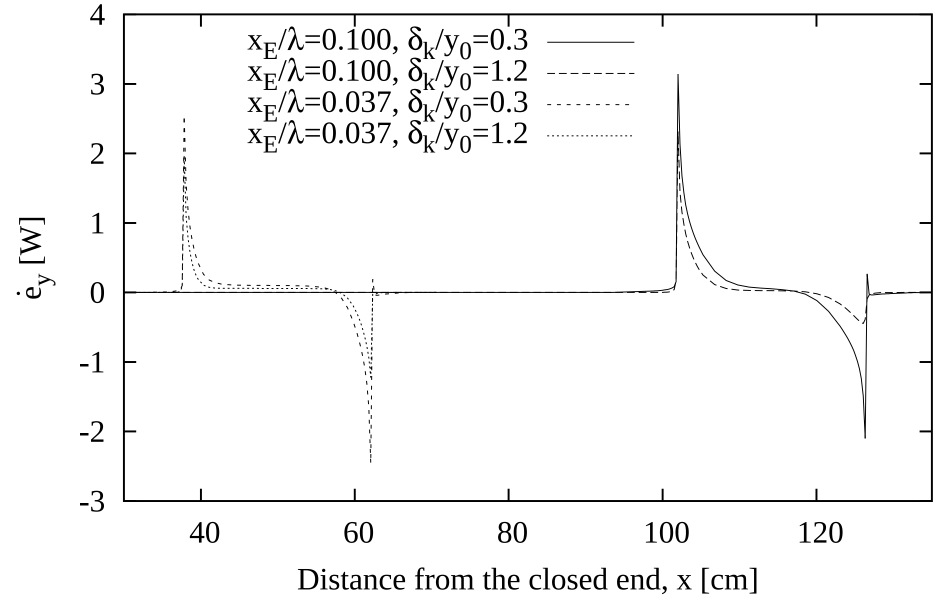

Figure 7.27: Energy flux density in the y-direction at the surface of the plate for different plate positions and spacings. M=0.03. (run 17; x_E/λ=0.1, δ_k/y_0=0.3, run 22; x_E/λ=0.1, δ_k/y_0=1.2, run 25; x_E/λ=0.037, δ_k/y_0=0.3, run 26; x_E/λ=0.037, δ_k/y_0=1.2)

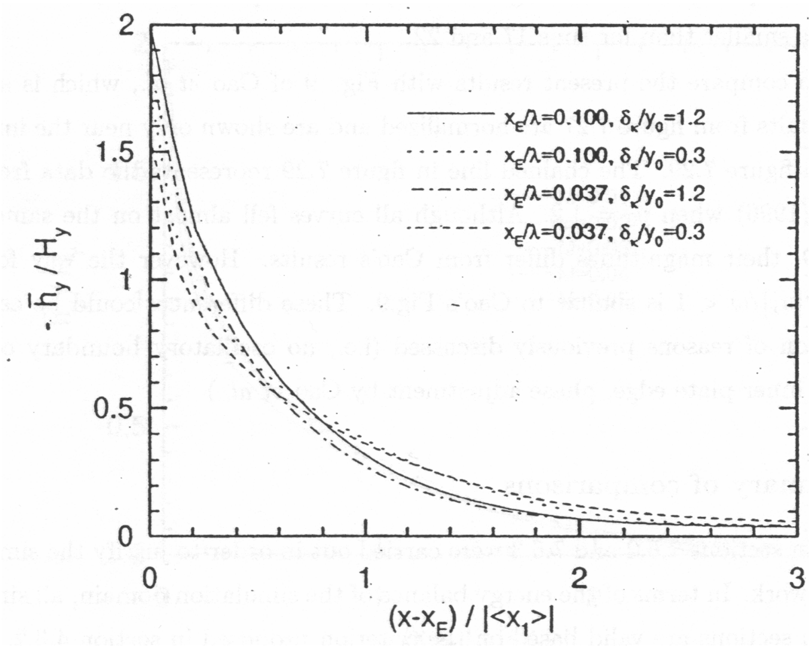

Figure 7.28: Normalized energy flux density in the y-direction at the surface of the plate for different plate positions and spacings. Fig. 9 of Cao *et al.*.

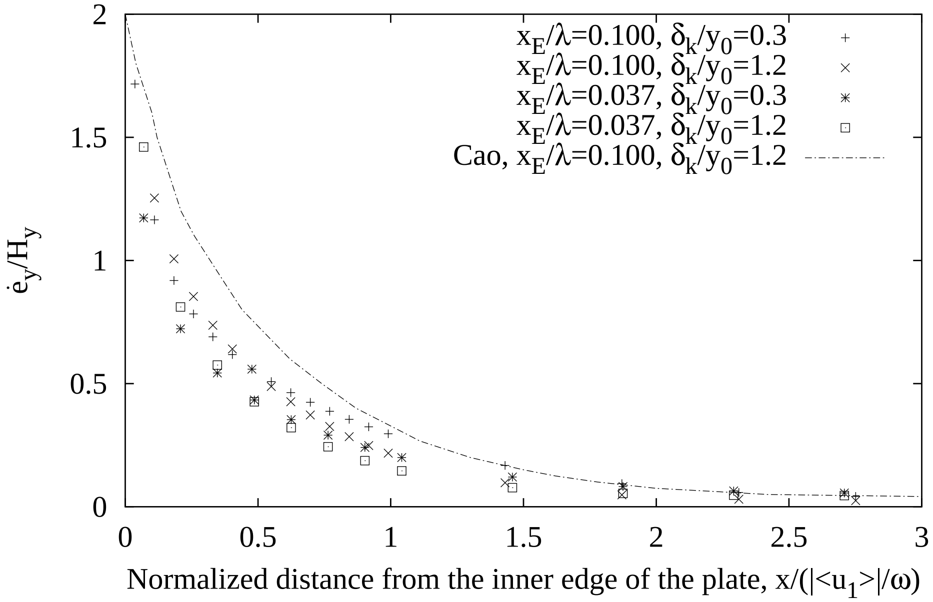

Figure 7.29: Normalized energy flux density in the y-direction at the surface of the plate for different plate positions and spacings. M=0.03. (run 17; x_E/λ=0.1, δ_k/y_0=0.3, run 22; x_E/λ=0.1, δ_k/y_0=1.2, run 25; x_E/λ=0.037, δ_k/y_0=0.3, run 26; x_E/λ=0.037, δ_k/y_0=1.2)

that the phase shift at the inner plate edge is always 90°. Good agreement was found between the present results and analytical results and between the present results and the results of Cao *et al.* for all cases where it would be expected.

Before discussing the details of the comparisons, the following points were noticed in thermoacoustic couple simulations in general.

The convergence (especially of temperature) was slower in the thermoacoustic couple model than was observed for the standing wave model. Slow convergence especially of temperature was also pointed out by Worlikar *et al.* (1998) where they had to terminate the simulation when the temperature convergence rate reached a certain value, while their adiabatic model with plate converged within 10 cycles (Worlikar *et al.* 1996).

As expected, the monotonic temperature rise in the simulation domain from cycle to cycle that was observed in the standing wave simulations also occurred in the thermoacoustic couple simulations. However, the rate of temperature rise was higher in the thermoacoustic couple simulations despite the fact that in the thermoacoustic couple simulation domain there is an isothermal plate which allows any accumulated energy to leave the domain by conduction to the plate.

In the current chapter, most simulations of thermoacoustic couples were stopped by monitoring the convergence rate of heat flux at the plate surface rather than waiting until the convergence rate of temperature no longer changed.

Before making comparisons, some preliminary tests were carried out. Tests in which the location of the oscillatory boundary was varied were described in section 7.5.2. These indicated that at higher Mach numbers, Cao *et al.* (1996) specifed the oscillatory boundary conditions too close to the plate for the simulation of a thermoacoustic couple in a standing wave. Their method of adjusting the phase shift between the pressure and the velocity at the inner plate edge by changing the conditions of the oscillatory boundary and forcing a constant phase shift in the y-direction make it less clear what exactly they were modeling. In the current work, standing wave conditions were used at the oscillatory boundary and no adjustments were made even when the oscillatory boundary condition was very close to the plate. This means that the simulation is not precisely that of an isothermal plate in a tube with a standing wave.

When simulating test cases with higher Mach numbers, the current work specified the oscillatory boundary at the same locations as those of Cao *et al.*. As the Mach numbers are increased, the current work indicated that the resonance of the standing wave was poorer. However, when the energy flux density calculated from the current work and that from Cao *et al.* are compared at the inner plate surface, there was close agreement for all Mach numbers. Agreement was good because the Mach number was varied at relatively large plate spacings (approximately six times the thermal penetration depth) where the adjustments of the boundary conditions, as indicated by results of Cao *et al.*, were minimal. This suggests that the simulations of Cao *et al.* also did not maintain the resonance. It must also be noted that while the energy flux density at the inner plate agrees, agreement of the phase shift at point E was poor.

Poor agreement was observed in energy flux density both in the x and y-direction between the current work and the results of Cao *et al.*, when plate spacings were varied while the Mach number was kept at 0.03. The results of the current work indicate that the resonance improved as the plate spacings were reduced, while agreement with the results of Cao *et al.* becomes poorer. It is expected that Cao *et al.* made more adjustments of the oscillatory boundary at smaller y_0. It must be noted that the simulations of Cao *et al.* became unstable when the half plate spacings was smaller than $0.83\delta_{km}$.

Normalization quantities H_x and H_y differ from those of Cao *et al.*, especially at small y_0, as in the current work, they are calculated purely analytically (as described in section 7.6.1) while in the work of Cao *et al.*, they are calculated using the amplitude and phase of each variables obtained from the simulation results. It would have been more appropriate to compare the data before normalization, if they were available.

Agreement between numerically calculated temperatures and velocities and the first order analytical solutions (the method of calculation is described in section 7.6.1) compared at the plate center is best at lower Mach numbers and larger plate spacings (M=0.01, $\delta_{km}/y_0 = 0.3$).

Errors in the temperature were more dependent on the relative location of the oscillatory boundary than were errors in velocity, although the relative magnitudes of the errors in temperature are smaller. (Initially it appeared as though they were dependent on the Mach number but tests with various locations of the oscillatory boundary at M=0.01 and 0.03 showed that the cause of disagreement was due to the fact that the oscillatory boundaries were specified too close to the plate.)

Errors in temperature stayed constant when plate spacings were varied at M=0.03, while errors of velocity increased rapidly as the plate spacings were reduced. These are mainly because temperature is a function of pressure amplitude while velocity depends on the pressure gradient. Both errors reduced when the domain length was shorter. This is due to the fact that at the same Mach number, the distance of the oscillatory boundary from the plate outer edge relative to the particle displacement evaluated at the plate outer edge, increases when the domain is shorter.

Although the magnitudes of energy balance error in the simulation domain, $\dot{Q}_{Error}$ were acceptable for all simulations tested, it was found that they were larger when the oscillatory boundary conditions are specified very close to the plate outer edge. $\dot{Q}_{Error}$ was dependent also on the plate spacing.

Cao *et al.* (1996) matched the analytical velocity and temperature at point S (figure 7.1) with those obtained numerically. This was not done in the current work and the agreement between the numerical and analytical results does not appear to be as good as that reported by Cao *et al.*. Forcing this fit is one reason for this better agreement and it is expected that similar results would be obtained in the current work if a similar fit was made.

The current work simulated thermoacoustic couples using standing wave conditions at the oscillatory boundary that was located sufficiently away from the plate. In cases when the ideal standing wave condition was specified too close to the plate, the physical situation of the simulation changes (i.e. an ideal standing wave is forced near a thermoacoustic couple plate). Attempts to adjust the conditions of the oscillatory boundary condition to reflect the conditions of the flow field around a plate in a thermoacoustic couple, unless accurately done, will only bring complexity to the simulation model and can be avoided at the expense of additional computation. The credence of the reliability of the current simulation is enhanced by the fact that the phase shift at the center of the plate agreed well with the analytical solution for conditions where one should expect agreement.

Though specifying pressure and the velocity to be that of a standing wave is not quite accurate when a plate is introduced in the simulation domain particularly at the higher Mach number, test results in tables 7.4 and 7.5 indicate that the standing wave condition is appropriate when BC34 is specified not too close to the plate edge. (This also indicates that the energy dissipated near the plate ($\dot{E}_{plt}$) is negligible given the limited accuracy of the simulation as discussed in section 4.3.2)

When heat is transferred to the plate, an equivalent amount of energy must flow into the domain through BC34 to maintain the energy balance of the simulation domain. That energy can be in the form of a work flux which can be manifested as phase difference between the pressure and the velocity. However, if this phase difference is 90 degrees there is no work flux. Because in the current work, standing wave conditions are specified at BC34 (i.e. the first two terms of equation (2.20) are zero over a cycle), the only form of energy flux through BC34 is in the form of heat.

This suggests that the net energy flux entered into the simulation domain through BC34 in the form of heat changes into the acoustic work after entering the simulation domain to maintain the resonance which is less likely to happen.

Cao *et al.* adjusted a phase shift between the pressure and the velocity at the oscillatory boundary in an iterative manner until the correct energy balance is obtained between the heat flux at the plate and the work flux entering the right domain of the boundary. However, specifying the boundary condition differently in the present work resulted in good agreement with the results of Cao *et al.* at conditions where a valid comparison could be made (see section 7.6.3).

Given these results and noting that BC34 is specified far enough away from the plate that results are unaffected by the location of the boundary, the present method of specifying BC34 conditions is considered to be suitable for the the present simulations. It is also apparent that due to the limitation of the accuracy of simulations in the current work, it is not possible to identify the form of energy flux entering BC34.

Therefore, further investigations of the present model are an appropriate next step towards the building of a heat exchanger model.

7.7 Further investigation of the thermoacoustic couple model

In this section, the results of simulations tested in section 7.6.2 and 7.6.3 are further investigated. Particular focus is placed on the plate spacing dependency of energy exchange between the plate and the gas. These investigations give useful fundamental information for designing heat exchangers.

7.7.1 Further investigation of plate space dependency

Plate spacing is one of the crucial factors in determining the performance of heat exchangers in thermoacoustic devices. It is important to investigate the thermoacoustic effect with various plate spacings especially at smaller plate spacings that are claimed by Hofler (Swift 1994) to be more efficient for heat exchangers (see section 2.5.5).

Cao *et al.* (1996) were unable to simulate smaller plate spacings (closer to Hofler's preferred value for plate spacing in heat exchangers) since their simulations became unstable. Using PHOENICS, solutions converged at plate spacings that were as small as the thermal penetration depth.

In figure 7.21, the time averaged energy flux density at the surface of the plate showed some interesting dependency on the plate spacing, especially at the outer plate edge, that was not identified by Cao *et al.*.

In order to further investigate the space dependency of the energy flux in the current work, time averaged energy flux vectors are shown in figures 7.30 and 7.31 for spacings δ_{km}/y_0=0.3 (run 17), 1.2 (run 22) and 1.6 (run 23). The reason runs 22 and 23 were chosen is that at $\delta_{km}/y_0 = 1.2$, the characteristic result in which energy flux left the right hand end of the plate and entered into the left hand end of the plate changed to one in which energy flux entered each end of the plate.

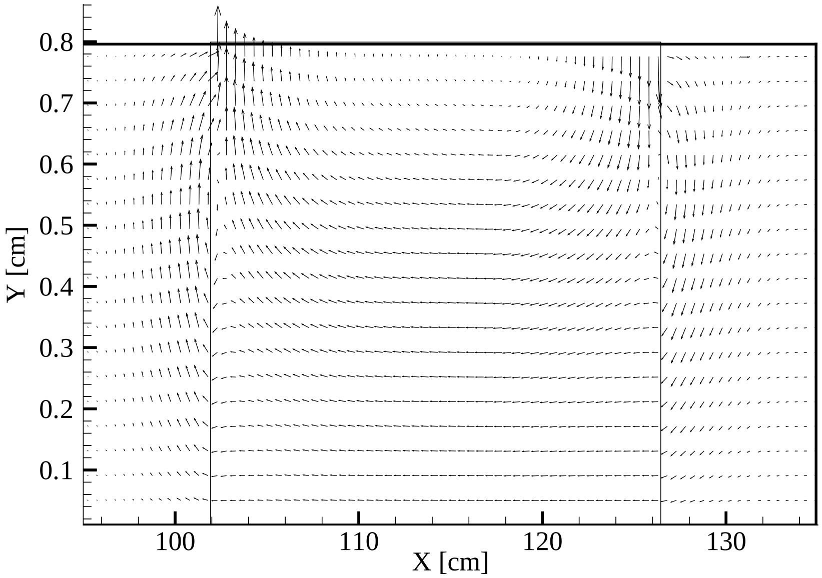

Figure 7.30: Time averaged energy flux vector when $\delta_{km}/y_0 \simeq 0.3$ (run 17). Scaling of the figure y_0/domain length in the x-direction=0.03, vector are shown only at every second cell in the x and y-directions. M=0.03.

When δ_{km}/y_0=0.3 (figure 7.30), the time averaged energy vectors leaving the plate outer edge head towards BC34 near the plate surface and turn back towards the inner plate edge at approximately the thermal penetration distance away. Energy vectors near the inner plate edge also start to point towards the plate edge at the thermal penetration depth away from the surface.

When δ_{km}/y_0=1.2 (figure 7.31(a)), the time averaged energy vectors leaving the plate outer edge start to head towards the inner plate edge soon after they leave the plate outer edge. Energy vectors near the inner plate edge also head directly towards the plate.

When δ_{km}/y_0=1.6 (figure 7.31(b)), the time averaged energy vectors at both plate edges are directed towards the plate surface and there is no cycle averaged net heat carried from the outer edge to the inner plate edge.

The mechanism of the energy transfer can be displayed more clearly by drawing energy lines which are shown in figures 7.32 and 7.33 with energy line spacing $\Delta E \simeq 3$ W. (It must

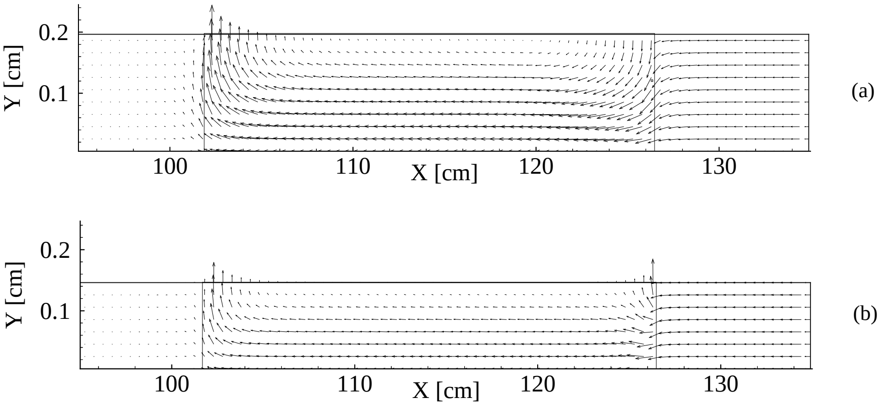

Figure 7.31: Time averaged energy flux vector when (a) $\delta_{km}/y_0 = 1.2$ (run 22), (b) $\delta_{km}/y_0 = 1.6$ (run 23). Scaling of the figure y_0/domain length in the x-direction = 0.03, vectors are shown only at every second cell in the x and y-directions. M=0.03.

be noted that an ΔE contains error of up to 20% and should be considered only a visual guide). These plots show that total energy flux leaving the outer edge of the plate and flowing into the inner edge, also reduces as the plate spacing is decreased which can be seen more clearly in the energy flux at the plate surface in figure 7.34. The figure is same as figure 7.21 except only shown on the plate surface. When δ_{km}/y_0=1.6, energy flux is into the plate at both ends. This is because, as the plate spacing is reduced, as shown in table 7.8, energy dissipation at the plate surface increases (although $\dot{S}_{gen}$ is calculated within the whole domain, all test cases showed that it concentrated near plate region).

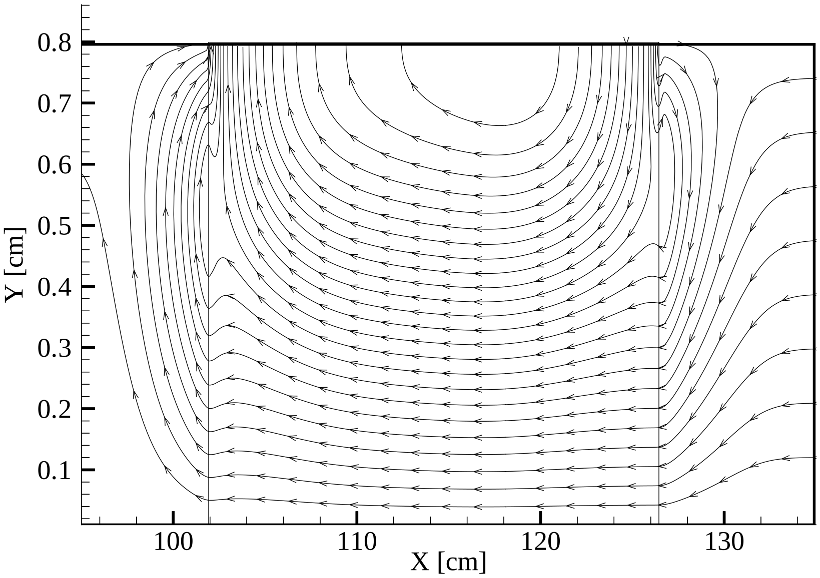

Figure 7.32: Time averaged energy lines when $\delta_{km}/y_0 = 0.3$ (run 17). M=0.03.

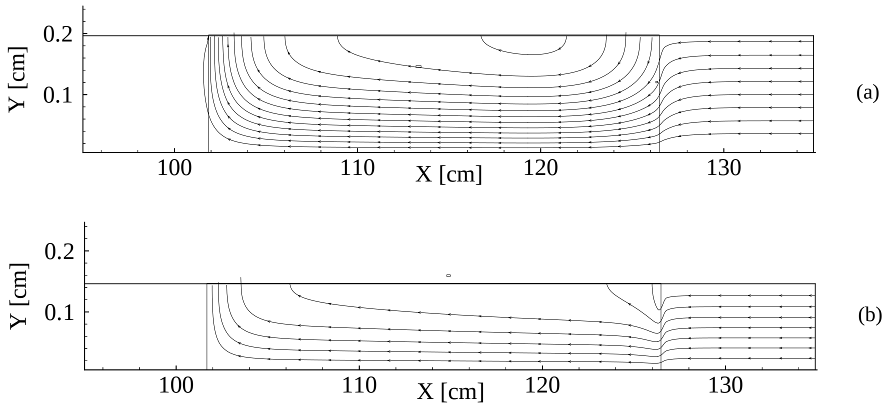

Figure 7.33: Time averaged energy lines when (a) $\delta_{km}/y_0 = 1.2$ (run 22) and (b) $\delta_{km}/y_0 = 1.6$ (run 23). M=0.03.

Figure 7.34 also shows that the width of the peak decreases as the plate spacing is reduced. This suggests that the thermal boundary layer develops more rapidly when the plate spacing is small.

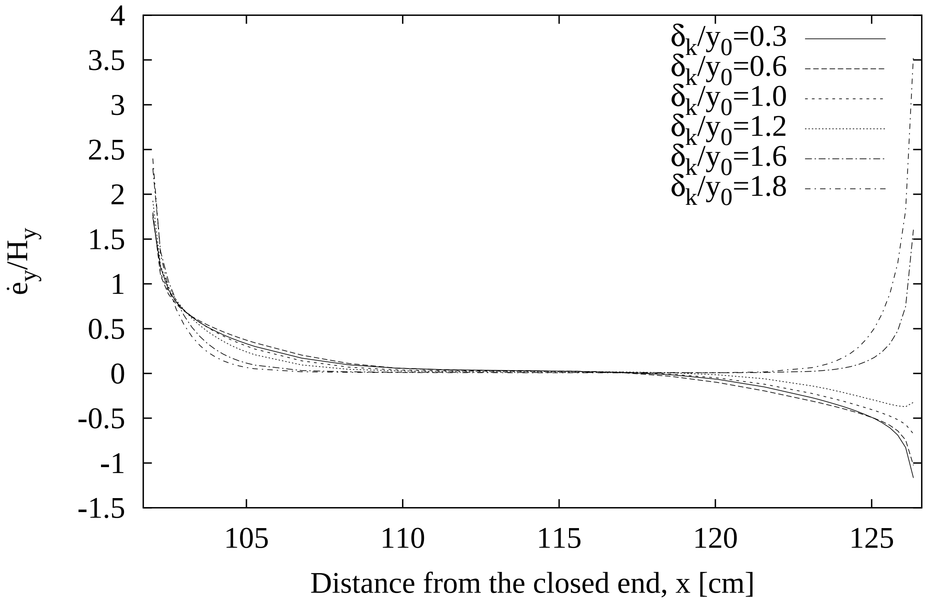

Figure 7.34: Time averaged energy flux near the plate for different plate spacings (run 17; δ_k/y_0=0.3, run 20; δ_k/y_0=0.6, run 21; δ_k/y_0=1.0, run 22; δ_k/y_0=1.2, run 23; δ_k/y_0=1.6, run 24; δ_k/y_0=1.8).

The direction of heat flux at the plate surface is reflected in the distribution of the time averaged temperature fields. Figures 7.35 and 7.36 show the time averaged temperature distributions in the x-direction at three y locations (y=0, $y_0/2$ and y_0), for plate spacings $\delta_{km}/y_0 = 0.3$ and 1.2 and $\delta_{km}/y_0 = 0.3$ and 1.6 respectively. The time averaged temper-

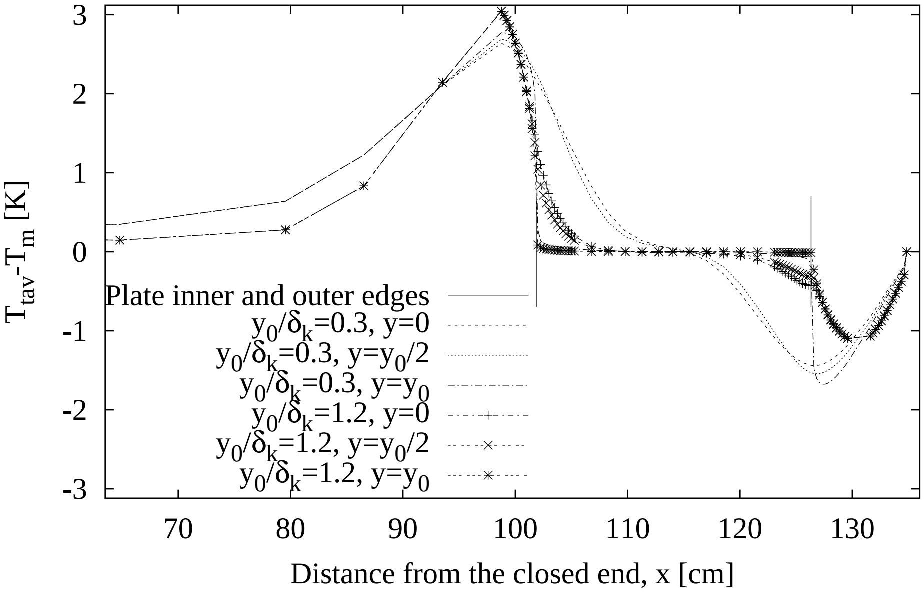

Figure 7.35: Time averaged temperature distribution in the x-direction for the various plate spacings (run 17; $\delta_{km}/y_0 = 0.3$, run 22; $\delta_{km}/y_0 = 1.2$) at three different y-locations (y=0, $y_0/2$, y_0).

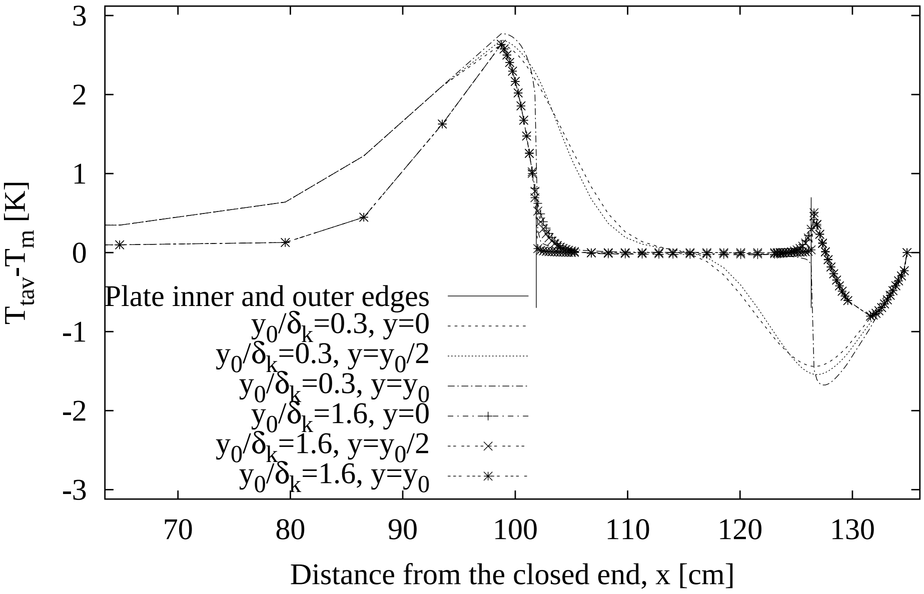

Figure 7.36: Time averaged temperature distribution in the x-direction for the various plate spacings (run 17; $\delta_{km}/y_0 = 0.3$, run 23; $\delta_{km}/y_0 = 1.6$) at three different y-locations (y=0, $y_0/2$, y_0).

ature distributions also show that, as the plate spacing is reduced, the thermal boundary layer develops more rapidly.

In order to further investigate the flow field, the instantaneous velocity fields are shown. Figures 7.37 and 7.38 show instantaneous velocity vectors at 2/8, 3/8, 4/8 and 5/8 and 6/8, 7/8, 8/8 and 1/8 of a cycle respectively when $\delta_{km}/y_0 = 0.3$ (run 17). The sequence of times was chosen in order to show the instantaneous velocity field at the time steps when velocity changes its direction on the same page.

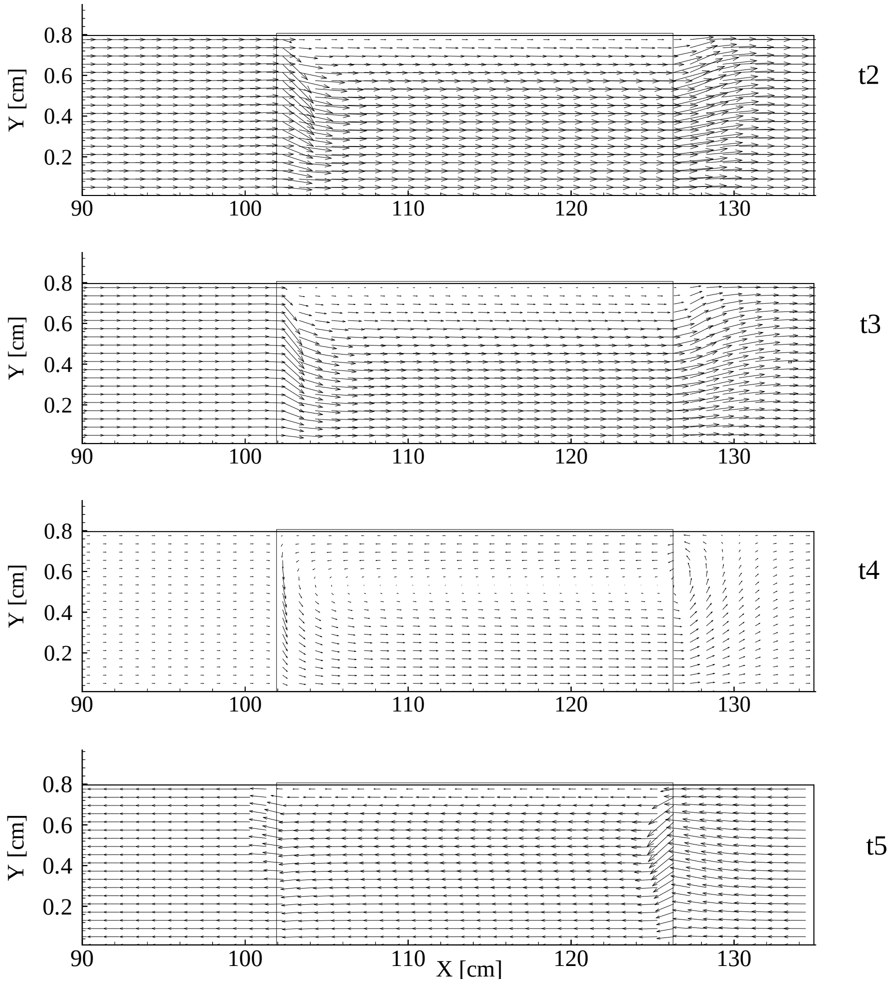

Figure 7.37: Instantaneous flow field of run 17 (δ_{km}/y_0=0.3) time steps near the first half of the cycle. (Note t2=$2\tau/8$, t3=$3\tau/8$, t4=$4\tau/8$, t5 =$5\tau/8$) Only every fourth vector is shown in the x-direction and every second in the y-direction.

Figures 7.39 and 7.40 show instantaneous velocity vectors at 2/8, 3/8, 4/8 and 5/8 and 6/8, 7/8, 8/8 and 1/8 of a cycle respectively when $\delta_{km}/y_0 = 1.2$ (run 22).

Figures 7.41 and 7.42 show instantaneous velocity vectors at 2/8, 3/8, 4/8 and 5/8 and 6/8, 7/8, 8/8 and 1/8 of a cycle respectively when $\delta_{km}/y_0 = 1.6$ (run 23).

Overall, sudden changes in the velocity profile are observed only at both edges of the plate at most time steps. The velocity profile develops more rapidly at the smaller plate

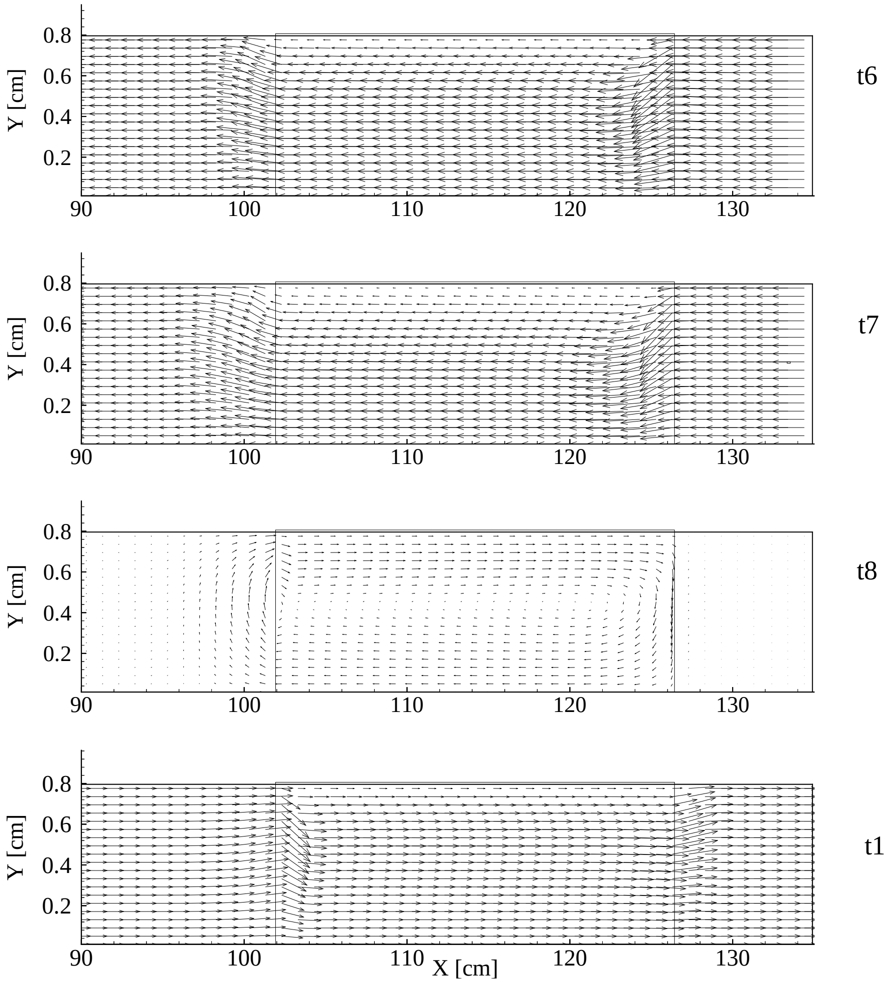

Figure 7.38: Instantaneous flow field of run 17 (δ_{km}/y_0=0.3) time steps near the end of the cycle. (Note t6=$6\tau/8$, t7=$7\tau/8$, t8=τ, t1=$\tau/8$)

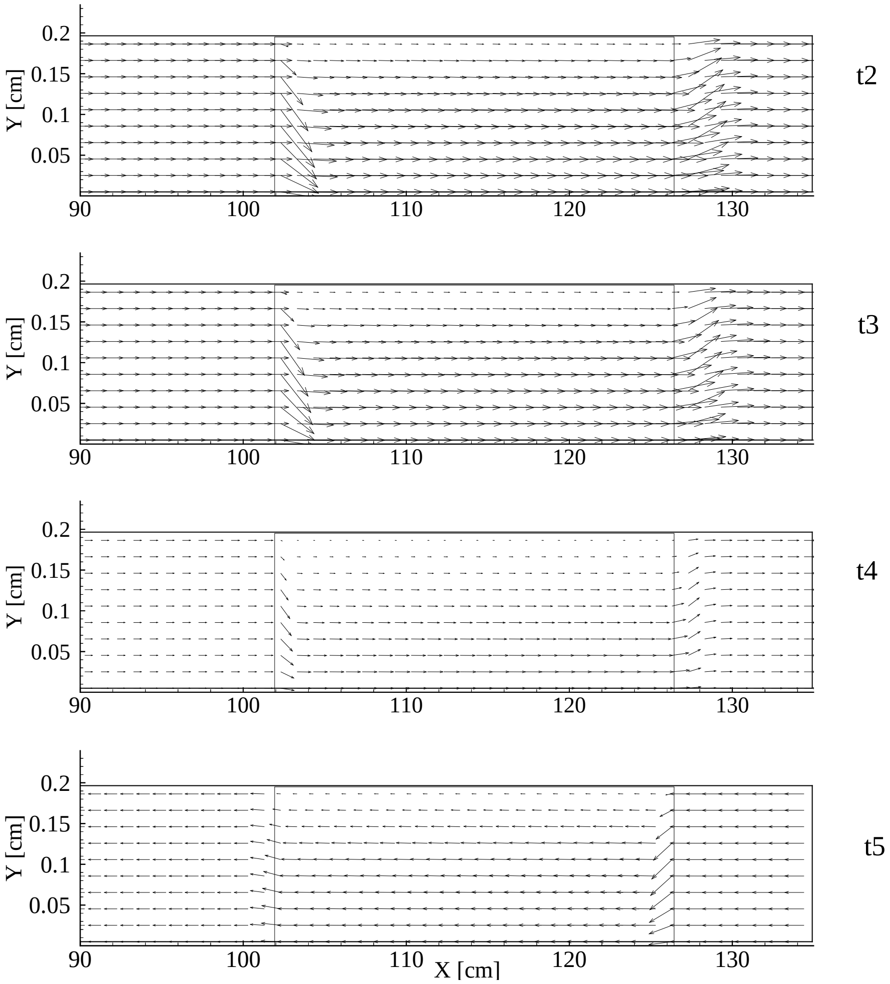

Figure 7.39: Instantaneous flow field of run 22 (δ_{km}/y_0=1.2) time steps near the first half of the cycle. (Note t2=$2\tau/8$, t3=$3\tau/8$, t4=$4\tau/8$, t5 =$5\tau/8$) Only every fourth vector is shown in the x-direction and every second in the y-direction.

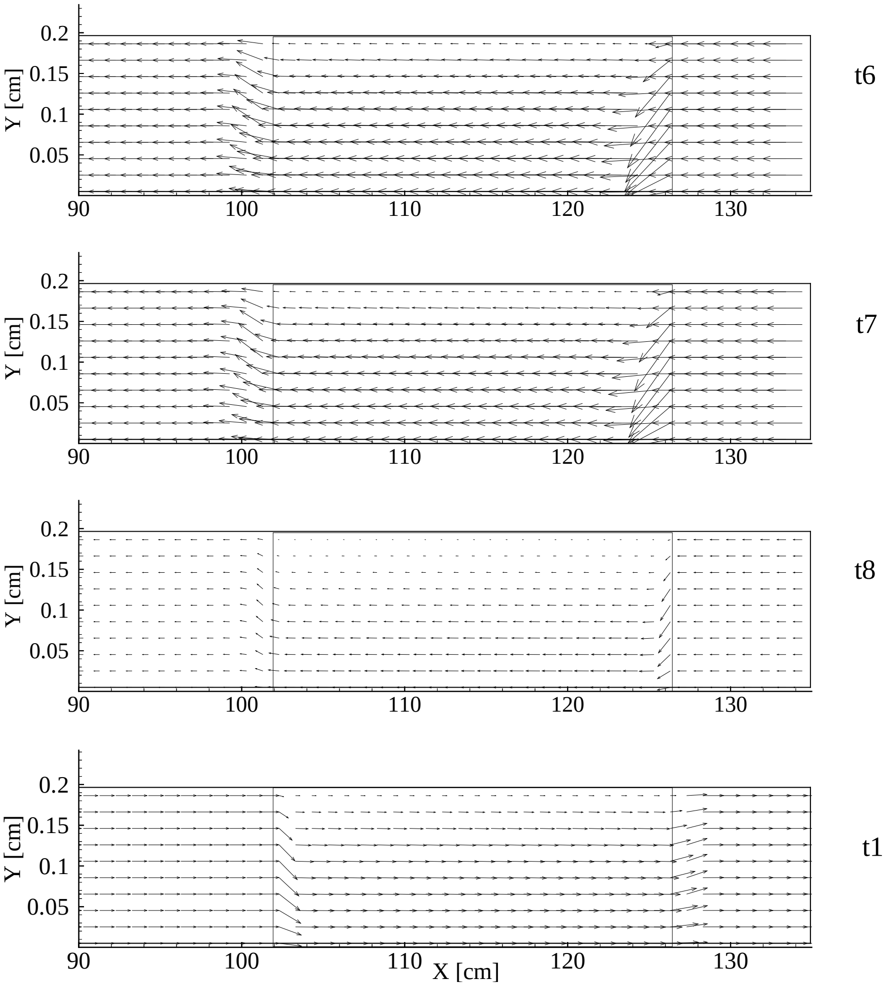

Figure 7.40: Instantaneous flow field of run 22 (δ_{km}/y_0=1.2) time steps near the end of the cycle. (Note t6=6τ/8, t7=7τ/8, t8=τ, t1=τ/8)

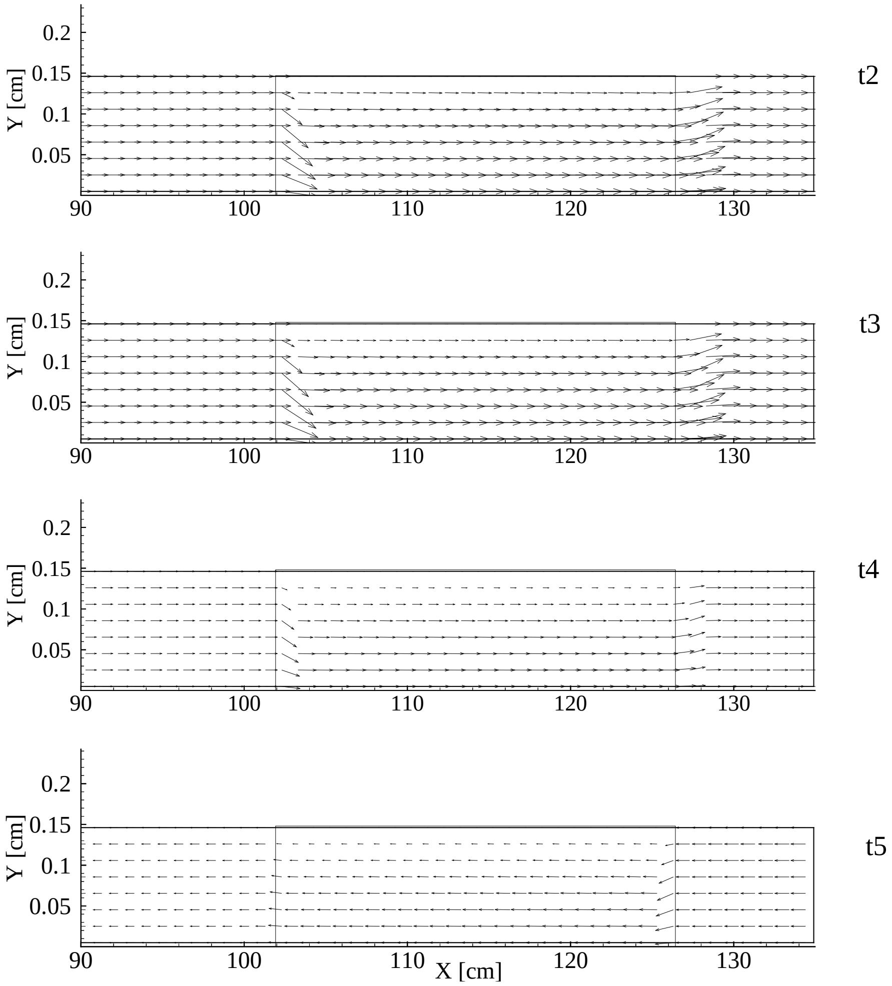

Figure 7.41: Instantaneous flow field of run 23 (δ_{km}/y_0=1.6) time steps near the first half of the cycle. (Note t2=$2\tau/8$, t3=$3\tau/8$, t4=$4\tau/8$, t5 =$5\tau/8$) Only every fourth vector is shown in the x-direction and every second in the y-direction.

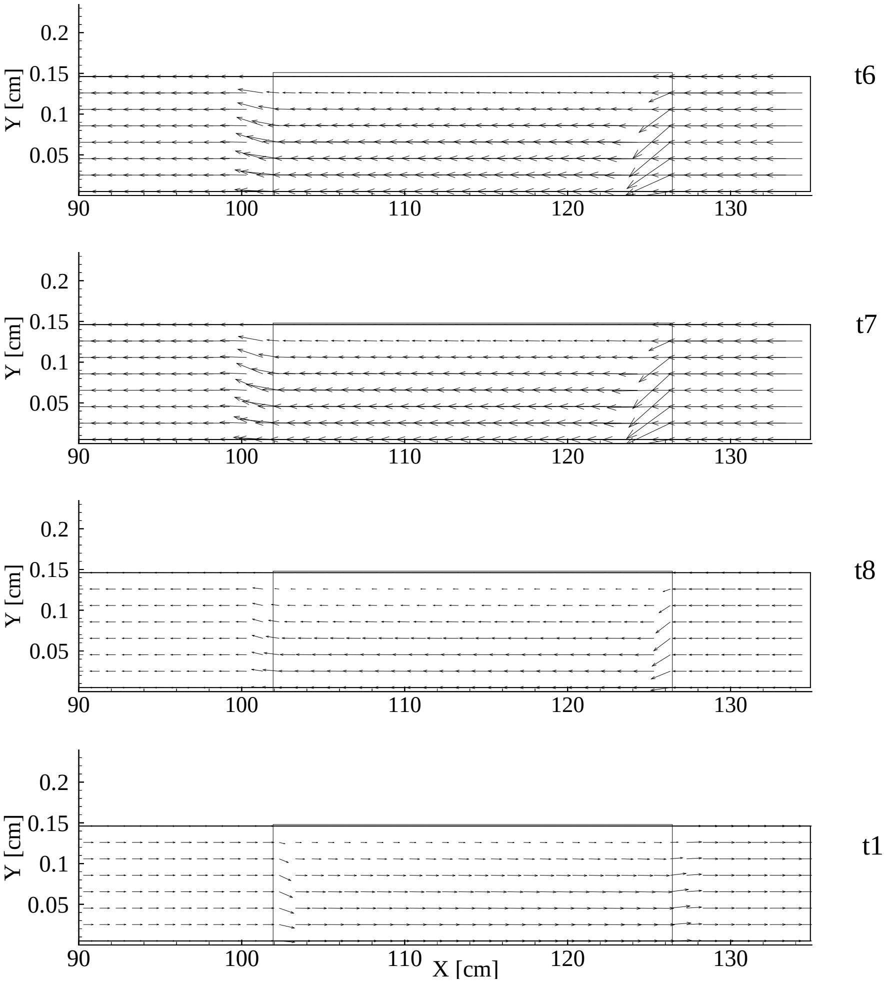

Figure 7.42: Instantaneous flow field of run 23 (δ_{km}/y_0=1.6) time steps near the end of the cycle. (Note t6=6τ/8, t7=7τ/8, t8=τ, t1=τ/8)

spacings.

When $\delta_{km}/y_0 = 0.3$, instantaneous velocity vectors at time step $t = 4\tau/8$ (when the flow changes direction), show a pattern which is characteristic of a vortical motion over the plate. At this time step, the flow near the plate and the flow near the center of the passage are in opposite directions. For the smaller plate spacing $\delta_{km}/y_0 = 1.2$ and 1.6, there is no difference of the direction of flow within the passage at any time steps shown. However, since these plots only show instantaneous vectors, particle tracking techniques must be used in order to determine whether recirculatory flow exists. The flow fields for $\delta_{km}/y_0 = 1.2$ and 1.6 are similar except that those when δ_{km}=1.6 show less y-displacement. This is not surprising as the domain height for both cases is smaller than the boundary layer thickness so viscous effects extend across the passage. For larger plate spacings, the viscous effects are confined close to the plate.

In order to check if there is vortical motion near the plate, nine particles, are tracked over two cycles at steady state using the method described in section 4.5.2. These starting points of the particles are shown in figure 4.3. The paths taken by particles 1 to 9 for runs 17, 22 and 23 are shown in figures 7.43, 7.44 and 7.45 respectively.

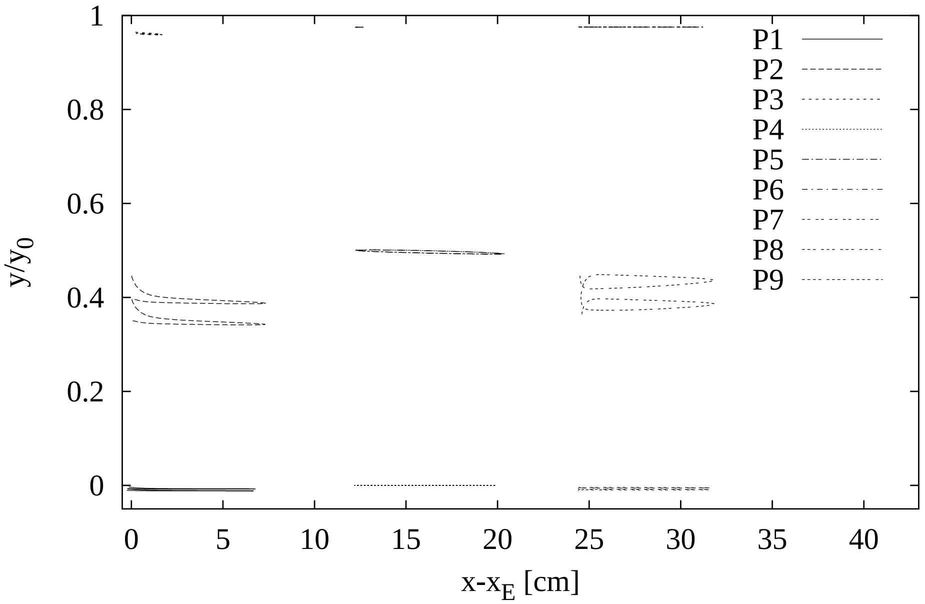

Figure 7.43: Particle path of particles 1 to 9 (P1 to P9) when $\delta_{km}/y_0 = 0.3$ (run 17).

Although there are some inevitable inaccuracies in particle tracking using this technique (see section 4.5.2), there are some obvious differences in traces for particles at different locations in the domain.

Particles 3, 6, 9 and 1, 4, 7 and 5 move mainly in the x-direction with very little y-movement, although for smaller plate spacing there is more y-movement for particles 1, 4, 7. Particles 3 and 6 travel less than a quarter of the distance of the other particles both in figure 7.43 and in figure 7.45.

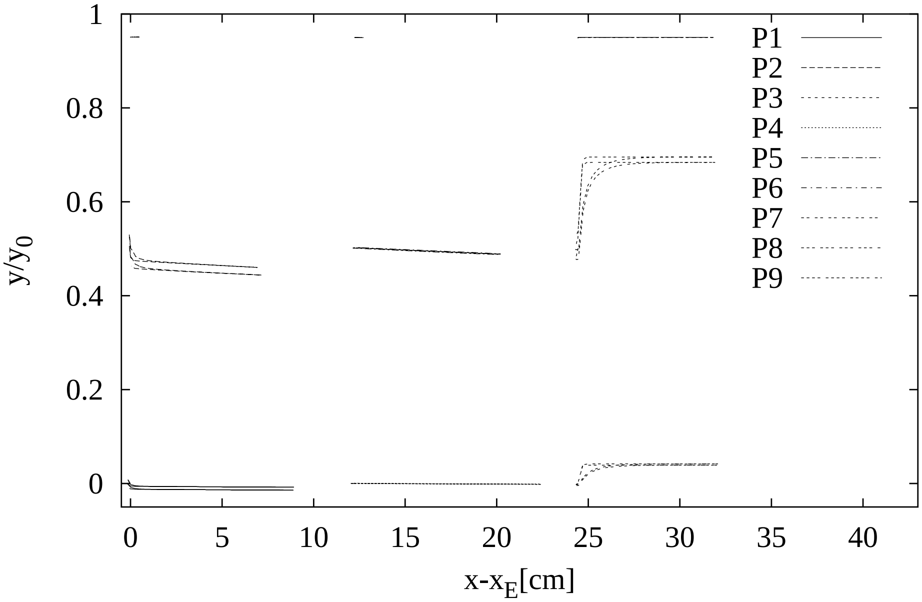

Figure 7.44: Particle path of particles 1 to 9 (P1 to P9) when $\delta_{km}/y_0 = 1.2$ (run 22).

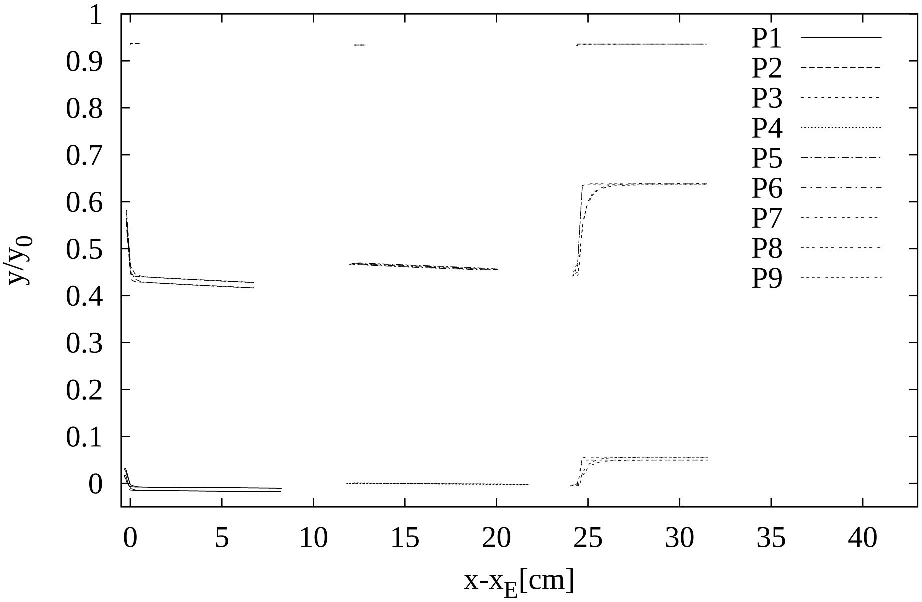

Figure 7.45: Particle path of particles 1 to 9 (P1 to P9) when $\delta_{km}/y_0 = 1.6$ (run 23).

The largest differences are found in the movement of particles 2 and 8 for the case when $\delta_{km}/y_0 = 0.3$ and $\delta_{km}/y_0 = 1.2$ and 1.6. When $\delta_{km}/y_0 = 1.2$ and 1.6, the particle traces show that particles 2 and 8 return to their original positions with error that is less than 3% and 2% of the plate spacing distance respectively.

However, when $\delta_{km}/y_0 = 0.3$, the difference between the initial and the final position is $0.05y_0$, and it is noted that y_0 is approximately five times that when $\delta_{km}/y_0 = 1.6$. The error test in section 4.5.2 using two different time steps indicated an uncertainty of $0.01y_0$. Therefore, the difference between the starting and finishing points for particle 2 and 8 when $\delta_{km}/y_0 = 0.3$ is too great to be considered as a numerical error. This indicates that over a number of cycles, particles are moving away from the plate at these locations which presumably must be compensated for by other particles to replace them from elsewhere in the domain. Therefore, one could speculate that there is a larger scale, lower frequency vortical motion just outside the plate edges.

This coincides with observation of by Ozawa *et al.* (1999). Ozawa *et al.* visualized acoustic streaming in the resonator with or without plates, at a drive ratio of 0.2%. Without plates, there are well known large scale vortices in between the pressure node and antinode due to acoustic streaming. When Ozawa introduced a single plate or a multiple layer of plates spaced much wider apart than the thermal penetration depth, he observed a large vortex at either edge of the plates for both cases. The plate lengths he used were approximately 1/10th of the wave length which is of a similar order to the plate length used in the current work. The frequency of the vortical motion was not mentioned in that work. It must be noted that the current work does not include the wall effect of the resonator in the simulation domain yet the current simulation still indicated the possibility of vortical motion just outside both edges of the plate for smaller spacings. It is suggested that more particles outside the plate should be traced in future work to clarify this point.

The appearance of vortical motion outside both edges of the plate at larger plate spacings does not coincide with the plate spacing at which the characteristic of cycle-averaged heat flux changed from being out of the plate at one end to into the plate at each end.

In order to further investigate this, more particles around the plate should be traced. Experimental results are also required to validate simulation results of the current work.

7.7.2 Entropy generation in thermoacoustic couples

In this section, the dependence of entropy generation on plate spacing and drive ratio are shown based on the test cases run in section 7.3.

Although in chapter 3 a heat exchanger design method based on second law analysis was developed for thermoacoustic engines, it is not directly applicable to thermoacoustic couples as there is no net heat flux added to or extracted from the plate. Therefore, the relationship between the results shown in this section and the parameters considered in section 3.3 will not be discussed.

In figure 7.46, the volume averaged entropy generation rates versus plate spacing (runs 17 and 20 to 24) are shown, along with the analytically calculated entropy generation rates at the plate surface. (The vertical line in the figure indicates the magnitude of the thermal penetration depth.) To calculate the volume averaged entropy generation, equation (3.8) was evaluated at each cell, multiplied by the cell volume and summed over the whole domain. The sum was then divided by the domain volume. Entropy generation at the plate surface was calculated using equation (2.39) devided by the mean temperature and was then area averaged. To be precise, the entropy generation per unit volume in figure 7.46 to 7.49 is the entropy generation over the whole simulation domain divided by the volume of the whole simulation domain. Analytically calculated entropy generation agrees with the numerical results at larger plate spacings which was expected as the analytical expression was derived based on the assumption that $y_0 >> \delta_{km}$. Entropy generation is much higher than that predicted analytically at smaller plate spacings. For all plate spacings, for all cases, the difference between the entropy generation calculated over the whole domain and that in the plate section was less than 1% .

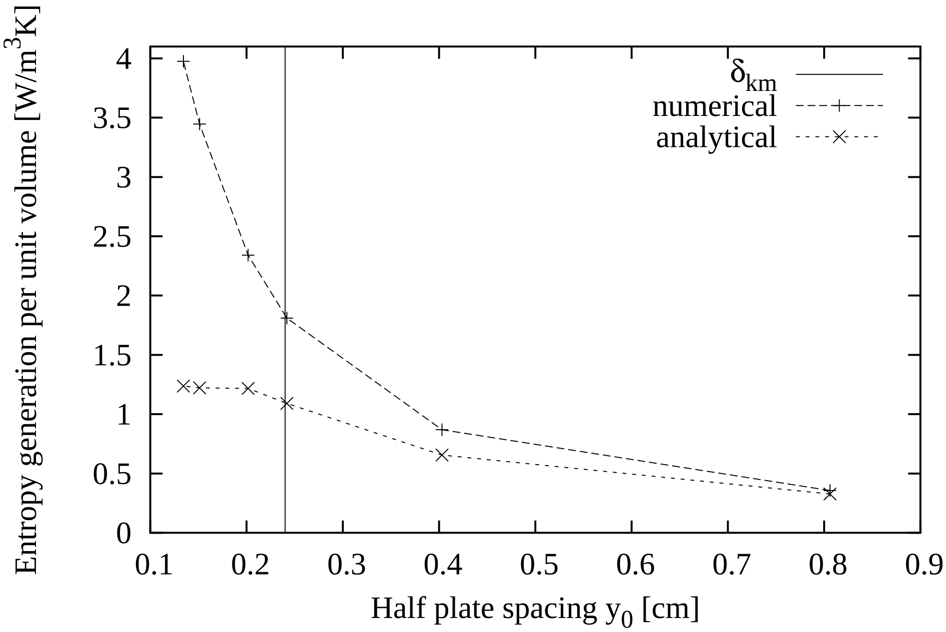

Figure 7.46: $\dot{S}_{gen}$ versus half plate spacing y_0. (run 17; y_0 $\simeq$0.81cm, run 20; y_0 $\simeq$0.41cm, run 21; y_0 $\simeq$0.24cm, run 22; y_0 $\simeq$0.20cm, run 23; y_0 $\simeq$0.15cm, run 24; y_0 $\simeq$0.13cm)

In order to investigate what physical mechanisms contribute to entropy generation, terms in equation (3.8) are grouped and labeled as follows.

- Term 1 : $\frac{K}{T^2}(\frac{\partial T}{\partial y})^2$
- Term 2 : $\frac{\mu}{T}(\frac{\partial v_x}{\partial y})^2$
- Term 3 : The reminder of the terms in equation (3.8). $\Big(\frac{K}{T^2}(\frac{\partial T}{\partial x})^2,\ -\frac{\mu}{T}\frac{2}{3}(\frac{\partial v_x}{\partial x}+\frac{\partial v_y}{\partial y})^2,$

$$\frac{2\mu}{T}((\frac{\partial v_y}{\partial y})^2 + (\frac{\partial v_x}{\partial x})^2),\ \frac{\mu}{T}((\frac{\partial v_y}{\partial x})^2 + 2\frac{\partial v_y}{\partial x}\frac{\partial v_x}{\partial y})\Big)$$

These terms are plotted for runs 17 and 20 to 24 in figure 7.47 as a function of plate spacings. Figure 7.47 shows that the dominant parameters leading to entropy generation are y gradients of temperature and y gradients in the x-component of velocity (terms 1 and 2) respectively. As expected from chapter 3, term 1, the entropy generated due to temperature gradients, increases as the plate spacing increases. Although, term 1 starts to decrease when $y_0 \geq 0.24$, term 1 integrated over the whole domain does increase as a function of plate spacings. This indicates that the rate of increase in term 1 drops when the plate spacing is larger than twice the thermal penetration depth. This can be explained by the fact that the temperature gradient is large only within the thermal boundary layer.

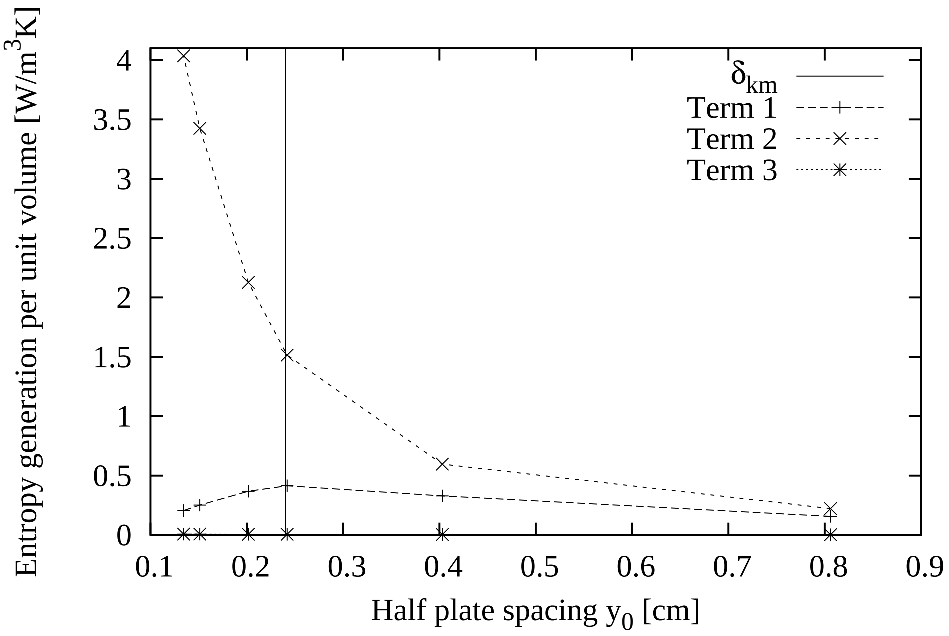

Figure 7.47: Dominant terms of $\dot{S}_{gen}$ versus y_0. (run 17; y_0 ≃0.81cm, run 20; y_0 ≃0.41cm, run 21; y_0 ≃0.24cm, run 22; y_0 ≃0.20cm, run 23; y_0 ≃0.15cm, run 24; y_0 ≃0.13cm)

Term 2, the entropy generation due to the viscous effects increases quadratically as the plate spacing is reduced.

Next, entropy generation over the whole simulation domain versus the drive ratio (or Mach number) is shown in figure 7.48 using the simulation results of runs 1 to 5 when $y_0 = 3\delta_{km}$. This quadratic dependence was expected from the fact that the dominant terms in equation (3.8) vary with the square of temperature and velocity. The analytically calculated energy dissipation at the plate surface and the numerically calculated entropy generation over the whole domain agree at all drive ratios to within approximately 10%. This indicates that most dissipation occurs at the plate surface for this plate spacing and for all drive ratios tested. Again terms 1 to 3 of equation (3.8) are plotted in figure 7.49. Again, terms 1 and 2 are dominant and the magnitudes of each increase as the drive ratio increases.

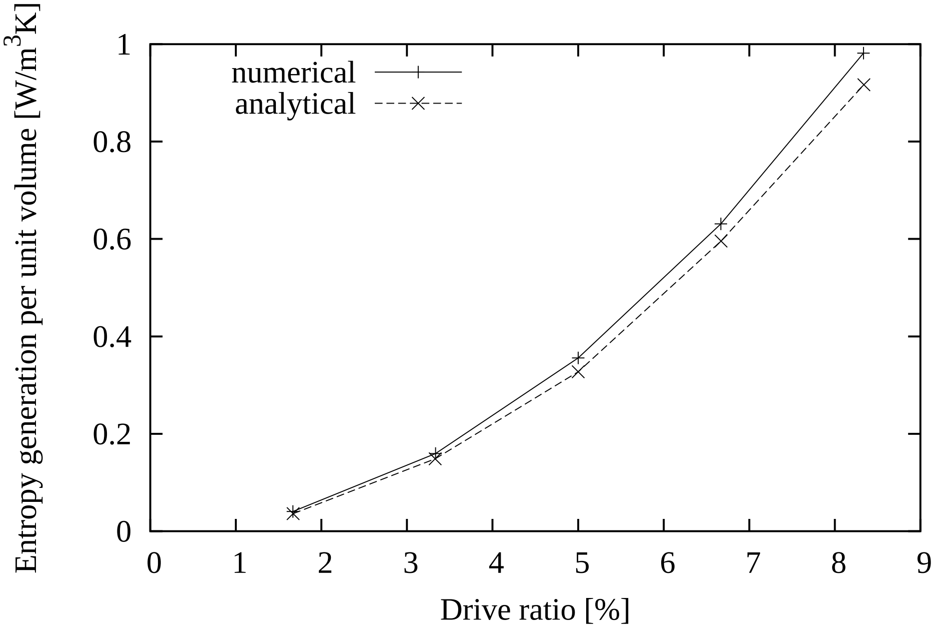

Figure 7.48: $\dot{S}_{gen}$ versus drive ratio. $\delta_{km}/y_0 = 0.3$. (run 15; Drive ratio≃1.7%, run 16; 3.4%, run 17; 5.1%, run 18; 6.8%, run 19; 8.5%)

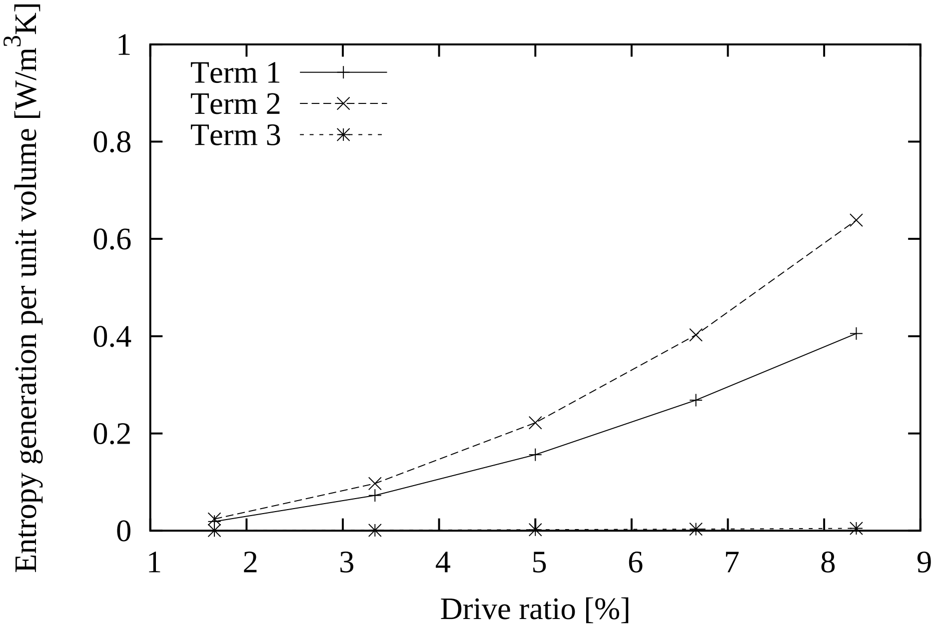

Figure 7.49: Dominant terms of $\dot{S}_{gen}$ versus the drive ratio. (run 15; Drive ratio≃1.7%, run 16; 3.4%, run 17; 5.1%, run 18; 6.8%, run 19; 8.5%)

Overall, one should observe less entropy generation per unit volume at lower Mach numbers and larger plate spacings. However, one should not simply apply this finding to the design of heat exchangers in thermoacoustic devices. This is because in a thermoacoustic couple, there is ideally no net heat transfer to or from plates. In heat exchangers in a thermoacoustic device, cycle averaged heat transfer takes place. In order to obtain the same amount of heat transfer through a heat exchanger with sparsely spaced plates that could be obtained with closely spaced plates, more surface area may be required. However, having a longer plate does not necessary increase the effective surface area for heat transfer, as most heat transfer occurs at the plate edges. The optimum plate spacings for heat exchangers will depend on the magnitude of the entropy generation due to the temperature gradient in the heat exchangers.

It would have been very useful to observe the distribution of entropy generation over the plate, however due to limited resources, these data are not available from the current work.

7.8 Summary

This chapter has demonstrated the capability of PHOENICS to simulate the thermoacoustic effect by comparing the simulation results of the current work, with first order analytical solutions and the simulation results of Cao *et al.* (1996).

However, comparisons have indicated some issues with the oscillatory boundary conditions of both the current work and that of Cao *et al.* (1996).

In the current work, it has been shown that in order to accurately simulate a thermoacoustic couple in a standing wave, oscillatory boundary conditions must be specified at least a few times the particle displacement distance away from the plates. When Cao *et al.* specify the oscillatory boundary conditions close to the plate edge, they introduce a traveling wave component into the oscillatory boundary to account for the way in which the plates affect the flow field. However, the fact that they did not consider the y-direction and the time dependence of the flow field raise questions about the accuracy of their simulations.

The current work did not consider such an adjustment but investigated the validity of the simulation when a standing wave boundary conditions are applied at the oscillatory boundary. The purpose of the current work was ultimately to simulate heat exchanger plates next to a regenerator. Oscillatory boundary conditions considered to simulate heat exchangers in thermoacoustic engines are tested in the next chapter.

Having specified the oscillatory boundary far enough away from the plates that specifying them further away did not affect the results, simulations were carried out at various plate spacings and Mach numbers. The simulation results were investigated using various data such as the y-component of the energy flux density (both instantaneous values and values time averaged at the plate surface), time averaged energy vectors, instantaneous velocity fields, time averaged temperature fields, entropy generation rates and the particle traces.

The time averaged energy flux at the plate surface showed that there was significant time averaged heat transfer only within the particle displacement distance of the ends of the plates. Therefore, as the Mach number was increased and the particle displacement distance increased, the width of the region where the net energy transfer is seen increased. Entropy generation increased quadratically with an increasing Mach number.

As the plate spacing is reduced, both the thermal and the viscous boundary layers develop more rapidly at the plate edges. It was also observed that energy dissipation increased rapidly as the plate spacing was reduced.

At larger plate spacings, there was an indication of larger scale vortical motion outside the plate edges. However, in order to confirm this, more particles need to be considered.

The findings in this chapter give some qualitative indications to the design of heat exchangers in thermoacoustic engines.

Chapter 8

Simulation of heat exchangers

8.1 Introduction

There are no numerical simulations of heat exchangers in thermoacoustic devices reported in the literature. In this chapter a first attempt at doing such simulations is reported. The thermoacoustic couple simulations presented in chapter 7 provide some important insight into what will be required in order to simulate heat exchangers in thermoacoustic engines. They also indicate some of the problems that are likely to be encountered.

Before going on to simulate heat exchangers, there are a number of additional tests with thermoacoustic couples which are instructive.

As a first step towards simulation of heat exchangers in thermoacoustic engines, the thermoacoustic couple is considered again. The length of the plates in the couple is made very short, of the order of the particle displacement distance, which is the typical plate length of heat exchangers in existing thermoacoustic engines. This leads to some interesting effects, such as particle traces for particles near the plates moving in loop for thermoacoustic couples with very short plates.

Simulations under operating conditions that are closer to existing thermoacoustic engines are also tested.

Then the oscillatory boundary conditions presented in chapter 5 for simulating heat exchanger plates which are of varying complexity are tested. In terms of energy balance error in the simulation domain, results indicate that only one of these boundary conditions may be suitable for simulation of heat exchangers but only for a limited number of operating conditions. However, inspection of time averaged energy vector indicate a lack of convergence near the open boundary. This suggest that even this boundary condition was not suitable. Further studies are required to improve this type of simulation and this is discussed further in chapter 9.

8.2 Preliminary tests for the heat exchanger simulations based on thermoacoustic couple simulations

8.2.1 Plate length tests

The lengths of heat exchanger plates (in the x-direction) for thermoacoustic engines are conventionally suggested to be set to the particle displacement distance, $2u_1/\omega$. This proposal is based on the description of the heat exchange mechanism as a gas parcel oscillates between the heat exchanger and the edge of the regenerator, as described in Swift (1988). (See section 2.5.5 for more details.) It has been considered that heat exchanger plate lengths should not be longer than $2u_1/\omega$ (to avoid thermoacoustic effects) nor shorter than this length (to avoid a gas parcel passing over the heat exchanger plate without rejecting heat). However, in reality, the gas cannot be discretized as a gas parcel, and one would expect that there would be thermoacoustic effects occurring even on very short plates. It is also expected that there will be further errors in simulations of heat transfer over a plate that is as short as the particle displacement distance, merely due to the fact that the number of cells over the plate is restricted by the simulation time and their accuracy.

The purpose of this section is first to test the validity and the accuracy of short plate simulations when the number of cells over the plate in the x-direction is constrained by the simulation time. This is done in subsection 8.2.1.1. Then in subsection 8.2.1.2, thermoacoustic effects over short plates are investigated.

Simulations performed in this section are for plates of length u_1/ω and $2u_1/\omega$ for half plate spacings of $3.3\delta_{km}$, $\delta_{km}/2$ and $\delta_{km}/3$. The operating conditions considered are similar to those of case 1 of table 7.1. An ideal standing wave boundary condition is applied about four times the particle displacement distance away from the plate outer edge. Tests in chapter 7 indicated that this was far enough away from the plates for the results to be unaffected by the location of the oscillatory boundary conditions.

8.2.1.1 Grid size test

The grid size in the x-direction was varied for the case when the plate length is $2u_1/\omega$ and the plate half spacing is $3.3\delta_{km}$. They were tested at Courant numbers of 0.24, 0.16 and 0.08 with the time step, Δt=0.28%. The results of simulations are listed in table 8.1. Cases 2 to 4 are simulations when the plate length is $2u_1/\omega$ and case 1 is when the plate length is u_1/ω. The grid sizes used for case 4 are the same as those used to simulate run 10 in section 7.5.1. The plate lengths are approximately 1/10 of those used in section 7.5.1 and if we use the same grid size in the x-direction (Δx), there will only be a small number of grid points on the plate.

Tables 8.1 indicate that the simulation errors (based on the energy balance, $\dot{Q}_{Error}$) are all less than 0.5% and simulation is considered valid by the criterion proposed in

Case		1	2	3	4
Plate length		u_1/ω	$2u_1/\omega$	$2u_1/\omega$	$2u_1/\omega$
Courant no.		0.24	0.24	0.16	0.08
$\Delta p_{cy}/P_A$	[%]	6.6e-3	6.1e-3	5.9e-3	1.2e-2
$\Delta u_{cy}/u_A$	[%]	1.2e-2	1.1e-2	9.6e-2	1.7e-2
$\Delta T_{cy}/T_A$	[%]	6.0e-2	4.5e-2	4.5e-2	4.2e-2
$\Delta \rho_{cy}/\rho_A$	[%]	4.1e-2	3.2e-2	3.0e-2	3.3e-2
$\Delta Tb_{cy}/T_A$	[%]	2.9e-2	3.2e-2	3.1e-2	3.4e-2
u_{err}/u_A	[%]	4.0e0	2.4e0	2.4e0	2.5e0
T_{err}/T_A	[%]	2.0e1	1.9e1	1.8e1	1.4e1
$\dot{E}y_{pl}$	[W]	-7.4e-3	2.2e-3	3.9e-3	-1.1e-3
$\dot{E}x_{cen}$	[W]	-2.3e-2	-2.3e-2	-2.3e-2	-2.3e-2
$\dot{E}x_{BC34}$	[W]	-3.3e-2	-3.7e-2	-3.7e-2	-3.7e-2
q_A	[W]	3.7e-2	4.2e-2	3.5e-2	2.6e-2
ex_{ABC34}	[W/m^2]	8.8e2	8.8e2	8.8e2	8.8e2
H_x	[W/m^2]	-9.6e2	-9.6e2	-9.6e2	-9.6e2
H_y	[W/m^2]	-5.4e1	-5.5e1	5.4e1	-5.4e1
$\dot{Q}_{Error}$	[%]	2.3e-1	1.5e-1	1.3e-1	2.0e-1
$\dot{E}_{diss}pl$	[W]	5.4e-3	1.1e-2	1.1e-2	1.1e-2
$\dot{S}_{gen}T_0$	[W]	6.8e-3	1.2e-2	1.2e-2	1.3e-2
$\Delta P_A/P_A$	[%]	7.6e0	7.4e0	7.4e0	7.5e0
Cycles		40	54	51	44
$\Delta x/\lambda$		8.2e-5	8.2e-5	1.2e-4	2.5e-4

Table 8.1: Short plate tests with operating conditions similar to case 1 in table 7.1 (M=0.01, P_m=1.0E4Pa, f=100Hz, T_m=300K). Δt=0.28%, $y_0=3.3\delta_{km}$, δ_{km}=0.24cm, $\Delta y/\delta_{km}$ = 8.3e-2.

section 4.3.2.

By inspecting the table, it can be seen that cycle averaged energy flux at the plate surface, $\dot{E}y_{pl}$, for all grid sizes (for cases 2 to 4) is 'near zero'. (For example, for case 3, $\dot{E}y_{pl}$, the cycle averaged energy flux at the plate surface is approximately 0.05% of the maximum amplitude of the fluctuating energy flux within the domain.)

In order to view the differences in results between each grid size (cases 2 to 4), time and area averaged energy fluxes at the plate surface, $\dot{e}_y$, for cases 2 to 4 are shown in figure 8.1. (A detailed description of this curve is in given in section 8.2.1.2.) Although all the curves do not coincide and the height and the width of peaks are different, there is no characteristic difference in the distribution of energy flux density at the plate surface. In addition, the differences in $\dot{E}y_{pl}$, the integral of each of the curves over the plate, are less than 1% of the maximum amplitude of energy flux in the simulation domain. The results for Courant number of 0.16 and 0.24 are very similar over most of the plate with the major difference occurring near the edges of the plate. As discussed in section 7.5.1, the peak height is not a good indicator because the results are not at the same x-locations. It is concluded that a Courant number of 0.16 is close to the value required for independence at this condition. However this comes at the expense of large computation times.

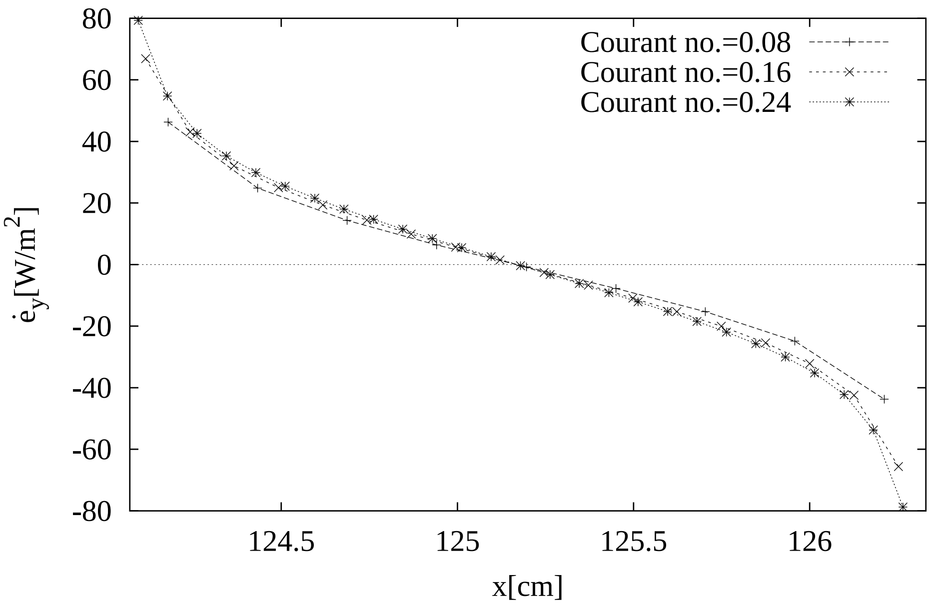

Figure 8.1: Time and area averaged energy flux (y-component) at the surface of the plate for various Courant numbers. $L{=}2u_1/\omega$, $y_0{=}3.3\delta_{km}$ (case 2; Courant no.=0.24, case 3; Courant no.=0.16, case 4; Courant no.=0.08)

Due to the limitation of computational resources, subsequent tests from section 8.2.2 were limited to a Courant number of 0.08 ($\Delta x/\lambda{=}2.54 \times 10^{-4}$) even though for this level of Courant number $\dot{e}_y$ still show some grid size dependence. Therefore, the results in section 8.2.2 should be interpreted qualitatively rather than quantitatively. (Only in the tests in section 8.2.1.2 the finest grid, $\Delta x/\lambda$=8.2e-5 is used for further investigations.)

8.2.1.2 Thermoacoustic effects on short plates

In this section, the short plate simulations of section 8.2.1.1 are further investigated along with the simulation results for a very small plate spacing.

Simulation results for the cases when the plate lengths are u_1/ω and $2u_1/\omega$ and the plate half spacings are $\delta_{km}/2$ and $\delta_{km}/3$ are listed in table 8.2.

Case		5	6	7	8
Plate length		u_1/ω	$2u_1/\omega$	u_1/ω	$2u_1/\omega$
y_0		$\delta_{km}/2$	$\delta_{km}/2$	$\delta_{km}/3$	$\delta_{km}/3$
$\Delta p_{cy}/P_A$	[%]	1.2e-2	1.2e-2	1.1e-2	7.8e-2
$\Delta u_{cy}/u_A$	[%]	2.1e-2	2.2e-2	2.0e-2	1.3e-2
$\Delta T_{cy}/T_A$	[%]	5.9e-2	5.0e-2	7.0e-2	5.5e-2
$\Delta \rho_{cy}/\rho_A$	[%]	4.2e-2	3.6e-2	5.0e-2	3.9e-2
$\Delta Tb_{cy}/T_A$	[%]	3.8e-2	4.0e-2	3.8e-2	4.0e-2
u_{err}/u_A	[%]	2.5e0	3.6e0	3.8e0	6.7e0
T_{err}/T_A	[%]	1.4e0	2.4e-1	1.4e-1	1.3e-1
$\dot{E}y_{pl}$	[W]	1.0e-2	2.4e-2	1.9e-2	3.8e-2
$\dot{E}x_{cen}$	[W]	-3.5e-3	-3.5e-3	2.3e-3	2.3e-3
$\dot{E}x_{BC34}$	[W]	-1.3e-2	-2.0e-2	-1.5e-2	-2.5e-2
q_A	[W]	2.0e-2	2.0e-2	1.7e-2	1.8e-2
ex_{ABC34}	[W/m^2]	8.8e2	8.7e2	8.7e2	8.6e2
H_x	[W/m^2]	-3.6e3	-3.6e3	-7.8e3	-7.9e3
H_y	[W/m^2]	-8.8e0	-8.9e0	-2.7e0	2.7e0
$\dot{Q}_{Error}$	[%]	4.8e-2	9.2e-2	6.1e-3	1.9e-2
$\dot{E}_{diss}pl$	[W]	3.0e-3	6.0e-3	2.0e-3	4.0e-3
$\dot{S}_{gen}T_0$	[W]	1.5e-2	3.0e-2	2.3e-2	4.4e-2
$\Delta P_A/P_A$	[%]	6.1e0	4.6e0	4.6e0	2.7e0
Cycles		51	60	46	52
$\Delta y/\delta_{km}$		4.2e-2	4.2e-2	2.8e-2	2.8e-2

Table 8.2: Short plate tests with operating conditions similar to case 1 in table 7.1 (M=0.01, P_m=1.0E4Pa, f=100Hz, T_m=300K). Δt=0.28%, $\Delta x/\lambda$=8.2e-5, δ_{km}=0.24cm.

Energy balance errors, $\dot{Q}_{Error}$, for all cases are less than 0.1%. Overall, energy balance errors are considerably smaller than those for the long plate simulations. The reason is that the energy being dissipated at the plate surface is an order of magnitude smaller than that for the long plate while the maximum amplitude of the energy flux is the same. As a consequence, the relative difference between $\dot{E}x_{BC34}$ and $\dot{E}y_{pl}$ is smaller.

The energy dissipation, given by $\dot{S}_{gen}T_0$, for run 3 in table 7.4 was approximately ten times that for case 2, where the testing plate length was 11 times longer. For the smaller plate spacing test (y_0=$\delta_{km}/2$, case 6), when the plate length was increased by ten times (see run 29 in table B.2 of appendix B for detailed results), the energy dissipation was greater approximately by eight times. These suggest that the energy dissipation in the domain is approximately proportional to the surface area of the plate.

In order to view the heat pumping effect on the short plates, the time averaged heat flux at the plate surface, $\dot{e}_y$ is plotted in figure 8.2 for both plate lengths when $y_0 = 3.3\delta_{km}$. The simulation domain in the x-direction is normalized by the plate length. The figure shows that the heat transfer is in opposite directions at the inner and outer plate edges. This indicates that heat is pumped from the outer edge to the inner edge of the plate. The shapes of the curves are very similar to those for the long plates, such as that in figure 7.17, except that for the short plates, there is no flat region (where $\dot{e}_y$ is near zero) in the curve.

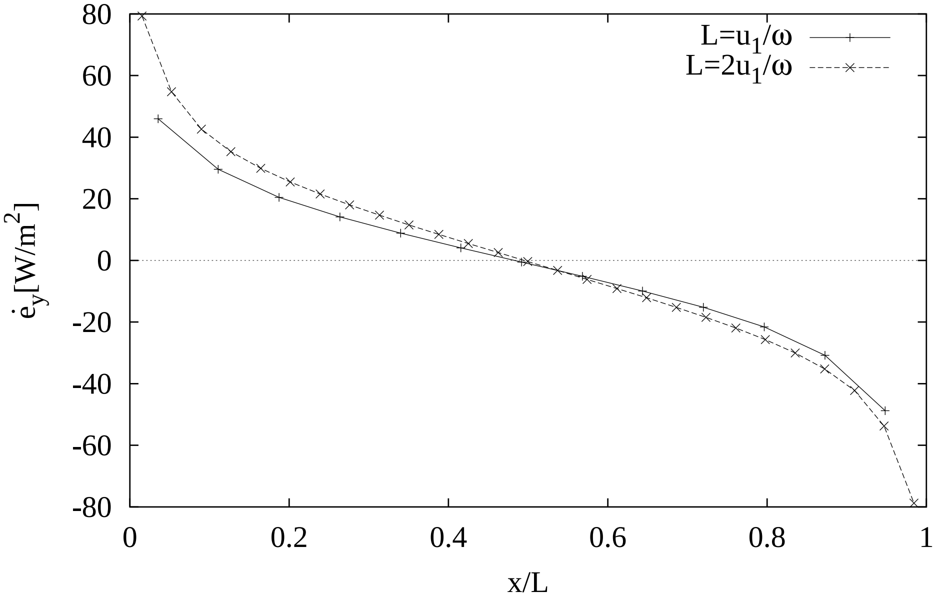

Figure 8.2: Time averaged energy flux density in the y-direction at the surface of the short plates when $y_0 = 3.3\delta_{km}$. (case 1; L=u_1/ω, case 2; L=$2u_1/\omega$)

The time averaged energy flux pumped from the outer to the inner end of the plate is approximately proportional to the plate length. It is interesting to compare the cycle averaged energy flux into the plate for the different plate length. Results showing this are presented in figure 8.3. For the longest plate (case 1 of chapter 7), the results is shown only at the outer end of the plate. The figure shows that the distance from the plate edge where significant heat transfer occurs is approximately the particle displacement distance. For the operating conditions tested, this suggests that when the plate is more than four times longer than the particle displacement distance, the net amount of heat transfer from one end of the plate to the other is equal if the plate spacings are the same. This is speculated to apply to test cases with various Mach numbers, given the fact that the distance from the plate edge where the significant heat transfer occurs was proportional to the Mach numbers. (See figure 7.24 in section 7.6.3.)

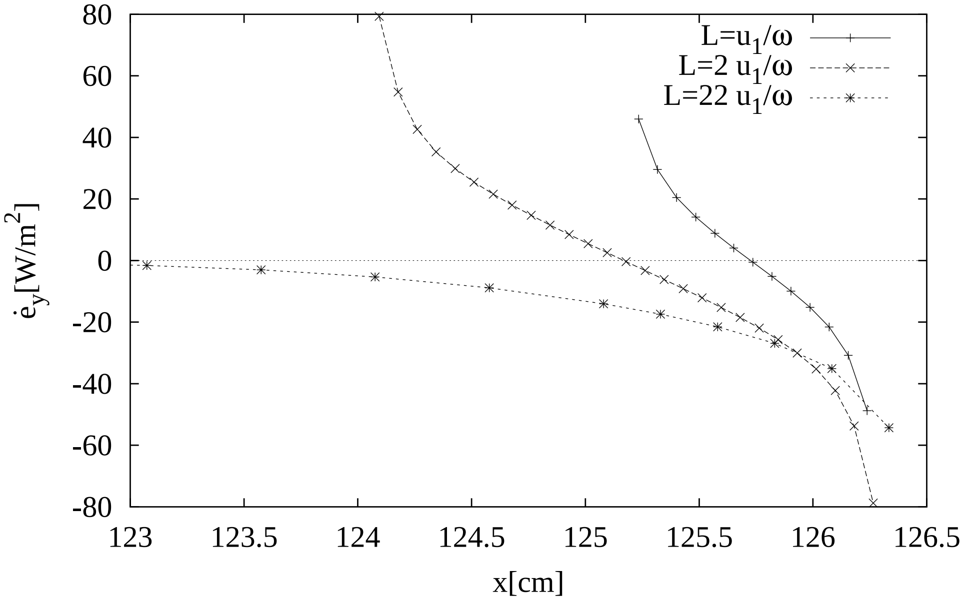

Figure 8.3: Time averaged energy flux (y-component) at the outer edge of the plate for three different plate lengths (case 1; $L{=}u_1/\omega$, case 2; $L{=}2u_1/\omega$, and run 3 of table 7.4; $L{=}22u_1/\omega$). $y_0{=}3.3\delta_{km}$, $2u_1/\omega{=}2.3$cm. The outer edges of all plates are at $x{\simeq}126.2$cm. The inner edges of the plates are at $x{\simeq}125.2$, 124.2 and 101.2cm respectively.

In order to display the heat pumping effect, the energy lines for the short plates (of lengths u_1/ω and $2u_1/\omega$) are shown in figures 8.4 and 8.5. The energy flux passing between subsequent energy flow lines, ΔE, is approximately 0.12W. The figure shows that there is energy flow into the domain through the right boundary and that less than 10% of this goes to the plate and the rest leaves the domain through the left boundary.

The approximate ratio of the magnitude of energy flux passing through the domain from right to left to the energy flux pumped from the outer to the inner edge of the plate is 1:2 when u_1/ω and 1:4 when $2u_1/\omega$. Although the amount of energy flux passing through the domain seems significant, the actual amount of the energy is less that 0.5% of the maximum fluctuating amplitude of the energy flux in the domain.

The dense spiral in figure 8.4 indicates an energy sink in that region. This clearly does not reflect the physical reality and is attributed to the accuracy limitations of the plotting package being used.

In order to compare the actual particle displacement distance with the plate length for cases 1 and 2, nine particles in the plate section were traced over a cycle at steady state. The resulting particle traces are shown in figures 8.6 and 8.7. The starting positions for

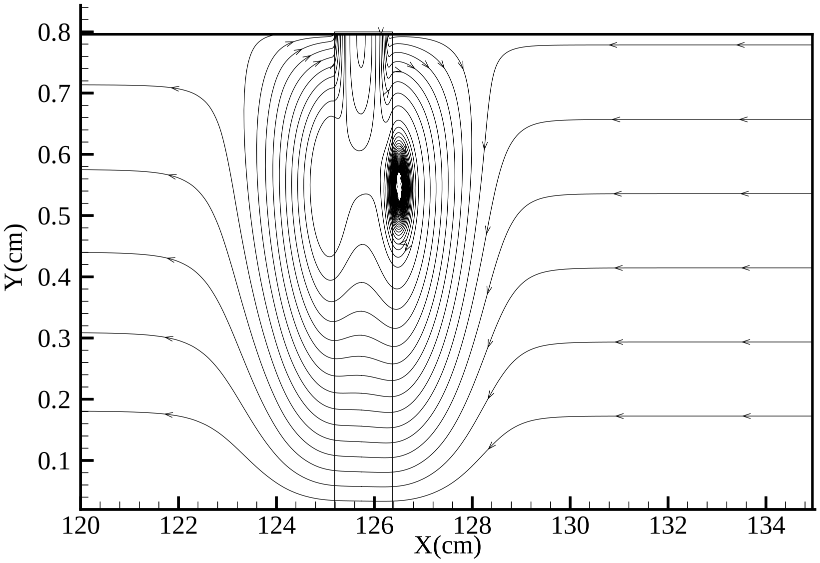

Figure 8.4: Time averaged energy line for case 1 when $L = u_1/\omega$.

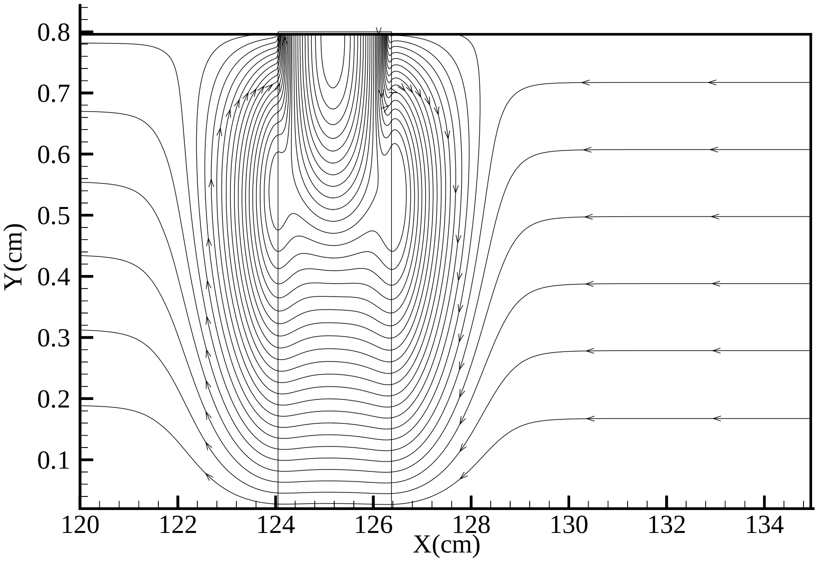

Figure 8.5: Time averaged energy lines for case 2 when $L = 2u_1/\omega$.

the particles are as described in section 4.5.2.

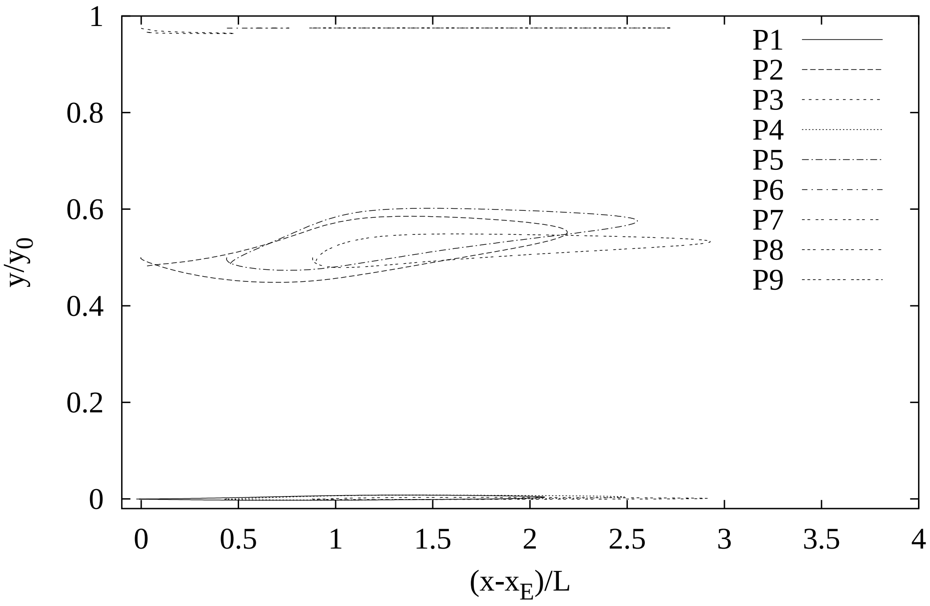

Figure 8.6: Particle trace of 9 particles over the plate for case 1 where $L = u_1/\omega$.

The results indicate that the particle displacements are twice the plate length in figure 8.6 and the same as the plate length in figure 8.7. These are in good agreement with the preliminary estimates of particle displacement distance which were calculated for the ideal standing wave at the same location.

The figures also show that particles 2, 5 and 8 (those at a quarter of the inter-plate spacing) have a large y-movement drawing loops.

The maximum difference between the initial and the final locations are approximately 2% of the y-domain length and given the accuracy of the particle trace (see section 4.5.2), the fact that particles 2, 5 and 8 of figure 8.6 and 8.7 do not return to their original positions is again an indication of a possible vortical motion outside the plate edge. However, there is no experimental data to show such a vortical motion outside the short plates.

With the long plate test in section 7.7.1, the heat pumping effect from the outer to the inner edge of the plate disappeared when the plate spacing was reduced to $y_0 = \delta_{km}/2$. In order to test if this also applies to the short plates, a plate spacing of $y_0 = \delta_{km}/2$ was tested for short plates (u_1/ω and $2u_1/\omega$). The results are listed in table 8.2 as cases 5 and 6.

The time averaged heat flux to the plates presented in figure 8.8 shows that a heat pumping effect exist at the plate surface even though the plate spacing is equal to the thermal penetration depth. The figure also suggest that at this plate spacing and length, the net amount of heat pumped is determined merely by the size of the plate surface area.

When the plate spacing was further reduced to y_0=$\delta_{km}/3$, the time averaged energy

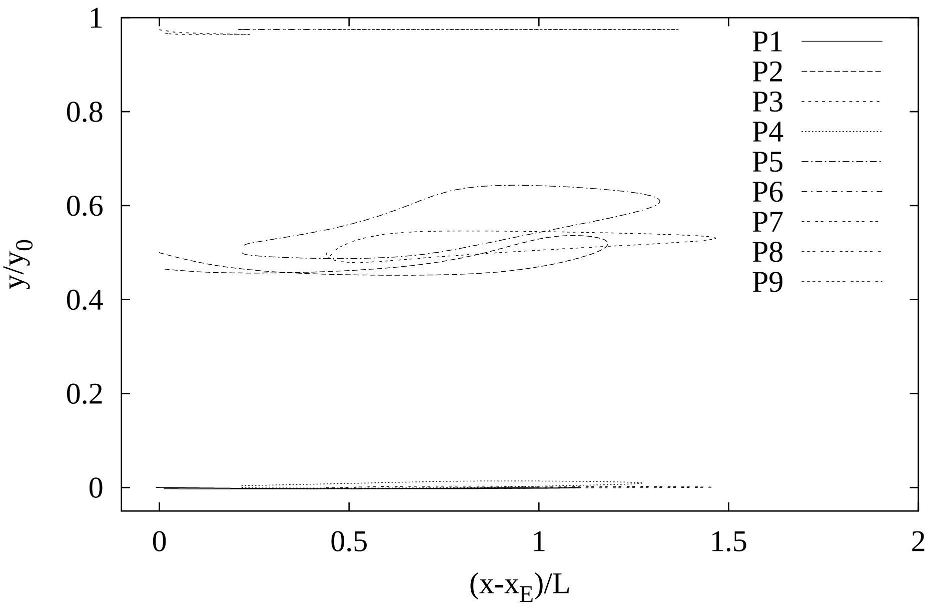

Figure 8.7: Particle trace of 9 particles over the plate for case 2 where $L = 2u_1/\omega$.

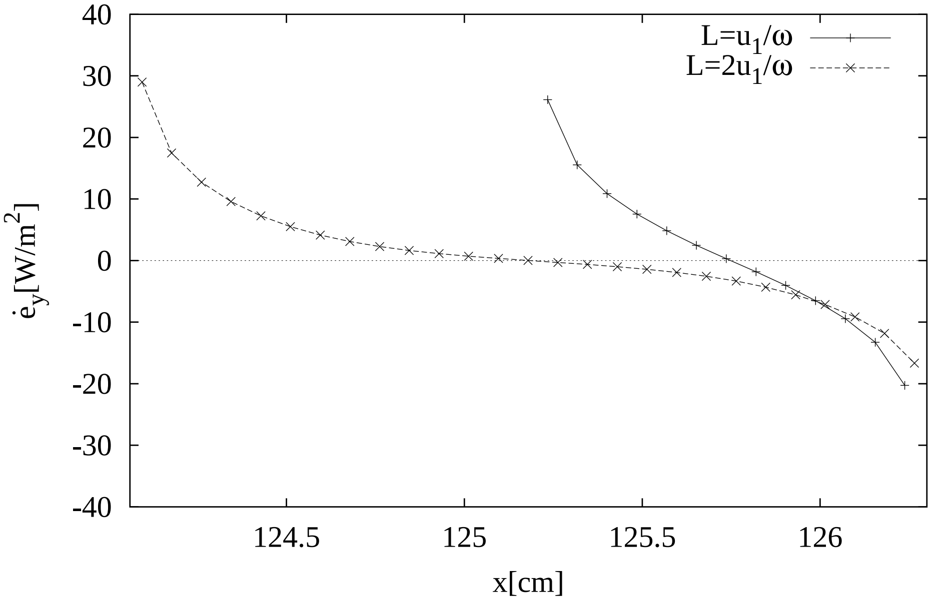

Figure 8.8: Time averaged energy flux density in the y-direction at the surface of the short plates when $y_0 = \delta_{km}/2$ (case 5; $L = u_1/\omega$, case 6; $L = 2u_1/\omega$). The outer edges of all plates are at $x \simeq 126.2$cm. The inner edges of the plates are at $x \simeq 125.2$ and 124.2 respectively.

density flux at the plate surface is as shown in figure 8.9. At this plate spacing, the energy dissipation was dominant and the heat pumping effects were no longer seen.

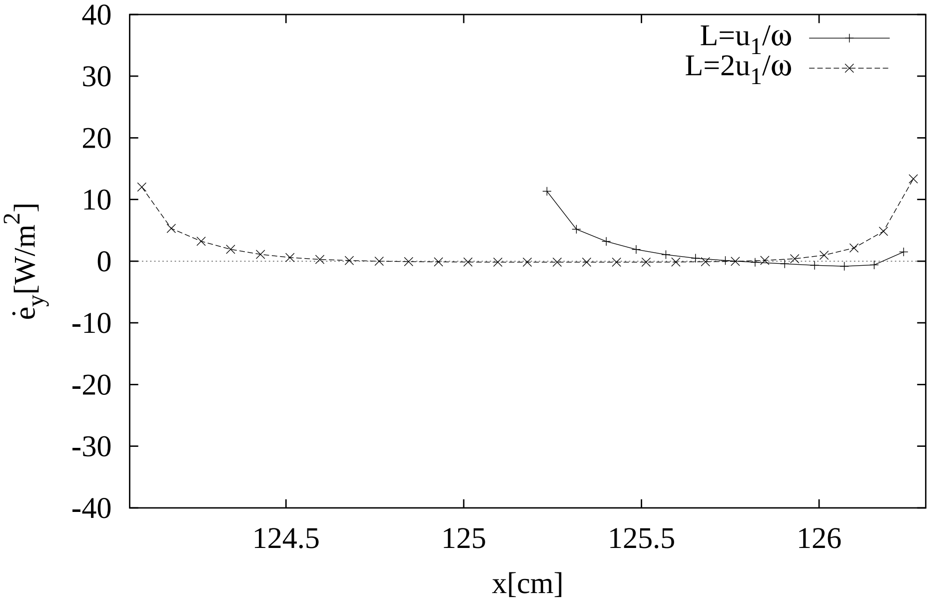

Figure 8.9: Time averaged energy flux density in the y-direction at the surface of the short plates when $y_0 = \delta_{km}/3$. The plate inner and the outer edges are at $x \simeq 125.2$cm and $x \simeq 126.2$cm respectively when L=u_1/ω (case 7). The plate inner and the outer edges are at $x \simeq 124.1$cm and $x \simeq 126.2$cm respectively when L=$2u_1/\omega$ (case 8).

The energy lines for the test cases with $y_0 = \delta_{km}/2$ and $\delta_{km}/3$ are presented in figures 8.10 and 8.11 respectively. Again ΔE is approximately 0.12 W. When $y_0 = \delta_{km}/2$, the heat pumping effects are reduced by approximately 1/8th in comparison to when $y_0 = 3\delta_{km}$. This corresponds to the amount by which y_0 was reduced. The energy lines at the plate outer edges remain almost normal to the plate for about one third of the half passage height. Energy vectors are shown along with the energy lines in figure 8.11 as a visual guide.

The particle traces for the cases when $y_0 = \delta_{km}/2$ were almost identical to figures 8.6 and 8.7, but the characteristic shapes of the particle traces changed when $y_0 = \delta_{km}/3$ as shown in figure 8.12. Traces for particles 2, 5 and 8 have y-displacements but there is no loop in tracks.

The plate spacing at which the heat flux to the plate changed from leaving out at the outer end and in at the inner end to being in at both ends was not the same as that where the shape of the particle tracks changed from being with loop to without loop.

8.2.2 Standard operating condition test

In order to avoid stiff-dimension problems, Cao *et al.* (1996) in their thermoacoustic couple simulations, chose a mean pressure of approximately one hundredth of atmospheric pressure

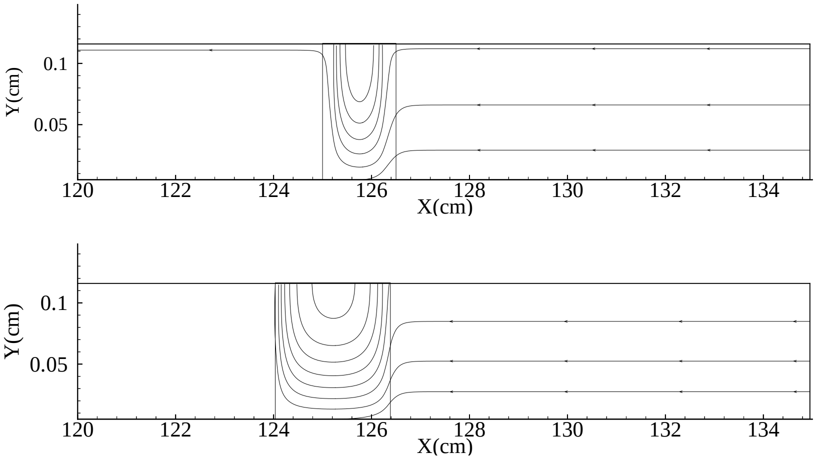

Figure 8.10: Time averaged energy lines for case 5 where $L = u_1/\omega$ and case 6 where $L = 2u_1/\omega$ when $y_0 = \delta_{km}/2$. (For the plate edge locations, see figure 8.9)

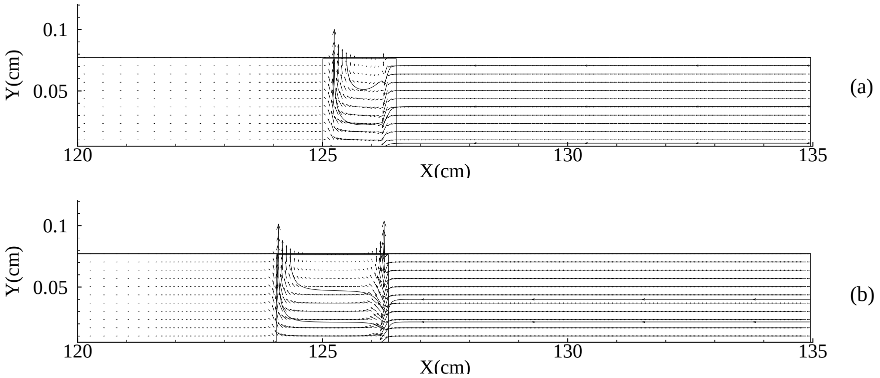

Figure 8.11: Time averaged energy lines for case 7 where $L = 2u_1/\omega$ and case 8 where $L = u_1/\omega$ when $y_0 = \delta_{km}/3$.

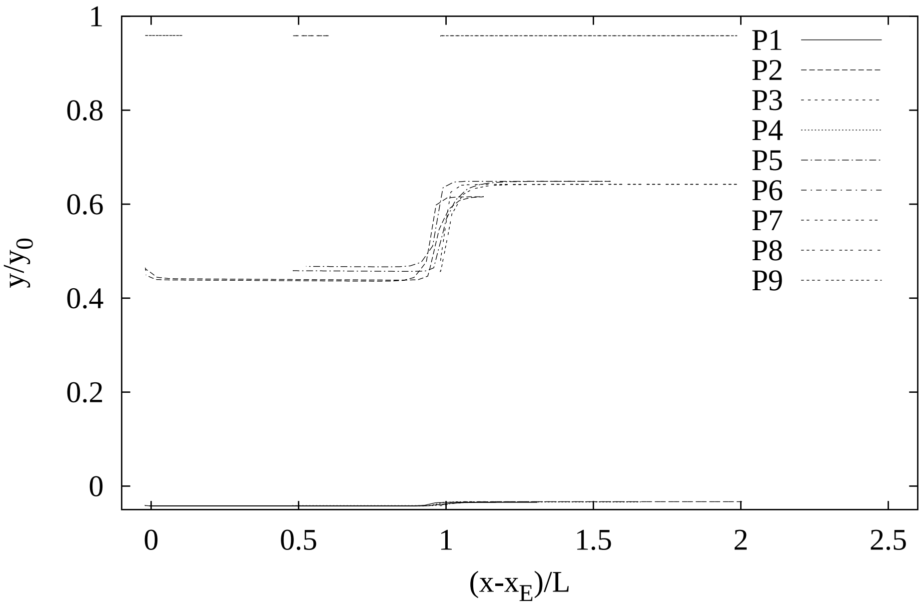

Figure 8.12: Particle trace of 9 particles (P1 to P9) over the plate for case 8 where $L = 2u_1/\omega$, y_0=$\delta_{km}/3$.

(assuming the mean operating temperature and frequency are of the order of 100K and 100Hz respectively). However, this mean pressure is two orders of magnitude smaller than that commonly used for existing operating thermoacoustic devices. Using a low mean pressure operating condition causes some of the non-dimensional parameters, such as Reynolds numbers, to be lower than those of existing devices if one were to keep other parameters similar to those of existing devices.

The purpose of this section is to test the validity of simulations to investigate the thermoacoustic effect for operating conditions closer to those of current thermoacoustic devices. In order to achieve this, the following cases were considered.

- All operating conditions were kept the same as case 1 in table 7.1 except the mean pressure was raised to 10^6 Pa. Re and $Re_{m\&t}$ rose by an order of magnitude but Re_{wo} remained constant. $Re_{m\&t}$ is still well below the critical Reynolds number described in section 2.5.3. Thus the assumption that the flow is laminar is still suitable for these test conditions.

- Same as above except the plate was shortened to the particle displacement distance.

Simulations were carried out for long plates with large plates spacing ($L \simeq 22u_1/\omega$, y_0=$3\delta_{km}$), and for short plates with various plate spacings ($L \simeq 2u_1/\omega$, y_0=$\delta_{km}/3$, $\delta_{km}/2$ and $3.3\delta_{km}$).

The results for these test cases are given as cases 9 to 12 in table 8.3. From these results, it can be seen that the energy balance errors are less than 1% and the simulations can be therefore considered to be valid according to the criteria proposed in section 4.3.2.

Case		9	10	11	12
Plate length		$22u_1/\omega$	$2u_1/\omega$	$2u_1/\omega$	$2u_1/\omega$
y_0		$3.3\delta_{km}$	$3.3\delta_{km}$	$\delta_{km}/2$	$\delta_{km}/3$
$\Delta p_{cy}/P_A$	[%]	6.7e-3	1.6e-2	8.9e-3	1.1e-2
$\Delta u_{cy}/u_A$	[%]	1.1e-2	2.3e-2	1.1e-2	1.6e-2
$\Delta T_{cy}/T_A$	[%]	5.8e-2	5.8e-2	4.8e-2	4.5e-2
$\Delta \rho_{cy}/\rho_A$	[%]	3.8e-2	4.2e-2	3.4e-2	3.2e-2
$\Delta Tb_{cy}/T_A$	[%]	3.6e-2	4.8e-2	4.6e-2	3.8e-2
u_{err}/u_A	[%]	3.2e0	2.4e0	3.6e0	6.8e0
T_{err}/T_A	[%]	5.7e-1	1.4e1	4.2e-1	1.4e-1
$\dot{E}y_{pl}$	[W]	1.1e0	-6.2e-2	2.5e-1	4.5e-1
$\dot{E}x_{cen}$	[W]	-2.0e-1	-2.3e-1	-3.5e-2	-2.3e-2
$\dot{E}x_{BC34}$	[W]	-9.4e-1	-3.2e-1	-1.9e-1	-2.5e-1
q_A	[W]	3.1e-1	2.7e-1	1.9e-1	1.6e-1
ex_{ABC34}	[W/m^2]	8.9e4	8.8e4	8.7e4	8.6e4
H_x	[W/m^2]	-9.5e4	-9.6e4	-3.6e5	-7.9e5
H_y	[W/m^2]	-6.2e2	-5.4e2	-8.9e1	-2.7e1
$\dot{Q}_{Error}$	[%]	5.0e-1	2.0e-1	1.3e-1	3.2e-1
$\dot{E}_{diss}pl$	[W]	1.1e-1	1.1e-1	6.0e-2	4.0e-2
$\dot{S}_{gen}T_0$	[W]	1.3e0	1.2e-1	3.2e-1	4.9e-1
$\Delta P_A/P_A$	[%]	5.7e0	7.4e0	4.6e0	2.7e0
Cycles		30	39	48	41
$\Delta y/\delta_{km}$		8.3e-4	8.3e-2	4.2e-2	2.1e-2

Table 8.3: Standard operating condition test with Δt=0.28%, $\frac{x_4-x_5}{2u_1/\omega}$=3.8e0, $\Delta x/\lambda$=2.5e-4, δ_{km}=0.024cm. (M=0.01, P_m=1.0E6Pa, f=100Hz, T_m=300K)

The time averaged energy lines are displayed in figure 8.13 for case 9. The location of the plate is indicated by thin vertical lines. The energy lines in figure 8.13 are very similar to those of run 1 (see figure 7.15) which was simulated at the operating conditions of Cao *et al.*. Again, the energy lines indicate a heat pumping effect. The energy flux between subsequent energy lines, ΔE, is approximately 3.0 W.

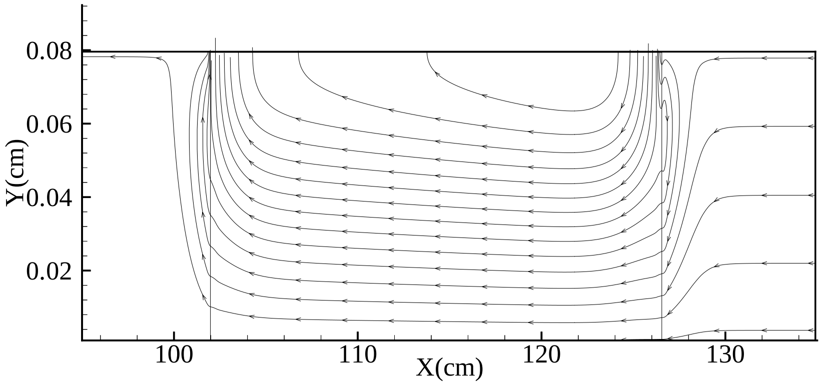

Figure 8.13: Time averaged energy line for case 9 (Long plate, large spacing).

The time averaged energy lines for case 10 are shown in figure 8.14, demonstrating a heat pumping effect on the plate surface. The number of energy lines leaving BC34 and hitting the plates is fewer than those of figure 8.13 since the plate length is less than 1/10th of that for case 9.

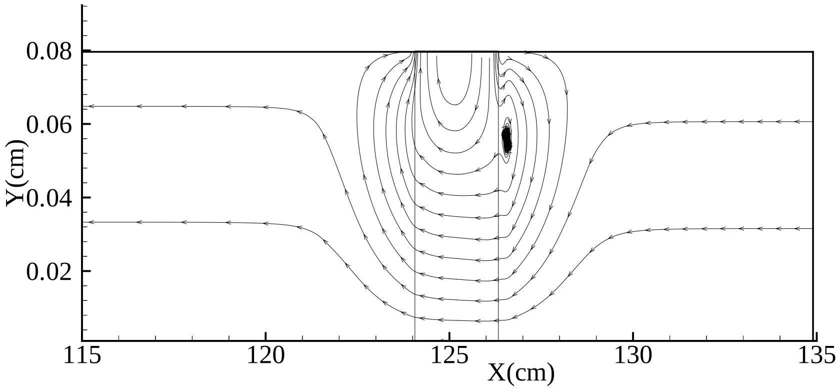

Figure 8.14: Time averaged energy lines for case 10 (Short plate, large spacing).

Time averaged energy lines for cases 11 and 12 are shown in figure 8.15 (energy vectors are also shown as a visual guide).

The thermoacoustic effects over the long and short plates for various plate spacings at standard operating conditions were very similar to those in sections 7.5.2 and 8.2.1.

Overall, validity of simulation of thermoacoustic engines under the standard operating condition was confirmed.

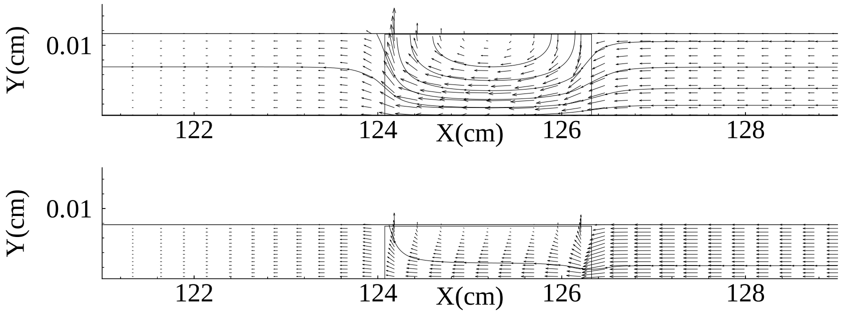

Figure 8.15: Time averaged energy lines for case 11 and 12 (Short plate, small spacing).

8.2.3 Summary of preliminary tests

The aims of the preliminary tests in section 8.2 were first to test if it is possible to simulate a short plate (one of the order of the particle displacement distance or less) and small plate spacings (of the order of thermal penetration depth or less) and then to investigate the thermoacoustic effects for short plates at various plate spacings. Then results were provided from tests to check the validity of simulations of thermoacoustic couples subject to operating conditions similar to those experienced by heat exchangers in existing thermoacoustic devices.

The values of $\dot{Q}_{Error}$ for all cases were less than 1%, which suggests that the simulations are valid for all conditions and geometries tested.

The findings in this section were that the heat pumping effects were observed even on the shortest plate. When the plate was 'short', the half plate spacing had to be reduced to $\delta_{km}/3$ for viscous dissipation to be dominant. In contrast, when the plate was 'long', heat pumping effects disappeared at $y_0{=}\delta_{km}/2$.

When $y_0{=}3\delta_{km}$, vortical motion was observed over the short plate. There was also an indication of larger scale vortical motion outside both edges of the plate. However, there are no experimental results to confirm this.

Changes of the characteristic shapes of the particle trace and energy lines did not occur at the same plate spacing.

Energy dissipation was approximately proportional to the surface area of the plate.

When the plate geometry was varied at standard operating conditions, the characteristics of the flow and energy fields for each different plate geometry were similar to those tested at the operating conditions of Cao *et al.* despite the fact that the Re and $Re_{m\&t}$ increased by 100 times. Subsequent tests of heat exchangers in thermoacoustic engines are simulated at the more typical operating conditions.

8.3 Testing of the heat exchanger model

As has been discussed in section 2.5, there has not been any experimental or numerical work to investigate oscillating heat transfer in the heat exchangers of thermoacoustic engines because of the complexity of the boundary conditions at the heat exchanger plate edge adjacent to the regenerator.

Simulations of thermoacoustic couples in section 7.5.2 in chapter 7 showed how the results and the energy balance errors in the domain are influenced by the location of the oscillatory boundary. They showed the importance of applying boundary conditions representative of those that would occur close to the plates in a thermoacoustic device and that applying 1-D standing wave condition close to the plates can lead to errors in the simulations. To work out which oscillatory boundary conditions to apply to the heat exchanger model, we could simulate an entire thermoacoustic device and look at the conditions at the ends of the heat exchanger plate. However, in order to simulate heat exchanger plates under various operating conditions, and to investigate their heat transfer mechanisms, many parametric studies would be required. Another possibility would be to extend the simulation domain to the center of the regenerator where the first order analytical model agrees well with the experimental results. However, operating conditions where the first order analytical model is appropriate are limited. In addition, the temperature gradient on the regenerator plate also needs to be assumed and the simulation results would be very sensitive to this assumption.

In section 5.2, simplified oscillatory boundary conditions were considered for simulating the regenerator-heat exchanger plate edge to avoid simulating the whole device. The oscillatory boundary conditions are based on existing analytical solutions at various level of approximation.

The purpose of this section is to test three out of six oscillatory boundary conditions considered in section 5.2. The first is the most idealistic heat exchanger - regenerator edge model that is not y-dependent. The Second model tested was based on the first order analytical model with values averaged in the y-direction. The third model has y-dependent values, and uses the first order analytical model.

8.3.1 On temperature boundary conditions

When testing the heat exchanger model using the boundary conditions suggested in section 5.2.3, the temperature of the heat exchanger plate and the mean of the oscillating temperature at BC34 are set equal in the current work. In an operational thermoacoustic device, the mean temperature of the heat exchanger plates is higher for a hot heat exchanger and lower for a cold heat exchanger than that at the regenerator edge. However, in the most ideal case (i.e. when viscosity is small and heat transfer in the x-direction is neglected), heat flux should be carried to or from the heat exchanger region without a mean temperature difference. Therefore in the current work, in order to observe and to investigate the heat carried from the regenerator end to the heat exchanger by the oscillatory flow (which would be by convection but not by conduction in the x-direction), the temperature of the plate, the mean temperature of the gas at BC34 and the initial gas temperature of the simulation domain were set equal.

8.3.2 Operating mode check

Huelsz and Ramos (1995) developed an analytical expression for the phase difference between the temperature and the pressure in the regenerator. They describe the mode of operation of the thermoacoustic engine (either a prime mover or heat pump) as a function of the phase difference between the temperature and the pressure and the temperature gradient imposed on the regenerator plates. For the ideal case where viscosity in the gas can be neglected and the heat capacity of the regenerator plate can be assumed to be infinite, the phase difference is determined only by the sign of the amplitude of the temperature, not by its magnitude. In such a case, it is possible to control the mode of operation by changing the sign of the temperature amplitude. (Although in a more practical case, the phase shift does depend also on the amplitude.)

In the idealistic case, when the sign of the temperature amplitude is changed to positive in equation (5.19) by adjusting the magnitude of dT_m/dx, the temperature profile imposed at BC34 is that of the gas near a regenerator plate functioning as a prime mover, as described in section 2.1. In that case, it is expected that there is net heat transfer from the heat exchanger plate to BC34 over a cycle (i.e. the plate is functioning as the hot heat exchanger of a prime mover). Conversely, when the temperature amplitude is set to negative, the heat exchanger plate should act as the ambient heat exchanger of the heat pump.

Therefore, in the heat exchanger model, the x-component of the energy flux at BC34, $\dot{E}_{xBC34}$ can be written as

$$\dot{E}_{xBC34} = \dot{E}_{diss} + \dot{E}\phi_{BC34}, \tag{8.1}$$

where $\dot{E}\phi_{BC34}$ is the convective energy flux (which can be heat or work flux) intentionally added or removed at BC34 by introducing a phase shift to either temperature or velocity as described in section 5.2 for the heat exchanger simulation model. Its magnitude can be calculated from the second term of equation (2.20). $\dot{E}_{diss}$ is the energy dissipated in the domain (see section 7.4 for a detailed description). $\dot{E}\phi_{BC34}$ is zero for a thermoacoustic couple model since the oscillatory boundary conditions used are the same as those of a standing wave. Convergence was monitored in the same manner as described in section 7.4.

In this section, in order to test if the boundary condition is functioning either as a prime mover or a heat pump, tests were made at the standard operating conditions that were tested in section 8.2.2. The half plate spacings tested were $y_0 = \delta_{km}/2$ and $3\delta_{km}$. Γ, the ratio of ΔT_m to ΔT_{crit}, was set to 1.3 and 0.7 for the prime mover and heat pump modes respectively. The critical temperature gradient was evaluated at the outer edge of the heat exchanger plate using equation (2.43). It is noted that this only gives a rough estimate of critical temperature gradient as it is from the single plate model.

The first type of boundary condition to be applied at BC34 is that labeled 'BC34-1' in table 5.1. This boundary condition applies the pressure and velocity for an ideal standing wave and the y-averaged temperature calculated from the single plate model (the 'single plate' model is described in section 2.1). With BC34-1, the pressure and velocity are not y-dependent and the temperature at BC34 is y-averaged. The phase shifts between the pressure and the temperature for BC34-1 are shown in table 8.4 as BC34-1ϕ_{PT} for test cases of a prime mover, a heat pump mode and a thermoacoustic couple. Results are shown for two different plate spacings ($\delta_{km}/2$ and $3\delta_{km}$).

The signs of $\dot{E}x_{BC34}$ in table 8.4 for each plate spacing show clearly the influence of phase shift, as described in section 7.4. When $\dot{E}x_{BC34}$ is positive, energy flows out of the simulation domain from BC34 and the boundary functions as a prime mover, but it functions as a heat pump when $\dot{E}x_{BC34}$ is negative.

Because of the sign convention used in the current work, described in section 7.4, when $\dot{E}y_{pl}$ is negative, the energy flows into the domain through the plate and when it is positive, it flows out. Ideally, when $\dot{E}x_{BC34}$ is positive, $\dot{E}y_{pl}$ should be negative and the magnitude should equal $\dot{E}x_{BC34}$ and vice versa when $\dot{E}x_{BC34}$ is negative.

When $y_0=\delta_{km}/2$ in prime mover mode, although $\dot{E}y_{pl}$ is negative, the magnitude is less than one third of the heat pump mode. However, at larger plate spacings, $\dot{E}y_{pl}$ hardly changes despite $\dot{E}x_{BC34}$ changing sign. Although the energy balance error, $\dot{Q}_{Error}$, in table 8.4 at its maximum is just under 10%, which was discussed in section 4.3.2 as being acceptable for the simulation to be considered valid, the fact that the change of $\dot{E}x_{BC34}$ had little influence on $\dot{E}y_{pl}$ when $y_0=3\delta_{km}$ indicates that there is a problem with non-y-dependent boundary conditions at larger plate spacings.

In order to visualize whether applying this boundary condition leads to the heat exchanger functioning as that in a prime mover or a heat pump, the time averaged y-components of the energy flux at the plate are shown in figures 8.16 and 8.17 for $y_0 = \delta_{km}/2$ and $3\delta_{km}$.

The difference in the time averaged energy flux at the surface of the plate for the heat pump and for the prime mover modes is distinct when $y_0 = \delta_{km}/2$. When the plate half spacing is $y_0 = 3\delta_{km}$, although the time averaged differences are small, the energy flux at the plate outer edge is influenced by the oscillatory boundary. However, the operating mode is not clearly distinguished.

Instantaneous plots of e_y at eight times during a cycle are shown in figures 8.18 and 8.19 for the case when $y_0=3\delta_{km}$. Again, only a small influence of the oscillatory boundary conditions is seen at the outer edge of the plate.

As an additional test, Γ, the ratio of ΔT_m to ΔT_{crit}, was changed to 1.6 and 0.4 for

MODE		Prime mover		Heat pump	
BC34-1 ϕ_{PT}		143.8	168.1	-36.2	-11.9
y_0		$\delta_{km}/2$	$3\delta_{km}$	$\delta_{km}/2$	$3\delta_{km}$
$\Delta p_{cy}/P_A$	[%]	8.8e-3	2.3e-2	9.1e-3	1.0e-2
$\Delta u_{cy}/u_A$	[%]	1.1e-2	3.3e-2	1.2e-2	1.1e-2
$\Delta T_{cy}/T_A$	[%]	7.4e-2	8.4e-2	7.2e-2	8.1e-2
$\Delta \rho_{cy}/\rho_A$	[%]	5.1e-2	6.3e-2	5.2e-2	5.2e-2
$\Delta Tb_{cy}/T_A$	[%]	5.6e-2	6.2e-2	5.3e-2	6.7e-2
u_{err}/u_A	[%]	4.0e0	6.7e0	4.0e0	6.7e0
T_{err}/T_A	[%]	3.6e-1	1.8e1	3.2e-1	1.4e1
$\dot{E}y_{pl}$	[W]	1.2e-1	4.3e0	4.2e-1	4.2e0
$\dot{E}x_{cen}$	[W]	-3.4e-2	-2.2e-1	-3.5e-2	-2.2e-1
$\dot{E}x_{BC34}$	[W]	2.9e-1	1.7e0	-2.9e-1	-1.7e0
q_A	[W]	1.9e-1	3.2e-1	1.9e-1	3.1e-1
ex_{ABC34}	[W/m^2]	9.8e3	2.4e4	1.0e4	2.4e4
H_x	[W/m^2]	-3.6e5	-9.7e4	-3.6e5	-9.7e4
H_y	[W/m^2]	-8.9e1	-5.5e3	-8.9e1	-5.5e2
$\dot{Q}_{Error}$	[%]	1.0e0	8.8e0	3.8e-1	3.9e0
$\dot{E}_{diss}pl$	[W]	6.0e-2	1.1e-1	6.0e-2	1.1e-1
$\dot{S}_{gen}T_0$	[W]	3.1e-1	1.2e-1	3.1e-1	1.2e-1
$\Delta P_A/P_A$	[%]	4.2e-1	-3.4e0	3.7e-1	-3.5e0
Cycles		25	26	24	26
$\Delta y/\delta_{km}$		4.2e-2	8.3e-2	4.2e-2	8.3e-2

Table 8.4: Operating mode test using BC34-1. $\Delta x/\lambda$=2.5e-4, δ_{km}=0.024cm.

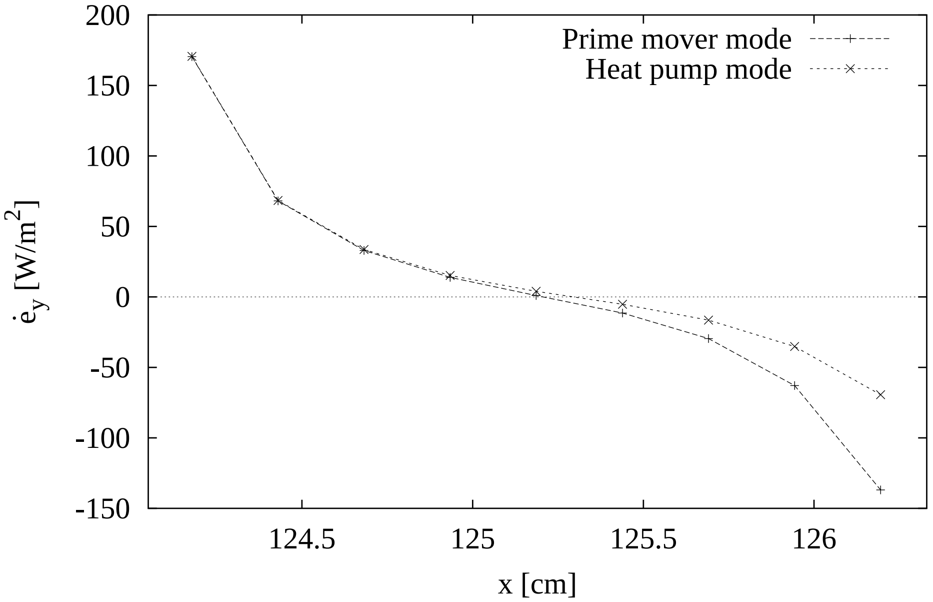

Figure 8.16: Time averaged energy flux density in the y-direction at the surface of the plate when the plate spacing $y_0 = \delta_{km}/2$.

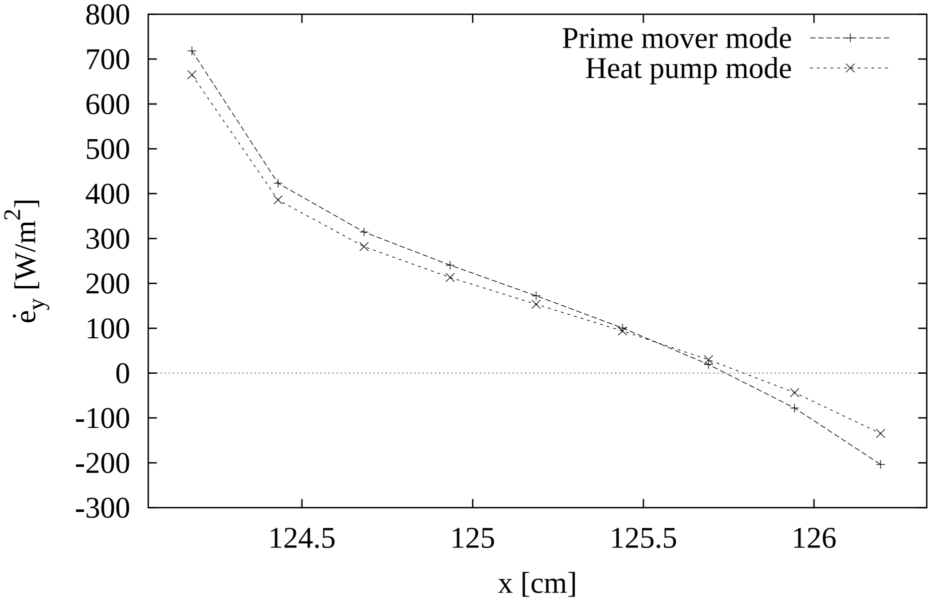

Figure 8.17: Time averaged energy flux density in the y-direction at the surface of the plate when the plate spacing $y_0 = 3\delta_{km}$.

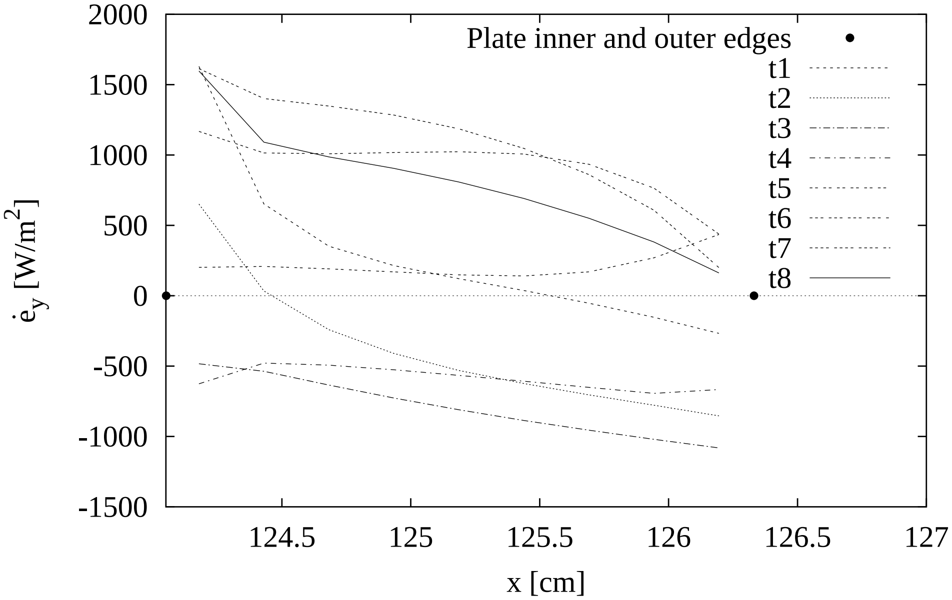

Figure 8.18: Instantaneous energy flux density in the y-direction at the surface of the plate when the plate spacing $y_0 = 3\delta_{km}$, in prime mover mode.

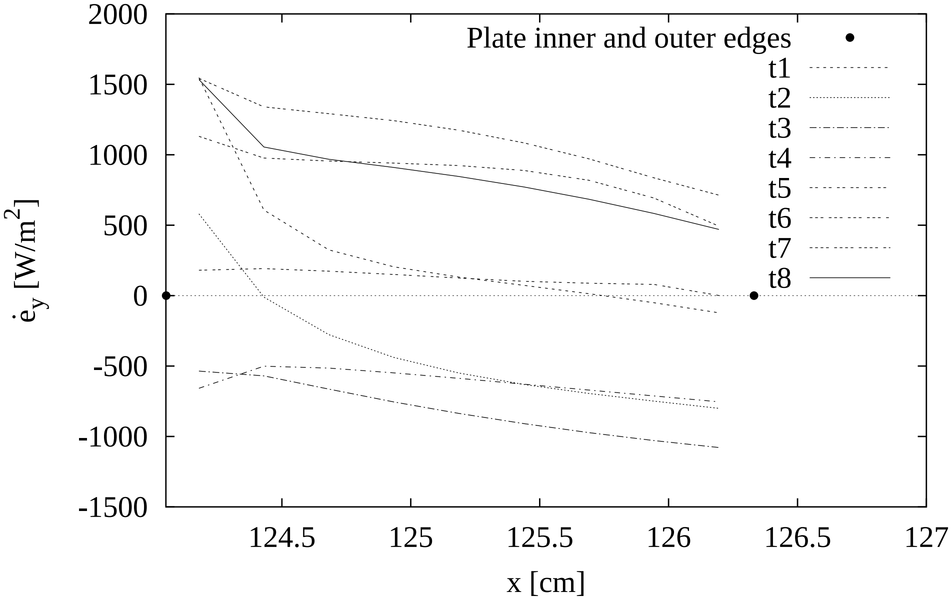

Figure 8.19: Instantaneous energy flux density in the y-direction at the surface of the plate when the plate spacing $y_0 = 3\delta_{km}$, in heat pump mode.

the prime mover and heat pump modes in order to get a clearer difference between the two operating modes. For BC34-1, changing dT_m/dx does not change the phase shift, but the temperature amplitudes at the boundary are increased by a factor of two for this case. For $y_0 = 3\delta_{km}$, only the prime mover mode was tested as the energy balance error, $\dot{Q}_{Error}$, did not show any improvement when the larger temperature amplitudes were imposed at the boundary. On the contrary, it worsened. Further tests were not considered. The results of the simulations are in table B.3 given in appendix B.

The time averaged energy flux $\dot{e}_y$ at the surface of the plate is shown in figure 8.20 for BC34-1. Results are shown for Γ=0.4, 0.7 1.3 and 1.6. The differences in the peak

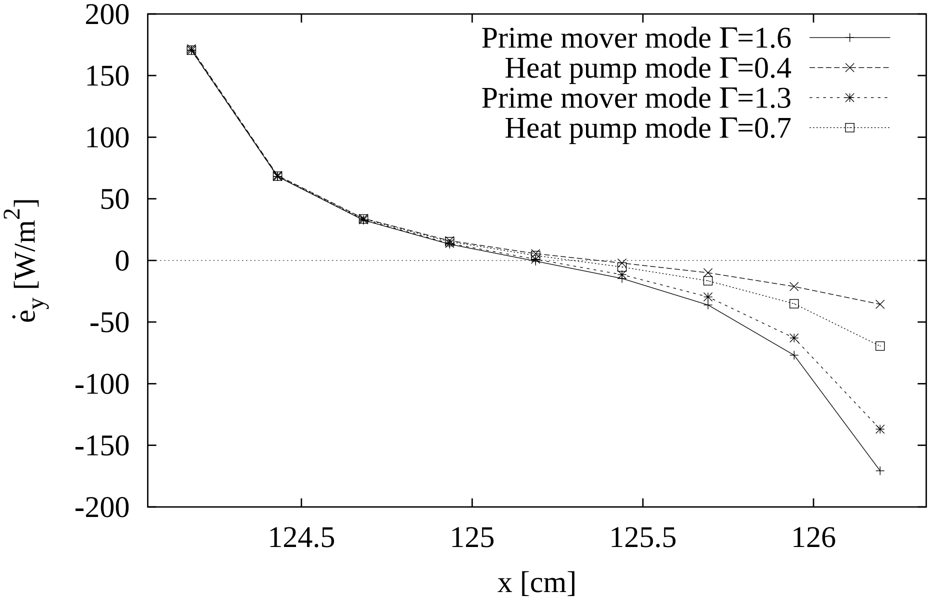

Figure 8.20: Time averaged energy flux density in the y-direction at the surface of the plate when the plate spacing $y_0 = \delta_{km}/2$ for Γ =0.4, 0.7, 1.3 and 1.6 times the critical temperature gradient.

magnitudes of the y-component of time averaged energy flux density, $\dot{e}_y$ at the outer plate edge varies further when Γ is varied over a wider range. The cycle averaged energy lines for the prime mover mode and the heat pump mode are shown in figures 8.21 and 8.22. There is very little difference between the heat pump and the prime mover mode (except at BC34), even for the simulations with $y_0 = \delta_{km}/2$ which showed a distinct change in the cycle averaged energy flux at the plate surface, $\dot{E}y_{pl}$. Also, the energy lines near BC34 from the prime mover seem non-physical. In order to identify what causes the energy lines to bend so sharply near BC34, energy vectors are shown in figures 8.23 and 8.24 for both the prime mover and the heat pump mode.

There is an obvious discontinuity between vectors at BC34 and those one cell before, even for the heat pump mode. The results there suggest that there is not an energy balance for cells near the boundary over a cycle. (The cycle averaged energy flux leaving the cells

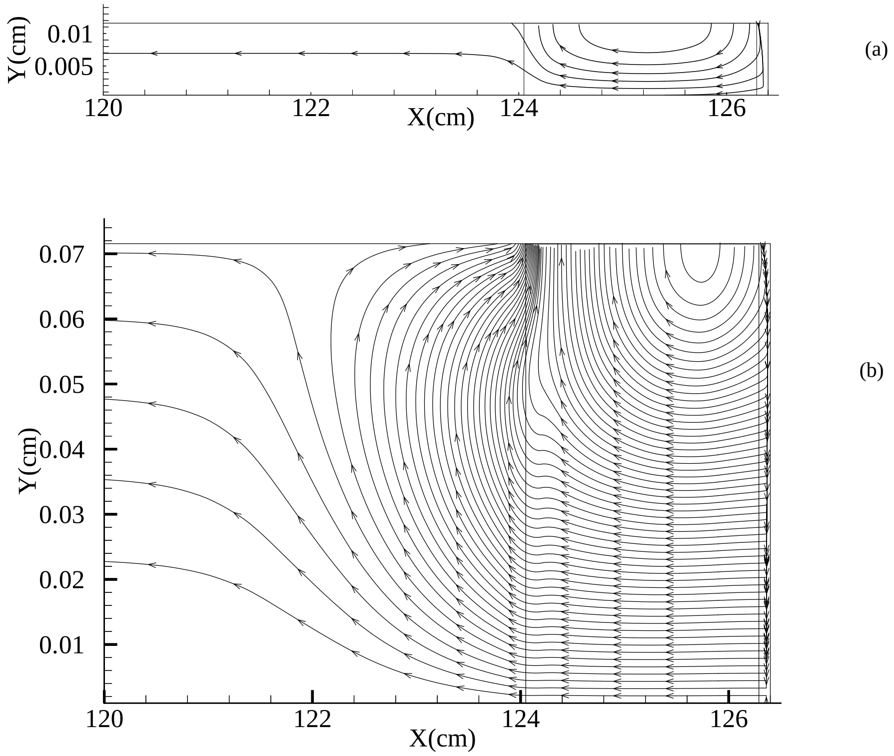

Figure 8.21: Time averaged energy lines when (a) $y_0 = \delta_{km}/2$, (b) $y_0 = 3\delta_{km}$ in prime mover mode. Boundary condition type BC34-1. Γ=1.3.

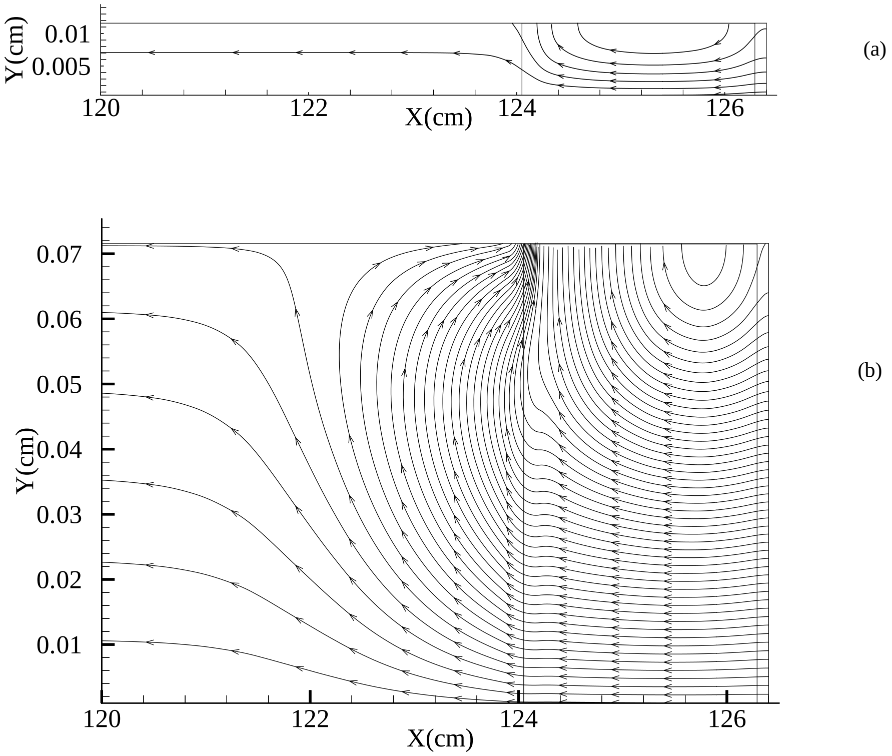

Figure 8.22: Time averaged energy lines when (a) $y_0 = \delta_{km}/2$, (b) $y_0 = 3\delta_{km}$ in heat pump mode. Boundary condition type BC34-1. Γ=1.7.

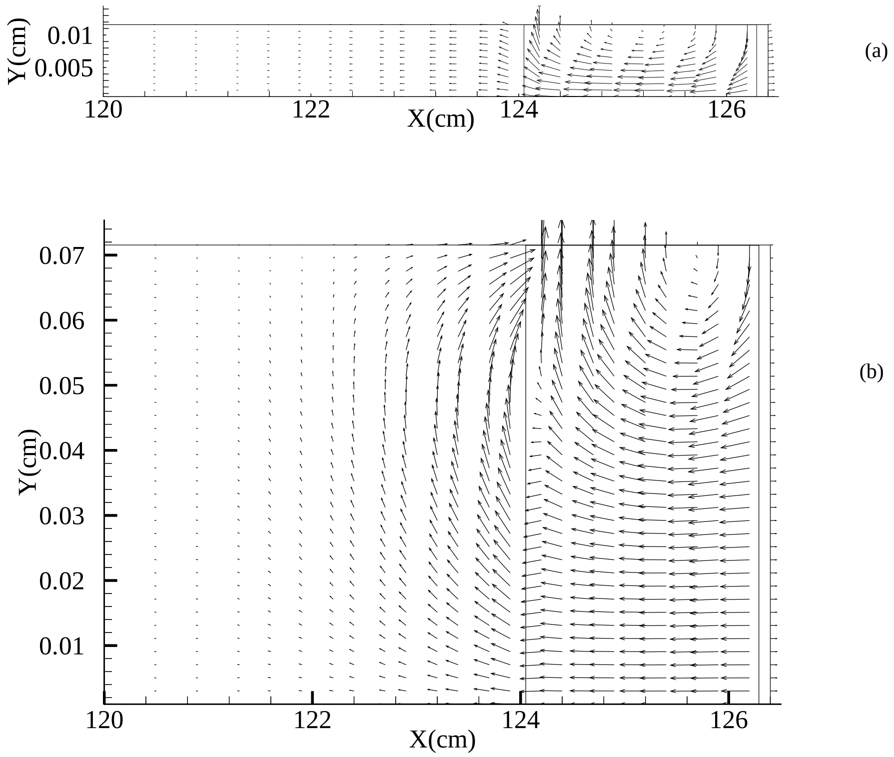

Figure 8.23: Time averaged energy vectors when (a) $y_0 = \delta_{km}/2$, (b) $y_0 = 3\delta_{km}$ in prime mover mode. Boundary condition type BC34-5.

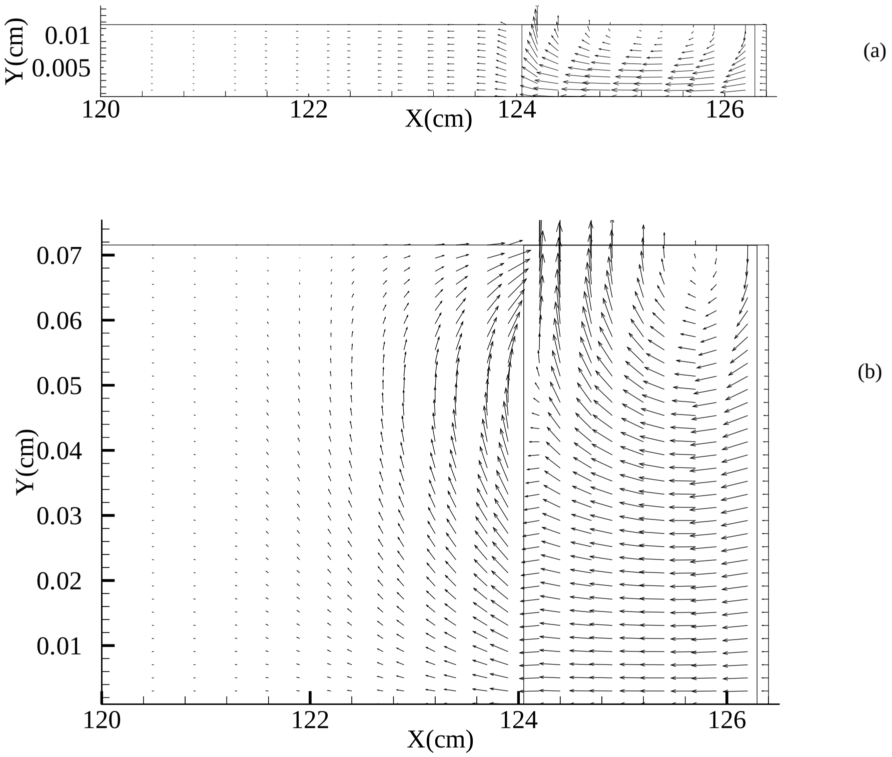

Figure 8.24: Time averaged energy vectors when (a) $y_0 = \delta_{km}/2$, (b) $y_0 = 3\delta_{km}$ in heat pump mode. Boundary condition type BC34-6.

exceed any entering them.) This indicates that, although the energy balance error for test cases when $y_0=\delta_{km}/2$ were less than 1% and the time averaged energy flux at the plate surface for the heat pump and the prime mover mode showed distinct change as the phase shift of temperature was changed in BC34-1, the simulation is still not valid.

As discussed in section 7.5.3, for the thermoacoustic couple simulation, when specifying the oscillatory boundary condition very close to the plate, it is very important to supply accurate temperature and velocity profiles as boundary conditions.

Based on this idea, two other types of boundary conditions, BC34-5 and BC34-6 discussed in section 5.2.3, were tested for both the prime mover and the heat pump modes for $y_0 = \delta_{km}/2$ and $3\delta_{km}$.

The conditions for BC34-6 are calculated from the first order analytical solution with BC34-5 being the y-average of BC34-6. However, it must be noted that BC34-6 uses the fluctuating temperature and velocity calculated from an analytical solution that does not include end effects. Also, for all test cases, the pressure at BC34 was assumed to be that of an ideal standing wave. This approximation was appropriate for all thermoacoustic couple simulations tested in chapter 7.

The simulation results for all test cases using BC34-5 and BC34-6 are shown in tables 8.5 and 8.6 respectively. The time averaged energy flux at BC34, $\dot{E}x_{BC34}$, in tables 8.5 and 8.6 indicate that for BC34-5 and BC34-6, adjustment of the operating mode by changing dT_m/dx around the critical temperature gradient is not appropriate. The y-component of the time averaged energy flux, $\dot{e}_y$ is shown in figures 8.25 and 8.26. The results show that there are only very minor differences in $\dot{e}_y$ for all cases. Although the results for $y_0 = 3\delta_{km}$ show slightly larger differences, the energy balance errors, $\dot{Q}_{Error}$, are large and the validity of the simulation is questionable. Although y-dependent boundary conditions were applied using BC34-6, simulations when $y_0 = \delta_{km}$ again showed larger values for $\dot{Q}_{Error}$.

By inspecting $\dot{E}x_{BC34}$ for all test simulations using BC34-5 and BC34-6, the operating mode is not clear even when the plate spacing is small. The results of tests presented in this section indicate that for $y_0=\delta_{km}/2$, the operating mode change was clearest when the simplest boundary conditions, BC34-1 was used. This is despite the fact that other boundary conditions were expected to be closer to those which would occur in an operational device. For the larger plate spacing ($y_0=3\delta_{km}$) the results indicate that BC34-1 did not produce a change in operating mode. For $y_0=3\delta_{km}$ the more complex boundary conditions, BC34-5 and BC34-6 did affect heat transfer to the plate but the prime mover mode did not produce an energy flow out of the domain through BC34. This indicate that although the oscillatory boundary conditions, BC34-5 and BC34-6 are based on the first order analytical mode, it is not appropriate to apply them at the plate edge where the flow fields are expected to differ from those at the place center. It is apparent that more appropriate boundary conditions must be found if a simulation of the present for is to be used to model heat exchangers in thermoacoustic engines.

MODE		Prime mover		Heat pump	
y_0		$\delta_{km}/2$	$3\delta_{km}$	$\delta_{km}/2$	$3\delta_{km}$
$\Delta p_{cy}/P_A$	[%]	7.5e-3	8.7e-3	1.2e-2	1.1e-2
$\Delta u_{cy}/u_A$	[%]	9.0e-3	1.3e-2	1.5e-2	1.3e-2
$\Delta T_{cy}/T_A$	[%]	4.0e-2	5.7e-2	5.5e-2	5.8e-2
$\Delta \rho_{cy}/\rho_A$	[%]	3.0e-2	3.8e-2	3.8e-2	4.1e-2
$\Delta Tb_{cy}/T_A$	[%]	3.3e-2	4.7e-2	4.6e-2	4.9e-2
u_{err}/u_A	[%]	3.9e0	6.4e0	3.9e0	6.4e0
T_{err}/T_A	[%]	2.8e-1	1.7e1	2.8e-1	1.4e1
$\dot{E}y_{pl}$	[W]	6.4e-1	3.9e0	6.7e-1	3.8e0
$\dot{E}x_{cen}$	[W]	-3.5e-2	-2.1e-1	-3.4e-2	-2.1e-1
$\dot{E}x_{BC34}$	[W]	-3.3e-1	3.4e0	-3.7e-1	3.5e-1
q_A	[W/m^2]	1.9e3	3.1e3	1.9e3	3.0e3
ex_{ABC34}	[W/m^2]	1.1e4	1.9e4	1.1e4	2.6e4
H_x	[W/m^2]	-3.6e5	-9.7e4	-3.6e5	-9.7e4
H_y	[W/m^2]	-8.9e1	-5.5e2	-8.9e1	-5.5e2
$\dot{Q}_{Error}$	[%]	7.2e-1	1.0e1	6.8e-1	5.9e0
$\dot{E}_{diss}pl$	[W]	6.0e-2	1.1e-1	6.0e-2	1.1e-1
$\dot{S}_{gen}T_0$	[W]	3.1e-1	1.2e-1	3.1e-1	1.2e-1
$\Delta P_A/P_A$	[%]	3.6e-1	-4.3e0	4.6e-1	-3.9e0
Cycles		49	43	44	46
$\Delta x/\lambda$		2.5e-4	2.5e-4	2.5e-4	2.5e-4
$\Delta y/\delta_{km}$		4.2e-2	8.3e-2	4.2e-2	8.3e-2

Table 8.5: Operating mode test with BC34-5.

MODE		Prime mover		Heat pump	
y_0		$\delta_{km}/2$	$3\delta_{km}$	$\delta_{km}/2$	$3\delta_{km}$
$\Delta p_{cy}/P_A$	[%]	1.1e-2	7.3e-3	3.3e-3	6.5e-3
$\Delta u_{cy}/u_A$	[%]	1.4e-2	9.8e-3	3.7e-3	8.9e-3
$\Delta T_{cy}/T_A$	[%]	5.3e-2	5.8e-2	6.0e-2	5.8e-2
$\Delta \rho_{cy}/\rho_A$	[%]	3.7e-2	4.0e-2	4.1e-2	4.0e-2
$\Delta Tb_{cy}/T_A$	[%]	4.5e-2	4.6e-2	5.3e-2	4.9e-2
u_{err}/u_A	[%]	3.9e0	6.6e0	3.9e0	6.6e0
T_{err}/T_A	[%]	2.8e-1	1.8e1	2.7e-1	1.4e1
$\dot{E}y_{pl}$	[W]	7.5e-1	3.7e0	7.8e-1	4.0e0
$\dot{E}x_{cen}$	[W]	-3.4e-2	-2.1e-1	-3.5e-2	-2.1e-1
$\dot{E}x_{BC34}$	[W]	-3.9e-1	4.9e0	-4.5e-1	8.2e-1
q_A	[W/m^2]	1.9e3	3.1e0	1.9e0	3.1e0
$\dot{E}y_{plam}$	[W/m^2]	1.8e3	2.9e0	1.8e0	2.8e0
ex_{ABC34}	[W/m^2]	1.7e4	4.7e1	1.7e1	3.6e1
H_x	[W/m^2]	-3.6e5	-9.7e4	-3.6e5	-9.7e4
H_y	[W/m^2]	-8.9e1	-5.5e2	-8.9e1	-5.5e2
$\dot{Q}_{Error}$	[%]	8.2e-1	1.2e1	7.7e-1	6.8e0
$\dot{E}_{diss}pl$	[W]	6.0e-2	1.1e-1	6.0e-2	1.1e-1
$\dot{S}_{gen}T_0$	[W]	3.4e-1	1.3e-1	3.4e-1	1.3e-1
$\Delta P_A/P_A$	[%]	6.3e-1	4.0e0	7.1e-1	-4.0e0
Cycles		44	35	45	35
$\Delta x/\lambda$		2.5e-4	2.5e-4	2.5e-4	2.5e-4
$\Delta y/\delta_{km}$		2.1e-2	8.3e-2	2.1e-2	8.3e-2

Table 8.6: Operating mode test with BC34-6.

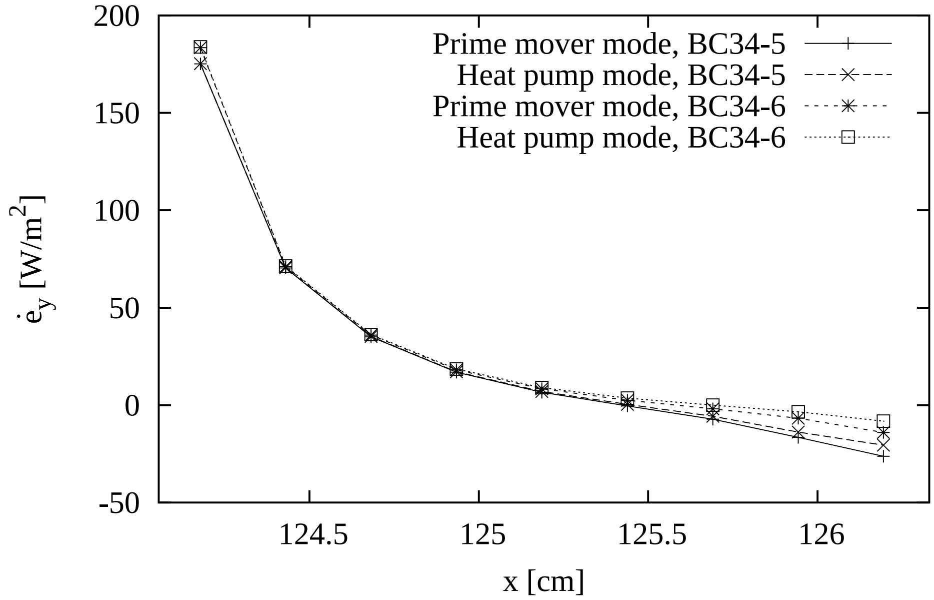

Figure 8.25: Time averaged energy flux density in the y-direction at the surface of the plate when the plate spacing $y_0 = \delta_{km}/2$ when using BC34-5 and BC34-6.

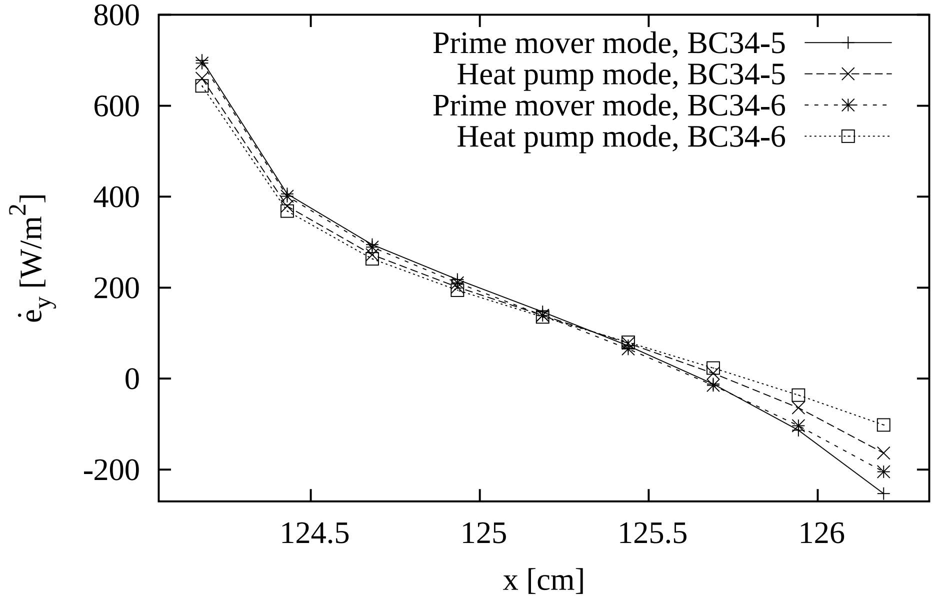

Figure 8.26: Time averaged energy flux density in the y-direction at the surface of the plate when the plate spacing $y_0 = 3\delta_{km}$ when using BC34-5 and BC34-6.

8.4 Discussion of results

In this chapter, the boundary conditions that were proposed in chapter 5 for simulating a regenerator edge close to a heat exchanger plate were tested.

Before testing the actual heat exchanger models, simulations of short plates, where the plate length is the same as or half of the particle displacement distance, were tested for large and small plate spacings. It was found that the short plate still functions as a thermoacoustic couple for both spacings. It was also found that the energy dissipated at the plate surface is proportional to the plate surface area.

The thermoacoustic couple simulations were also tested under conditions more representative of those used in existing devices. Although the mean pressure was raised by 100 times, energy lines were very similar to simulations run under the operating conditions used by Cao *et al.* (1996) for long and short plates at various plate spacings.

In heat exchanger simulation tests, when the half plate spacing was set to half the thermal penetration depth ($y_0 = \delta_{km}/2$), boundary condition type BC34-1 (BC34-1 uses the pressure and velocity of a standing wave and the y-averaged temperature from the single plate model) was capable of changing the time averaged heat flux at the surface of the plate when Γ, the ratio of the mean temperature gradient to the critical temperature gradient, was changed. However, by inspection of energy flux vectors near BC34, where they changed direction very sharply and there was an apparent lack of energy balance for cells near the boundary over a cycle, it appears that the simulation is not valid even though the energy balance error over the domain was within the limits of other simulations.

Results of the simulations using boundary conditions BC34-5 and BC34-6, (BC34-5 and BC34-6 both use the first order analytical solutions) indicated a similar discontinuity at BC34.

When the half plate spacing is three times the thermal penetration depth ($y_0 = 3\delta_{km}$), all simulations had energy balance errors between 3 and 10%. Although 10% was proposed as being an allowable error magnitude for the simulations to be considered valid (as discussed in section 4.3.2), the fact that the change of direction of energy flux at the oscillatory boundary had little influence on results in the simulation domain makes this criteria doubtful. This large error is attributed to the fact that the y-dependence of the flow field is ignored at the oscillatory boundary near the plate.

When the y-dependency can be ignored, as in the case of smaller plate spacings, the simulations converge with smaller energy balance errors. Further investigations are required to find numerically and experimentally more appropriate boundary conditions for larger plate spacings. To do this, the simulation or construction of the whole device may be necessary for the reasons discussed in section 8.3.

Although the simulation model was not sufficient to give any design indication of heat exchangers, the simulation results for the short plate thermoacoustic couple gives some useful information when combined with the simulation results from chapter 7. For regenerator plates, of interest is the amount of heat pumped. When the length of the plate is increased beyond four times the particle displacement distance, no more heat is pumped. Given this information, the regenerator plate design should be determined by considering the required temperature gradient, the thermal properties of the materials being used and the operating conditions. For heat exchanger plates, the length does not necessarily have to be the particle displacement distance of the gas if the reason of choosing that length was to avoid unnecessary heat pumping effects over the plate as described in Swift 1988. The current study showed that there can be a heat pumping effect on plates as short as half of the particle displacement distance. In terms of energy dissipation, plate spacing is a more crucial factor since energy dissipation increases quadratically with the plate spacings but it increases only linearly with the plate length.

Chapter 9

Conclusion and recommendations

The current work is one of the first attempts to investigate and improve heat exchangers in thermoacoustic engines. In the course of this attempt, second law analysis for heat exchangers in thermoacoustic engines was developed and its validity discussed.

Following this, numerical simulations of thermoacoustic couples under various operating conditions were carried out using the commercial software PHOENICS, which is capable of solving the full Navier Stokes equations. The results indicated some new facts regarding heat pumping effects in the thermoacoustic couple that are useful for the design of heat exchangers in thermoacoustic engines that had never previously been discussed in the literature. Details of these facts are summarized in section 9.1.

The current work considered oscillatory boundary conditions required to simulate only the heat exchanger plate while taking account of a regenerator being next to the heat exchanger. The simulation of the heat exchanger section alone had never been attempted previously due to the complexity of the boundary conditions. The purposes of simulating only the heat exchanger region were to reduce the computational time and to be able to see how conditions there affect the performance of heat exchangers.

Although the boundary conditions considered were not capable of simulating the heat exchanger plate under all operating conditions, findings from this attempt will be useful for future work. Details of the heat exchanger simulations are summarized in section 9.2.

As this work was one of only a few to investigate the thermoacoustic engines numerically and to consider the design of heat exchangers, a number of issues remain which need to be improved, particularly in the numerical simulations. More experimental work is also required to justify the numerical simulations. Further work which is required to fulfill the goal of establishing the design strategy for heat exchangers in thermoacoustic engines is discussed in section 9.3.

9.1 On the numerical simulation of thermoacoustic couple

Thermoacoustic couple simulations were carried out for various drive ratios (or Mach numbers) and plate spacings. Mean pressures and plate location were also varied.

The oscillatory boundary condition used for thermoacoustic couple simulation emulated the conditions of an ideal standing wave, yet allowed energy flux. The current work clearly showed that the standing wave boundary conditions must not be located too close to the thermoacoustic couple plate because the flow field near the plate is strongly y-dependent and the time dependency is not sinusoidal. The forcing of the standing wave condition too close to the plate lead to an incorrect model of a thermoacoustic couple plate in a standing wave. Tests in the current work also indicated poor convergence when the standing wave conditions were applied close to the plate.

Even when the standing wave boundary conditions were located far enough away, that specifying them further away did not change the simulation results, there were some issues with energy dissipation in the simulation domain. Because in the current work allowed energy flux to go through only the plate and the oscillatory boundary, any energy dissipation within the simulation domain had to leave through the plate. In order to maintain the energy balance of the simulation domain, the same amount of energy must pass through the oscillatory boundary as exits through the plate. For thermoacoustic couple simulations, the energy flux though the oscillatory boundary was equal to the energy dissipation in the domain. However, when simulating heat exchangers, using boundary conditions which enable a heat flux to be carried by convection, it became difficult to clearly distinguish between the energy flux by convection and dissipation at the oscillatory boundary. The limited accuracy of the software also adds to the difficulty of this problem, because the energy flux is a second order quantity (which is a consequence of the interaction of pressure, velocity, temperature and density fluctuations), and the number of the significant figures used in PHOENICS was limited to single precision.

It is suggested that when simulating thermoacoustic effects, where second order energy fluxes (particularly time averaged quantities) are the principal interest, a code written in double precision or higher precision should be used. (Single precision was sufficient for the standing wave simulations, because the energy flux was not of concern.)

Despite the limitation of the code being used, there was sound agreement between test cases simulated in the current work and analytical solutions and between the current work and the numerical simulation of Cao *et al.* (1996) at the operating conditions and geometries where the analytical solutions and the results of Cao *et al.* are appropriate.

In the current work thermoacoustic couple conditions that have not previously been simulated were investigated. These include cases with plate spacings as small as the thermal penetration depth and the plate lengths as short as half of the particle displacement distance.

The simulation results showed that a heat pumping effect can be seen not only on the long plates but also on the shortest plates tested when plate spacings are greater than the thermal penetration depth. As the plate spacing approaches the thermal penetration depth, energy dissipation near the plate increases quadratically and no heat pumping effect can be observed. Energy dissipation was uniform over the plate.

Time averaged heat transfer to and from the plates was concentrated at the edges of the plates for all test cases. The width of the region where there was substantial heat transfer, was proportional to the particle displacement distance when tested at various Mach numbers with large plate spacing. At constant Mach numbers, this width decreased as the plate spacing was reduced.

Particle traces for the test case with the largest plate spacing and a long plate showed evidence of a larger scale vortical motion outside both edges of the plate. The short plate simulations also indicated this vortical motion outside the plates. In addition, particle traces indicated that the gas between the plate surface and the symmetrical boundary prescribes a path with a loop in it. However, to confirm the presence of vortical motion out side the plates (especially for the short plate), more particles should be traced, and visualization experiments are required. As the plate spacing was reduced, indications of the vortical motion disappeared.

The appearance of vortical motion does not coincide with the plate spacing at which the characteristic of cycle-averaged heat flux changed from being out of the plate at one end to into the plate at each end.

A number of suggestions for the design of regenerators and heat exchangers can be drawn from these simulation results. The results showed that in terms of the total amount of heat pumped, it is not necessary to have plates longer than four times the particle displacement distance. Any extra surface area contributes to energy dissipation. However, when a certain temperature difference is required along the plate, as is the case of the regenerator plate, short plates will result in large temperature gradients along the plate, in which case there will be heat conduction losses along the plate.

For the design of heat exchangers, plate spacing of the order of the thermal penetration depth as suggested by Hofler may not be appropriate since the energy dissipation increase with the inverse square of the plate spacing. Plate length on the other hand is less crucial in energy dissipation as it is only proportional to the plate surface area. Therefore, plate spacing should be determined carefully using second law analysis.

9.2 On the numerical simulation of heat exchangers

In order to simulate heat exchanger plates, the oscillatory boundary was placed very close to the plate. Both y-dependent and non y-dependent boundary conditions with various degrees of approximation were considered to try to specify conditions at the heat exchanger-regenerator junction. In all cases, purely sinusoidal time dependency was assumed.

Y-averaged conditions were considered appropriate in cases where the heat exchanger and regenerator plates are not aligned and both components had small spacings. On the other hand, as the thermoacoustic couple simulations indicated, an inaccurate specification of the boundary conditions close to the plates could cause poor convergence.

Oscillatory boundary conditions were tested by changing the temporal phase of temperature. Simulations seemed valid (in terms of the energy balance for the simulation domain) only for the plate spacing of the order of the thermal penetration depth when the simplest, y-averaged, oscillatory boundary condition were applied. However, there was a discontinuity in energy vectors near the open boundary.

For simulation results with larger plate spacings or ones using y-dependent boundary conditions, although they were acceptable in terms of the energy balance for the simulation domain (given the accuracy of the code), energy vector plots indicated a lack of convergence near the open boundary.

9.3 Future work

Having attempted simulations of thermoacoustic couples and heat exchangers in thermoacoustic engines, some suggestions for future work are as follows.

As an extension of simulations in the current work, more particles need to be traced near the plate. In particular particles near the plate edges should be traced over more cycles. The distribution of energy dissipation should also be investigated.

To find exact boundary conditions that are appropriate at the heat exchanger-regenerator junction for heat exchanger simulations, it would be necessary to simulate an entire thermoacoustic device, including a minimum of two heat exchangers and a regenerator, and to monitor the pressure, temperature and velocity at the heat exchanger-regenerator junction. This is still a challenge numerically and the small length scales make it difficult to measure experimentally using conventional instrumentation. Investigation of acoustic streaming and turbulence inside thermoacoustic devices is also important.

After these investigations, a method of simulating the heat exchanger section alone should be re-considered in order to develop a better heat exchanger model. Second law analysis should become useful only after an improved heat exchanger model is developed.

Appendix A

Unit used in the current simulation

In this appendix, typical operating conditions, geometries and some important variables from Swift (1992) are listed in SI unit and in units using cm, g and cs (centi second).

Variables	Magnitude	SI unit	Magnitude	[cm,g,cs]
x	3.0E0	[m]	3.0E2	[cm]
Δx	1.1E-3	[m]	1.1E-1	[cm]
y	2.0E-4	[m]	2.0E-2	[cm]
Δy	4.0E-5	[m]	4.0E-3	[cm]
t	8.3E-3	[s]	8.3E-1	[cs]
dt	1.7E-5	[s]	1.7E-3	[cs]
f	1.2E2	[1/s]	1.2E0	[1/cs]
u	2.9E0	[m/s]	2.9E0	[cm/cs]
p_m	1.4E6	[N/m^2]=[Kg/s^2m]	1.4E3	[g/cs^2cm]
ρ	6.8E-1	[kg/m^3]	6.8E-4	[g/cm^3]
ν	6.3E-5	[m^2/s]	6.3E-3	[cm^2/cs]
μ	1.8E-5	[kg/m·s]	1.8E-6	[g/cm· cs]
c_p	5.2E3	[J/kgK]=[m^2/s^2K]	5.2E3	[cm^2/cs^2K]
R	2.1E3	[J/kg·K]=[m^2/ks^2]	2.1E3	[cm^2/Kcs^2]
K	3.1E-1	[W/m·K]=[$kg \cdot m/s^3 \cdot K$]	3.1E-2	[g·cm/cs^3 K]
Q	6.0e2	[W]=[Kg·m^2/s^3]	6.0e3	[$g \cdot cm^2/cs^3$]

Table A.1: Magnitudes of variables using cm, g and cs.

Appendix B

Results tables

This appendix contains tables B.1, B.2 and B.3 of simulation results described in chapter 6, 7 and 8 respectively.

ϕ_i	[rad]	0	$\pi/4$	$\pi/2$	π
$\Delta p_{cy}/P_A$	[%]	1.3e-2	1.4e-2	2.8e-2	5.4e-2
$\Delta u_{cy}/u_A$	[%]	1.5e-2	1.4e-2	2.8e-2	4.8e-2
$\Delta T_{cy}/T_A$	[%]	2.1e-2	2.1e-2	3.4e-2	5.5e-2
$\Delta \rho_{cy}/\rho_A$	[%]	1.9e-2	1.7e-2	2.8e-2	5.3e-1
$\Delta Tb_{cy}/T_A$	[%]	1.9e-3	2.0e-2	2.0e-2	7.5e-3
p_{err}/p_A	[%]	9.7e-1	9.7e-1	9.8e-1	9.6e-1
u_{err}/u_A	[%]	9.0e-1	8.9e-1	9.0e-1	8.9e-1
T_{err}/T_A	[%]	1.2e0	1.2e0	1.1e0	1.1e0
$\dot{E}x_{cen}$	[W]	-1.4e-1	-1.4e-1	-1.4e-1	-1.3e-1
$\dot{E}x_{BC34}$	[W]	-1.4e-1	-1.4e-1	-1.4e-1	-1.4e-1
ex_{ABC34}	[W/m^2]	2.8e4	2.8e4	2.8e4	2.8e4
$\dot{S}_{gen}T_0$	[W]	2.1e-7	2.1e-7	2.1e-7	2.1e-7
$\Delta P_A/P_A$	[%]	1.7e0	1.7e0	1.7e0	1.6e0
Cycles		40	40	39	33
$\Delta x/\lambda$		2.1e-3	2.1e-3	2.1e-3	2.1e-3
$\Delta y/\delta_{km}$		2.1e-1	2.1e-1	2.1e-1	2.1e-1

Table B.1: Results with various starting temporal phase of oscillatory boundary conditions when the domain length is $5\lambda/32$ for case 1 (in table 6.1) with Δt=0.42%. ϕ_i is the initial time phase offset for p,u and T.

Run		27	28	29
$\frac{x_4-x_5}{2u_1/\omega}$		1.1e-1(1 cell)	1.9e0	3.8e0
$\Delta p_{cy}/P_A$	[%]	4.9e-3	1.5e-2	6.5e-3
$\Delta u_{cy}/u_A$	[%]	4.6e-3	1.5e-2	6.4e-3
$\Delta T_{cy}/T_A$	[%]	5.0e-2	5.6e-2	4.7e-2
$\Delta \rho_{cy}/\rho_A$	[%]	3.2e-2	5.1e-2	3.6e-2
$\Delta Tb_{cy}/T_A$	[%]	3.6e-2	4.3e-2	2.7e-2
u_{err}/u_A	[%]	2.6e-1	2.3e1	2.4e1
T_{err}/T_A	[%]	3.1e0	1.3e0	1.4e0
$\dot{Q}_{pl}$	[W]	7.7e-2	2.4e-1	2.3e-1
$\dot{E}y_{pl}$	[W]	7.1e-2	2.3e-1	2.2e-1
$\dot{E}x_{cen}$	[W]	-1.9e-3	-2.2e-3	-2.1e-2
$\dot{E}x_{BC34}$	[W]	-1.3e-1	-1.3e-1	-1.2e-1
q_A	[W/m^2]	2.3e2	2.8e2	2.7e2
ex_{ABC34}	[W/m^2]	9.8e2	8.2e2	8.1e2
H_x	[W/m^2]	-3.5e3	-3.5e3	-3.5e3
H_y	[W/m^2]	-1.1e1	-1.1e1	-1.1e1
$\dot{Q}_{Error}$	[%]	1.4e0	2.4e0	2.2e0
$\dot{E}_{diss}pl$	[W]	6.3e-2	6.3e-2	6.3e-2
$\dot{S}_{gen}T_0$	[W]	2.1e-1	2.4e-1	2.4e-1
$\Delta P_A/P_A$	[%]	8.7e-1	9.2e-1	9.7e-1
Cycles		26	25	35

Table B.2: Dependence of the simulation results on the location of the oscillatory boundary, when y_0=$\delta_{km}/2$. $2u_1/\omega$=2.28cm when evaluated at the plate outer edge. Plate length, L = 24.5cm, δ_{km} = 0.242 and $\Delta x/\lambda$=2.5e-4, $\Delta y/\delta_{km}$=2.1e-2.

MODE		Prime mover		Heat pump
BC34-1 ϕ_{PT}	[deg.]	-144	-168	36.2
Spacing		$\delta_{km}/2$	$3\delta_{km}$	$\delta_{km}/2$
$\Delta p_{cy}/P_A$	[%]	5.9e-3	1.4e-2	1.3e-2
$\Delta u_{cy}/u_A$	[%]	7.3e-3	1.8e-2	1.7e-2
$\Delta T_{cy}/T_A$	[%]	7.7e-2	7.0e-2	6.9e-2
$\Delta \rho_{cy}/\rho_A$	[%]	5.0e-2	4.9e-2	5.2e-2
$\Delta Tb_{cy}/T_A$	[%]	6.2e-2	5.5e-2	5.5e-2
u_{err}/u_A	[%]	4.0e0	6.7e0	4.0e0
T_{err}/T_A	[%]	3.8e-1	1.9e1	3.0e-1
$\dot{Q}_{pl}$	[W]	1.7e-2	4.8e0	6.2e-1
$\dot{E}y_{pl}$	[W]	-3.5e-2	4.4e0	5.7e-1
$\dot{E}x_{cen}$	[W]	-3.4e-2	-2.1e-1	-3.4e-2
$\dot{E}x_{BC34}$	[W]	5.8e-1	3.4e0	-5.7e-1
q_A	[W/m^2]	1.9e3	3.2e3	1.9e3
ex_{ABC34}	[W/m^2]	9.8e3	2.4e4	1.0e4
H_x	[W/m^2]	-3.6e5	-9.7e4	-3.6e5
H_y	[W/m^2]	-8.9e2	-5.5e2	-8.9e1
$\dot{Q}_{Error}$	[%]	1.2e0	1.1e1	4.6e-3
$\dot{E}_{diss}pl$	[W]	6.0e-2	1.1e-1	6.0e-2
$\dot{S}_{gen}T_0$	[W]	3.1e-1	1.2e-1	3.1e-1
$\Delta P_A/P_A$	[%]	4.3e-1	-3.4e0	4.0e-1
Cycles		25	34	27
$\Delta y/\delta_{km}$		4.2e-2	8.3e-2	4.2e-2

Table B.3: Operating mode test using BC34-1 with the larger temperature amplitude. Γ=1.6 and 0.4 for prime mover and heat pump mode respectively. $\Delta x/\lambda$=2.5e-4

Appendix C

Investigation of spikes in energy flux distributions near the plate

Small tests are made in this appendix to investigate the cause of spikes observed in the time averaged energy flux density just out side of plate edges.

In section 7.6.3, plots of the y-component of energy flux density from the simulation results of Cao *et al.* and of the current work in figure 7.17 show sound agreement. However, one notable difference is that in the current simulations, spikes that appeared at just outside the plate edges in Cao *et al.* appeared only on the outer edge of the plate.

The spikes can be considered as a pure numerical error as the boundary just outside the plate lies on the symmetrical boundary where there should not be any energy flowing in the y-direction. Although the spike has no physical meaning and its magnitudes are not significant, the cause of the spikes are investigated to ensure that it is not a serious problem with serious nature.

The fact that the spike appears on the side, where oscillatory boundary conditions are specified, suggests that the spike is caused by forcing the ideal boundary condition too close to the plate outer edge. (Cao *et al.* (1996) specifies oscillatory boundary conditions on both sides of plate edges and the spikes appear just outside both edges of the plate as in Figure 4 of Cao *et al.* (1996).) This can be checked by moving the oscillatory boundary conditions further away from the plate edge, which was done in section 7.5.2 with the results shown in figure 7.7. The figure is enlarged near the plate outer edge and shown in figure C.1 for runs 3 to 5. In all cases, spikes appeared and the location of the oscillatory boundary conditions did not affect the presence of magnitude of the spikes. The slight offset in peak positions coincides with the offset of the x-coordinate of grid center for each case.

In order to see if there is any discontinuity in the y-component of the energy flux near where the spikes are, the instantaneous plot of the y-component energy flux near the inner and the outer plate edge are displayed in figure C.3 and C.4 respectively. Non-zero values outside the plate edges in both figures are numerical errors because ideally there

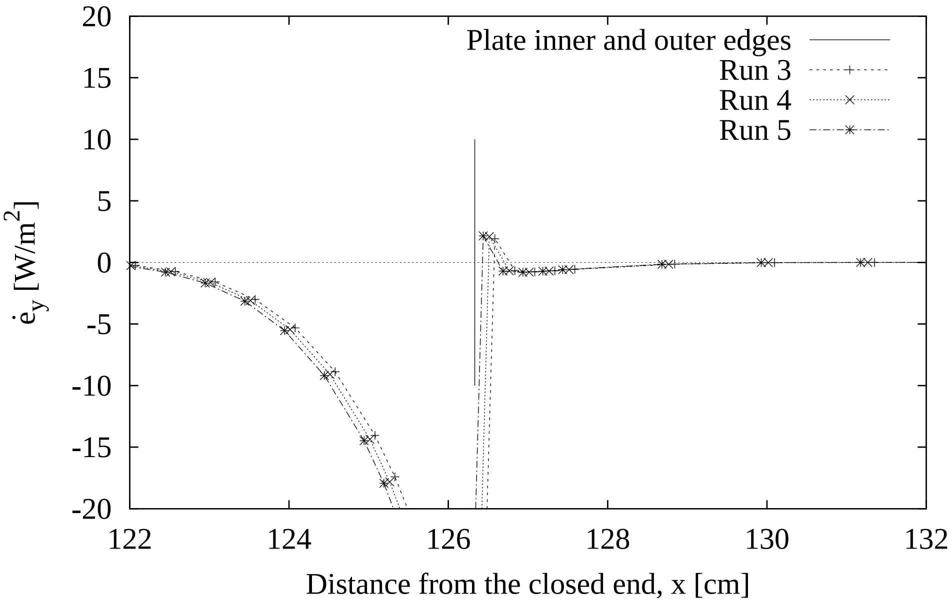

Figure C.1: Enlarged figure 7.7 at outer plate edge

is no energy flux in the y-direction through the symmetrical boundary. The amplitude of fluctuation of e_y on the cell just outside the outer plate edge is approximately twice as much as that of inner plate edge. The errors outside of both edges of the plate are larger on the positive side (in y-direction). This is reflected in the time averaged e_y at the inner plate edge as shown in figure C.4, where e_y near the plate outer edge has a smoother transition. Because the peaks of time averaged e_y are in opposite directions, the error appears as a small spike at just outside of the plate outer edge.

As described in section 5.2.3, the differences in the current model and the model of Cao *et al.* is the fact that the oscillatory boundary conditions are forced only on one side of the plate and the simulation domain is extended to the rigid end of the other side. However, tests in this appendix do not show that it is caused from forcing oscillatory boundary conditions close to the plate outer edges and that the spikes are not of a serious nature. In order to further investigate, more details of the results of Cao *et al.* (1996) such as instantaneous plots of energy flux density would be needed.

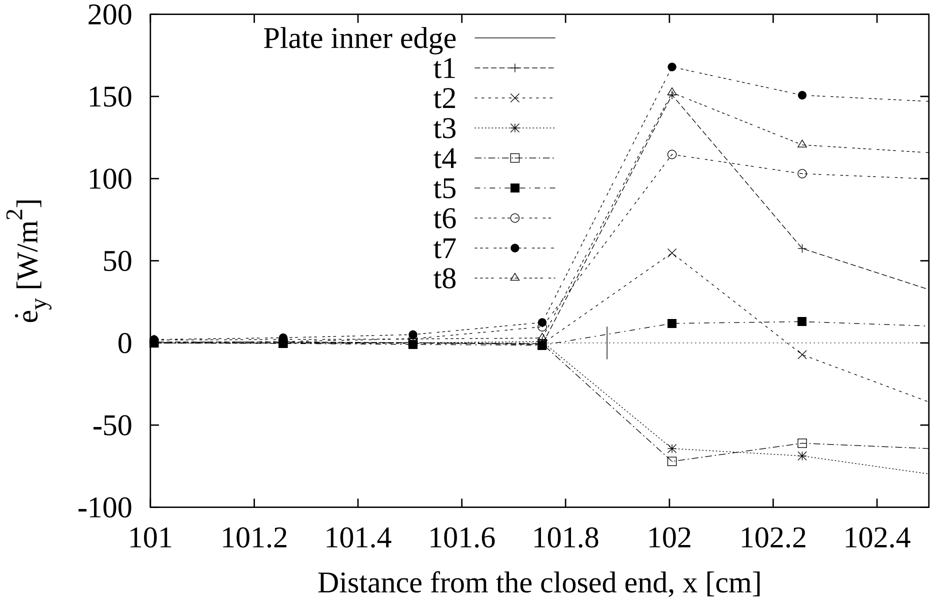

Figure C.2: Instantaneous energy flux density at the plate surface of run 17, enlarged at the inner edge of the plate.

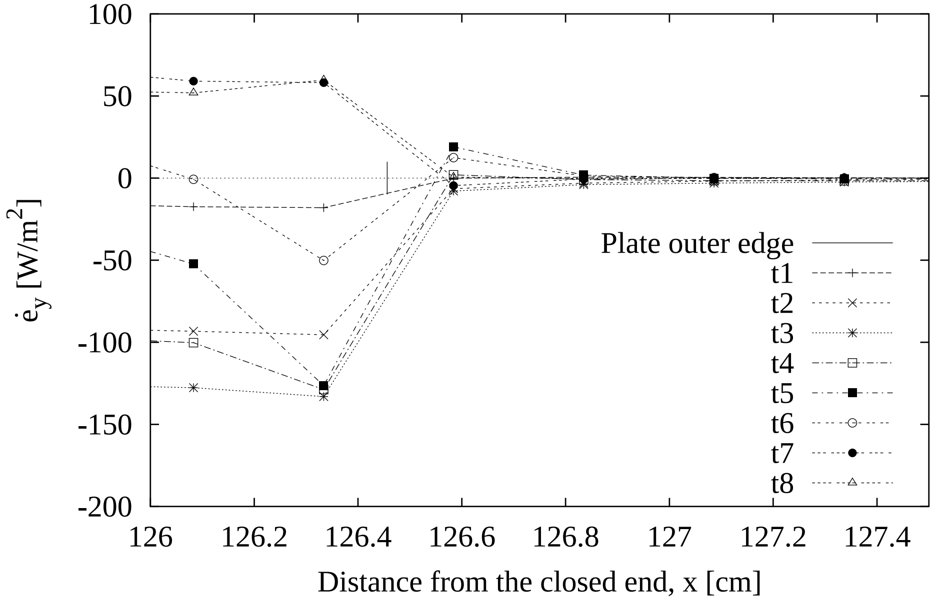

Figure C.3: Instantaneous energy flux density at the plate surface of run 17, enlarged at the outer edge of the plate

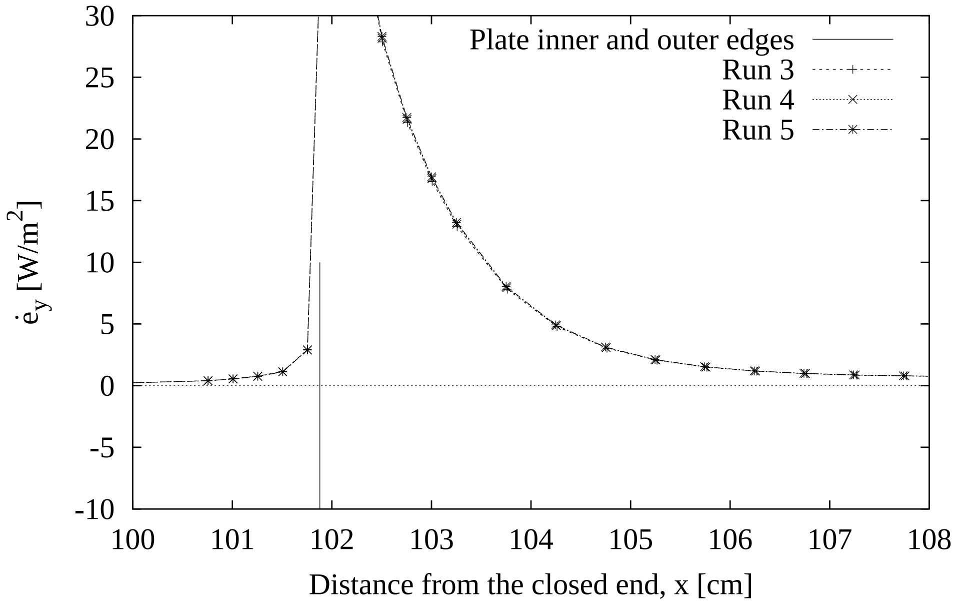

Figure C.4: Enlarged figure 7.7 at inner plate edge

Bibliography

Aggarwal, S. K. and Manhapra, A. (1989). Use of heatlines for unsteady buoyancy-driven flow in a cylindrical enclosure. *Transactions of the ASME*, 111:576–578.

Ahn, K. H. and Ibrahim, M. (1991). A 2-d oscillating flow analysis in stirling engine heat exchangers. *NASA Technical report*, pages 1–7. Report No. NASA TM - 103781 ICOMP-91-04.

Alefeld, G. (1987). Efficiency of compressor heat pumps and refrigerators derived from the second law of thermodynamics. *Rev.Int.Froid*, 10:331–341.

Alefeld, G. (1989). Second law analysis for an absorption chiller. *Newsletter of the IEA Heat Pump Center*, 7(2):54–57.

Alefeld, G. (1990). What are thermodynamic losses and how to measure them ? In *A FUTURE FOR ENERGY*, pages 271–279, Firenze, Italy. Proceedings of the Florence World Energy Research Symposium.

Anderson, D. A., Tannehill, J. C., and Pletcher, R. H. (1984). *Computational Fluid Mechanics and Heat Transfer*. Hemisphere Publishing Corporation, New York.

Arnott, W. P., Rapset, R., and Bass, H. E. (1991). General formulation of thermoacoustics for stacks having arbitrarily shaped pore cross sections. *J. Acoust. Soc. Am.*, 90(6):3228–3237.

Atchley, A. A. (1988). Acoustically generated temperature gradients in short plates. *J. Acoust. Soc. Am.*, 84:S36, Suppl. 1.

Atchley, A. A. (1989). The measurement of thermoacoustic phenomena using thermoacoustic couples. *J. Acoust. Soc. Am.*, 86:S109, Suppl. 1.

Atchley, A. A., Bass, H. E., and Hofler, T. J. (1990). Development of nonlinear waves in a thermoacoustic engine prime mover.

Barrett and *et al.* (1994). *TEMPLATES for The Solution of Linear Systems:Building Blocks for Iterative Methods.*

Bejan, A. (1982a). *Entropy generation through heat and fluid flow.* John Wiley & Sons, Inc., New York.

Bejan, A. (1982b). Second law analysis in heat transfer and thermal design. *Advances in heat transfer*, 15:1–58.

Bejan, A. (1987). The thermodynamic design of heat and mass transfer processes and devices. *Heat and Fluid Flow*, 8(4):258–275.

Bird, R. B., Stewart, W. E., and Lightfoot, E. N. (1960). *Transport Phenomena.* John Wiley & Sons, Inc., New York.

Cao, N., Olson, J. R., Swift, G. W., and Chen, S. (1996). Energy flux density in a thermoacoustic couple. *J. Acoust. Soc. Am.*, 99(6):3456–3464.

Carmody, S. A. and Shelton, S. V. (1993). Direct second law analysis of advanced absorption cycles utilizing an ideal solution model. volume 31, pages 369–373. International Absorption Heat pump Conference ASME 1993.

CHAM Development Team (1991a). *TR140 - The PHOTON User Guide.* CHAM, Bakery House, 40 High Street, Wimbledon Village, London SW19 5AU, UK.

CHAM Development Team (1991b). *TR141 - The AUTOPLOT User Guide.* CHAM, Bakery House, 40 High Street, Wimbledon Village, London SW19 5AU, UK.

CHAM Development Team (1991c). *TR200a - The PHOENICS Reference Manual Part a:PIL.* CHAM, Bakery House, 40 High Street, Wimbledon Village, London SW19 5AU, UK.

CHAM Development Team (1991d). *TR200b - The PHOENICS Reference Manual Part b:FORTRAN.* CHAM, Bakery House, 40 High Street, Wimbledon Village, London SW19 5AU, UK.

Chapman, S. and Cowling, T. G. (1970). *The mathematical theory of non-uniform gases.* Cambridge University Press, London, 3rd edition.

Coppens, A. B. and Sanders, J. V. (1968). Finite amplitude standing waves in rigid walled tubes. *J. Acoust. Soc. Am.*, 43(3):516–529.

Dean, C. E., Grassmayer, W. A., Smith Jr., J. L., and Lienhard, J. H. (1993). Experiments on heat transfer under conditions of oscillating pressure and flow. Presented at ASME Winter Annual Meeting, New Orleans, Louisiana.

Devalba, M. and Rispoli, F. (1991). Conjugate heat transfer in oscillating fluid flow in a stirling engines. *IECEC 91' 26th*, 5:170–175.

Draoui, A., Allard, F., and Beghein, C. (1991). Numerical analysis of heat transfer by natural convection and radiation in participating fluids enclosed in square cavities. *Numerical heat transfer, Part A*, 20:253–261.

Ferziger, J. H. and M.Perić (1997). *Computational methods for fluid dynamics.* Springer.

Fischer, S. K. (1993). Total equivalent warming impact: a measure of the global warming impact of CFC alternatives in refrigerating equipment. *Int.J.Refrig.*, 16(6):423–428.

Gabrielson, T. B. (1991). Development of a thermoacoustic transducer for generation of underwater sound. *J. Acoust. Soc. Am.*, 90(5):2628–2636.

Gaitan, D. F., Gopinath, A., and Atchley, A. A. (1994). Experimental study of acoustic turbulence and streaming in a thermoacoustic stack. *J. Acoust. Soc. Am.*, 96(5):Pt.2, 3220.

Garrett, S. L. (1992). Thermoacoustic refrigerators. *J. Acoust. Soc. Am.*, 91(1):517–518.

Garrett, S. L. (1993a). Thermoacoustic refrigeration. Breckenridge Hilton, Breckenridge, CO. AFEAS workshop.

Garrett, S. L. (1993b). Thermoacoustic refrigerators for space applications. *Journal of Thermophysical and Heat Transfer*, 7(4):595–599.

Gedeon, D. (1986). Mean-parameter modeling of oscillating flow. *Transactions of the ASME*, 108:513–518.

Godshalk, K. M. (1991). Miniaturization of a thermoacoustic pressure wave generator. *Advances in Cryogenic Engineering*, 37:955–961. Part B.

Goldstein, S., editor (1965). *Modern developments in fluid dynamics.* Dover Publications Inc., New York. Composed by the Fluid motion panel of the aeronautical research committee and others.

Gopinath, A. (1992). *Convective heat transfer in acoustic streaming flows.* PhD thesis, University of California, Los Angeles.

Herman, C. and Wetzel, M. (1998). Expanding the applications of holographic interferometry to the quantitative visualization of oscillatory thermofluid processes using temperature as tracer. *Experiments in Fluids*, 24:431–446.

Herman, C., Wetzel, M., and Volejinik, M. (1994). Experimental visualization of heat transfer and fluid flow processes in a thermoacoustic device. *J. Acoust. Soc. Am.*, 96(5):Pt.2, 3220.

Hevert, H. W. and Hevert, S. C. (1980). Second law analysis: An alternative indicator of system efficiency. *Energy*, 5:865–873.

Hino, M., Kashiwayanagi, M., Nakayama, A., and Hara, T. (1983). Experiments on the turbulence statistics and the structure of a reciprocating oscillatory flow. *J.Fluid Mech.*, 131:363–400.

Hino, M., Sawamoto, M., and Takasu, S. (1976). Experiments on transition to turbulence in an oscillatory pipe flow. *J.Fluid Mech.*, 75(2):193–207.

Hiramatsu, M., Ishimaru, T., and Ohkouchi, T. (1991). Numerical analysis on inner - fins for intercooler. *Nihon Kikai gakkai*, 57(539):176–182.

Hofler, T. J. (1986). *Thermoacoustic refrigerator design and performance.* PhD thesis, University of California, San Diego.

Hofler, T. J. (1988). Accurate acoustic power measurements with a high-intensity driver. *J. Acoust. Soc. Am.*, 83(2):777–786.

Hofler, T. J. (1990). Performance of a short parallel plate thermoacoustic stack with arbitrary plate separation. volume 88, page S94.

Hofler, T. J. (1994). Numerical study of various thermoacoustic refrigerator configurations. *J. Acoust. Soc. Am.*, 96(5):3220.

Huelsz, G. and Ramos, E. (1995). On the phase difference of the temperature and pressure waves in the thermoacoustic effect. *International Communication in Heat and Mass Transfer*, 22(1):71–80.

Ibrahim, M., Hashim, W., Tew, R. C., and Dudenhoefer, J. E. (1992). Heat transfer in oscillating flows with sudden change in cross section. *IECEC 92'*, pages 5.503–5.508.

Ibrahim, M. and Kannapareddy, M. (1991). Instantaneous heat transfer coefficient based upon two-dimensional analyses of stirling space engine components. *IECEC 26th*, 6:149–159.

Ibrahim, M., Tew, R. C., and Dudenhoefer, J. E. (1989). Further two-dimensional code development for stirling engine space engine components. *IECEC 25th 89'*, 6:329–335.

Ishikawa, H. and Hobson, P. A. (1996). Optimization of heat exchanger design in a thermoacoustic engine using a second law analysis. *International Communication in Heat and Mass Transfer*, 23(3):325–334.

Jeong, E. S. (1995). Effects of axial temperature gradient on momentum and heat transfer with oscillating pressure and flow. *KSME Journal*, 9(2):225 – 239.

Jeong, E. S. and Smith Jr., J. L. (1992). An analytic model of heat transfer with oscillating pressure. *General papers in Heat transfer ASME*, 204:97–104.

Kawahashi, M. and Arakawa, M. (1996). Nonlinear phenomena induced by finite amplitude oscillation of air column in closed duct. *JSME International Journal, Series B*, 39(2):280–286.

Kawamoto, A., Ozawa, M., and Arikawa, F. (1997). Temperature distribution along stack in an acoustic resonance tube (discussion on advanced linearized theory). *Nihon kikai gakkai B*, 63(605):290–298.

Kimura, S. and Bejan, A. (1983). The "heat line" visualization of convective heat transfer. *Transactions of the ASME*, 105:916–919.

Kinsler, L. E. and Frey, A. R. (1962). *Fundamentals of acoustics.* John Wiley & Sons, Inc., New York, second edition.

Koehler, W. J., Patankar, S. V., and Ibele, W. E. (1990). Numerical prediction of turbulent oscillating flow in a circular pipe. *IEEE 90'*, 5:398–406.

Kornhauser, A. A. and Smith Jr., J. L. (1988). Application of a complex nusselt number to heat transfer during compression and expansion. pages 1–8. Presented at The Winter Annual Meeting of The America Society of Mechanical Engineers, Chicago, Illinois.

Kornhauser, A. A. and Smith Jr., J. L. (1989a). Application of a complex nusselt number. *IECEC 89*, 89(5):2347–2353.

Kornhauser, A. A. and Smith Jr., J. L. (1989b). Heat transfer with oscillating pressure and oscillating flow. *IECEC 89*, 89(5):2347–2353.

Kotas, T. J. and Shakir, A. M. (1986). Exergy analysis of a heat transfer process at subenvironmental temperature. *Computer-Aided Engineering of Energy Systems*, 3:87–92.

Kunihiro, K., Kawamoto, A., and Ozawa, M. (1998). Flow visualization of acoustic streaming in a resonance tube with stack. *35th Japan heat transfer symposium paper collection*, pages 843–844.

Kuzmina, A. G. (1992). Thermoacoustic oscillations in cyrostats: new results. *Cryogenics*, 32(1):11–19.

Lamb Sir, H. (1932). *Hydrodynamics.* Cambridge University Press, Cambridge, sixth edition.

Landau, L. D. and Lifshitz, E. M. (1959). *Fluid Mechanics.* Pergamon press, London.

Lee, K. P. (1983). A simplistic model of cyclic heat transfer phenomena in closed spaces. *18th IECEC*, pages 720–723.

Majumdar, D. and Amon, C. H. (1991). Heat and momentum transport in oscillatory viscous flows. *Heat Transfer in Unsteady flows*, 158:1–8.

Merkli, P. and Thomann, H. (1975). Transition to turbulence in oscillating pipe flow. *J.Fluid Mech.*, 68:567–575.

Migliori, A. and Swift, G. W. (1988a). Liquid-sodium thermoacoustic engine. *Appl. Phys. Lett.*, 53(5):355–357.

Migliori, A. and Swift, G. W. (1988b). Performance of liquid-sodium thermoacoustic engine. *J. Acoust. Soc. Am.*, 84(Suppl.1):S37.

Minner, B. L., Braun, J. E., and Mongeau, L. C. (1997). Theoretical evaluation of the optimal performance of a thermoacoustic refrigerator. Number PH-97-12-2, pages 873–887. ASHRAE Transactions:Symposia.

Morse, P. M. and Ingard, K. U. (1986). *Theoretical acoustics.* Princeton University Press, New Jersey.

Mozurkewich, G. (1995). Heat transfer from a cylinder in an acoustic standing wave. *J. Acoust. Soc. Am.*, 98(4):2209–2216.

Nyborg, W. L. M. (1965). *Physical Acoustics, Volume IIB.* Academic Press.

Ohmi, M. and Iguchi, M. (1982). Critical reynolds number in an oscillating pipe flow. *Bulletin of JSME*, 25(200-4):165–172.

Ohmi, M., Iguchi, M., Kakehashi, K., and Masuda, T. (1982). Transition to turbulence and velocity distribution in an oscillating pipe flow. *Bulletin of JSME*, 25(201):365–371.

Olson, J. R. and Swift, G. W. (1996). Energy dissipation in oscillating flow thorough straight and coiled pipes. *J. Acoust. Soc. Am.*, 1(1):un.

Olson, J. R. and Swift, G. W. (1997). Acoustic streaming in pulse tube refrigerators: Tapered pulse tubes. *Cryogenics*, 37:769–776.

Oshida, I. and Fujishiro, T. (1991). *Netsurikigaku (Thermodynamics).* Shoukabou, Tokyo, 23 edition.

Ozawa, M. (1997). Onpa de kitai wo reikyaku suru. *Cho-onpa TECHNO '97.6.*, pages U01–04.

Ozawa, M. and Kawamoto, A. (1991). Lumped parameter modeling of heat transfer enhanced by sinusoidal motion of fluid. *International Journal in Heat and Mass Transfer*, 34(12):3083–3094.

Ozawa, M., Kunihiro, K., and Kawamoto, A. (1999). Flow visualization of acoustic streaming in a resonance tube refrigerator. *Technology Reports of Kansai University, March*, (41):35–44.

Patankar, S. V. (1981). A calculation procedure for two dimensional elliptic problems. *Numerical Heat Transfer*, 4:409–426.

Patankar, S. V. and Spalding, D. B. (1972). A calculation procedure for heat, mass and momentum transfer in three-dimensional parabolic flows. *International Journal in Heat and Mass Transfer*, 15:1787–1806.

Pfriem, H. (1940). Periodic heat transfer at small pressure fluctuations. Technical Report NACA-TM-1048, National Advisory Committee for Aeronautics.

Pierce, A. D. (1989). *Acoustics.* Acoustical Society of America, New York, second edition.

Rayleigh, J. W. S. (1878). The explanation of certain acoustical phenomena. *Nature*, 18:319–321.

Rott, N. (1969). Damped and thermally driven acoustic oscillations in wide and narrow tubes. *Z.Angew Math. Phys.*, 20:230–243.

Rott, N. (1973). Thermally driven acoustic oscillations. part ii:stability limit for helium. *J.Appl.Math.Phys. (ZAMP)*, 24:54–72.

Rott, N. (1974). The heating effect connected with non-linear oscillations in a resonance tube. *J.Appl.Math.Phys. (ZAMP)*, 25:619–634.

Rott, N. (1975). Thermally driven acoustic oscillations, part iii : Second-order heat flux. *J.Appl.Math.Phys. (ZAMP)*, 26:43–49.

Rott, N. (1980). Thermoacoustics. *Adv. in Appl. Mech*, 20:135–175.

Rott, N. and Zouzoulas, G. (1976). Thermally driven acoustic oscillations, part iv:tubes with variable cross section. *ZAMP*, 27:197–224.

Sergeev, S. I. (1966). Fluid oscillations in pipes at moderate reynolds numbers. *Fluid Dynamics*, 1:21–22.

Simon, T. W. and Seume, J. R. (1988). A survey of oscillating flow in stirling engine heat exchangers. *NASA Contractor Report 182108.*

Smith, A. L. (1993). *The development of a model for oscillating heat transfer within a thermoacoustic engine.* Under graduate thesis, The University of Queensland, Brisbane.

Smith Jr., J. L., Lienhard, J. H., Alexander, V., Tziranis, K., and Ho, Y. (1992). M.I.T. stirling cycle heat transfer apparatus. *27th IEEE*, 5:5.509 – 5.516.

Spalding, D. B. (1991). *The PHOENICS Beginner's Guide TR100.* CHAM, Bakery House, 40 High Street, Wimbledon Village, London SW19 5AU, UK.

Suzuki, K., Xi, G. N., Inaoka, K., and Hagiwara, Y. (1994). Mechanism of heat transfer enhancement due to self-sustained oscillation for an in-line fin array. *International Journal in Heat and Mass Transfer*, 37(Suppl 1):83–96.

Swift, G. W. (1988). Thermoacoustic engines. *J. Acoust. Soc. Am.*, 84(4):1145–1180.

Swift, G. W. (1989). A thermoacoustically driven orifice pulse tube cryocooler. *J. Acoust. Soc. Am.*, 85(Suppl.):S47.

Swift, G. W. (1992). Analysis and performance of a large thermoacoustic engine. *J. Acoust. Soc. Am.*, 92(3):1151–1563.

Swift, G. W. (1994). Personal correspondence.

Swift, G. W. (1997). Thermoacoustic natural gas liquifier. pages LA–UR–97–950, Houston. DOE Natural Gas Conference, can also be found on http://lib-www.lanl.gov/la-pubs/00412750.pdf.

Swift, G. W. and *et al.*(1989). Acoustic cryocooler. *United States Patent (19)*, (19). Patent Number 4,953,366.

Swift, G. W., Migliori, A., Hofler, T., and Wheatley, J. (1985). Theory and calculations for an intrinsically irreversible acoustic prime mover using liquid sodium as primary working fluid. *J. Acoust. Soc. Am.*, 78(2):767–781.

Tang, X. and Cheng, P. (1993). Correlations of the cycle averaged nusselt number in a periodically reversing pipe flow. *International Communication in Heat and Mass Transfer*, 20:161–172.

Tew, R. C. and Geng, S. M. (1992). Overview of NASA supported thermodynamic loss research. *IECEC 1992'*, 5:5.489–5.494.

Tew, R. C., Thieme, L. G., and Dudenhoefer, J. E. (1989). Recent stirling engine loss understanding results. *IECEC 25th 89'*, 5:377–385.

Tominaga, A. (1998). *Nestuonkyo-ko-gaku no kisoko-gaku (Fundamentals Thermoacoustics.* Uchida Rokakuho, Tokyo, 1 edition.

Tomiyama, A., Ichikawa, Y., Morioka, K., and Skaguchi, T. (1991). A numerical method for solving natural convection dominating flows. *Nihon kikai gakkai*, 57(538):128–133.

Tomiyama, A. and Takahashi, R. (1990). Convergence of iterative methods for implicit solution schemes of fluid flows. *Nihon genshiryoku gakkai*, 32(2):85–94.

Versteeg, H. K. and Malalasekera, W. (1995). *An introduction to computational fluid dynamics, The finite volume method.* Longman Scientific & Technical, Longman House, Burnt Mill, Harlow Essex CM20 2JE, England, 1st edition.

Ward, B. and Swift, G. (1993). *Design Environment for Low-Amplitude Thermoacoustic Engine DELTAE Version 1.1 Tutorial and User's Guide.* Los Alamos National Laboratory. Can be accessed on http://www.lanl.gov/thermoacoustic/doc-options.html.

Ward, W. C. and Merrigan, M. A. (1992). Recent developments in thermoacoustically driven low frequency projectors. Transducers for sonic and ultrasonic: Third International workshop.

Watanabe, M., Prosperetti, A., and Yuan, H. (1997). A simplified model for linear and nonlinear processes in thermoacoustic prime movers 1. Model and linear theory. *J. Acoust. Soc. Am.*, 102(6):3484–3496.

Wetzel, M. and Herman, C. (1996). Design issues of a thermoacoustic refrigerator and its heat exchangers. volume 9, pages 137–144. HTD-Vol. 331, National Heat Transfer Conference.

Wheatley, J. (1982). A perspective on the history and future of low-temperature refrigeration. *Physica*, 109 & 110B:1764–1774.

Wheatley, J. and Cox, A. (1985). Natural engines. *Physics Today*, pages 50–58.

Wheatley, J. and *et al.*(1989). Heat-driven acoustic cooling engine having no moving parts. Technical report. U.S. Patent 4,858,441.

Wheatley, J., Hofler, T., Swift, G. W., and Migliori, A. (1983). Experiments with an intrinsically irreversible acoustic heat engine. *Physical review letters*, 50(7):499–502.

Wheatley, J., Hofler, T., Swift, G. W., and Migliori, A. (1985). Understanding some simple phenomena in thermoacoustics with applications to acoustical heat engines. *Am.J.Phys.*, 53(2):147–162.

Wheatley, J., Swift, G. W., and Migliori, A. (1986). The natural heat engine. *Los Alamos Science*, pages 2–29.

Worlikar, A. S. and Knio, O. M. (1996). Numerical modeling of thermoacoustic refrigerator. Part I: Unsteady flow around the stack. *Journal of Computational Physics*, 127(5):424–451.

Worlikar, A. S., Knio, O. M., and Klein, R. (1998). Numerical modeling of thermoacoustic refrigerator ii. stratified flow around the stack. *Journal of Computational Physics*, 144:299–324.

Xiao, J. H. (1995a). Thermoacoustic heat transportation and energy transformation, part 1: Formulation of the problem. *Cryogenics*, 35(1):15–19.

Xiao, J. H. (1995b). Thermoacoustic heat transportation and energy transformation, part 2: Isothermal wall thermoacoustic effects. *Cryogenics*, 35(1):21–26.

Yagyu, S. and Smith Jr., J. L. (1991). A study of gas spring heat transfer for non-sinusoidal piston motion. *Proceedings of ASME 1991*, pages 1–7.

Yazaki, T., Tominaga, A., and Narahara, Y. (1979). Stability limit for thermally driven acoustic oscillation. *Cryogenics*, pages 393–396.

Yazaki, T., Tominaga, A., and Narahara, Y. (1980). Experiments on thermally driven acoustic oscillations of gaseous helium. *Journal of low temperature physics*, 41(1/2):45–60.

Yuan, H., Karpov, S., and Prosperetti, A. (1997). A simplified model for linear and nonlinear processes in thermoacoustic prime movers 1. Nonlinear oscillations. *J. Acoust. Soc. Am.*, 102(6):3497–3506.

Yuan, Z. and Dybbs, A. (1992). Oscillating flow and heat transfer in a stirling engine regenerator. *Fundamentals of heat transfer in a porous media ASME*, 193:73 – 85.